UNIVERSITY OF CALIFORNIA
SANTA CRUZ

CHEMICAL ABUNDANCE TRENDS IN THE MILKY WAY DISK: IMPLICATIONS ON THE ORIGIN OF THE GALACTIC THICK DISK

A dissertation submitted in partial satisfaction of the
requirements for the degree of

DOCTOR OF PHILOSOPHY

in

ASTRONOMY AND ASTROPHYSICS

by

Judy Y. Cheng

June 2012

The Dissertation of Judy Y. Cheng
is approved:

Professor Constance M. Rockosi, Chair

Professor Rebecca A. Bernstein

Professor Puragra GuhaThakurta

Tyrus Miller
Vice Provost and Dean of Graduate Studies

Table of Contents

List of Figures

List of Tables

Abstract

Chemical Abundance Trends in the Milky Way Disk:

Implications on the Origin of the Galactic Thick Disk

by

Judy Y. Cheng

Detailed observations of the Milky Way can be used to test predictions from simulations of disk formation and evolution, and they serve to complement large galaxy surveys at high redshift. The observed elemental abundances of old stars in the Milky Way disk, and how they vary with location in the Galaxy, provide powerful constraints on the chemical enrichment and assembly history of the disk. We present trends in [Fe/H] and [α/Fe] as a function of Galactocentric radius R and distance from the plane $|Z|$ using main sequence turnoff stars observed by the Sloan Extension for Galactic Understanding and Exploration survey. We find that the thick disk of the Milky Way has no radial metallicity gradient and is chemically homogeneous, whether thick disk stars are identified by their location (i.e., far from the midplane) or by their chemistry (i.e., α-enhanced). Follow-up observations from the High Resolution Echelle Spectrometer at the W. M. Keck Observatory show that the α-, iron peak, and neutron capture elemental abundances of stars at $|Z| \sim 0.5$ kpc also resemble those in the solar neighborhood. In addition, we find that the high-α population has a short radial scale length. The observed chemical homogeneity is consistent with a cosmological origin for the α-enhanced thick disk, in which stars far from the midplane of the disk formed at early times during a chaotic period of high gas accretion when the disk was turbulent and clumpy. The observations can only be explained by radial mixing processes, such as disk heating during a minor merger or internal radial migration processes, if mixing was extremely efficient.

To Mom and Dad:

Mom, here is that essay you were asking about.

Acknowledgments

To my advisor Connie Rockosi, I couldn't have done this without you. You have made me a much better and more confident scientist and writer. Thank you for knowing when I needed the extra encouragement and for making me feel like I could always be myself.

To my thesis committee, Rebecca Bernstein and Raja GukaThakurta. Your positive attitudes and support have made the hurdles to graduation much less intimidating.

To my collaborators, Heather Morrison, Ralph Schönrich, Young Sun Lee, Tim Beers, and David Lai, thanks for the many suggestions and thorough readings that have improved the content of this thesis. For useful science discussions, I would like to thank Jonathan Bird, Janet Colucci, Eileen Friel, Inese Ivans, Heather Jacobson, Sarah Loebman, Sara Lucatello, Katie Schlesinger, and Jennifer Sobeck.

To my early teachers and advisors, Karim Gangji, Bill Blair, Ravi Sankrit, Mark Morris, You-Hua Chu, Jenny Graves, and Sandy Faber, thanks for your guidance and for taking an interest in me.

To all my friends and family, thank you for the moral support. To Shawn, Tinting, Yuka, Ari, Hana, Jordan, and Kiki for alleviating my homesickness. To Jason and Connie Cheng for welcoming me to the California branch of the family. To Alvin for suggesting that I write my thesis about the Milky Way. To Nick, Evan, Katherine, Javiera, Laura, Stefano, Valentino, Feña, and Anna for putting up with me in and out of the office.

This thesis is dedicated to my parents, who always let me find my own way, even if they don't understand what it is I do all day.

The text of this dissertation includes reprints of the following previously published material: (i) Cheng, J. Y.; Rockosi, C. M.; Morrison, H. L.; Schnrich, R. A.; Lee, Y. S.; Beers, T. C.; Bizyaev, D.; Pan, K.; Schneider, D. P. 2012, The Astrophysical Journal, 746, 149 (Chapter 2), and (ii) Cheng, J. Y.; Rockosi, C. M.; Morrison, H. L.; Lee, Y. S.; Beers, T. C.; Bizyaev, D.; Harding, P.; Malanushenko, E.; Malanushenko, V.; Oravetz, D.; Pan, K.; Schlesinger, K. J.; Schneider, D. P.; Simmons, A.; Weaver, B. A. 2012, The Astrophysical Journal, 752, 51 (Chapter 3). Small changes in the text have been made to fit these chapters in the context of this document. The image at the end of Chapter 2 was part of a Sloan Digital Sky Survey (SDSS-III) press release and presented at a press conference at the American Astronomical Society Meeting in January 2012.

The data presented in Chapters 2 and 3 were obtained as part of SDSS-III. Funding for SDSS-III has been provided by the Alfred P. Sloan Foundation, the Participating Institutions, the National Science Foundation, and the U.S. Department of Energy Office of Science. The SDSS-III web site is http://www.sdss3.org/. SDSS-III is managed by the Astrophysical Research Consortium for the Participating Institutions of the SDSS-III Collaboration including the University of Arizona, the Brazilian Participation Group, Brookhaven National Laboratory, University of Cambridge, Carnegie Mellon University, University of Florida, the French Participation Group, the German Participation Group, Harvard University, the Instituto de Astrofisica de Canarias, the Michigan State/Notre Dame/JINA Participation Group, Johns Hopkins University, Lawrence Berkeley National Laboratory, Max Planck Institute for Astrophysics, Max Planck Institute for Extraterrestrial Physics, New Mexico State University, New York University, Ohio State University, Pennsylvania State University, University of Portsmouth, Princeton University, the Spanish Participation Group, University of Tokyo, University of Utah, Vanderbilt University, University of Virginia, University of Washington, and Yale University.

The data presented in Chapter 4 were obtained at the W. M. Keck Observatory, which is operated as a scientific partnership among the California Institute of Technology, the University

of California and the National Aeronautics and Space Administration. The Observatory was made possible by the generous financial support of the W.M. Keck Foundation. This research has made use of the Keck Observatory Archive (KOA), which is operated by the W. M. Keck Observatory and the NASA Exoplanet Science Institute (NExScI), under contract with the National Aeronautics and Space Administration. The authors wish to recognize and acknowledge the very significant cultural role and reverence that the summit of Mauna Kea has always had within the indigenous Hawaiian community. We are most fortunate to have the opportunity to conduct observations from this mountain.

Chapter 1

Introduction

The nitrogen in our DNA, the calcium in our teeth, the iron in our blood, the carbon in our apple pies were made in the interiors of collapsing stars. We are made of starstuff. – Carl Sagan

One way to study galaxy formation is to examine the properties of distant galaxies and watch the formation in action. The more distant these galaxies are, the farther back in time we are looking, and the most distant galaxies provide us with snapshots of the earliest phases of galaxy formation. A complementary approach to these large surveys is to study our own galaxy, the Milky Way, as a case study with which to test various theories of galaxy formation. While galaxy surveys provide bulk information about an ensemble of galaxies, observations of the Milky Way provide detailed information about the chemical and kinematic properties of individual stars and distinct stellar populations.

The specifics of the Galaxy's past—the amount of gas it accreted, the number of smaller galaxies it ate up, and the number of generations of stars that were born—have implications on what we see today. Because stars only fuse atoms in their cores, the chemical compositions of their atmospheres still reflect the composition of the gas out of which they formed. Old stars observed in the Milky Way, like fossils on Earth, are imprinted with chemical signatures that

offer clues about the early life of the Galaxy. Astronomers thus act as "Galactic archaeologists," using properties of old stars in the Galaxy to understand the environment in which they formed, i.e., the nascent Milky Way.

Because all elements heavier than helium were made in stars, the chemical composition of a stellar population allows us to piece together their star formation history. When stars explode at the ends of their lives, the heavy elements are returned to the interstellar medium (ISM) and will be incorporated into future generations of stars. Each successive generation includes more and more heavy elements in its composition. The metallicity of a stellar population is an indicator of how many generations of stars have come and gone, and the ratios of different elemental abundances provide constraints on the timescales over which these generations formed. Moreover, by looking at different locations in the Galaxy, we can examine how the star formation history in the center of the Galaxy compares to the outskirts, shedding light on how different parts of the Galaxy were put together.

In this thesis, we examine the chemical properties—the "starstuff"—of old stars in a large volume of the Milky Way to understand how some of these stars ended up in a thick disk, on orbits that take them very far from the midplane of the Galactic disk.

1.1 Thick Disk Formation: Hierarchical Versus Secular Processes

Traditionally the Galactic disk is thought of as two components: a thin disk of young metal-rich stars and gas, and a thick disk of older, more metal-poor stars (e.g., Gilmore et al. 1995, Chiba & Beers 2000, Bensby et al. 2004, Ivezić et al. 2008). The existence of a thick disk was first noted by Gilmore & Reid (1983), and subsequent studies have reported that it has a scale height about three times larger and a scale length slightly longer than the thin disk (e.g., Siegel et al. 2002, Jurić et al. 2008, de Jong et al. 2010). Compared to the thin disk, the

thick disk has a higher velocity dispersion and lags in rotation compared to the thin disk (e.g., Chiba & Beers 2000, Soubiran et al. 2003, Bensby et al. 2003). In addition, its stars have been shown to be chemically distinct from those of the thin disk, with different trends in α-, r-, and s-process element abundances (e.g., Edvardsson et al. 1993, Prochaska et al. 2000, Reddy et al. 2003; 2006, Bensby et al. 2003; 2005, Brewer & Carney 2006).

Observations of nearby edge-on spiral galaxies show that thick disks are common (e.g., Dalcanton & Bernstein 2002) and have kinematics, structural parameters, and stellar populations similar to the Galactic thick disk (Yoachim & Dalcanton 2005; 2006; 2008a). The ubiquity of thick disks in external galaxies, as well as the similarity in their properties, suggests that whatever process is responsible for the existence of the thick disk is at work in the formation and evolution of all disk galaxies. Furthermore, because the thick disk is old, the properties of its stars can be used as a fossil record of the disk's early formation at $z \sim 2$.

How stars end up in a thick disk, far from the plane of the Galaxy, is still an open question. As stars move through the potential of the Galaxy, their initially circular orbits are perturbed by inhomogeneities such as molecular clouds and spiral waves (e.g., Jenkins & Binney 1990, Jenkins 1992, Aumer & Binney 2009). This increases their random motions ("disk heating") and is the main source of the correlation between age and velocity dispersion seen in the solar neighborhood (Nordström et al. 2004). These mechanisms, however, do not increase the dispersion in the vertical direction to the level required to explain the large vertical heights reached by thick disk stars (Binney & Tremaine 2008). In this work, we consider four particular scenarios of thick disk formation that have been the focus of recent theoretical and observational studies. Scenarios 1-3 rely on external mechanisms that have been proposed wherein stars can end up in a thick disk within the context of the hierarchical structure formation predicted by ΛCDM cosmology. Scenario 4 requires an internal process than can occur in a disk in complete isolation.

In Scenario 1, present-day thick disk stars formed first in a thin disk, which then

experiences "vertical heating" as a result of one or more minor mergers (e.g., Villalobos & Helmi 2008, Read et al. 2008, Kazantzidis et al. 2008; 2009, Purcell et al. 2009, Bird et al. 2012). The satellites impart orbital energy to the stars in the initial disk, which is converted into random motions, resulting in a large increase in the vertical extent of the disk. This is especially true at large radii, where many simulated disks show pronounced flares (e.g., Bournaud et al. 2009). Halo merger histories in cosmological N-body simulations suggest that minor mergers are common; Stewart et al. (2008) estimate that 70% of Milky Way-sized halos have experienced a 1:10 merger within the last 10 Gyr. Observationally, streams in the outskirts of the Milky Way (e.g., Newberg et al. 2002, Belokurov et al. 2007) and other galaxies (e.g., Ibata et al. 2001, Martínez-Delgado et al. 2010) provide evidence of recent accretion events. In addition, Schwarzkopf & Dettmar (2000) find that thick disks are more common in galaxies undergoing mergers, which suggests that a galaxy's merging history may play an important role in determining the structure of the disk.

Scenario 2 also involves mergers and accretion, and can be distinguished from Scenario 1 by where thick disk stars are formed. In this scenario, present-day thick disk stars formed outside of the Galaxy in satellites or "pre-galactic" clumps which were directly accreted into a thick disk. The simulations of Abadi et al. (2003) suggest that after a merger most of the stars in the thick disk component are stars that originally formed in the satellite. Yoachim & Dalcanton (2006) proposed a scenario in which pre-galactic clumps of stars and gas were accreted; while the gas fell to the midplane, the stars ended up on orbits that take them to a large distance from the plane.

Scenario 3 posits that present-day thick disk stars formed where they are seen today, through chaotic merging of gas-rich clumps at high redshift (e.g., Brook et al. 2004; 2005, Bournaud et al. 2009). Gas is accreted into a turbulent disk with high velocity dispersion, similar to the clump-cluster galaxies seen at high redshift (e.g., Elmegreen & Elmegreen 2005) and predicted by the picture of cold mode accretion (e.g., Dekel et al. 2009, Krumholz & Dekel

2010, Krumholz & Burkert 2010). These clumpy disks are gravitationally unstable, and stars formed in these clumps will have high velocity dispersions and will end up in a thick disk.

Scenario 4, however, does not rely on any external influences. Recent work has highlighted the potential importance of radial migration, an internal secular process, in disk growth and evolution (e.g., Roškar et al. 2008b, Schönrich & Binney 2009a;b, Martínez-Serrano et al. 2009). Stars that originate at small radii have larger vertical velocity dispersions (e.g., Lewis & Freeman 1989), and their outward migration causes the disk to become thicker at all radii, forming a component that looks like a thick disk (Schönrich & Binney 2009b, Loebman et al. 2011). Radial migration can occur when stars interact with transient spiral arms (Sellwood & Binney 2002) or a steady bar and spiral pattern (Minchev & Famaey 2010, Brunetti et al. 2011).

Understanding the origin of the thick disk, then, is crucial to identifying the most important processes that shaped the formation of the Galaxy at early times. If the thick disk is a relic of hierarchical growth as in Scenarios 1-3, then the Milky Way is largely a product of its environment. Alternatively, if the thick disk is a result of internal processes as in Scenario 4, then the Milky Way would look the same regardless of its surroundings.

Each of these scenarios makes predictions about the kinematic and chemical properties of stars in the Milky Way. Sales et al. (2009), for example, showed that the expected distributions of orbital eccentricities could be used to distinguish between the four scenarios. Consequently, Dierickx et al. (2010) and Wilson et al. (2011) used observations of stars from the Sloan Digital Sky Survey (SDSS; York et al. 2000) and the RAdial Velocity Experiment (RAVE; Steinmetz et al. 2006), respectively, to argue against thick disk formation via minor mergers (Scenarios 1 and 2). In the data, there were too few high-eccentricity stars compared to the simulation predictions. Di Matteo et al. (2011), however, showed that for Scenario 1, the expected distribution in eccentricities depended on the orbital parameters and properties of the satellite galaxy assumed. Additional observations, such as the chemical properties of stars, are needed to further constrain these thick disk formation scenarios.

1.2 Chemical Abundances and Metallicity Gradients: Probes of Star Formation History and Galaxy Assembly

The ratios of different elemental abundances in a stellar population are intimately linked to its star formation history. Because different elements come from different nucleosynthetic processes in stars with different lifetimes, these elements are injected back into the ISM on different timescales. For example, α- and r-process elements are produced in Type II supernovae (SNe) and are returned early to the ISM because their progenitors are short-lived massive stars. Iron peak elements, however, are primarily produced in Type Ia SNe and are returned later to the ISM because their progenitors are white dwarfs, which are low mass stars at the end of their evolution. Lastly, s-process elements are produced in asymptotic giant branch (AGB) stars. These evolved stars are indicative of an intermediate age population, because only stars of a limited mass range ever reach this evolutionary stage.

Figure 1.1 shows a schematic diagram of how the iron abundance, or metallicity, [Fe/H] and α-element enhancement [α/Fe] can be used to infer the star formation history of a stellar population. Early on, when [Fe/H] is low, Type II SNe are the main contributors of heavy elements to the ISM and [α/Fe] is high; at later times, when [Fe/H] is higher, Type Ia SNe become the main contributors and [α/Fe] decreases. If a population forms rapidly (red) it will be enhanced in α-elements at higher metallicities than a population that forms over an extended period of time (blue). Thick disk stars in the solar neighborhood, which are identified using their kinematic properties, have been found to be enhanced in α-elements (e.g., Edvardsson et al. 1993, Prochaska et al. 2000, Mashonkina & Gehren 2000; 2001, Reddy et al. 2003; 2006, Bensby et al. 2003; 2005, Brewer & Carney 2006). Their abundances indicate that these stars must have formed rapidly over a short period (1-3 Gyr), before Type Ia SNe could contribute

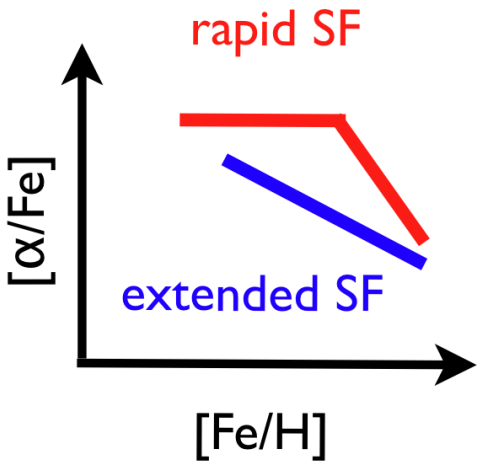

Figure 1.1: Schematic diagram showing abundance trends for stellar populations with different star formation histories. Relative abundances of different elements, for example the ratio of α-elements to iron, can be used as an indicator of the timescale over which star formation occurred.

very much iron to the interstellar medium (Gratton et al. 2000, Mashonkina et al. 2003, Bensby et al. 2004).

In addition, the elemental abundances can be used to constrain the kinds of environments in which the stars could have formed. Kirby et al. (2008) argue that the presence of extremely metal-poor stars ([Fe/H] < -3.0) in dwarf spheroidals show that similar objects could have built up the Milky Way halo. Ruchti et al. (2010; 2011) argue that thick disk stars are too α-enhanced to have formed in objects like present-day dwarf galaxies, which had more extended star formation histories (e.g., Tolstoy et al. 2009). The chemical properties of thick disk stars is thus a powerful tool for understanding the chemical enrichment and star formation history of the Galaxy.

Furthermore, the spatial variation of the chemical properties of the Galaxy is imprinted with information about how the galaxy was assembled. One simple illustration of this link is the inside-out growth scenario, in which the inner parts of the disk started forming stars first and became chemically enriched earlier. This is shown schematically in the top row of Figure 1.2, where blue, green, and red indicate metal-poor, intermediate-metallicity, and metal-rich stellar

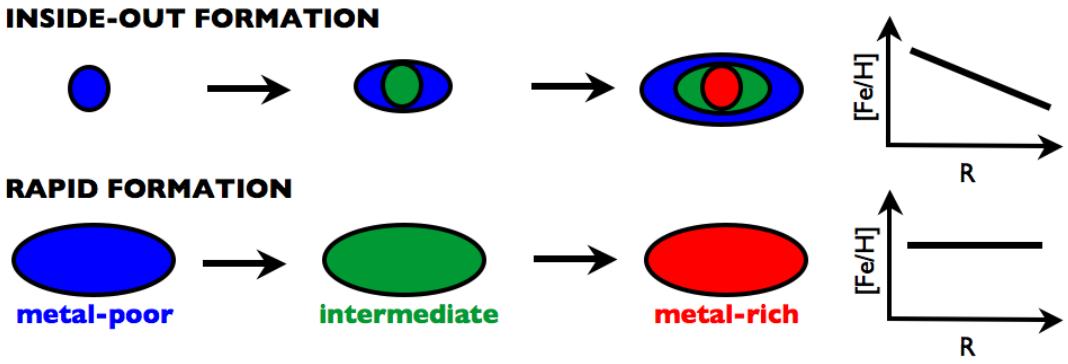

Figure 1.2: Schematic diagram showing inside-out growth (top) and rapid formation (bottom), and the expected behavior of the metallicity [Fe/H] as a function of Galactocentric radius R.

populations, respectively. In this case, the radial metallicity gradient is negative—the metallicity [Fe/H] decreases with increasing Galactocentric radius R. Another possibility is that the disk formed rapidly, with stars forming in all parts of the disk at once. This is shown schematically in the bottom row of Figure 1.2. The end result is a chemically homogeneous disk with a flat radial metallicity gradient—[Fe/H] is the same at all R. A third possibility is that the disk forms inside-out, but the stars get mixed around in the disk, taking them away from where they formed. The gradient will become weaker, or if mixing is very strong, the gradient can be completely erased.

The metallicity gradient, Δ[Fe/H]/ΔR, of old stars in the Milky Way provides an observational constraint to distinguish between possible formation mechanisms for the thick disk. For example, if thick disk stars originated in a thin disk and were subsequently heated by a minor merger (Scenario 1), then they should show a negative radial metallicity gradient that is characteristic of inside-out growth. Vertical heating of the disk should preserve the radial metallicity gradient if the radial motions are not dramatically affected by the heating mechanism. If the radial motions are affected, however, the gradient may get smeared out. If thick disk stars originated outside of the Galaxy and were deposited in the thick disk via accretion events (Scenario 2), then the metallicity distribution will have no pattern and may

exhibit clumpiness (Abadi et al. 2003).

If thick disk stars originated in turbulent clumps at times of high gas accretion rates (Scenario 3), the short timescale for star formation means that no gradient is expected because different locations in the disk do not experience different chemical enrichment (Brook et al. 2005). If thick disk stars originated in a thin disk and were pushed to larger radii through radial migration (Scenario 4), then the original gradient would become washed out into a shallow or nonexistent radial metallicity gradient (Roškar et al. 2008a, Sánchez-Blázquez et al. 2009). The presence of a metallicity gradient, then, would rule out Scenario 3, and the strength of the gradient would place quantitative constraints on the amount of radial mixing that could have occurred (Scenarios 1 and 4). In any case, the metallicity gradient of old disk stars will provide an important constraint that can be tested using detailed simulations of Milky Way-like galaxies (e.g., Guedes et al. 2011).

In addition to overall metallicity [Fe/H], abundances of other elements provide further observational constraints that must be explained by the various thick disk formation scenarios. Lee et al. (2011b) and Bovy et al. (2011; 2012), for example, use α-element abundances to explore the kinematic and structural properties of different stellar populations in the Milky Way. The eventual goal in these types of studies is to use even more elemental abundances to infer the common origins of stars with similar chemical signatures through "chemical tagging" (Freeman & Bland-Hawthorn 2002).

1.3 Spectroscopic Observations: SEGUE and HIRES

In this thesis, we use two samples of stars to tackle the question of how the chemical abundances of stars in the Milky Way disk vary as a function of location in the Galaxy. In Chapters 2 and 3, we use a large sample of stars outside the solar neighborhood with medium resolution spectroscopic observations ($R \sim 2,000$). For these stars, we have limited chemical

abundance information, but the large homogeneous sample allows us to examine the metallicity distribution in the disk as a function of both Galactocentric radius R and distance from the Galactic plane $|Z|$. In Chapter 4, we use followup high-resolution spectroscopic observations ($R \sim 48,000$) of a small subsample of these stars to gather information for many more individual elements. These results represent some of the first detailed abundance analyses for disk stars outside the solar neighborhood.

The medium resolution spectra were obtained by the Sloan Extension for Galactic Understanding and Exploration (SEGUE; Yanny et al. 2009) survey, part of the SDSS, which has collected spectra of ∼350,000 stars in the Milky Way. For all of these stars, metallicity [Fe/H] and α-enhancement [α/Fe] have been determined by the SEGUE Stellar Parameter Pipeline (SSPP; Lee et al. 2008a;b, Allende Prieto et al. 2008a, Smolinski et al. 2011, Lee et al. 2011a). An illustration of the spatial coverage of the Milky Way provided by SDSS/SEGUE is shown in Figure 1.3. We use a sample of $\sim$ 7000 main sequence turnoff stars located at low Galactic latitude in the region 6 kpc $< R <$ 16 kpc, 0.15 kpc $< |Z| <$ 1.5 kpc. These lines of sight are aimed at high enough latitude to avoid the dust in the midplane of the disk and at low enough latitude to still be probing the disk of the Galaxy. The high resolution spectra were obtained for 37 stars at $|Z| \gtrsim 0.5$ kpc using the High Resolution Echelle Spectrometer (HIRES; Vogt et al. 1994) at the W. M. Keck Observatory.

In Chapter 2, we present the radial metallicity gradient of the Milky Way disk at four vertical heights above the midplane. We find that the radial metallicity gradient becomes flat far from the plane of the Galaxy, at $|Z| > 1$ kpc, where the thick disk is expected to be the dominant stellar population. In Chapter 3, we present the [α/Fe] distribution as a function of R and $|Z|$. We find evidence that the high-α population, which is typically associated with the thick disk, has a short radial extent. In Chapter 4, we present the abundances of 17 α-, iron peak, and s-process elements for 37 stars at $|Z| \gtrsim 0.5$ kpc. We find that the abundances of high-α stars are consistent with thick disk stars in the solar neighborhood over a radial range

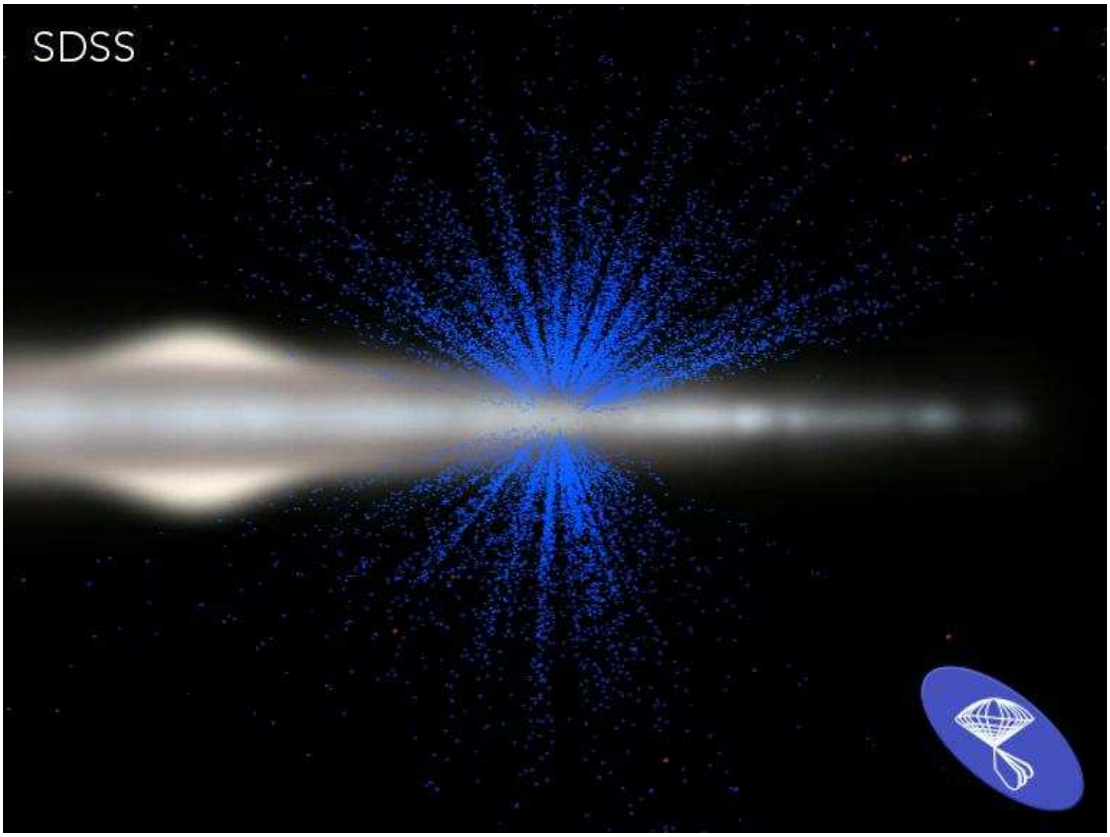

Figure 1.3: Illustration of the coverage of the Milky Way provided by the Sloan Digital Sky Survey (SDSS). Blue points represent stars observed by SDSS; in Chapters 2 and 3, we use a subset of this sample. [Credit: Gal Matijevic, University Ljubljana, Slovenia]

$6 < R < 9$ kpc. Our observations are consistent with a cosmological origin for the α-enhanced thick disk, in which stars far from the midplane of the disk formed at early times during a chaotic period of high gas accretion when the disk was turbulent and clumpy (Scenario 3). The observations can only be explained by radial mixing processes, such as disk heating during a minor merger (Scenario 1) or internal radial migration processes (Scenario 4), if mixing was extremely efficient.

Chapter 2

Metallicity Gradients in the Milky Way Disk as Observed by the SEGUE Survey

2.1 Introduction

2.1.1 Metallicity Gradients

The spatial variation in the metallicity distribution of old stars in the Milky Way disk system is linked to the formation and evolution of the Galaxy. The metallicity of stars at a particular place in the disk depends on the gas accretion rate, star formation history, and subsequent evolution at that location. For example, in the simplest picture of "inside-out" disk formation, low angular momentum gas falls to the center of the halo first, forming stars earlier and becoming chemically enriched much faster than the outer disk (e.g., Larson 1976, Matteucci & Francois 1989, Chiappini et al. 1997, Prantzos & Boissier 2000). In this scenario, heavy element

abundances in the interstellar medium generally decrease as a function of Galactocentric radius, i.e., the metallicity gradient is negative. The presence of radial flows (e.g., Lacey & Fall 1985, Goetz & Koeppen 1992, Portinari & Chiosi 2000, Spitoni & Matteucci 2011) and the nature of the early infalling gas (e.g., Cresci et al. 2010), however, have significant impacts on the chemical evolution of the disk. The exact nature of these processes is not yet fully understood and can lead to a gradient in the early disk that is weaker or even reversed compared to the simplest picture. Thus, observations of both the slope and temporal evolution of the radial metallicity gradient of the disk provide strong observational constraints for chemical evolution models (e.g., Chiappini et al. 2001, Cescutti et al. 2007, Magrini et al. 2009).

The radial metallicity gradient of the Milky Way disk has been measured using a number of different tracers, including Cepheids and open clusters, yielding a value between ~ -0.01 and -0.09 dex kpc^{-1} (e.g., Caputo et al. 2001, Friel et al. 2002, Chen et al. 2003, Luck et al. 2006, Lemasle et al. 2008, Sestito et al. 2008, Pedicelli et al. 2009, Pancino et al. 2010, Carrera & Pancino 2011, Luck & Lambert 2011). These tracers represent the composition of the interstellar gas at the time that they were formed, thus the wide variety of tracers studied probe the metallicity gradient at different times. This simple picture, however, can be complicated by processes that change the orbits of stars, such as dynamical heating from perturbations like spiral structure, molecular clouds, or minor mergers, which can make gradients shallower or wash them out completely.

In addition to the steepness and time evolution of the gradient, nonlinear features in the metallicity distribution provide further observational constraints. Some authors, for example, have noted the presence of a discontinuity in the radial metallicity gradient at a Galactocentric radius of $R \sim 10 - 12$ kpc, beyond which the metallicity gradient becomes shallower or flat (i.e., slope close to or equal to zero) for both open clusters (e.g., Twarog et al. 1997, Yong et al. 2005, Carraro et al. 2007b, Sestito et al. 2008) and Cepheids (e.g., Andrievsky et al. 2002c, Yong et al. 2006, Pedicelli et al. 2009). Whether this transition is characterized by a sharp break or by a

smoother transition is still unclear (see for example, Pancino et al. 2010, Jacobson et al. 2011a).

Several possible explanations for the reported discontinuity have been put forward. Andrievsky et al. (2004) argue that the presence of the Galactic bar and spiral arms may influence the star formation rate and flow of gas throughout the disk, affecting the amount of chemical enrichment that occurs at different radii. Yong et al. (2005) favor star formation in the outer disk, triggered by small accretion events. This scenario was supported by the enhanced abundances of α- and r-process elements of open clusters in the outer disk (e.g., Carraro et al. 2004, Yong et al. 2005). More recent work, however, indicates that these initial measurements may have been too high, and the outer disk clusters have abundances consistent with those in the inner disk (e.g., Carraro et al. 2007b, Bragaglia et al. 2008, Friel et al. 2010).

In this Chapter, we present the radial metallicity gradient, Δ[Fe/H]/ΔR, of the Milky Way disk, as a function of height above the plane $|Z|$, using a sample of 7010 field stars from the Sloan Extension for Galactic Understanding and Exploration (SEGUE; Yanny et al. 2009), part of the Sloan Digital Sky Survey (SDSS; York et al. 2000). The sample covers Galactic coordinates 6 kpc $< R <$ 16 kpc, 0.15 kpc $< |Z| <$ 1.5 kpc, where R is the cylindrical Galactocentric radius and $|Z|$ is absolute distance from the plane.

Our field stars are older than the open clusters and Cepheids used in previous gradient measurements in the literature and serve to extend the observations of the metallicity distribution of the disk to older tracers, which can provide constraints on the strength of the gradient at early times and on how much radial mixing occurred. Previous work with field stars has indicated that the disk has no radial metallicity gradient far from the midplane (Allende Prieto et al. 2006, Jurić et al. 2008, Katz et al. 2011). Our sample will be useful as a comparison for both studies of open clusters and Cepheids close to the midplane and studies of field stars at large heights above the plane.

Additionally, we examine whether a discontinuity in the radial metallicity gradient exists in the old disk stars. While the distances derived for individual field stars are less accurate

than for other tracers, our sample is sufficiently large to divide into bins of $|Z|$, which allows for an examination of the metallicity distribution in the disk as a function of both R and $|Z|$. The distinction between R and $|Z|$ is important, as many of the outer disk tracers in the literature are also located far from the midplane, and the question of whether the reported trends are a function of R, $|Z|$, or both, needs to be assessed.

2.1.2 Thick Disk Formation

This work is further motivated by the idea that the metallicity gradient of the old disk may be used as an observational constraint to distinguish between possible formation mechanisms for the thick disk. Traditionally, the Galactic disk can be thought of as the sum of two components: a thin disk of young metal-rich stars and a thick disk of older, more metal-poor stars (e.g., Gilmore et al. 1995, Chiba & Beers 2000, Bensby et al. 2004, Ivezić et al. 2008). The existence of the Milky Way's thick disk was first noted by Yoshii (1982) and Gilmore & Reid (1983), and thick disks with similar kinematics, structure, and stellar populations have since been observed to be a common feature in nearby spiral galaxies (Dalcanton & Bernstein 2002, Yoachim & Dalcanton 2005; 2006; 2008a).

The ubiquity of thick disks in external galaxies, as well as the similarity of their properties, suggests that whatever process is responsible for their existence is important in the formation and evolution of disk galaxies. Furthermore, because the thick disk is old, the properties of its stars can be used as a "fossil record" of the disk's early formation. How stars end up in a thick disk, far from the plane of the Galactic disk, remains an open question.

Several mechanisms for thick disk formation have been proposed, four of which are discussed below. Within the context of the hierarchical structure formation predicted by ΛCDM cosmology, a thick disk may arise through (1) the puffing up or vertical heating of a pre-existing thin disk during a minor merger (e.g., Villalobos & Helmi 2008, Read et al. 2008, Kazantzidis et al. 2008; 2009, Purcell et al. 2009, Bird et al. 2012); (2) the direct accretion of stars formed

in satellites that merged with the Galaxy (Abadi et al. 2003); or (3) star formation in an early turbulent disk phase during a period of high gas accretion (e.g., Brook et al. 2004; 2005, Bournaud et al. 2009). Even in the absence of cosmological accretion, a thick disk may also arise through (4) radial migration of stellar orbits (e.g., Schönrich & Binney 2009a;b, Loebman et al. 2011).

Each of these scenarios is motivated by both theory and observations. Halo merger histories in cosmological N-body simulations suggest that the types of mergers required by Scenarios 1 and 2 are common; Stewart et al. (2008) estimate that 70% of Milky Way-sized halos have experienced a 1:10 merger within the last 10 Gyr. Streams in the halo of the Milky Way (e.g., Newberg et al. 2002, Belokurov et al. 2007) and other galaxies (e.g., Ibata et al. 2001, Martínez-Delgado et al. 2010) provide observational evidence of such accretion events. Other recent work, however, has emphasized the importance of smooth gas accretion in the growth of disk galaxies (Brooks et al. 2009, Dekel et al. 2009), which can lead to a turbulent disk with high velocity dispersion as in Scenario 3. Observational support for this picture includes the clump-cluster galaxies (Elmegreen & Elmegreen 2005) and the thick chain and spiral galaxies (Elmegreen & Elmegreen 2006) seen at high redshift. Lastly, Sellwood & Binney (2002) and Roškar et al. (2008b;a) showed that resonant interactions between stars and transient spiral waves can change the radii of stellar orbits while keeping them on circular orbits, leading to the kind of radial mixing necessary for Scenario 4. Observations of nearby stars indicate that radial migration is an important process that may shape the correlations between the kinematics, metallicities, and ages of stars in the solar neighborhood (Haywood 2008).

While there is evidence that the mechanisms described above—minor mergers, early gas accretion, and radial migration—are at play in galaxy formation, the question of which mechanism, if any, is the *dominant* force behind thick disk formation remains unanswered. Recent work by Sales et al. (2009) is an example of how the kinematics predicted by the four different scenarios—in particular, the distribution of stars' orbital eccentricities—can be used

to test the various scenarios. This approach has been taken observationally by Dierickx et al. (2010) and Wilson et al. (2011), using stars from the SDSS and the RAdial Velocity Experiment (RAVE; Steinmetz et al. 2006), respectively. Both studies disfavor the minor merger scenarios, as they do not observe enough stars with high orbital eccentricities. Numerical simulations by Di Matteo et al. (2011), however, suggest that the observed eccentricity distribution can be obtained in the minor merger scenario given different orbital parameters and satellite properties than those used in the Sales et al. (2009) analysis. The conflicting interpretations show the need for other observational constraints. In this Chapter we examine the radial metallicity gradient, Δ[Fe/H]/ΔR, as a function of height above the Galactic plane, $|Z|$, in order to further distinguish between different thick disk formation scenarios.

For example, if thick disk stars originated in a thin disk and were subsequently heated by a minor merger, as in Scenario 1, then the observed radial metallicity gradient depends on the amount of mixing in the radial direction. If most of the heating occurs in the vertical direction, the thick disk will have the same metallicity gradient as the initial thin disk. Simulations, however, show that there can be substantial heating in the radial direction (e.g., Hayashi & Chiba 2006, Kazantzidis et al. 2009, Bird et al. 2012), which suggests that the gradient may be more shallow or flat than expected. If thick disk stars originated outside of the Galaxy and were deposited in the thick disk via accretion events, as in Scenario 2, then the metallicity distribution may exhibit clumpiness. The simulations of Abadi et al. (2003) showed that a single disrupted satellite roughly ends up in a torus of stars; several disrupted satellites would make up the thick disk by contributing stars of different metallicities at different radii.

If thick disk stars originated in a turbulent gas disk at high redshift, as in Scenario 3, the short timescale for star formation makes the thick disk chemically homogeneous, with no metallicity gradient (Brook et al. 2005, Bournaud et al. 2009). If thick disk stars originated in a thin disk and were pushed to larger radii through radial migration, as in Scenario 4, then the original gradient would become washed out into a shallow or nonexistent radial metallicity

gradient (Roškar et al. 2008a, Sánchez-Blázquez et al. 2009). The presence of a gradient, then, would rule out chemical homogeneity (Scenario 3), while the strength of the gradient would constrain the amount of disk heating by minor mergers (Scenario 1) and radial migration (Scenario 4). Examining old disk stars in a large volume, beyond the solar neighborhood, will allow one to distinguish between the various scenarios.

In contrast to many previous studies, we do not assign our stars to a thin disk or thick disk component. For samples of nearby stars in the solar neighborhood, this division is often done by assuming that the thick disk has a larger velocity dispersion and a slower mean rotation (i.e., thick disk stars are kinematically hot), as in the cases of Bensby et al. (2003) and Venn et al. (2004). Another method of separating thin and thick disk stars is by their chemistry, as Lee et al. (2011b) do using [Fe/H] and [α/Fe]; they favor this type of division because a star's composition is less likely to change than its spatial location or kinematics. Schönrich & Binney (2009b) have used mock observations to show that separating thin and thick disk stars using chemistry versus kinematics yields samples with different properties.[1] In addition, whether or not the thin disk and thick disk are truly distinct components is still an open question, with some studies arguing that the two components arise from a smooth correlation between chemical and kinematic properties (see discussions by Haywood 2008 and Ivezić et al. 2008).

Because our sample is not restricted to the solar neighborhood, we can compare the stellar populations of the thin disk and thick disk based on stars' locations instead of their kinematics or chemistry, which allows us to avoid assuming a specific model for the Milky Way disk. In this Chapter, we do not assign individual stars to the thin disk or thick disk. Instead, we will use the term *thick disk* to refer to stars that are currently found at large distances from the plane on their orbits; the term *thin disk* refers to stars that are found close to the Galactic mid-plane. Based on double-exponential fits to the vertical scale heights of the stellar density

[1] For example, a star assigned to the thin disk using chemical criteria may be assigned to the thick disk using kinematic criteria if it belongs to the inner disk and is in the tail of the rotational velocity distribution. According to the Schönrich & Binney (2009b) model, this explains the tail of thick disk stars with high [Fe/H] and why most of the thick disk stars in the Bensby et al. (2003) and Venn et al. (2004) samples are located at radii within the solar circle.

distribution in the disk (e.g., Jurić et al. 2008, de Jong et al. 2010) we expect the thick disk to be the dominant population above $|Z| \sim 1.0$ kpc.

Previous analyses of samples outside of the solar neighborhood have found no radial metallicity gradient at vertical heights $|Z| > 1.0$ kpc (Allende Prieto et al. 2006, Jurić et al. 2008, Katz et al. 2011). Our sample is complementary because our lines of sight are located at relatively low Galactic latitude and we can directly compare the radial metallicity gradients of the thin and thick disks (up to $|Z| = 1.5$ kpc) using the same sample. In addition, we can explore whether the reported discontinuity in the outer disk is a purely *radial* trend or if a *vertical* trend is contributing to the observed flattening of the gradient at large R.

This Chapter is organized as follows: the sample selection and data are described in §4.2. We then describe our methods of determining distances and correcting for the selection function in §§2.3 and 2.4, respectively. Our gradient measurements are presented in §4.3. Error analysis is presented in §4.2.5. We discuss the results in §4.4 and conclude with a summary in §2.8. For readers who are only interested in the results, we recommend skipping §§2.4 and 4.2.5. Further description of our weighting scheme, introduced in §2.4, is provided in Appendix A. Throughout our analysis we adopt the Galactocentric radius of the Sun, $R_{\mathrm{GC},\odot} = 8.0$ kpc.

2.2 Data

2.2.1 Sample Selection

We measure the metallicity gradient of old main sequence turnoff (MSTO) stars in low Galactic latitude fields from the SEGUE survey (Yanny et al. 2009, Aihara et al. 2011, Eisenstein et al. 2011; C. M. Rockosi et al. 2012, in preparation). These stars allow us to reach the largest distances probed by main sequence stars within the fixed magnitude limits of the survey. The data were obtained using the same telescope (Gunn et al. 2006), camera (Gunn et al. 1998), and filter system (Fukugita et al. 1996) as the SDSS. The old MSTO is

selected to be in the blue part of the color-magnitude diagram (CMD), as described in detail below, and can be identified using the SDSS Data Release 7 (DR7; Abazajian et al. 2009) version of the Catalog Archive Server[2] as targets with `sspParams.zbclass=STAR,SpecObjAll.primTarget=2048`, and `PlateX.programName = seglow%`. We also require that there are no repeat observations so that each star is only counted once. An equivalent query in Data Release 8[3] (DR8; Aihara et al. 2011) is `SpecObjAll.class = STAR, SpecObjAll.primTarget = 2048, PlateX.programName = seglow%`, and `PlateX.isPrimary = 1`, where the last requirement removes repeat observations.

The `programName` qualifier selects our targets from a subset of 22 SEGUE plug-plates[4] that comprise the "low-latitude" pointings, which are restricted to Galactic latitudes $8^\circ < |b| < 16^\circ$ (see §3.15 of Yanny et al. 2009). These lines of sight are high enough to avoid the young star-forming disk, as well as the regions with the most crowding and highest reddening, but also sufficiently low that they have a long sightline through the disk. The lines of sight fall into roughly two groups in Galactic longitude: seven at $50^\circ < l < 110^\circ$ and another four toward the anticenter, $170^\circ < l < 210^\circ$.

Each plate covers 7 deg^2 on the sky, with targets in the magnitude range $16 < g < 20$, where the magnitudes have not been corrected for extinction. In this Chapter, we will refer to any reddening- or extinction-corrected magnitudes and colors with subscripts $g_{\rm SFD}$ and g_0, for corrections derived from Schlegel et al. (1998; hereafter SFD98) and isochrone fitting (see §2.3), respectively. Table 2.1 lists the properties of the 11 lines of sight (two plates per pointing) included in our sample, ordered by the median extinction $E(B-V)$, obtained from SFD98. For the total sample, $E(B-V)$ varies between 0.05 and 1.07 mag. On average, there were 600-700 spectra obtained per line of sight.

For most of the SEGUE survey, which was at high Galactic latitude, targets are iden-

[2]http://casjobs.sdss.org/CasJobs/
[3]http://skyservice.pha.jhu.edu/casjobs/
[4]Hereafter we simply refer to the SDSS/SEGUE "plug-plates" as "plates."

Table 2.1: Properties for 11 Lines of Sight

Plates		R. A. (deg)	Decl. (deg)	l (deg)	b (deg)	$E(B-V)$[a]	$N_{\rm spectra}$
2712	2727	105.6	12.4	203.0	8.0	0.09	744
2536	2544	286.7	39.1	70.0	14.0	0.15	661
2534	2542	277.6	21.3	50.0	14.0	0.17	672
2554	2564	303.0	60.0	94.0	14.0	0.19	734
2678	2696	98.1	26.7	187.0	8.0	0.24	766
2556	2566	330.2	45.1	94.0	-8.0	0.31	728
2668	2672	79.5	16.6	187.0	-12.0	0.33	830
2681	2699	71.5	22.0	178.0	-15.0	0.41	758
2537	2545	334.2	69.4	110.0	10.5	0.49	708
2538	2546	323.1	73.6	110.0	16.0	0.65	716
2555	2565	312.4	56.6	94.0	8.0	0.82	511

[a] Median value for spectra in line of sight using values from SFD98.

tified as MSTO stars based on their $(u-g)_{\rm SFD}$ and $(g-r)_{\rm SFD}$ colors (see Yanny et al. 2009). In *ugr* color space, it is possible to separate the MSTO stars from metal-poor halo stars because of the large ultraviolet excess of metal-poor stars. In the low-latitude pointings, however, two issues arise. First, the *u*-band magnitudes and their uncertainties are unreliable due to the large extinction in these regions. Second, it is impossible to use a single constant selection in $(g-r)_{\rm SFD}$ that will yield the same stellar population along every line of sight because the reddening in these fields is, on average, much higher and more variable than in the high-latitude fields. For these low-latitude fields, we use a targeting procedure that is more robust to reddening, which will reliably choose the stars at the blue edge of the CMD. Starting with the photometric objects identified as stars in the imaging, this selection procedure is as follows.

1. We remove all stars with $g > 20$ and $i < 14.2$ (using magnitudes *uncorrected for extinction*) to ensure that the targets are sufficiently bright for high-quality spectroscopy in the expected exposure time.

2. The 7 deg^2 area of each plate is large enough that the extinction can be highly variable across the plate, and there are always many more targets than fibers available. We remove the regions of highest extinction from consideration to maximize the number of useful spectra. For each half of the plate, we calculate the 75th percentile of the $E(B-V)$ distribution using the total line-of-sight extinction from SFD98. This procedure is done

for each half independently to ensure that the targets are approximately evenly distributed over the plates, since the reach of the fibers is only about half of the plate diameter.

3. We remove all objects with $E(B-V)$ larger than the higher of the two 75th percentile values. Taking the higher value ensures that there are enough usable targets on each half of the plate to fill all the fibers given their limited reach across the plate. This should not bias the sample, as we do not expect that the objects behind more extinction are intrinsically any different from those that are unobscured. This is especially true for distant objects that are located far behind the dust. *The magnitudes used throughout the rest of this procedure are corrected using the SFD98 extinction values.* The SFD98 extinction was applied so that stars in the same approximate luminosity range were targeted along each line of sight, despite the large variation in extinction among the different lines of sight.

4. We examine the $(g-r)_{\rm SFD}$ distribution in bins of $g_{\rm SFD}$, each 1 mag wide. For each distribution, we find the peak, which is the $(g-r)_{\rm SFD}$ color of the MSTO in each g-magnitude bin. In addition, we determine the half maximum on the blue side; this is $(g-r)_{\rm half-max}$.

5. The red cut for each bin is defined as $(g-r)_{\rm cut} \equiv (g-r)_{\rm half-max} + 0.25$. We fit a line to $(g-r)_{\rm cut}$ as a function of $g_{\rm bin}$, where $g_{\rm bin}$ is the mean $g_{\rm SFD}$ of all the stars in each bin.

6. All stars on the blue side of the line are defined as candidate spectroscopic targets with equal probability of being selected. Targets are randomly chosen from the resulting candidate list.

Though the $(g-r)_{\rm SFD}$ color of the population may change from field to field because of varying amounts of extinction, the identification of the MSTO stars as the bluer population holds for all lines of sight. As a result, this method is more robust to reddening than the standard color cuts for normal SEGUE plates. Halo contamination is expected to be low in these plates,

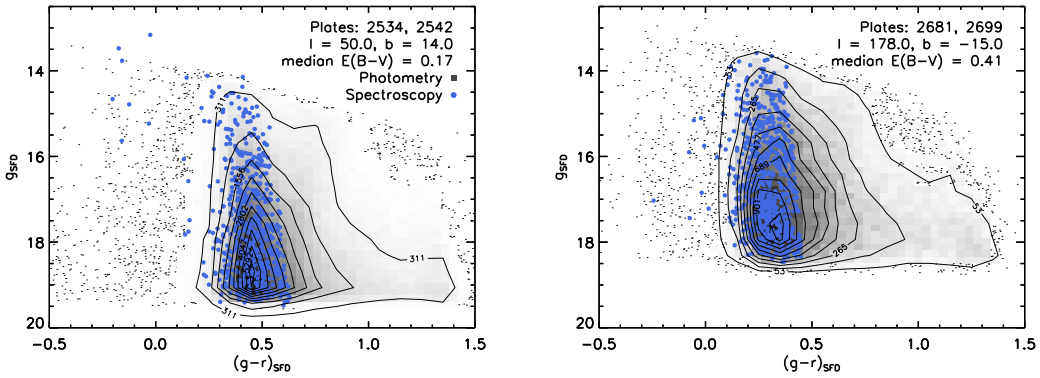

Figure 2.1: Main sequence turnoff (MSTO) selection. Spectroscopic targets (blue circles) are a randomly-selected subset of the MSTO stars identified using the photometry of all objects in the field (grayscale and contours). The contour labels indicate the number of stars per 0.375 by 0.1 mag $g_{\rm SFD}$-$(g-r)_{\rm SFD}$ bin. The results are shown for two lines of sight with low and high extinction (left and right, respectively), as measured by SFD98.

compared with the higher-latitude pointings (see further discussion in §2.6.2). The color cut, however, will bias our sample against metal-rich stars, which have redder colors. The severity of the bias depends on how much the MSTO color changes with metallicity, which in turn depends on the ages of stars at each metallicity (see further discussion in §§2.6.1 and 2.6.3).

Figure 2.1 shows the results of the procedure outlined above for two lines of sight with low and high extinction (median $E(B-V) = 0.17$ and 0.41, respectively). The density of objects identified as stars in the photometry are plotted in grayscale and contours, while MSTO stars in our spectroscopic sample are plotted as blue circles. All photometric objects bluer than the red limit of the spectroscopic sample were considered as candidates for spectroscopy, but only a randomly selected subset of those were actually observed. In the 22 low-latitude plates, spectra of 7828 MSTO stars were taken. We keep the targets with good photometry and spectra with signal-to-noise ratio (S/N) > 10 pixel^{-1}, where each pixel corresponds to ~ 1Å. We remove any stars which have large discrepancies (> 0.1 mag) in $g-r$ color between different photometric reductions. We also remove rare blue stars with $(g-r)_{\rm SFD} < -0.25$. The resulting sample contains 7655 spectra with a mean S/N~ 30 pixel^{-1}.

Table 2.2: Cluster Metallicities Measured by the SSPP

Cluster[a]	$[Fe/H]_{Lit}$	$[Fe/H]_{SSPP}$	$[Fe/H]_{Lit} - [Fe/H]_{SSPP}$
M3	-1.50	-1.43	-0.07
M71	-0.82	-0.74	-0.08
NGC2158	-0.25	-0.29	+0.04
NGC2420	-0.20[b]	-0.31	+0.11
M35	-0.16	-0.24	+0.08
M67	+0.05[c]	+0.00	+0.05
NGC6791	+0.30	+0.29	+0.01

[a] Cluster data are also presented in Smolinski et al. (2011), with the exceptions of NGC2420 and M67. A full comparison of the SSPP for all data in the SEGUE cluster samples will be presented in C. M. Rockosi et al. (2012, in preparation). [b] Jacobson et al. (2011a). [c] Randich et al. (2006).

2.2.2 SEGUE Stellar Parameter Pipeline: Accuracy in Regions of High Extinction

The SEGUE Stellar Parameter Pipeline (SSPP; Lee et al. 2008a) estimates the effective temperature $T_{\rm eff}$, surface gravity log g, and metallicity [Fe/H] for each spectroscopic target in the survey. We use stellar parameters from the version of the SSPP used for DR8, which includes improved [Fe/H] estimates at both high and low metallicities (Smolinski et al. 2011). The SSPP has been extensively tested using globular and open clusters, where true cluster members are identified using their metallicities and radial velocities (Lee et al. 2008b, Smolinski et al. 2011).

We verify that these results hold for cluster members in our temperature and surface gravity range (5000 K $< T_{\rm eff} <$ 7000 K, log $g > 3.3$). Table 2.2 shows the comparison between the literature values (Column 2) and the SSPP for cluster members in our temperature and surface gravity range (Columns 3 and 4). The offsets in [Fe/H] between the literature values and the SSPP are small (within 0.1 dex), and we see no trends with $T_{\rm eff}$, [Fe/H], and S/N. These tests show that we can reliably measure trends in [Fe/H] throughout our entire sample volume, and that the absolute values of the metallicities presented in the Chapter are accurate to 0.1 dex or better.

Each parameter is estimated using multiple methods: 11 for $T_{\rm eff}$, 10 for log$g$, and 12

for [Fe/H]. For $T_{\rm eff}$ in particular, these methods include spectral fitting and χ^2-minimization using grids of synthetic spectra (ki13, k24, NGS1), measuring line indices (WBG, HA24, HD24), neural networks using training sets of both real and synthetic spectra (ANNRR, ANNSR), and $g-r$ color predictions ($\rm T_K, T_G, T_I$). See Lee et al. (2008a) for complete details on each of these individual methods. Some methods use only the spectra as input, some use only the photometry, and some use both. The individual estimates of each parameter are averaged to obtain a final adopted value. Each individual estimate is valid for some range of $(g-r)_{\rm SFD}$ color and S/N, which determines whether it will be included in the final average. A more complicated decision tree is used for [Fe/H] and is described in detail in the Appendix of Smolinski et al. (2011). We have 7605 stars that have good stellar parameters; their temperatures fall in the range 5000 K $< T_{\rm eff} <$ 7000 K, making them F and G dwarfs.

Before using the SSPP parameters, we test whether the parameter estimates are affected by high Galactic extinction. The SSPP was designed to analyze the normal SDSS and SEGUE data at high Galactic latitude and uses photometry that has been corrected for extinction using the reddening maps of SFD98. These extinction values reflect the total line-of-sight extinction, which means that the colors of less distant stars will be overcorrected; they will be too blue. This effect is likely to result in a systematic error in the parameters estimated by those methods in the SSPP that use the photometry.

If this overcorrection affects our sample, we expect estimates that use the photometry to be systematically different when the extinction is high. The left panels of Figure 2.2 show the discrepancy between the individual $T_{\rm eff}$ estimates and the adopted value as a function of $E(B-V)$. Whether or not the estimate includes the photometry is indicated in the bottom left of each righthand panel. We have only plotted estimates that were accepted by the SSPP (i.e., the target falls in the $(g-r)_{\rm SFD}$ or S/N range in which the particular method is reliable). As expected, the photometry-dependent estimates of $T_{\rm eff}$ (k24, WBG, $\rm T_K, T_G, T_I$) are systematically higher (i.e., the color is bluer), compared to the adopted value, for the highest values of extinction.

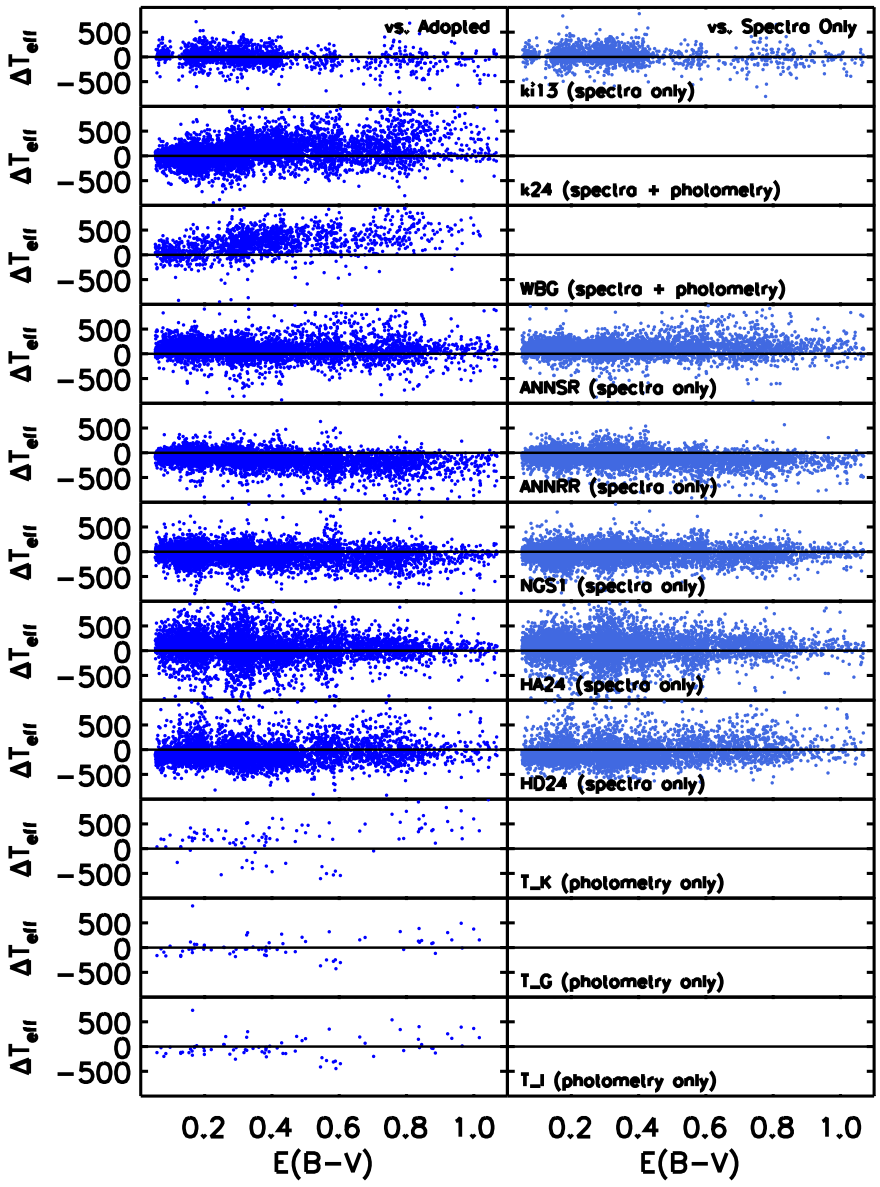

Figure 2.2: Left panels: differences between individual SSPP temperature estimates and the adopted values as a function of SFD98 extinction $E(B-V)$. For estimates that include photometry (k24, WBG, T_K, T_G, T_I), the deviation from the adopted value increases with extinction, indicating that the temperatures are overestimated due to overcorrection when using the SFD98 extinction values. Right panels: differences between individual SSPP temperature estimates and the spectra-only values as a function of extinction. The trend is no longer evident in the spectra-only estimates, indicating that the spectra-only temperature is more reliable for highly extincted objects.

To remove this effect, we calculate new averaged values of $T_{\rm eff}$ using only the estimates from methods that exclude the photometry (ki13, ANNSR, ANNRR, NGS1, HA24, HD24). The right panels of Figure 2.2 show the discrepancy between the individual $T_{\rm eff}$ estimates and the newly calculated spectra-only value as a function of $E(B-V)$. In contrast to the left panels, there is no clear trend in $\Delta T_{\rm eff}$ with extinction for the individual spectra-only estimates, which suggests that our new spectra-only average of the temperature is more reliable. At $E(B-V) > 0.8$, the median discrepancy between the new spectra-only estimate and the original adopted value is about $100 - 200$K, which is comparable to the expected errors of the SSPP $T_{\rm eff}$. We show in §2.6.3 that this could amount to a systematic error in the distance of $\sim 20\% - 25\%$. For the remainder of this Chapter, $T_{\rm eff}$ will refer to the spectra-only value.

No trend with extinction is observed in the photometry-dependent estimates of [Fe/H] (k24, WBG, CaIIK2, CaIIK3, ACF, CaII), so we keep the adopted values. This provides a more robust result, as the adopted value is an average of a larger number of estimators.

2.3 Distances

To calculate distances to each target, we use the spectra-only $T_{\rm eff}$ and SSPP [Fe/H], plus the theoretical isochrones of An et al. (2009)[5], which have been shown to be good matches to *ugriz* cluster fiducials. We do not make use of the SSPP log g estimate, as it is relatively inaccurate near the turnoff, where the expected range of gravities is small compared to the errors. Twelve sets of An et al. (2009) isochrones at metallicities in the range $-3.0 <$ [Fe/H] $< +0.4$ are available, with each set having a range of ages up to 15.8 Gyr. The distance uncertainties are discussed in §2.6.3.

We assign all stars in the sample to the isochrone with the closest metallicity. We then find the mean temperature for the stars in each metallicity bin by fitting a Gaussian to the distribution of effective temperatures. We identify the age of the isochrone with the turnoff

[5]http://www.astronomy.ohio-state.edu/iso/sdss.html

Table 2.3: Mean Isochrone Ages as a Function of [Fe/H]

[Fe/H]		[α/Fe]	log $\langle T_{\rm eff} \rangle$	$\langle T_{\rm eff} \rangle$ (K)	log $\langle$age$\rangle$	$\langle$age$\rangle$ (Gyr)	$N_{\rm obj}$
[Fe/H]	< -2.50	+0.4	3.768	5864	10.2	15.8	9
-2.50 < [Fe/H]	< -0.75	+0.3	3.768	5864	10.20	15.8	880
-0.75 < [Fe/H]	< -0.40	+0.2	3.775	5958	10.05	11.2	2695
-0.40 < [Fe/H]	< -0.25	0.0	3.772	5912	10.05	11.2	1527
-0.25 < [Fe/H]	< -0.15	0.0	3.772	5912	10.00	10.0	857
-0.15 < [Fe/H]	< -0.05	0.0	3.772	5912	9.95	8.9	732
-0.05 < [Fe/H]	< +0.05	0.0	3.763	5796	10.00	10.0	480
+0.05 < [Fe/H]	< +0.15	0.0	3.763	5796	9.95	8.9	229
+0.15 < [Fe/H]	< +0.30	0.0	3.763	5796	9.85	7.1	142
+0.30 < [Fe/H]		0.0	3.763	5796	9.70	5.0	54

temperature closest to the measured mean temperature; we refer to this as the *turnoff age of the mean temperature*, or TAMT, for each metallicity. Targets hotter than the mean temperature cannot be placed on the TAMT isochrone, so younger isochrones must be used; these targets are assigned to the oldest possible age (i.e., the oldest isochrone where the target is cooler than the turnoff).

Figure 2.3 shows a schematic picture of how ages are assigned to targets depending on their effective temperatures. The top panel shows six representative isochrones at solar metallicity, while the bottom three panels show how stars are assigned to these isochrones based on their place in the $T_{\rm eff}$ distribution. The procedure described above is shown in the panel labeled "TAMT" while the panels labeled "TO" and "ZAMS" show two other age assumptions that we use to estimate our distance errors (§2.6.3). Table 2.3 lists the TAMT determined by finding the mean temperature for each metallicity bin for the 7605 stars in our sample. To test the effect of using different stellar evolutionary models, we also calculate the TAMT using the isochrones of the Dartmouth[6] group (Dotter et al. 2008) and find that the results are within 0.05 dex of those listed in Table 2.3.

Once we have assigned a given target to an isochrone with a particular age and metallicity, we use the isochrone to obtain the predicted $g - r$ color for the target's spectra-only $T_{\rm eff}$ by linearly interpolating on the isochrone in temperature-color space. A comparison of the

[6]http://stellar.dartmouth.edu/∼models/grid.html

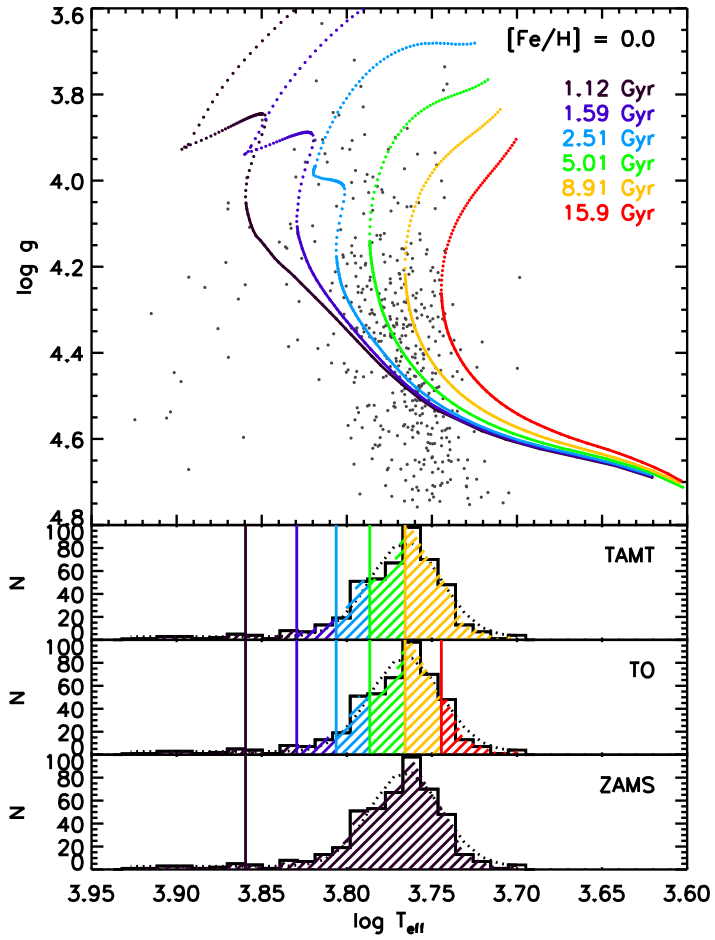

Figure 2.3: Determination of isochrone ages for solar metallicity targets ($-0.05 <$ [Fe/H] < 0.05, gray dots). Isochrones are shown in the top panel, with the temperature distribution in the bottom three panels. In practice, the set of isochrones used at each metallicity includes all available ages, but for clarity we show only six — the oldest, the youngest, and those located at the mean and 1σ, 2σ, and 3σ values of the temperature distribution. The colors in the lower panels indicate which isochrones in the top panel are used to calculate distances for those targets. We show how ages are assigned to our targets making three possible age assumptions: turnoff age of the mean temperature (TAMT), turnoff (TO), and zero-age main sequence (ZAMS). TAMT: for each metallicity, most targets are assigned to a single age (the TAMT) at which the turnoff temperature is closest to the measured mean of the temperature distribution of the SEGUE targets. Targets hotter than the mean are assigned the oldest possible age (i.e., the oldest isochrone where the target is cooler than the turnoff). TO: all targets are assigned to the oldest possible age, even those cooler than the mean of the temperature distribution. ZAMS: all targets are assigned to the youngest possible age. The TAMT assumption is used in our analysis, while the TO and ZAMS assumptions are used to test the accuracy of our distance estimates (see §2.6.3).

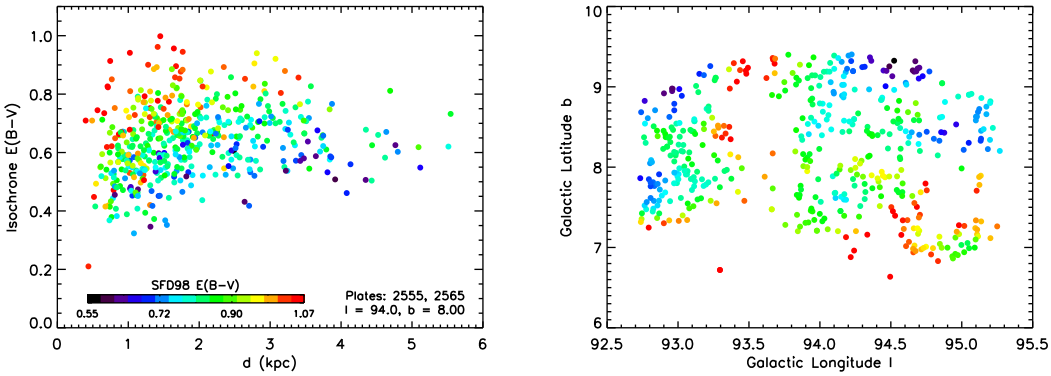

Figure 2.4: Estimates of the extinction derived from isochrone fitting provide a picture of the dust distribution along a given line of sight. The left panel shows the isochrone extinction as a function of derived distance, d, from the Sun. At small d the isochrone extinction is smaller than the SFD98 value (indicated by color symbols), but at large d it asymptotes to the SFD98 value. For this line of sight, which has the highest median $E(B-V)$ of our 11 fields, most of the dust is found within 2 kpc of the Sun. The scatter in isochrone extinction for a given value of SFD98 extinction may reflect the patchiness of the dust on the plane of the sky. This effect is seen in the right panel, which shows multiple separate patches that have the same SFD98 extinction values, but may have different distributions of dust along the line of sight. The color coding in the right panel is the same as in the left.

predicted and observed $g-r$ gives an estimate of the *isochrone extinction* in $g-r$, which is also used to determine the extinction in the g band. The isochrone extinction is an improvement over the SFD98 values because it does not assume that the target lies behind all of the dust in the line of sight. We step through this procedure for the two isochrones with the nearest values of [Fe/H] and then linearly interpolate to find the predicted apparent and absolute magnitudes. The apparent magnitude, now corrected using the isochrone extinction, along with the predicted absolute magnitude in the g-band, yield the distance.

In addition to being used in the distance calculation, the isochrone extinction provides information about the dust distribution along different lines of sight in the field. The left panel of Figure 2.4 shows the isochrone extinction as a function of the derived distance for one line of sight, with the color indicating the SFD98 value. There is good general agreement between the two extinction estimates, especially on a relative scale. Quantitatively, the agreement is poorest for small distances where the targets are in front of some of the dust, but asymptotes

to better agreement at large distances. This is consistent with the idea that the SFD98 values are overestimates because they include all of the dust in the given line of sight. For the line of sight shown, most of the dust is located within 2 kpc of the Sun, beyond which the isochrone extinction is approximately constant as a function of distance.

The scatter in the left panel of Figure 2.4 may be explained by the patchiness of the extinction on the plane of the sky. The right panel of Figure 2.4 shows that the distribution of $E(B-V)$ varies on small scales. The scatter in the left panel is expected if each region of high extinction has a different dust distribution along the line of sight. The agreement between the isochrone extinction and the SFD98 values provides a sanity check which indicates that our isochrone extinction estimates are reliable.

Sixty-two stars in our sample (0.8%) end up with negative values of isochrone extinction. Three kinds of stars fall into this category: (1) 17 stars are outliers with very blue $g-r$ colors. These stars do not contribute to the final measurement; after we apply our weighting scheme they receive a CMD weight of zero (see §2.4). (2) 7 stars exhibit large changes in $g-r$ color between different photometric reductions and are likely to be catastrophic errors, possibly due to blending in the relatively crowded, low-latitude fields. (3) The remaining 38 stars tend to be faint, and likely have negative reddening because the errors in their temperatures cause their predicted $g-r$ colors to be redder than their observed colors. We only see these stars in fields where the reddening is low; in fields where reddening is higher, the observed $g-r$ is much redder than the predicted $g-r$, so the temperature errors are not large enough to cause stars to have negative reddening. We expect just as many objects to have temperature errors that cause their predicted $g-r$ colors to be bluer, and we leave all of these objects in our sample, which should give us a more symmetric distribution of errors in our distances.

With distances for all of our targets, we obtain the spatial distribution of our sample in Galactic coordinates R and $|Z|$, as shown in Figure 2.5. The SEGUE targets are shown as blue dots. Our radial coverage extends mostly to Galactocentric radii at the solar circle and

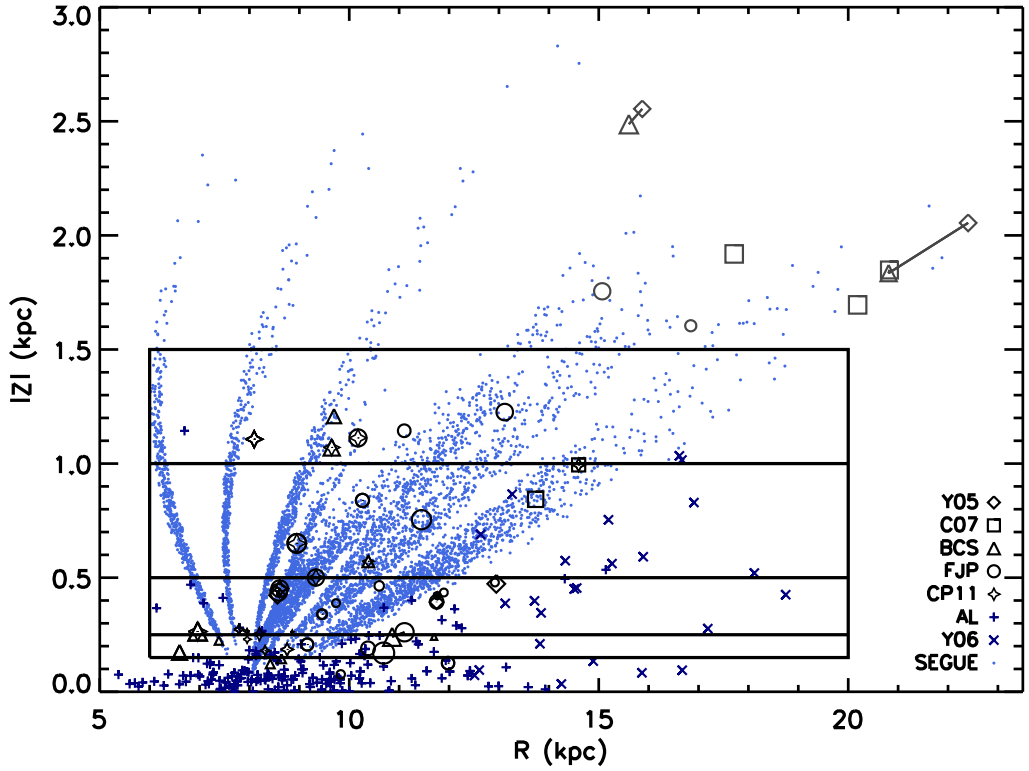

Figure 2.5: Spatial distribution of our sample (blue dots) in Galactic coordinates R and $|Z|$. We divide our sample into four $|Z|$ slices, indicated by the black boxes. Open cluster and Cepheid data are plotted with open symbols and pluses/crosses, respectively (see §2.7.2 for details). Objects from the literature located at $|Z| > 1.5$ kpc are plotted in gray. We note that all of the outer disk clusters from the literature are located at large $|Z|$. Multiple literature values for a single cluster are connected by lines.

beyond, though at low $|Z|$ it is confined just to the solar circle. About one-third of our sample is located below the Galactic plane; the $b < 0°$ lines of sight cover the entire radial range outside of the solar circle. Forty-eight open clusters and 190 Cepheids analyzed in the literature using high-resolution spectra are also shown (open symbols and crosses, respectively). These data have been used to study the radial metallicity gradient of the disk and will serve as comparison samples. The properties of the open clusters are listed in Table 2.4, and the data are described in more detail in §2.7.2.

Table 2.4: Open Clusters with High-resolution Observations

Cluster	l	b	d (kpc)	R (kpc)	Z (kpc)	[Fe/H]	Age (Gyr)	Reference
Be17	176.0	-3.6	2.7	10.7	-0.17	-0.15	10.1	Friel et al. (2005)
Be20	203.5	-17.3	8.6	15.9	-2.55	-0.49	4.1	Yong et al. (2005)
	203.5	-17.4	8.3	15.6	-2.49	-0.30	6.0	Sestito et al. (2008)
Be22	199.9	-8.1	6.0	13.7	-0.84	-0.32	3.3	Villanova et al. (2005)
Be25	226.6	-9.7	11.4	17.7	-1.92	-0.20	5.0	Carraro et al. (2007b)
Be29	197.9	8.0	14.8	22.4	+2.05	-0.54	4.3	Yong et al. (2005)
	198.0	8.0	13.2	20.8	+1.83	-0.31	4.0	Sestito et al. (2008)
	198.0	8.1	13.2	20.8	+1.85	-0.44	4.5	Carraro et al. (2004)
Be31	206.2	5.1	5.3	12.9	+0.47	-0.53	5.3	Yong et al. (2005)
Be32	208.0	4.4	3.1	10.9	+0.24	-0.29	5.5	Sestito et al. (2006)
	208.0	4.4	3.4	11.1	+0.26	-0.30	5.9	Friel et al. (2010)
Be39	223.5	10.1	4.3	11.4	+0.75	-0.21	7.0	Friel et al. (2010)
Be73	215.3	-9.4	9.8	16.8	-1.60	-0.22	1.5	Carraro et al. (2007b)
Be75	234.3	-11.1	9.1	15.1	-1.76	-0.22	4.0	Carraro et al. (2007b)
Blanco1[a]	15.6	-79.3	0.3	8.0	-0.26	+0.04	0.1	Ford et al. (2005)
	15.6	-79.3	0.3	8.0	-0.26	+0.20	0.1	Edvardsson et al. (1995)
Cr261	301.7	-5.5	2.8	7.0	-0.26	-0.22	6.0	Friel et al. (2003)
	301.7	-5.5	2.8	7.0	-0.26	+0.13	6.0	Sestito et al. (2008)
	301.7	-5.5	2.8	7.0	-0.27	-0.03	6.0	Carretta et al. (2005)
	301.7	-5.5	2.8	7.0	-0.26	-0.01	6.0	De Silva et al. (2007)
M67	215.6	31.7	0.9	8.6	+0.45	+0.00	4.3	Santos et al. (2009)
	215.7	31.9	0.8	8.6	+0.42	+0.02	4.3	Yong et al. (2005)
	215.6	31.7	0.9	8.6	+0.45	+0.03	4.3	Friel et al. (2010)
	215.6	31.7	0.8	8.6	+0.44	-0.01	4.3	Jacobson et al. (2011b)
	215.6	31.7	0.9	8.6	+0.45	+0.02	4.3	Friel & Boesgaard (1992)
	215.6	31.7	0.9	8.6	+0.45	-0.03	4.3	Tautvaišiene et al. (2000)
	215.6	31.7	0.9	8.6	+0.45	+0.03	4.3	Randich et al. (2006)
	215.6	31.7	0.9	8.6	+0.45	+0.03	4.3	Pace et al. (2008)
Mel66	260.5	-14.2	4.4	9.6	-1.07	-0.38	4.0	Gratton & Contarini (1994)
	260.5	-14.2	4.4	9.6	-1.07	-0.33	4.0	Sestito et al. (2008)
Mel71[a]	228.9	4.5	3.2	10.3	+0.25	-0.30	0.2	Brown et al. (1996)
NGC1193	146.8	-12.2	5.8	13.1	-1.23	-0.22	4.2	Friel et al. (2010)
NGC1245	146.6	-8.9	3.0	10.6	-0.46	-0.04	1.1	Jacobson et al. (2011b)
NGC1817	186.1	-13.1	1.5	9.5	-0.34	-0.16	1.1	Jacobson et al. (2011b)
	186.1	-13.1	1.5	9.5	-0.34	-0.07	1.1	Jacobson et al. (2009)
NGC188	122.8	22.5	1.7	8.9	+0.65	-0.03	6.3	Jacobson et al. (2011b)
	122.8	22.5	1.7	8.9	+0.65	+0.12	6.3	Friel et al. (2010)
	122.8	22.5	1.7	8.9	+0.65	+0.01	6.3	Randich et al. (2003)
NGC1883	163.1	6.2	3.9	11.8	+0.42	-0.20	0.7	Villanova et al. (2007)
	163.1	6.2	3.9	11.8	+0.42	-0.01	0.7	Jacobson et al. (2009)
NGC1901[a]	279.0	-33.6	0.4	8.0	-0.23	-0.08	0.8	Carraro et al. (2007a)
NGC2112[a]	205.9	-12.6	0.9	8.8	-0.19	-0.09	2.0	Brown et al. (1996)
	205.9	-12.6	0.9	8.8	-0.19	+0.16	2.0	Carraro et al. (2008)
NGC2141	198.1	-5.8	3.9	11.8	-0.39	-0.14	2.5	Yong et al. (2005)
	198.0	-5.8	3.9	11.8	-0.39	+0.00	2.4	Jacobson et al. (2009)

Table 2.4: Open Clusters with High-resolution Observations, continued

Cluster	l	b	d (kpc)	R (kpc)	Z (kpc)	[Fe/H]	Age (Gyr)	Reference
NGC2158	186.6	1.8	4.0	12.0	+0.13	-0.28	1.9	Jacobson et al. (2011b)
	186.6	1.8	4.0	12.0	+0.13	-0.03	1.9	Jacobson et al. (2009)
NGC2194	197.3	-2.3	1.9	9.8	-0.08	-0.08	0.9	Jacobson et al. (2011b)
NGC2204	226.0	-16.2	4.1	11.1	-1.14	-0.23	2.0	Jacobson et al. (2011a)
NGC2243	239.5	-18.0	3.6	10.2	-1.11	-0.42	4.7	Jacobson et al. (2011a)
	239.5	-18.0	3.6	10.2	-1.11	-0.48	4.7	Gratton & Contarini (1994)
NGC2324	213.4	3.3	4.2	11.7	+0.24	-0.17	0.6	Bragaglia et al. (2008)
NGC2355	203.4	11.8	1.9	9.7	+0.39	-0.08	0.8	Jacobson et al. (2011b)
NGC2420	198.1	19.6	2.5	10.3	+0.84	-0.57	2.2	Jacobson et al. (2011b)
	198.1	19.6	2.5	10.3	+0.84	-0.20	2.2	Jacobson et al. (2011b)
NGC2425	231.5	3.3	3.3	10.4	+0.19	-0.15	2.5	Jacobson et al. (2011b)
NGC2477	253.6	-5.8	1.2	8.4	-0.12	+0.07	1.0	Bragaglia et al. (2008)
NGC2506	230.6	9.9	3.3	10.4	+0.57	-0.24	1.7	Mikolaitis et al. (2011)
	230.6	9.9	3.3	10.4	+0.57	-0.20	1.7	Carretta et al. (2004)
NGC2539[a]	233.7	11.1	1.4	8.9	+0.26	+0.13	0.4	Santos et al. (2009)
NGC2660	265.9	-3.0	2.8	8.6	-0.14	+0.04	1.0	Sestito et al. (2006)
NGC3680[a]	286.8	16.9	0.9	7.8	+0.27	-0.04	1.2	Pace et al. (2008)
	286.8	16.9	0.9	7.8	+0.27	-0.03	1.2	Santos et al. (2009)
	286.8	16.9	0.9	7.8	+0.27	+0.04	1.2	Smiljanic et al. (2009)
NGC3960	294.4	6.2	2.1	7.4	+0.22	+0.02	0.9	Sestito et al. (2006)
NGC6253	335.5	-6.2	1.6	6.6	-0.17	+0.46	3.0	Carretta et al. (2007)
	335.5	-6.3	1.6	6.6	-0.17	+0.36	3.0	Sestito et al. (2007)
NGC6791[a]	70.0	10.9	5.9	8.1	+1.11	+0.37	4.4	Peterson & Green (1998)
	70.0	10.9	5.9	8.1	+1.11	+0.30	4.4	Boesgaard et al. (2009)
	70.0	10.9	5.9	8.1	+1.11	+0.47	4.4	Carretta et al. (2007)
	70.0	10.9	5.9	8.1	+1.11	+0.38	4.4	Carraro et al. (2006)
	70.0	10.9	5.9	8.1	+1.11	+0.35	4.4	Origlia et al. (2006)
NGC6819	74.0	8.5	8.2	9.7	+1.21	+0.09	2.7	Bragaglia et al. (2001)
NGC6939[a]	95.9	12.3	1.2	8.2	+0.25	+0.00	2.2	Jacobson et al. (2007)
NGC7142	105.0	9.0	3.2	9.3	+0.50	+0.13	4.0	Jacobson et al. (2008)
	105.0	9.0	3.2	9.3	+0.50	+0.08	4.0	Jacobson et al. (2007)
NGC752[a]	137.1	-23.2	0.5	8.3	-0.18	+0.01	1.1	Sestito et al. (2004)
	137.1	-23.2	0.5	8.3	-0.18	-0.09	1.1	Hobbs & Thorburn (1992)
NGC7789	115.5	-5.4	2.2	9.2	-0.21	-0.04	1.8	Jacobson et al. (2011b)
	115.5	-5.4	2.2	9.2	-0.21	+0.02	1.8	Jacobson et al. (2011b)
Ru4	222.0	-5.3	4.7	11.9	-0.43	-0.09	0.8	Carraro et al. (2007b)
Ru7	225.4	-4.6	6.0	12.9	-0.48	-0.26	0.8	Carraro et al. (2007b)
Sau1	214.7	7.4	13.2	20.2	+1.70	-0.38	5.0	Carraro et al. (2004)
To2	232.0	-6.9	8.3	14.6	-0.99	-0.50	2.2	Brown et al. (1996)
	232.0	-6.9	8.3	14.6	-0.99	-0.28	2.2	Frinchaboy et al. (2008)
	232.0	-6.9	8.3	14.6	-0.99	-0.31	2.2	Villanova et al. (2010)

[a] Spatial and age information from WEBDA.

We use our sample of MSTO stars to measure the metallicity gradient of the old disk in four different $|Z|$ slices, as indicated by the black lines in Figure 2.5. Taking thin and thick disk scale heights to be $\sim$ 300 and 900 pc, respectively, the lower two slices (0.15 kpc $< |Z| <$ 0.25 kpc and 0.25 kpc $< |Z| <$ 0.5 kpc) are dominated by the thin disk. The third slice (0.5 kpc $< |Z| <$ 1.0 kpc) is made up of a mix of the thin and thick disks, and the fourth slice (1.0 kpc $< |Z| <$ 1.5 kpc) is dominated by the thick disk. Of our sample, 7180 stars fall into these four slices.

Dividing our sample in this way allows a comparison of the radial metallicity gradient of the thin disk to that of the thick disk, as well as to distinguish between *radial* and *vertical* trends. We note that *all* of the distant clusters that have been used to study the behavior of the *radial* metallicity gradient in the outer disk ($R >$ 15 kpc) are located at least 1.5 kpc from the Galactic midplane; these are shown in gray in Figure 2.5.

2.4 Correcting for Selection Biases: Weights

To use field stars to determine the metallicity distribution in the disk, we must understand how the spectroscopic sample is drawn from the underlying population. As there are many more stars than it was possible for SEGUE to obtain spectra, we must assess whether the spectroscopic sample is truly representative of all of the stars in the disk. It likely is not, because our stars are selected to be the bluer stars in the CMD, making our selection biased against metal-rich and older stars, which have redder colors. The severity of the metallicity bias will depend on the ages of metal-rich stars; the older and more metal rich they are, the more likely they are to fall out of our sample. To correct for this bias, we employ a weighting scheme to step backward in our sample selection and reconstruct the properties of the underlying parent population. We describe the scheme briefly below; further details are in Appendix A.

There are three major ways in which the spectroscopic sample is different from the

parent population along each line of sight: (1) the photometric objects in regions with the highest extinction were not considered for spectroscopy. (2) Not all candidates for spectroscopy are observed. (3) We observe only MSTO stars using a color cut that is biased against redder metal-rich stars.

Each star in our sample is given three weights corresponding to the three differences listed above: (1) the *area weight*, $W_{\rm A}$, which depends on the coverage of targets on the plane of the sky in each line of sight; (2) the *CMD weight*, $W_{\rm CMD}$, which depends on the target's location in the CMD and corrects for the random selection of a subsample of all candidates for spectroscopy that pass the MSTO selection; and (3) the *LF weight*, $W_{\rm LF}$, which depends on the target's $T_{\rm eff}$, [Fe/H], and location in the CMD, and corrects for the metallicity bias of the MSTO selection. The total weight, W, is the product of the three weights $W_{\rm A}$, $W_{\rm CMD}$, and $W_{\rm LF}$. After removing targets with $W = 0$, we are left with a sample of 7010 stars. Details about how each of these weights is calculated can be found in Appendix A.

Figure 2.6 shows the distribution of the total weight (black) and each individual weight, as a function of R, in four slices of $|Z|$. The panels on the right show the distribution of weights. $W_{\rm A}$ (green) is the smallest contribution and does not vary significantly. $W_{\rm LF}$ (red) is relatively constant as a function of R and $|Z|$, with the distribution having a width of $\sim 0.5-1.0$ dex. Since $W_{\rm LF}$ is relatively constant, a systematic error in $W_{\rm LF}$, which could arise from using the wrong luminosity function, will not cause a spurious change in the ratio of metal-poor to metal-rich stars.

$W_{\rm CMD}$ (blue) shows the most variation because it normalizes for the fact that there are more stars in the inner disk than the outer disk. Although the variations in $W_{\rm CMD}$ are large, this weight is less uncertain than $W_{\rm LF}$, as it only requires counting objects in each bin. Figure 2.6 shows that the change in the total weight W mostly follows the change in $W_{\rm CMD}$.

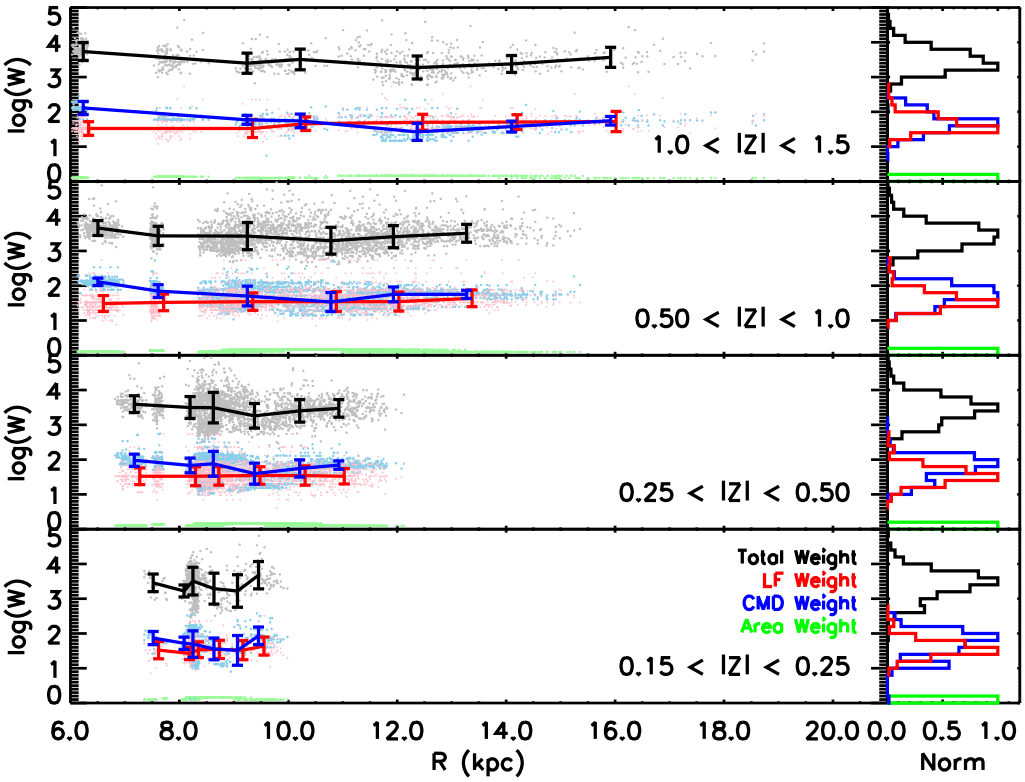

Figure 2.6: Variation in weights as a function of R and $|Z|$. The variation in the total weight W (black) is mostly dependent on the CMD weight $W_{\rm CMD}$ (blue). The LF weight $W_{\rm LF}$ (red) is fairly constant at all locations, with the width of the distribution being $\sim 0.5 - 1.0$ dex. The area weight $W_{\rm A}$ (green) is the smallest contribution and does not vary greatly between different lines of sight. While $W_{\rm CMD}$ shows the most dramatic variation, it is also less uncertain than $W_{\rm LF}$ because it only requires counting objects in CMD bins.

2.5 Results: Radial Metallicity Gradients

The total weights are applied to each target, allowing us to use our sample of MSTO stars to estimate the properties of the underlying parent population. We divide our sample into four slices of $|Z|$: (1) 0.15 kpc $< |Z| <$ 0.25 kpc, (2) 0.25 kpc $< |Z| <$ 0.5 kpc, (3) 0.5 kpc $< |Z| <$ 1.0 kpc, and (4) 1.0 kpc $< |Z| <$ 1.5 kpc. Within each $|Z|$ slice, we fit a linear gradient to the data, weighting each target by the total weight determined using the scheme described in §2.4.

Figure 2.7 shows the radial metallicity gradients for all four $|Z|$ slices for both the

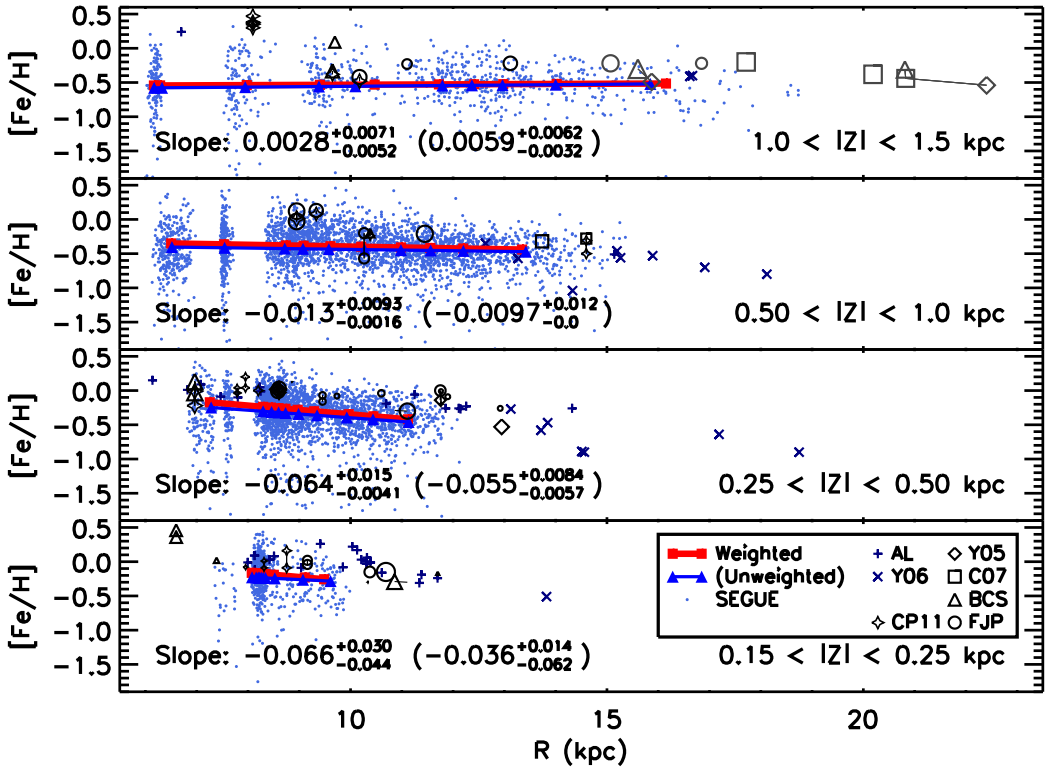

Figure 2.7: Metallicity [Fe/H] vs. Galactocentric radius R in four $|Z|$ slices. Light blue points indicate the SEGUE data. The weighted median metallicity and the derived linear fit are shown as red squares, with the numerical values in the bottom left of each panel. The blue triangles and values in parentheses show the results we would have obtained if no corrections for known selection effects had been applied. The spacing of the symbols indicates the radial distribution of the targets. Open symbols and pluses/crosses are open clusters and Cepheids from the literature (see §2.7.2 for details). The sizes of the open cluster symbols indicate their ages (smaller symbols for younger clusters). At low $|Z|$ (< 0.5 kpc) our derived gradient is consistent with published values. At high $|Z|$ (> 0.5 kpc) the constant [Fe/H] is consistent with the cluster metallicities reported by Yong et al. (2005) in the outer disk.

unweighted and weighted cases (blue triangles and red squares, respectively). The weighted slopes are indicated in the bottom left corner of each panel, with the unweighted values in parentheses. The quoted errors are derived from the Monte Carlo simulations described in §2.6.3 and include only the random errors from uncertainties in the stellar parameters. See §2.6.3 for a discussion of the systematic errors. The large symbols and navy blue plusses/crosses show the positions and metallicities for open clusters and Cepheids from the literature (see

§2.7.2).

In the low $|Z|$ slices ($|Z| < 0.5$ kpc), we obtain values that are consistent with the -0.06 dex kpc^{-1} determined by Friel et al. (2002) for open clusters and by Luck et al. (2006) for Cepheids. Our major result is that in the high $|Z|$ slices ($|Z| > 0.5$ kpc), the slope is flat for the entire radial range 6 kpc $< R <$ 16 kpc. The constant median [Fe/H] in the highest slice ($|Z| > 1.0$ kpc) is consistent with the metallicities reported by Yong et al. (2005) and others at large R.

Our results are summarized in Figure 2.8, which shows the measured slopes as a function of vertical height $|Z|$. The horizontal dotted lines show the values in the literature published by Friel et al. (2002) and Luck et al. (2006) for open clusters and Cepheids, respectively, which are consistent with the values we obtained for the low $|Z|$ slices. Again, the red squares show the values obtained after we apply our weights, and the blue triangles show the values obtained using the unweighted data without any corrections for the selection function. The observed trend—flattening slope with increasing $|Z|$—is seen in both the unweighted and weighted cases.

To test the robustness of this result, we re-measured the gradient for various subsamples of our data. The purple symbols in Figure 2.8 show the results if we exclude likely halo stars (see §2.6.2). The gray symbols show the values obtained for restricted ranges in R (7.3 kpc $< R <$ 12.6 kpc and 7.8 kpc $< R <$ 10.5 kpc). These measurements were done to test that the flattening of the radial gradient is truly a trend in $|Z|$, and not just a result of the wider range in R that is observed in the high $|Z|$ bins. The two restricted ranges in R correspond to the extent of observations in the two lower $|Z|$ bins. Figure 2.8 shows that gradient becomes flat with or without weighting and independent of the range in R observed.

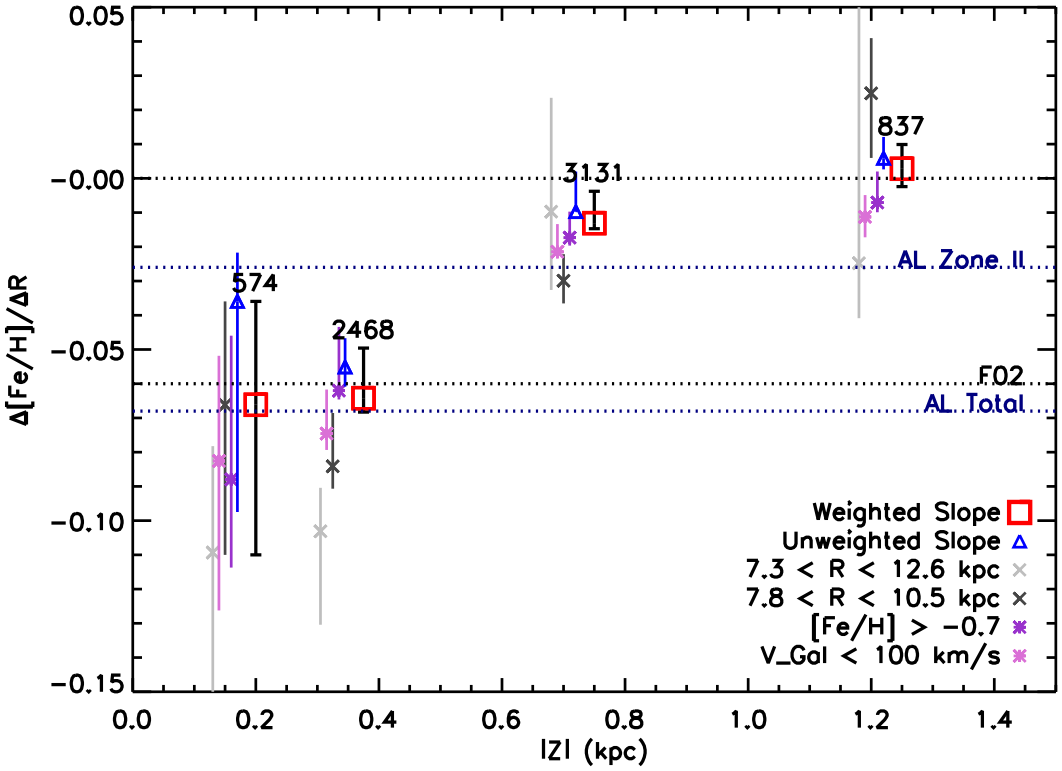

Figure 2.8: Measured gradient, Δ[Fe/H]/ΔR, vs. vertical height, $|Z|$. The horizontal black dotted lines indicate a flat gradient and the gradient measurement published by Friel et al. (2002) using open clusters. The horizontal blue dotted lines indicate the gradient measurements published by Luck et al. (2006) using Cepheids for the ranges 6.6 kpc $< R <$ 10.6 kpc (zone II) and 4.0 kpc $< R <$ 14.6 kpc (their total sample). The red squares and blue triangles show the measured gradients (weighted and unweighted, respectively) as a function of height above the Galactic plane presented in this work. The slope becomes flat at high $|Z|$ using both the weighted and unweighted results. The number of objects in each $|Z|$ slice is indicated above the symbols. The gray symbols show the results obtained for restricted ranges in R. The purple symbols show the results obtained when probable halo contaminants are removed (see §2.6.2). In each case, the trend of the gradient becoming more shallow with distance from the plane is still observed, which indicates that our result does not arise due to the increase in the radial range or contamination from the halo.

2.6 Errors

2.6.1 Metallicity Bias

As described in §2.2.1, our sample of MSTO stars is chosen by making a cut in $(g-r)_{\rm SFD}$, which likely biases it against redder, more metal-rich stars. Theoretical isochrones

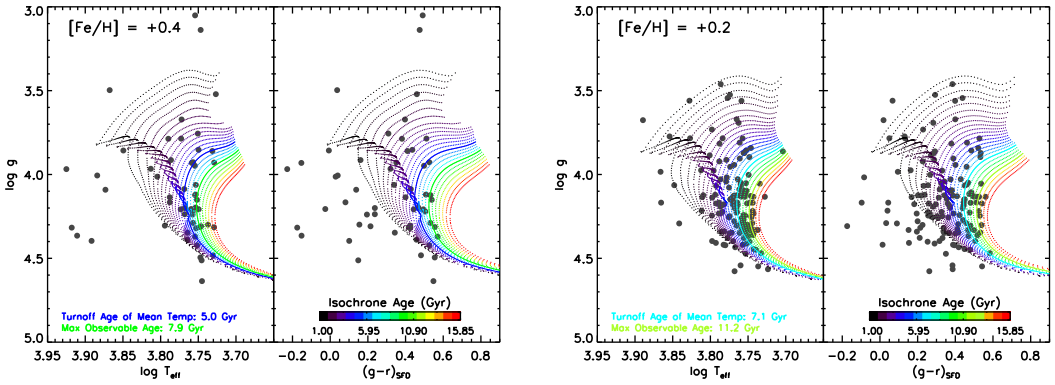

Figure 2.9: Maximum observable ages for metal-rich stars. We compare the SEGUE data (gray circles) with theoretical isochrones (color, An et al. 2009) to estimate the oldest main sequence turnoff stars that would fall in our sample. The TAMT (see Table 2.3) and maximum observable age are shown as solid lines. For [Fe/H]= +0.4 (left panel), the coolest/reddest stars may be as old as $\sim$ 8 Gyr; for [Fe/H]= +0.2 (right panel), the coolest/reddest stars that fall in our sample may be as old as $\sim$ 11 Gyr. Based on the measured ages of nearby stars (Bensby et al. 2005, Casagrande et al. 2011), we do not expect there to be a significant population of old, metal-rich stars which would be excluded from our sample.

give us an idea of the significance of this bias. Figure 2.9 shows the temperature and $(g-r)_{\rm SFD}$ distributions of metal-rich stars in our sample ([Fe/H] $\geq$ +0.2, gray circles) against the theoretical isochrones of An et al. (2009; color). We estimate that the maximum observable ages of stars at [Fe/H] = +0.4 and +0.2 are $\sim$ 8 and 11 Gyr, respectively. At each metallicity, this corresponds to the turnoff age of the coolest/reddest stars that pass the selection criteria for our sample. The TAMT and maximum observable age are shown as solid lines. Based on the measured ages of nearby stars (Bensby et al. 2005, Casagrande et al. 2011), very few stars with metallicities [Fe/H] $>$ +0.2 are older than 8 Gyr. We therefore expect that metal-rich stars are well represented in our sample. For stars with metallicities [Fe/H] $\leq$ 0.0, there is no significant bias against stars of any age. We do the same test using isochrones from both Dotter et al. (2008) and the Padova[7] group (Girardi et al. 2004), and we find that the temperature of the turnoff for a given age does not vary significantly between the different stellar evolution models, so the above conclusions about the metallicity bias are robust.

[7]http://stev.oapd.inaf.it/cmd

The arguments presented above suggest that the metallicity bias resulting from our color selection does not eliminate a significant fraction of the disk population from our sample. However, the color selection also causes metal-rich stars to be under represented in our data. We use mock catalogs from the models of Schönrich & Binney (2009a) to quantify how well we correct for this effect and recover the true metallicity distribution in our sample. We show below (§2.6.3) that we are able to measure the true gradients within the errors and reproduce the trends as a function $|Z|$ when we apply the weighting scheme described in §2.4 and Appendix A.

2.6.2 Halo Contamination

Since we are interested in the metallicity distribution of the Galactic disk, we must assess whether our sample may be contaminated by halo objects. Our sample does not reach $R < 5$ kpc, where the bulge is expected to be a significant population. One way to quantify the amount of contamination is by examining different multi-component models for the Galaxy, in particular, those of Jurić et al. (2008) and de Jong et al. (2010). For the lines of sight in our sample, these two models predict total halo contaminations of $\sim 2\%$ and $\sim 0.8\%$, respectively. In the most distant $|Z|$ bin, the predicted contaminations increase to $\sim 11\%$ and $\sim 5.6\%$, respectively. The difference in the predictions can be almost entirely attributed to the discrepant local densities for the halo that were derived (0.51% by Jurić et al. 2008 and 0.17% by de Jong et al. 2010).

Both models, however, predict that the anticenter lines of sight, aimed toward the outer disk, will be more contaminated by halo stars. This is especially true in the Jurić et al. (2008) model, which predicts that the two lines of sight that reach the largest values of R will have $17\% - 18\%$ contamination (compared to $9\% - 13\%$ in the other lines of sight). If there is indeed more halo contamination in the outer regions, this should push our measured gradient to be steeper, since there will be more metal-poor halo stars at large R compared to the inner disk. However, we see the opposite effect, that the gradient is flatter in the highest $|Z|$ bins.

Looking at the data, we do not see evidence for significant halo contamination. Halo stars, which have large velocities and are more metal poor than disk stars, can generally be identified using their kinematics or chemistry. To assess the effect that such stars may have on our results, we recalculate the gradient after applying two different cuts to remove potential halo stars from the data: (1) a metallicity cut that removes all stars with [Fe/H] < -0.7, and (2) a kinematic cut that removes all stars with $V_{\rm Gal} < 100$ km s^{-1} to remove stars with the largest velocity offset relative to the projection of the local standard of rest, where $V_{\rm Gal} = V_R + 220 \cdot \cos b \cdot \sin l$ and V_R is the line-of-sight velocity measured from the SEGUE spectra. We only remove stars with $V_{\rm Gal} < 100$ km s^{-1} along lines of sight with $50 < l < 130^\circ$. We do not include the lines of sight directed toward the Galactic anticenter because the local standard of rest is tangent to those directions and the projection does not give a meaningful velocity. The two cuts remove ~ 700 and ~ 100 stars, respectively. The gradients we measure using each of these cuts are not significantly different from our main results, as shown by the purple symbols in Figure 2.8.

2.6.3 Mock Catalog Analysis

To quantify the errors in our analysis, we utilize mock observations generated from the models of Schönrich & Binney (2009a). By using a model where we know the true stellar parameters, distances, and metallicity distributions of the targets, we can test whether we are able to reliably reproduce the ground truth after applying our observational selection to the mock catalogs and performing the same analysis procedures. As the purpose is merely to assess how accurately we can measure quantities such as distances and metallicity gradients, this way of testing our methods is not dependent on having a *correct* model for the Galaxy. We do, however, need a model that can reproduce some basic properties of the observed stellar populations. Schönrich & Binney (2009a) have shown that their model provides a good match to the properties of stars in the solar neighborhood as observed by the Geneva-Copenhagen

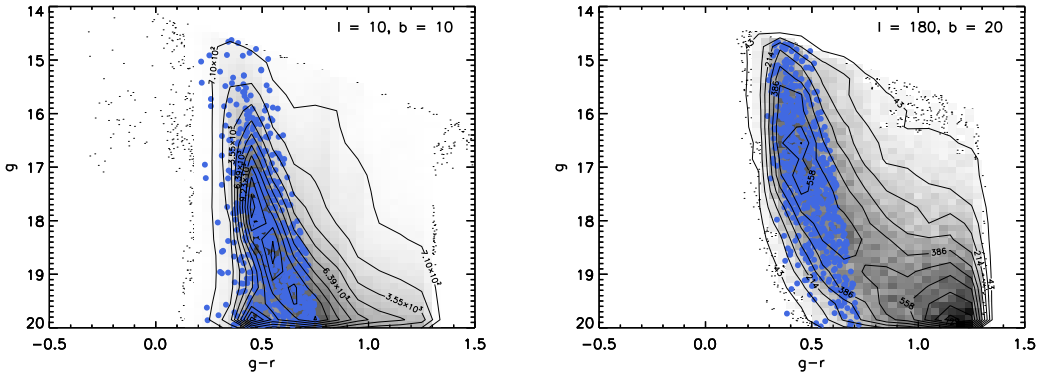

Figure 2.10: Mock catalog MSTO selection. This figure is analogous to Figure 2.1, but using simulated observations from Schönrich & Binney (2009a). The full sample of stars (grayscale and contours) is put through the same sample selection as the real data to yield an analogous MSTO sample (blue circles). The similarity between the CMDs of the real and mock data shows that we are using a reasonable model of the Galaxy to test our errors.

Survey (Nordström et al. 2004).

We use a mock catalog, provided by R. Schönrich, of 6,701,170 stars with *ugriz* colors, stellar parameters, and distances along 10 lines of sight. Targets in the mock catalogs are assigned stellar parameters using the BaSTI[8] isochrones. We repeat the same sample selection described in §2.2.1 on the mock catalog to replicate the effects of using MSTO stars as tracers. Figure 2.10 is analogous to Figure 2.1 and shows the results of the random subsampling for two lines of sight. Though the model was not tuned to look like the SEGUE data, the model CMDs are good matches to the observations.

In our analysis, we use all 111,640 objects that fulfill the MSTO selection to estimate errors on the distance (§2.6.3). We draw many random subsamples of 6500 MSTO stars to estimate the systematic and random errors on our gradient measurement (§2.6.3), to simulate the effect of having a limited number of spectroscopic targets along each line of sight. We repeat the analysis using different random subsamples to assess how much the results change based on which particular targets are chosen for spectroscopy.

[8]http://albione.oa-teramo.inaf.it/

Errors in Distance Estimates

Systematic Errors: The main source of systematic error in the distance arises from assumptions we must make when choosing isochrones to estimate the luminosities of our stars. One source of error is the α-enhancement; An et al. (2009) adopt an α-enhancement scheme where each value of [Fe/H] has an assumed value of [α/Fe] (see Table 2). We do not expect the discrepancy between the target and isochrone [α/Fe] to have a large effect on the distance estimate. The [α/Fe] of stars in our sample (Lee et al. 2011a) are generally within 0.2 dex of the values assigned to the An et al. (2009) isochrones. Using the [Fe/H]-[α/Fe] grid of Dotter et al. (2008), we estimate that a 0.2 dex change in [α/Fe], at worst, leads to a $\sim 10\%$ change in the distance for a star on the zero-age main sequence.

For our sample, a larger source of uncertainty is the ages we assign to our targets; the slope of the main sequence becomes very steep at the turnoff, making the predicted distance a strong function of the chosen age. We compare the distance estimates obtained using three different age assumptions, which are shown schematically for stars at solar metallicity ($-0.05 <$ [Fe/H] < 0.05) in Figure 2.3:

1. *Turnoff age of the mean temperature (TAMT).* We use one isochrone for most of the stars in the metallicity bin—this is determined by finding the mean of the temperature distribution. Targets hotter than the MSTO are assigned to the oldest possible isochrone. This was the scheme used throughout our analysis (described in §2.3) and illustrated in the second panel of Figure 2.3.

2. *Turnoff (TO).* We use the oldest possible isochrone consistent with their measured temperature for all targets—this assumes that every star is located at the turnoff. In comparison to the TAMT assumption, this approach changes the distances for stars cooler than the mean temperature of the sample, as shown in the third panel of Figure 2.3.

3. *Zero-age main sequence (ZAMS).* We use the youngest possible isochrone for all targets—

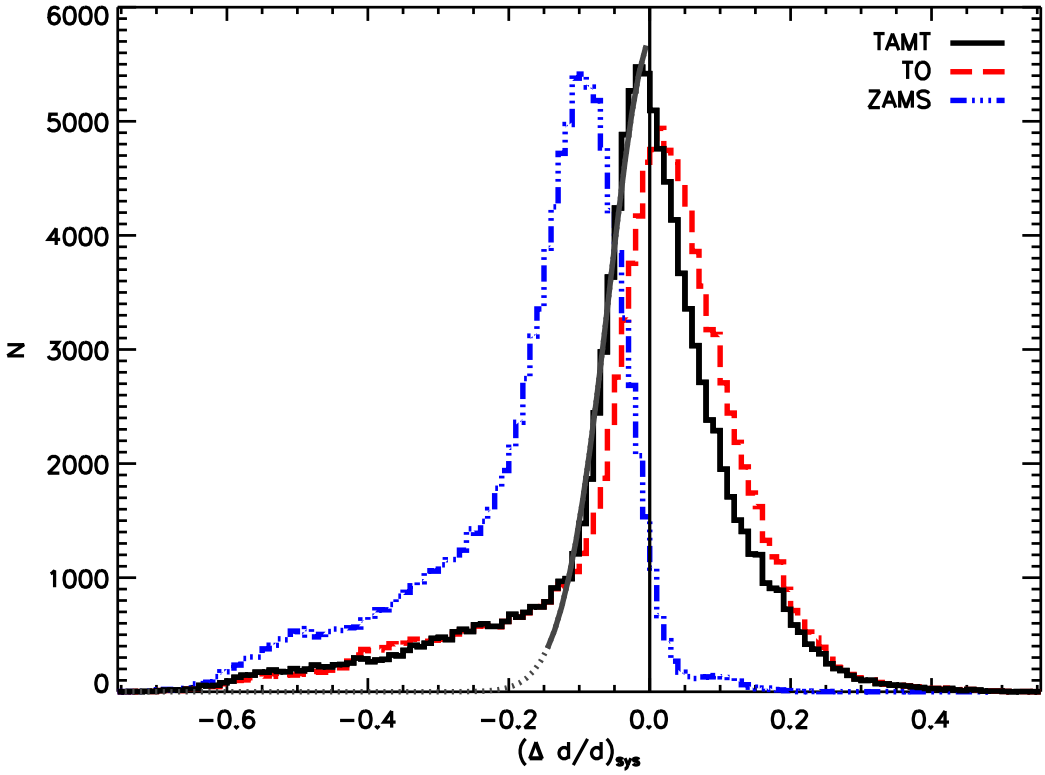

Figure 2.11: Fractional error distributions of solar metallicity stars ($-0.05 <$ [Fe/H] < 0.05) for three different age assumptions, as described in the text (see also Figure 2.3). The TAMT age assumption gives the best agreement between the calculated and true model distances. Based on the width of the distribution, we estimate the systematic error on our distance estimates to be $\sim 10\%$. The vertical line indicates where the fractional error is zero. The gray line is a Gaussian fit to the TAMT distribution where $-0.15 < (\Delta d/d)_{\rm sys} < 0.0$, which we use to estimate the fraction of subgiants in our sample ($\sim 15\%$).

this assumes that most targets are located on the zero-age main sequence, as shown in the fourth panel of Figure 2.3.

To assess the effect of the age assumption alone, we compare our calculated distance, d, to the true distance from the model, $d_{\rm model}$, for 111,640 mock targets at solar metallicity ($-0.05 <$ [Fe/H] < 0.05), where theoretical isochrones from different groups show the best agreement. Any disagreement between the isochrones used to generate the mock catalog and the isochrones used to calculate the distances will introduce an additional systematic error, which we discuss at the end of this section. The distributions of the systematic fractional error,

$(\Delta d/d)_{\rm sys}$, for all three age assumptions are shown in Figure 2.11, where the systematic fractional error is given by

$$\left(\frac{\Delta d}{d}\right)_{\rm sys} = \frac{d - d_{\rm model}}{d_{\rm model}}. \tag{2.1}$$

Based on the offsets of the distributions, the TO (red dashed line) and ZAMS (blue dash-dotted line) assumptions overestimate and underestimate the distances, respectively, though the ZAMS assumption does much worse. The TAMT (black solid line) assumption gives the best agreement between the calculated and model distances, with an error of $\sim 10\%$, based on the width of the $(\Delta d/d)_{\rm sys}$ distribution. Mock targets at other metallicities exhibit the same behavior, with the TAMT assumption giving the best distances with a mean error of $\sim 10\%$. This error includes the discrepancy between the isochrone [α/Fe] and that of individual stars, as the model stars have a range of [α/Fe] that do not exactly match the sequence of the An et al. (2009) isochrones.

Using the $(\Delta d/d)_{\rm sys}$ distribution, we can also estimate the number of subgiants in our sample by investigating the long tail of negative fractional errors. The gray line in Figure 2.11 shows a Gaussian fit to the TAMT histogram where $-0.15 < (\Delta d/d)_{\rm sys} < 0.0$—this range was chosen by eye to reflect the range where subgiants were not contributing to the distribution. By examining the discrepancy between the Gaussian fit and the long tail of negative $(\Delta d/d)_{\rm sys}$ values, we estimate the contamination by subgiants to be $\sim 15\%$; we obtain the same result if we take subgiants to be all stars with $(\Delta d/d)_{\rm sys} \leq -0.15$. We derive similar values for other metallicities as well.

We can also assess how an error in the value of the TAMT affects the distances that we obtain in our calculation. If we view the TO assumption as the TAMT assumption with an incorrect TAMT—one that is too old by 0.2 dex—we can estimate how much the distances change as a result. Comparing the TAMT and TO results in Figure 2.11, the peak $(\Delta d/d)_{\rm sys}$ values of the two assumptions are within 5%, which suggests that any error in the TAMT is smaller than the error from the age assumption scheme used.

The above analysis can be applied to stars at all metallicities. At each metallicity,

however, the peaks of the distributions are shifted up to $\sim 10\%$ because of differences between the stellar evolutionary models used (i.e., BaSTI and An et al. 2009 isochrones). This has the effect of increasing the width of the $(\Delta d/d)_{\rm sys}$ distribution to $\sim 15\%$ for the total sample, compared to $\sim 10\%$ for the solar metallicity sample. The peak of the distribution is at $\sim -8\%$. The results are similar when using the Dotter et al. (2008) isochrones: at a given metallicity, the peak of the distribution is shifted up to $\sim 10\%$. For the total sample, the width is $\sim 15\%$ and the peak of the distribution is at $\sim -3\%$.

Random Errors. The random error in the distances is dominated by uncertainties in the stellar parameters derived by the SSPP; errors in the magnitudes are trivial in comparison. We examine how the parameter errors propagate through our analysis by generating 500 Monte Carlo realizations of the mock catalog, with slightly perturbed values of the stellar parameters, and repeating the same distance measurements each time. For each realization we assign a Gaussian distribution of perturbations with widths of 200 K and 0.3 dex for $T_{\rm eff}$ and [Fe/H], respectively. These values are motivated by the errors estimated by Lee et al. (2008a). The resulting random fractional error, $(\Delta d/d)_{\rm rand}$, is given by

$$\left(\frac{\Delta d}{d}\right)_{\rm rand} = \frac{d_{\rm perturbed} - d}{d}, \tag{2.2}$$

where $d_{\rm perturbed}$ is the distance calculated with the new perturbed values of the stellar parameters. From the distribution of $(\Delta d/d)_{\rm rand}$, we estimate that the uncertainty in the SSPP parameters translates to a $\sim \%15 - 20\%$ error in the distance. These values correspond to the 68% confidence levels derived from the width of the distribution.

We can now calculate the total error in the distance, which combines the systematic and random errors from the age assumption and the stellar parameters, respectively. Because we include stars at all metallicities, we are also accounting for the uncertainties from discrepancies between the BaSTI and An et al. (2009) isochrones. The result is the total fractional error

$(\Delta d/d)_{\rm total}$, given by

$$\left(\frac{\Delta d}{d}\right)_{\rm total} = \frac{d_{\rm perturbed} - d_{\rm model}}{d_{\rm model}}. \tag{2.3}$$

We estimate that, including both the systematic and random errors, we have a total distance error of $\sim 20\% - 25\%$, with a larger contribution from the uncertainty in the stellar parameters determined by the SSPP. This total error is comparable to the size of the errors in the distances estimated by Gilmore et al. (1995) for their sample of MSTO stars.

Errors in the Metallicity Gradient Measurement

Systematic Errors. Using the same mock catalog, we also assess how well we measure the radial metallicity gradients in the disk. Figure 2.12 is the same as Figure 2.8, but shows the gradient results for the mock catalogs in four $|Z|$ slices. The true gradients, measured using the entire mock catalog, are shown as black circles. We draw 100 random samples (6500 MSTO stars each) from the mock catalog using the same selection criteria as the real data (§2.2.1) and follow the same analysis procedures, including accounting for the weights (§2.4 and Appendix A).

The filled symbols in Figure 2.12 show the mean gradient of the 100 realizations; the error bars indicate the standard deviation of the distribution. The smaller open symbols show the gradient measurements for one particular realization, with the error bar indicating the random error due to the uncertainty in the stellar parameters (see below).

The true gradients (open black circles) are generally within the errors of the weighted measurements (filled red squares), indicating that our measurements are reliable. More importantly, the weighted measurements show the same flattening trend with $|Z|$ as the true gradient. This is not seen in the unweighted gradient measurements (filled blue triangles). While the metallicity gradient in the model is steep compared to recent observations (e.g., Luck & Lambert 2011), our mock catalog analysis demonstrates that the weighting procedure is necessary to reproduce the flattening trend.

Random Errors. The error bars on the open symbols represent the random errors,

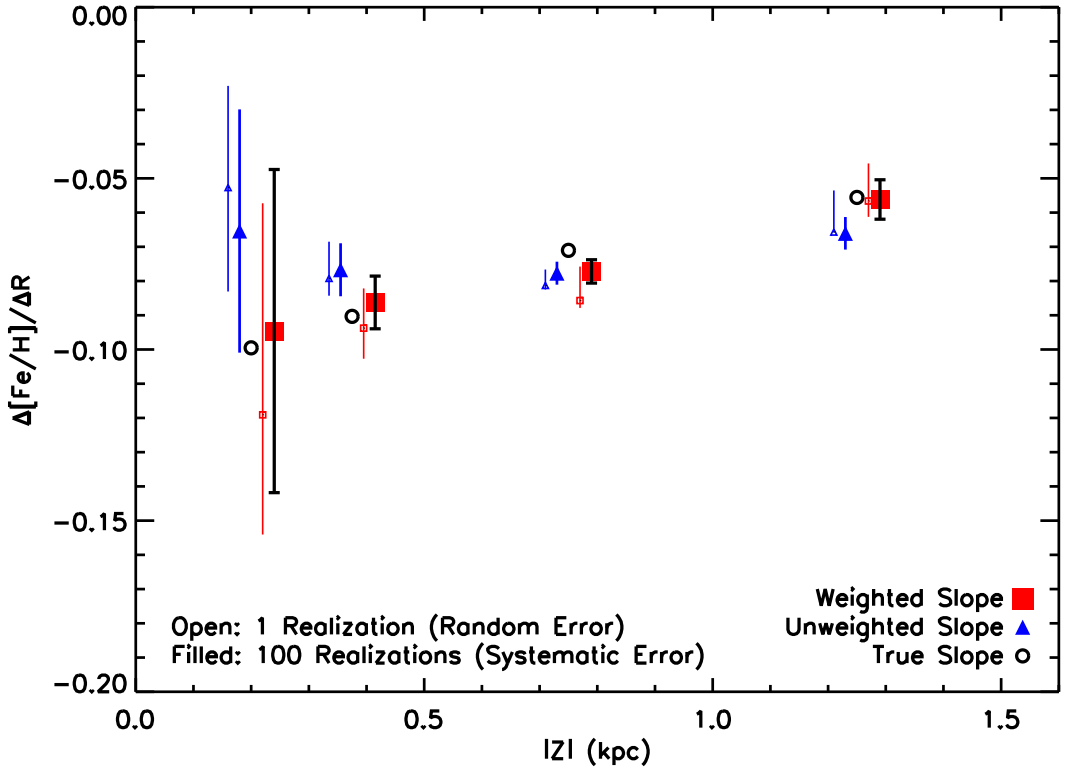

Figure 2.12: Measured gradient, Δ[Fe/H]/ΔR, vs. vertical height, $|Z|$, using mock samples. This figure is analogous to Figure 2.8, except the samples used are drawn from mock catalogs of the galaxy model of Schönrich & Binney (2009a). The mean and standard deviation for 100 such samples of MSTO stars are shown as filled symbols. The open symbols show the measured gradients for one particular random sample, with the error bars showing the random errors derived from Monte Carlo realizations using perturbed stellar parameters. The black circles show the true gradient, which is measured using all of the targets in the catalog. The true gradient generally falls within the errors presented for the weighted gradient (red squares) measured using the MSTO samples, which indicates that our method of measuring the gradient gives a reliable result. More importantly, we are able to reproduce the flattening trend seen in the true gradient. This is not true for the unweighted gradient measurements (blue triangles). Note that the vertical scale is different from that of Figure 2.8.

which are derived by running our full analysis on one sample of 6500 MSTO stars from the mock catalog, where we generate 500 Monte Carlo realizations of the mock data with perturbed stellar parameters. The error bars indicate the 68% confidence levels derived from the width of the distribution of slopes we obtain in the 500 realizations. This is the same procedure followed to determine the random distance errors in §2.6.3. The random errors are comparable to the

systematic errors on the gradient, although in some cases they are larger. The large error bars for the lowest $|Z|$ bin is due to a combination of the smaller number of stars and the smaller range in R.

2.7 Discussion

2.7.1 Comparison with Previous Studies

The median metallicity we find at $|Z| > 1$ kpc ([Fe/H] ~ -0.5) is consistent with the value published by Gilmore et al. (1995) for their stars located 1.5 kpc above the plane; the median $|Z|$ for our sample above 1 kpc is 1.24 kpc. Their sample also consisted of an in situ sample of F/G dwarfs, allowing for a direct comparison. This value is also in agreement with the mean of Soubiran et al. (2003; -0.48) and the mode of Katz et al. (2011; -0.52) at similar $|Z|$ heights. The G-dwarf sample of Lee et al. (2011b), also drawn from SEGUE, has median values of [Fe/H] within 0.1 dex of that of our sample as a function of $|Z|$.

Based on recent observations along two lines of sight, Katz et al. (2011) find that the similar metallicity distributions of their two fields at 2 kpc $< |Z| <$ 4 kpc are suggestive of a weak or non-existent radial gradient, although they cannot unambiguously rule it out. Our results are also consistent with the lack of a radial metallicity gradient found by both Allende Prieto et al. (2006), using spectra of 12,483 F/G stars from the SDSS, and Jurić et al. (2008), using photometric metallicities for millions of stars in the SDSS. However, both studies examine a much higher $|Z|$ sample with a limited R range at the vertical heights that our sample covers. The present study is complementary to these two studies in that we observe lower Galactic latitudes, and we are able to make a direct comparison of the thin disk and thick disk using the same homogeneous sample. Our results are based on a sample that has been carefully corrected for selection effects, and we use an improved version of the SSPP that is more accurate for metal-rich stars, which was not available for these previous analyses.

In their analysis of thick disk stars in the solar neighborhood, Bensby et al. (2003; 2005) find that abundance trends using O, Mg, and Fe do not vary as a function of R or $|Z_{\rm max}|$ in the region 5 kpc $< R <$ 7 kpc, 0 kpc $< |Z_{\rm max}| <$ 1.1 kpc, where $|Z_{\rm max}|$ is the maximum vertical height reached by the calculated stellar orbit. These detailed abundances, together with our finding of a flat metallicity gradient at large $|Z|$, are suggestive of a chemically homogeneous thick disk, although more observational data are needed to confirm this.

2.7.2 Comparison with Open Clusters and Cepheids

In Figures 2.5 and 2.7 we show open cluster and Cepheid data from the literature. These two classes of objects have been studied extensively with high-resolution spectroscopy and also span a large range in age, giving them the power to probe the chemistry of the interstellar medium at different times. Cepheids typically have lifetimes on the order of $\sim$ 100 Myr and trace the present metallicity distribution. Open clusters can have ages anywhere from less than a Gyr to greater than 10 Gyr and have been used to examine the temporal evolution of the disk's metallicity gradient.

We compare our old disk stars to a sample of open clusters with abundance determinations from high-resolution spectra. We note in particular 39 open clusters from the work of four groups that have studied clusters at $R >$ 10 kpc: 5 from Yong et al. (2005; Y05), 9 from Carraro et al. (Carraro et al. 2004; 2007b, Villanova et al. 2005, Frinchaboy et al. 2008; C07), 12 from Bragaglia, Carretta, Sestito, et al. (Bragaglia et al. 2001, Carretta et al. 2004; 2005; 2007, Sestito et al. 2006; 2007; 2008; BCS), and 19 from Friel, Jacobson, and Pilachowski (Friel et al. 2005; 2010, Jacobson et al. 2008; 2009; 2011a;b; FJP). Additional clusters from the compilation of Carrera & Pancino (2011; CP11, see their Table 12) are also included; we only consider those spatially coincident with our sample, i.e., those that are at least 150 pc from the midplane. Where we did not already have spatial and age information, parameters were obtained using the

WEBDA[9] open cluster database. Twenty-three clusters have measured abundances from more than one study, which provides an indication of the size of the uncertainties and systematics between groups. For clusters with more than one measurement, a line connects the symbols representing the different determinations.

Properties of the clusters are listed in Table 2.4. The open clusters have ages ranging from 0.6 to 10.1 Gyr; the median age is 2.0 Gyr, with only two clusters as old as 7 Gyr, which makes this cluster sample younger than the typical age of the stars in our sample (see Table 2.3). The ages of the clusters are indicated by the size of the symbols in Figure 2.5 and 2.7, with older clusters having larger symbols. It should be noted, however, that the cluster ages are derived using a variety of methods and are not on the same scale as those of the field stars considered in this study.

The Cepheid data are taken from Andrievsky et al. (2002b;a;c; 2004) and Luck et al. (2003; 2006) (AL), and Yong et al. (2006; Y06). Most of the Cepheids in these samples are too close to the midplane ($|Z| < 0.15$ kpc) to be directly compared to our sample. Those in the higher bins (0.5 kpc $< |Z| <$ 1.0 kpc), which are mostly from the Yong et al. (2006) sample, tend to be at larger radii than our MSTO stars. For consistency we have re-calculated R, $|Z|$ values using published l, b, and distances with $R_{\mathrm{GC},\odot} = 8.0$ kpc, where necessary.

Both Cepheids and open clusters appear to be slightly more metal rich than the median metallicities of the old disk stars. Systematic differences in [Fe/H] between different groups can be up to 0.2 dex, as shown by the clusters with multiple measurements (see Table 2.4 as well as the discussion in the Appendix of Friel et al. 2010). Given the good agreement between the SSPP and literature values, however, these systematic differences may not explain the discrepancy. As we do not see any obvious differences in metallicities between old and young clusters (large versus small open symbols), the cause of a possible discrepancy is unknown at this time. Understanding the differences between the different tracers will be crucial to understanding how the disk formed

[9] http://www.univie.ac.at/webda/

and its subsequent evolution.

At low $|Z|$, the slopes of the open clusters and field stars do not appear to be dramatically different, as expected given the good agreement between our measurement of the radial gradient in the low $|Z|$ bins and the values of Friel et al. (2002) and Luck et al. (2006; dotted lines in Figure 2.8). However, at high $|Z|$, there are three clusters with metallicities ~ 0.5 dex higher than the median [Fe/H] for field stars at small R (< 10 kpc). While a steeper slope in the inner regions of the disk (-0.13 dex kpc^{-1} at $R < 8$ kpc) has been reported for both open clusters and Cepheids (e.g., Pedicelli et al. 2009, Magrini et al. 2010), we do not see a steeper metallicity gradient at $R < 8$ kpc in our sample of old disk stars.

The question of how the radial metallicity gradient may change over time is still debated in the literature, with conflicting reports of flattening (e.g., Friel et al. 2002, Chen et al. 2003, Maciel et al. 2005), steepening (e.g., Stanghellini & Haywood 2010), and constant slopes (e.g., Magrini et al. 2009) as a function of time. If the gradient is steeper in the inner disk, as has been reported, the flatness of the gradient for old disk stars, at face value, implies that the radial metallicity gradient in the inner disk has grown steeper with time. Radial migration complicates this issue greatly, however, as the movement of stars from their initial orbits may wash out a previously existing gradient (e.g., Roškar et al. 2008a). Based on the observations presented here, we are not able to draw any clear conclusions about the time evolution of the metallicity gradient in the inner disk.

The disagreement in abundances between young and old tracers is not present in the outer disk, where the median metallicity of the old disk stars ([Fe/H] ~ -0.5) is consistent with the metallicities reported by Yong et al. (2005) for outer disk open clusters. Furthermore, the median metallicity of our sample at $|Z| > 1.0$ kpc is constant at *all* values of R, which suggests that the flattening of the gradient is due to a trend in $|Z|$. Given the change in the radial range spanned in each $|Z|$ bin, a superposition of the negative gradient at small $|Z|$ with a flat gradient at large $|Z|$ could result in an apparent discontinuity in the radial gradient.

This result suggests that when examining trends in the *radial* direction, it is important to take the *vertical* information into account. As shown in Figure 2.5, all of the outer disk clusters from the literature ($R > 15$ kpc) are located far from the Galactic plane; this has been noted in previous studies (e.g., Jacobson et al. 2011a, Carrera & Pancino 2011). In the present work, we find that the mean metallicity of these clusters is consistent with field stars located at *all* R at similar vertical heights ($|Z| > 1.0$ kpc), although our field star sample extends only to $R \sim 15$ kpc, whereas the clusters reach radial distances of 20 kpc or more. Based on our observations of old disk stars, whether the reported discontinuity is truly a feature of the *radial* metallicity gradient is unclear.

Our sample does not reach to sufficiently large radii at low latitudes; with the limited range in R at low $|Z|$, we cannot confirm that the trend is purely vertical. If the radial gradients we measure at $|Z| < 1.0$ kpc extend to large R (> 15kpc) *for all* $|Z|$, then the discontinuity in the radial metallicity gradient of the disk actually reflects the change in slope at different $|Z|$. Friel et al. (2010) have stressed the need for more high-resolution data of open clusters to build up a homogeneous, statistical sample; our work shows that it is also necessary to fully sample a range of both R and $|Z|$ to understand the metallicity trends in the disk. The large R, low $|Z|$ region of the Galaxy will be probed by future surveys such as APOGEE (Eisenstein et al. 2011).

2.7.3 Implications for Thick Disk Formation

The lack of a radial metallicity gradient far from the Galactic plane provides an observational constraint that must be matched by any viable scenario for thick disk formation, such as the four described in §4.1. A flat gradient, as we measure, may come most naturally out of a turbulent disk at high redshift (Scenario 3). If the thick disk formed rapidly at early times (e.g., Brook et al. 2004; 2005), then the thick disk would be chemically homogeneous, and the radial metallicity gradient far from the plane of the disk would be flat.

The observations can only be explained by current models of radial migration in isolated disks (e.g., Roškar et al. 2008a, Schönrich & Binney 2009a) if radial mixing is strong (Scenario 4). These models show that dynamical interactions with spiral arms can move stars from their initial orbits and make the gradient shallow, but the mechanism must be efficient if it is the dominant mechanism for forming the thick disk. The degree of radial mixing may be increased through dynamical interactions with the Galactic bar (Friedli et al. 1994, Martin & Roy 1994, Minchev & Famaey 2010).

Another possible way to increase the amount of radial mixing in a disk is to place the disk within a cosmologically motivated accretion history (Scenario 1). The simulations of Bird et al. (2012) show that stars can move far from their initial orbits in a disk that is bombarded by multiple minor mergers (e.g., Kazantzidis et al. 2008). Furthermore, the bombarded disk experiences more radial mixing at high $|Z|$ than an identical disk in isolation. At the midplane, however, both scenarios show about the same amount of mixing. The increased radial mixing at high $|Z|$ could be responsible for the lack of a radial gradient.

With our data alone, we cannot rule out the direct accretion of stars that originally formed in satellites that have been disrupted (Scenario 2). To assess whether the thick disk exhibits the predicted clumpiness, we would need to investigate the azimuthal variation within our sample or at more detailed abundances with followup observations. But observations of the orbital properties of stars in SDSS and RAVE (Dierickx et al. 2010, Wilson et al. 2011) show that there are not enough high-eccentricity stars to match what is seen in the simulations of Abadi et al. (2003). Furthermore, recent simulations (Read et al. 2008, Villalobos & Helmi 2008) predict lower numbers of stars being directly accreted during minor mergers than the 2003 simulations.

Other recent work using kinematic constraints — correlations between rotational velocity V_ϕ, [Fe/H], R, and $|Z|$ — have also favored a cosmological formation scenario for the thick disk (e.g., Spagna et al. 2010, Lee et al. 2011b), although they do not rule out Scenario 4. Both

of these papers stress the importance of further theoretical work. Only recently have simulations begun to include prescriptions for the formation of stars and their impact on the expected chemistry of the disk populations (e.g., Brook et al. 2005, Stinson et al. 2010, Loebman et al. 2011; and references therein). The measurement of the radial metallicity gradient at different heights above the plane is an additional observational constraint that can be used to test new, improved models for disk evolution and the next generation of simulations.

2.8 Summary

Using a sample of 7010 MSTO stars from the SEGUE survey, we measure the radial metallicity gradient, Δ[Fe/H]/ΔR, as a function of height above the plane $|Z|$, in the Milky Way disk. Near the midplane, where our sample is dominated by the thin disk, we see a negative radial metallicity gradient that is consistent with previously published values (Friel et al. 2002, Luck et al. 2006, Luck & Lambert 2011). At large vertical heights, where our sample is dominated by the thick disk, the radial metallicity gradient becomes flat, consistent with previous work (Allende Prieto et al. 2006) using a sample located at larger $|Z|$. Our sample, located at low Galactic latitude, covers a larger range in R at small $|Z|$ and allows us to make a direct comparison between the thin disk and thick disk using the same sample.

At $|Z| > 1.0$ kpc, the median metallicity of old disk stars is consistent with the open cluster metallicities reported by Yong et al. (2005) and others at large R. In addition, our sample of disk stars shows that the flat gradient at large vertical height $|Z|$ extends to small R. Because the outer disk clusters are all located at large $|Z|$, the reported discontinuity in the radial gradient is consistent with a transition found using tracers at small $|Z|$ to large $|Z|$. We stress that abundances need to be examined as a function of both R and $|Z|$ in order to truly understand the observed trends.

In contrast to the outer disk, open clusters and Cepheids in the inner disk at high

$|Z|$ have median metallicities $\sim$ 0.5 dex higher than old disk stars at the same R and $|Z|$; thus, far from the Galactic plane, the younger tracers do not exhibit the same flat metallicity gradient that is seen in the old disk stars. Whether this is indicative of a metallicity gradient that becomes steeper with time is unclear, as radial migration may play a role in erasing a pre-existing gradient in the old disk stars, and what that initial gradient in the early disk may be is still uncertain.

A flat radial metallicity gradient in the thick disk is consistent with the predictions of a gas-rich, turbulent disk at high redshift (Brook et al. 2005, Bournaud et al. 2009). It may also be consistent with the scenarios of radial migration (Roškar et al. 2008a, Schönrich & Binney 2009b, Minchev & Famaey 2010) or minor mergers (Kazantzidis et al. 2008, Bird et al. 2012), provided that mixing in the radial direction is strong. We also cannot exclude the direct accretion of stars from satellites in minor mergers (Abadi et al. 2003). While we are not able to conclusively rule out any of these scenarios, the change in the radial gradient as a function of height above the plane is an important observational constraint for future theoretical work.

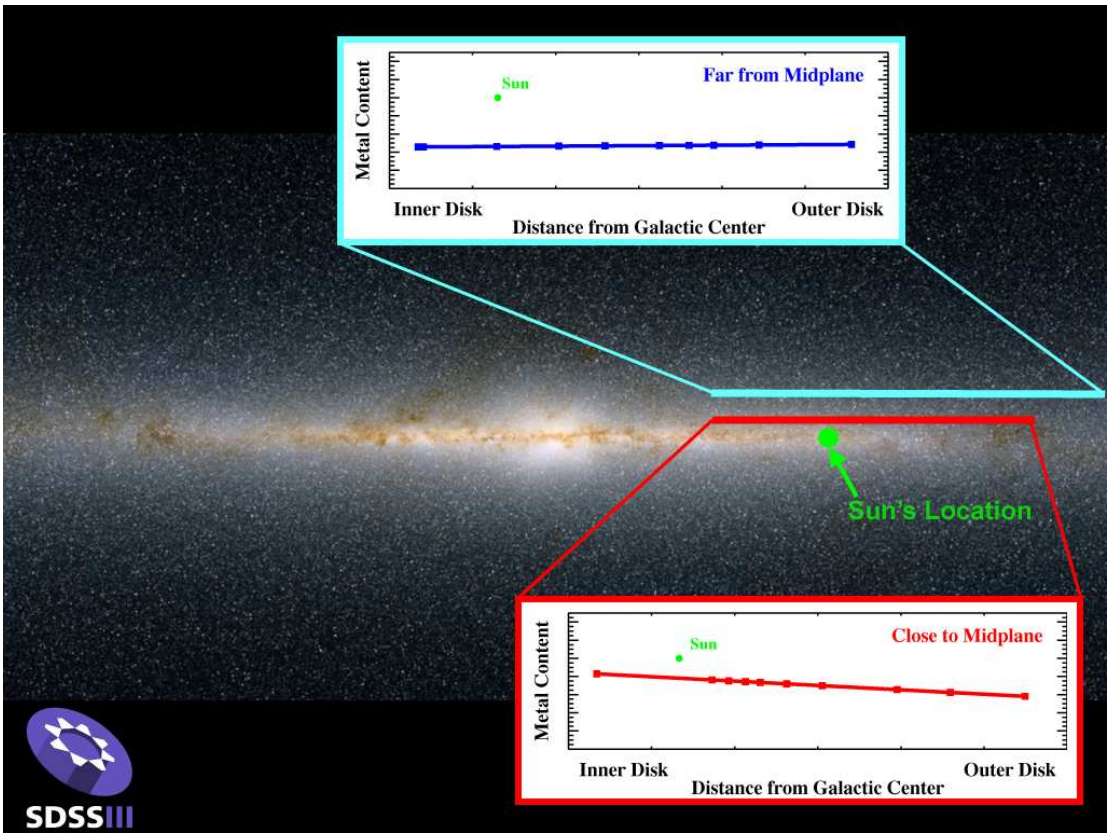

SDSS Press Release, January 2012: "Not All Who Wander Are Lost"[10]
[Credit: Judy Cheng and Connie Rockosi (University of California Santa Cruz); 2MASS Survey]

[10]http://www.sdss3.org/press/20120109.wander.php

Chapter 3

A Short Scale Length for the α-Enhanced Thick Disk of the Milky Way

3.1 Introduction

Detailed observations of the Galactic thick disk can be used to constrain the relative importance of cosmological accretion and secular processes in the formation and growth of the Milky Way disk. Thick disk stars are old ($>$ 8 Gyr, Bensby et al. 2005) and provide a fossil record of the Galaxy at $z \sim 2$. Observations of these old stars can serve as a complement to studies of distant galaxies at early times, many of which are seen to be thick, turbulent, clumpy, star-forming disks (e.g., Elmegreen & Elmegreen 2005; 2006, Förster Schreiber et al. 2009; 2011). Observations of nearby galaxies have shown that thick disks are common, with similar properties (Dalcanton & Bernstein 2002, Yoachim & Dalcanton 2005; 2006; 2008b;a), which suggests that thick disks are a generic feature of disk galaxies. Thus, the processes responsible for the existence

of the Milky Way thick disk may play an important role in the formation of all disk galaxies.

Several mechanisms have been proposed to explain the formation of the thick disk. Four such mechanisms are (1) vertical heating through minor mergers (e.g., Kazantzidis et al. 2008, Read et al. 2008, Villalobos & Helmi 2008, Kazantzidis et al. 2009, Purcell et al. 2009, Bird et al. 2012); (2) direct accretion of stars from satellites (Abadi et al. 2003); (3) in-situ formation during an early turbulent disk phase due to high gas accretion rates (e.g., Brook et al. 2004; 2005, Bournaud et al. 2009); and (4) radial migration of stellar orbits via resonant interactions with transient spiral structure (e.g., Roškar et al. 2008b;a, Schönrich & Binney 2009a;b, Loebman et al. 2011). Scenarios 1-3 fit within the context of hierarchical structure formation as predicted by ΛCDM cosmology, while Scenario 4 is possible in a disk in complete isolation. Each of these scenarios can be tested through comparisons with the observed chemical and kinematic properties of stars in the Milky Way.

Since the thick disk's discovery by star counts (Yoshii 1982, Gilmore & Reid 1983), an apparent dichotomy between thin and thick disk populations has been established. Stars belonging to the thick disk are older and more metal poor (e.g, Gilmore et al. 1995, Chiba & Beers 2000, Bensby et al. 2004, Ivezić et al. 2008). In addition, thick disk stars have chemical abundance patterns distinct from the thin disk, with thick disk stars being enhanced in α- and r-process elements (Edvardsson et al. 1993, Prochaska et al. 2000, Mashonkina & Gehren 2000; 2001, Reddy et al. 2003; 2006, Bensby et al. 2003; 2005, Brewer & Carney 2006). The results of these latter studies show that the scatter in the observed [α/Fe] is small, suggesting that thick disk stars formed quickly in a well-mixed interstellar medium.

The high [α/Fe] characteristic of thick disk stars indicates that they formed in a period of rapid star formation and chemical enrichment, during which Type II SNe were able to contribute significant amounts of α-elements into the interstellar medium before Type Ia SNe increased the abundance of iron-peak elements. The observed abundance trends of nearby thick disk stars have been used to estimate that the thick disk formed over a period of ∼1-3 Gyr (Grat-

ton et al. 2000, Mashonkina & Gehren 2001, Mashonkina et al. 2003, Bensby et al. 2004). The chemical properties of thick disk stars are thus a powerful tool for understanding the chemical enrichment and star formation history of the Galaxy.

Whether the enhanced [α/Fe] for thick disk stars in the solar annulus ($R_{\rm GC,\odot}$ = 8.0 kpc) is present for in-situ thick disk stars (i.e., those at large $|Z|$, where the thick disk is expected to dominate) remains an open question. Early in-situ studies examined only the [Fe/H] distribution (Gilmore et al. 1995). Analyses of more elements has largely been restricted to stars in the solar neighborhood, where stars are typically divided into thin and thick disk populations by their kinematics (e.g., Bensby et al. 2003; 2005). Recently, Bensby et al. (2011) examined the abundances of a sample of 119 red giants in the inner and outer disks using high-resolution spectroscopy and found evidence that the [α/Fe] trends observed in the inner disk do not extend to the outer disk (see also Bensby et al. 2010a, Alves-Brito et al. 2010). Thus, while many of the thick disk formation scenarios discussed above (such as the work of Brook et al. 2005 and Schönrich & Binney 2009b) are able to reproduce the dichotomy seen in the chemical properties of thin and thick disk stars in the solar neighborhood, observations have only begun to test the models at a wide range of R and $|Z|$ in the Galactic disk.

Using a sample of old disk stars from the Sloan Extension for Galactic Understanding and Exploration (SEGUE; Yanny et al. 2009) survey, we have begun to explore a larger volume of the Galaxy. We previously showed that the radial metallicity gradient in [Fe/H] becomes flat for stars located at vertical heights $|Z| > 1$ kpc from the Galactic plane, where the thick disk is expected to be the dominant population (Chapter 2). This result is consistent with a chemically homogeneous thick disk, which is predicted by thick disk formation during a period of early gas-rich accretion (Scenario 3). The flat gradient could also be explained if the strength of radial mixing is sufficient to erase a pre-existing gradient in the thin disk (Scenario 4).

Chapter 2 also demonstrated that the reported flattening trend in the radial metallicity gradient at $R \gtrsim 10$ kpc (Yong et al. 2005, Luck et al. 2006) could arise because all of the distant

tracers were located at large $|Z|$, where the radial gradient is flat. We found that the observed trend could result from a simple superposition of a negative radial gradient at small $|Z|$ with a flat radial gradient at large $|Z|$. Because the clusters discussed in the literature at large R were also located at large $|Z|$, it is unclear whether the observed trends are due to changes in the radial or vertical directions. Therefore, we stressed the importance of examining the trends in [Fe/H] as a function of both R and $|Z|$.

In this Chapter, we extend our analysis of abundance gradients in the Milky Way to examine the α-element abundance ratio, [α/Fe], as a function of both Galactocentric radius R and distance from the plane $|Z|$, using a sample of 5620 field stars from SEGUE. Our work is complementary to that of Bensby et al. (2011), as our sample of main sequence turnoff stars is more than an order of magnitude larger than their sample of 119 K giants. We use a subset of the sample from Chapter 2, which covers the region 6 kpc $< R <$ 16 kpc, 0.15 kpc $< |Z| <$ 1.5 kpc. We present our data and results in §4.2 and §4.3, respectively. In §3.4, we present estimates for the thin and thick disk scale lengths; the procedure and errors are described in more detail in Appendix B. We discuss the implications of our results in §4.4.

3.2 Data

Our sample consists of main-sequence turnoff stars from SEGUE (Yanny et al. 2009, Eisenstein et al. 2011), part of the Sloan Digital Sky Survey (SDSS; York et al. 2000). The data are obtained using the same CCD camera (Gunn et al. 1998), telescope (Gunn et al. 2006), and filter system (Fukugita et al. 1996) as the SDSS. In this paper, we use a subset of stars from the sample of 7605 main sequence turnoff stars in Chapter 2, which cover the region 6 kpc $< R <$ 16 kpc, 0.15 kpc $< |Z| <$ 1.5 kpc. Briefly, these stars are selected using a cut in $g - r$ color. Stellar parameters $T_{\rm eff}$, log g, [Fe/H], and [α/Fe] are determined from low resolution ($R \sim 2000$) spectra using the SEGUE Stellar Parameter Pipeline (SSPP; Lee et al. 2008a;b, Allende Prieto

et al. 2008a, Smolinski et al. 2011, Lee et al. 2011a). In the present work, we select the stars with sufficient signal to noise (S/N $>$ 20 pixel^{-1}, where each pixel corresponds to $\sim$ 1Å) for good [α/Fe] measurements, which yields 5771 stars with [α/Fe] measured to a precision of 0.1 dex (Lee et al. 2011a).

The S/N cut effectively imposes a magnitude limit, and because the [α/Fe] of a star will not affect its magnitude significantly, this magnitude limit does not bias our sample against low-α stars. Dartmouth isochrones (Dotter et al. 2008) show that a 0.2 dex difference in [α/Fe] is equivalent to $<$ 0.1 mag difference in g-band magnitude, which corresponds to a 10% error in distance. This is a small effect compared to the total error in distance $20\% - 25\%$ estimated in Chapter 2. Therefore, we do not expect any significant systematic differences between the volumes sampled by high- and low-α stars. In our sample, the high- and low-α stars span the same ranges in R and $|Z|$, and they are seen out to the same distances.

As described in Chapter 2, we assign a weight to each target to correct for selection effects. The weight accounts for three properties of the selection: (1) objects in regions with the highest extinction in each line of sight were not considered for spectroscopy. (2) Not all candidates for spectroscopy are observed. (3) The $g - r$ color cut introduces a bias against redder, metal-rich stars. We show in Chapter 2 that using the calculated weights successfully reproduces the true metallicity gradients in a mock catalog. For a detailed discussion of the selection biases and how we correct for them using our weighting scheme, see §4 and Appendix A.

In addition to the weights we calculated in Chapter 2, we apply a weight to account for the stars that are removed by the additional S/N cut imposed on this sample; this is a small effect compared to the other weights. Taking all stars with non-zero weights, we are left with a sample of 5620 main sequence turnoff stars. Most of the stars that are given weights of zero are very blue objects, which are likely to be hotter stars that are not on the main sequence (for more discussion see Appendix A).

Distances were determined using photometric parallax methods, by comparing the

SSPP stellar parameters and photometry to the theoretical isochrones of An et al. (2009), as described in Chapter 2. Using a mock catalog of stars generated from the model of Schönrich & Binney (2009a), we estimate the errors in the distances to be $\sim 20\% - 25\%$; see Chapter 2 for details.

3.3 Results

3.3.1 Abundance Trends as a Function of R and $|Z|$

Figure 3.1 shows [α/Fe] as a function of Galactocentric radius R, in four slices of $|Z|$, for our sample of main-sequence turnoff stars, color coded by [Fe/H]. Most of the high-α population is confined to small radii ($R < 10$ kpc), consistent with the results of Bensby et al. (2011), who found a lack of high-α stars in the outer disk. In our sample, this lack of high-α stars is seen at all $|Z|$.

Figure 3.2 shows abundance trends in [Fe/H] and [α/Fe]. The top left panel shows the solar neighborhood sample of Bensby et al. (2003; 2005), in which stars are assigned to the thin and thick disks (red and blue, respectively) according to their kinematics. In the solar neighborhood, kinematically hot stars (i.e., thick disk stars) are α-enhanced relative to kinematically cooler stars (i.e., thin disk stars) at the same [Fe/H]. The top right panel shows the total SEGUE sample, where we see two populations analogous to the solar neighborhood thin and thick disk stars: (1) low-α stars that, like solar neighborhood thin disk stars, appear to follow a linear trend, with [α/Fe] slightly decreasing as [Fe/H] increases, and (2) a tail of high-α stars that, like solar neighborhood thick disk stars, are more metal poor than the low-α population.

In the remainder of our analysis, we divide our sample into high- and low-α stars, with the goal of comparing the high-α (low-α) stars to the kinematically selected thick (thin) disk stars in the Bensby sample; this is similar to the chemical separation done by Lee et al. (2011b).

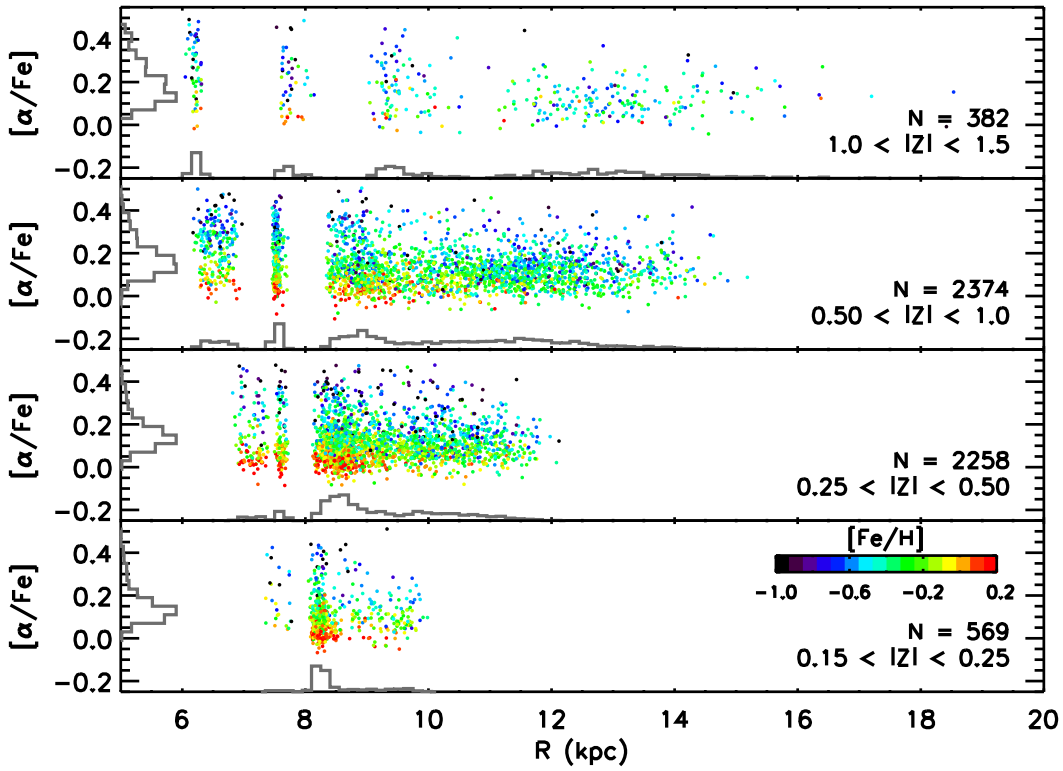

Figure 3.1: α-element abundance ratio [α/Fe] vs. Galactocentric radius R in four $|Z|$ slices. The SEGUE data are shown as dots, colored coded by [Fe/H]. At all $|Z|$, the majority of the high-α stars are located at small R (< 10 kpc).

We make the cut at [α/Fe]$= +0.2$, where the number of stars appears to drop dramatically at large R, as seen in Figure 3.1. This is marked by the horizontal dotted line in the top right panel of Figure 3.2. The number of high- and low-α stars is indicated in the top right corner in parentheses.

Finally, in the bottom four panels, we show the SEGUE sample divided into four $R, |Z|$ bins with cuts at $R = 10$ and $|Z| = 0.5$ kpc. The numbers in the top right corner of each panel indicate the weighted fractions of the high- and low-α populations, with the raw number of stars in parentheses. The weighting has the effect of slightly decreasing the fraction of high-α stars in each bin, but the effect is not dramatic. This is likely because selection on $g - r$ color is biased against metal-rich stars (see Chapter 2 for details); metal-poor stars, which are more likely to

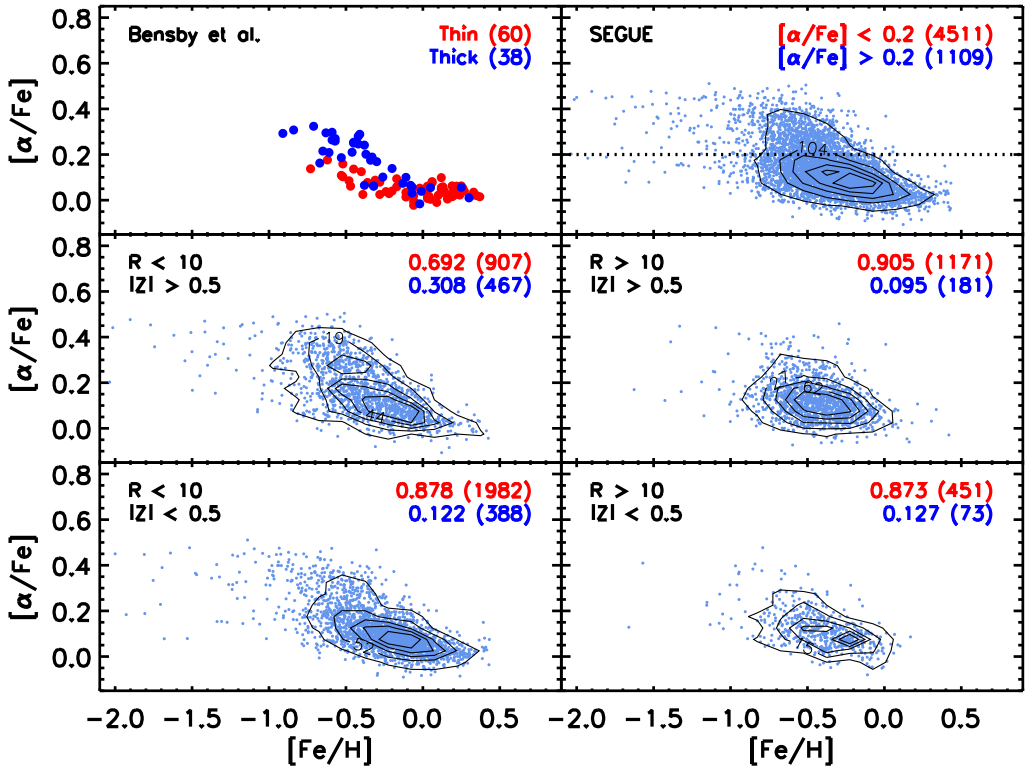

Figure 3.2: Abundance trends [α/Fe] vs. [Fe/H]. Top left panel: the solar neighborhood sample of Bensby et al. (2003; 2005), with thin and thick disk stars (red and blue, respectively) assigned according to their kinematics. Top right panel: the total SEGUE sample. The horizontal dotted line indicates where we make the distinction between low- and high-α stars. Bottom four panels: the SEGUE sample, divided into four bins of R and $|Z|$. The labels on the contours indicate the number of objects in a box with dimensions of 0.15 dex in [Fe/H] and 0.05 dex in [α/Fe]. In each panel, the weighted fraction of high- and low-α stars (blue and red, respectively) is indicated, with the raw number of stars in each population in parentheses. The abundance patterns at $R < 10$ kpc are similar to those seen for thin and thick disk stars in the solar neighborhood, with the fraction of high-α stars increasing at large $|Z|$. At $R > 10$ kpc, the fraction of high-α stars is low at *all* $|Z|$.

be high-α stars, are weighted less heavily to compensate for the bias.

At small R (< 10 kpc, left panels), we see the same high- and low-α populations as in the total SEGUE sample. The presence of two populations is especially evident at $|Z| > 0.5$ kpc. The fraction of high-α stars increases toward large $|Z|$ (> 0.5 kpc), from 12% to 31%, which is what we expect if the contribution from a high-α thick disk is greater far from the plane. At large R (> 10 kpc, right panels), in contrast to what is seen at small R, the fraction of high-α

stars does not increase at large $|Z|$ (> 0.5 kpc); the fraction is low at all $|Z|$. This observation at large R is inconsistent with the picture of a high-α population associated with a thick disk component, which should become more dominant at large $|Z|$ at all R. The main result of Figure 3.2 is that the [Fe/H]-[α/Fe] properties for stars at small R are consistent with those found for solar neighborhood stars, while at large R there is a lack of high-α stars. Furthermore, the fraction of high-α stars at large R does not increase with $|Z|$, as expected if there is a high-α, thick disk population in the outer disk.

The change in fraction of high-α stars at large R suggests that the chemical abundances of stars change with Galactocentric radius, even at large $|Z|$. But how can this result be reconciled with the flat radial metallicity gradient at $|Z| > 1.0$ kpc that we found in Chapter 2? Figure 3.3 shows the radial metallicity gradient Δ[Fe/H]/ΔR in four $|Z|$ slices for the total sample (gray, left column) and divided into low-α (pink, middle column) and high-α stars (blue, right column). For each sample, we fit a linear trend to the data, with each point weighted to account for selection biases, as in Chapter 2. The number of stars and the slope of a linear fit to the data are indicated in the bottom right corner of each panel.

The change in Δ[Fe/H]/ΔR with $|Z|$, as shown in Figure 3.3, is summarized in Figure 3.4. The radial gradient of the high-α sample (blue triangles) is flat at all R and $|Z|$, but it is not solely responsible for the flattening trend with $|Z|$ seen in the total sample (gray squares). The high-α stars do, however, make the gradients for the total sample flatter, especially at $|Z| > 1.0$ kpc, where the fraction of high-α stars is the largest. The flattening trend of the low-α sample (pink diamonds) is closely followed by the trend in the total sample. The results of Chapter 2 are also shown (black circles) in Figure 3.4. These are slightly different than the gradients measured for the total sample because of the S/N cut imposed on the sample in this work, but are still within the uncertainties. The errors are estimated using 500 Monte Carlo realizations of the data, where we perturb the stellar parameters $T_{\rm eff}$, [Fe/H], and [α/Fe] by the typical errors (200 K, 0.3 dex and 0.1 dex, respectively); see Chapter 2 for details.

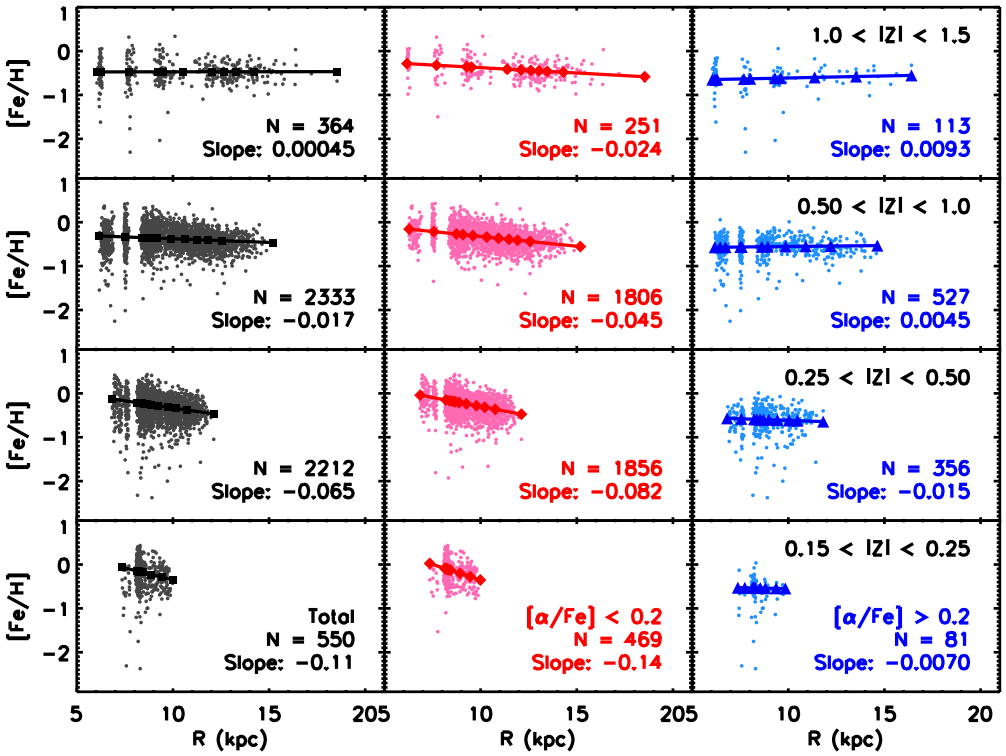

Figure 3.3: Galactocentric radius R vs. [Fe/H] in four $|Z|$ slices for high- and low-α stars. Left column: total sample. Middle column: low-α stars ([α/Fe] $< +0.2$). Right column: high-α stars ([α/Fe] $> +0.2$). In each panel the raw number of stars and the measured slope are indicated in the bottom right corner. The lines show a linear fit to the data, with each star weighted to account for selection biases. The spacing of the symbols on the linear relation indicates the radial distribution of the stars. The radial gradient in the total and low-α samples become flatter at large $|Z|$, while the radial metallicity gradient of the high-α sample is flat at all $|Z|$.

3.3.2 Kinematics of the High- and Low-α Populations

In addition to different chemical properties, thin and thick disk stars in the solar neighborhood exhibit different kinematic properties. A comparison of the kinematics of high-α stars at large and small R can help distinguish whether high-α stars at large R are the outer disk tail of the inner disk population, the high-α tail of the outer disk population, or a different population altogether. In this section we examine the rotational velocities V_ϕ of high- and low-α stars as a function of R and $|Z|$. For this analysis, we only consider 3985 stars, which have good proper motions, as described below.

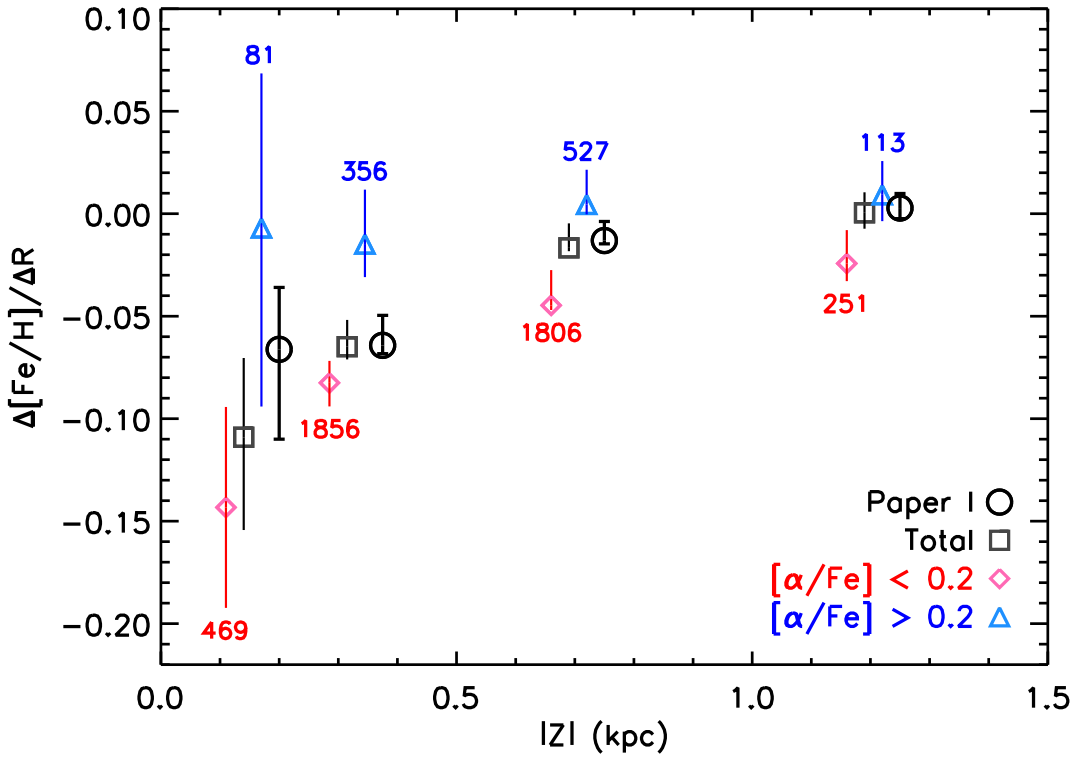

Figure 3.4: Radial metallicity gradient, Δ[Fe/H]/ΔR, vs. distance from the plane, $|Z|$, for high- and low-α stars. The radial gradients for the total sample in this work (gray squares) are consistent with those of Chapter 2, which were measured using a larger sample with a less strict S/N cut (black circles). The change in the radial gradient of the total sample as a function of $|Z|$ is driven by the change in the radial gradient of the low-α stars (pink diamonds); the radial gradient of the high-α stars (blue triangles) shows no obvious trend and is consistent with a flat gradient (slope of zero) at all $|Z|$. The number of stars used in each gradient measurement in the low- and high-α samples is indicated. The error bars reflect the random errors in the gradient measurement due to errors in the stellar parameters (see Chapter 2 for details).

We calculate three-dimensional velocities in Cartesian coordinates (U, V, W), and polar coordinates (V_R, V_ϕ, V_Z), using radial velocities along with proper motions obtained by combining the USNO-B and SDSS catalogs (Munn et al. 2004). We use the criteria of Kilic et al. (2006) to obtain a sample with clean proper motions: `sigRa < 525 mas, sigDec < 525 mas, match = 1, nFit = 6, dist22 >` $7''$, where `sigRa` and `sigDec` are the residual for the proper motion fit in right ascension and declination, `match` is the number of objects within a $1''$ radius, `nFit` is the number of plates the object was detected on, and `dist22` is the distance to the nearest

neighbor with $g < 22$. The efficacy of these criteria have been explored by Dong et al. (2011).

These selection criteria identify 3985 stars in our sample with reliable proper motions; this subsample has the same distributions in distance, magnitude, color, [Fe/H], and [α/Fe] as the larger sample of 5620 stars, so we treat it as a representative sample and do not apply any additional weights. Statistical errors on the proper motions are roughly $3-3.5$ mas yr^{-1}, which correspond to a tangential velocity error of $28-33$ km s^{-1} at a distance of 2 kpc.

In this section we present histograms, corrected using our weighting scheme, which are needed to properly account for the different sampling along different lines of sight. For example, there are many more stars in the lines of sight toward smaller R ($l < 90°$) compared those at the anti-center ($l \sim 180°$), but the number of spectra are approximately equal in all directions. Accounting for this effect is necessary to reproduce the correct distributions, but doing so magnifies the Poisson noise.

Figure 3.5 shows V_ϕ histograms for the Bensby sample (top left panel), the total SEGUE sample (top right panel), and the SEGUE sample in the four $R, |Z|$ bins (bottom four panels), similar to Figure 3.2. In each panel, as in Figure 3.2, the sample is divided into high- and low-α stars (blue and red, respectively) at [α/Fe]$= 0.2$. The shaded regions indicate errors estimated by generating 500 Monte Carlo realizations of our data, where we perturb the stellar parameters, radial velocities, and proper motions; the typical errors on the radial velocities and proper motions are 6.0 km s^{-1} and 3 mas yr^{-1}, respectively.

We calculate the mean rotational velocities $\langle V_\phi \rangle$ for each population (vertical solid lines) using an outlier-resistant algorithm, which trims values greater than three median absolute deviations from the median (vertical dotted lines in Figure 3.5). The numerical values of $\langle V_\phi \rangle$ are indicated in the top right corner of each panel, with the raw number of stars in parentheses. The errors on the means are indicated by the shaded regions surrounding the vertical solid lines. For the low-α samples, the error on the mean is $\sim 2-3$ km s^{-1}, while for the high-α samples, which have fewer stars, it is $\sim 4-10$ km s^{-1}.

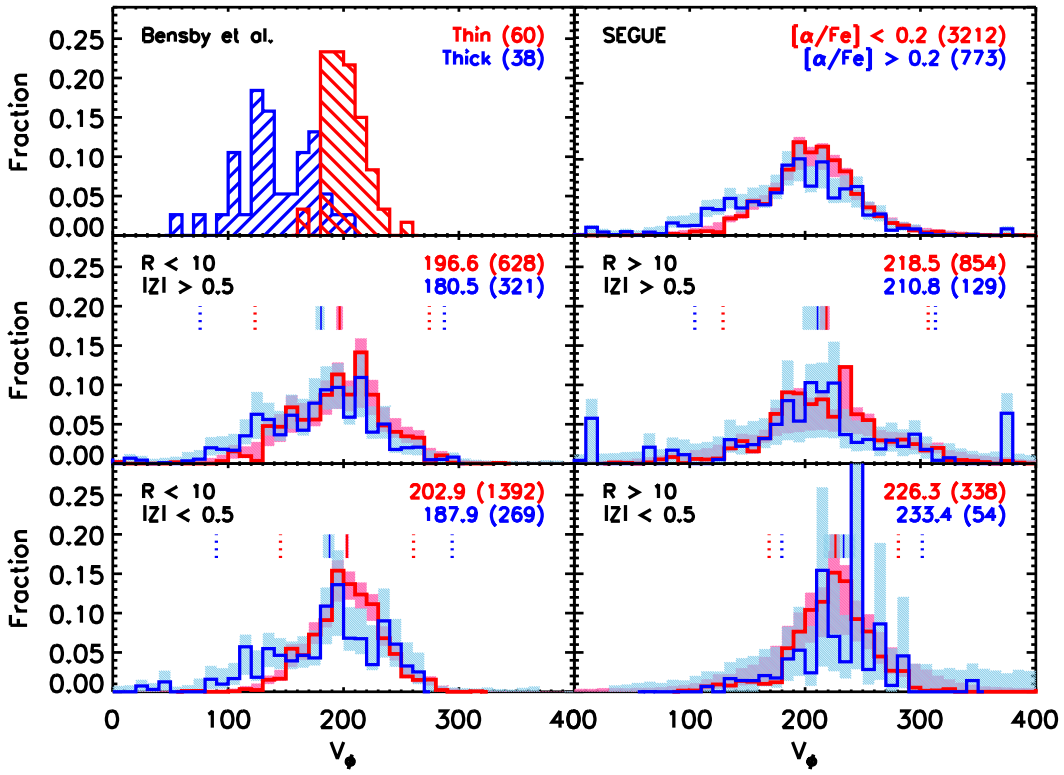

Figure 3.5: Weighted rotational velocity V_ϕ distributions for high- and low-α stars. Top left panel: the solar neighborhood sample of Bensby et al. (2003; 2005), with thin and thick disk stars (red and blue, respectively) assigned according to their kinematics. Top right panel: the SEGUE sample, with high- and low-α stars (blue and red, respectively) divided at [α/Fe]= +0.2. The shaded regions indicate the errors estimated using 500 Monte Carlo realizations of our data. Bottom four panels: the SEGUE sample, divided into four bins of R and $|Z|$. In the top right corner of each panel, the mean rotational velocity $\langle V_\phi \rangle$ of each population is indicated, with the raw number of stars in each population in parentheses. To calculate an outlier-resistant $\langle V_\phi \rangle$ (vertical solid lines), we exclude targets that are more than three median absolute deviations from the median value (vertical dotted lines). The errors on $\langle V_\phi \rangle$ are indicated by the surrounding shaded regions. At $R < 10$ kpc, the high-α stars lag in rotation behind the low-α stars by $\sim$15 km s^{-1}. At $R > 10$ kpc, the difference in $\langle V_\phi \rangle$ between high- and low-α stars is < 8 km s^{-1}, which is within the measurement errors. The different kinematic properties of high-α stars at large and small R suggest that they may be different populations with different origins.

At $R < 10$ kpc, the kinematics of high-α stars are consistent with those seen for thick disk stars in the solar neighborhood. Figure 3.5 shows that at all $|Z|$, they lag in rotation behind low-α stars by $\sim$15 km s^{-1}, in rough agreement with measurements in the literature (e.g., Chiba & Beers 2000, Soubiran et al. 2003, Carollo et al. 2010), which have values $\sim 20 - 50$ km s^{-1},

depending on how the thin and thick disk populations are separated. Like thick disk stars in the solar neighborhood, the high-α stars at $R < 10$ kpc also have wider distributions in V_Z and V_R. This result implies that they belong to a kinematically "hotter" population, which has larger random motions in the radial and vertical directions in addition to a larger lag in V_ϕ. For reference, the mean, median, median absolute deviation, and skewness of the populations' distributions in V_ϕ, V_Z, and V_R for both high- and low-α stars are tabulated in Table 3.1. The errors on $\langle V_\phi \rangle$ are indicated.

In addition, there is a large fraction of high-α stars with low V_ϕ (< 150 km s^{-1}); this tail is not present in the low-α population. One way to quantify this feature is to examine the skewness of the V_ϕ distributions of both populations. We find that for the high-α population, the skewness of the V_ϕ distribution is larger than for the low-α population; at $|Z| < 0.5$ kpc ($|Z| > 0.5$ kpc) the V_ϕ distribution of the high-α population has a skewness of $-1.77^{+0.3}_{-0.2}$ ($-1.27^{+0.4}_{-0.3}$), while the V_ϕ distribution of the low-α population has a skewness of $-0.50^{+0.3}_{-0.3}$ ($-0.20^{+0.2}_{-0.3}$).

The skewed shape of the V_ϕ distribution of both high- and low-α stars at $R < 10$ kpc is consistent with a population that is falling in density with increasing R. If stars that have slow (fast) rotational velocities are on orbits with guiding centers within (beyond) the solar circle, then they are interlopers from the inner (outer) disk (e.g., Binney & Merrifield 1998); the skewness of the distribution results from the higher stellar densities in the inner disk compared to the outer disk. Thus the larger skewness of the high-α population in V_ϕ is consistent with there being a steeper density gradient for high-α stars compared to that of low-α stars. The steeper density gradient of the high-α stars is consistent with the picture of the high-α population having a short scale length compared to the low-α population.

At $R > 10$ kpc, however, high- and low-α stars have the same mean rotational velocities, within the errors, and the fraction of high-α stars with low V_ϕ is comparable to that of the low-α stars. In addition, the widths of the V_Z and V_R distributions of high- and low-α stars are similar. While at $R < 10$ kpc, the different V_ϕ distributions are indicative of two populations

Table 3.1: Properties of Velocity Distributions

	$R<10, \lvert Z\rvert>0.5$						$R>10, \lvert Z\rvert>0.5$					
	V_ϕ		V_Z		V_R		V_ϕ		V_Z		V_R	
	Low-α	High-α	Low-α	High-α	Low-α	High-α	Low-α	High-α	Low-α	High-α	Low-α	High-α
Mean[a,b]	$196.6^{+2.7}_{-3.0}$	$180.5^{+3.1}_{-4.8}$	-2.4	-6.0	108.2	93.9	$218.5^{+2.7}_{-5.6}$	$210.8^{+8.3}_{-13.1}$	18.8	21.8	-34.0	-37.2
Median[a]	198.8	181.5	-0.6	-8.1	106.0	93.3	217.8	208.7	16.6	20.7	-30.5	-40.4
MAD[a,c]	25.2	35.3	24.5	41.5	37.0	43.8	29.6	34.8	33.3	31.0	31.9	35.5
Skew	$-0.50^{+0.3}_{-0.3}$	$-1.77^{+0.3}_{-0.2}$	0.08	0.34	0.20	-0.42	$0.03^{+0.3}_{-0.2}$	$-0.49^{+0.8}_{-0.4}$	-0.25	-0.07	1.77	0.23
	$R<10, \lvert Z\rvert<0.5$						$R>10, \lvert Z\rvert<0.5$					
	V_ϕ		V_Z		V_R		V_ϕ		V_Z		V_R	
	Low-α	High-α	Low-α	High-α	Low-α	High-α	Low-α	High-α	Low-α	High-α	Low-α	High-α
Mean[a,b]	$202.9^{+1.7}_{-1.3}$	$187.9^{+4.3}_{-5.8}$	1.1	-3.9	50.0	46.1	$226.3^{+3.8}_{-5.0}$	$233.4^{+10.2}_{-17.3}$	16.1	18.2	-41.1	-25.6
Median[a]	203.0	192.0	2.3	-6.5	52.9	46.3	224.9	240.7	15.1	11.7	-38.6	-10.4
MAD[a,c]	19.2	34.1	17.0	24.9	35.8	45.2	18.7	20.3	20.1	15.9	22.6	23.2
Skew	$-0.20^{+0.2}_{-0.3}$	$-1.27^{+0.4}_{-0.3}$	-0.13	-0.04	-0.18	-0.80	$-0.33^{+0.6}_{-0.3}$	$-0.70^{+1.2}_{-0.5}$	0.06	-0.07	-0.28	-0.98

[a] Mean, median, and MAD reported in km s^{-1}.

[b] Outliers clipped at three median absolute deviations.

[c] Median absolute deviation.

with different structural parameters, at $R > 10$ kpc, we are unable to distinguish between the kinematics of high- and low-α stars. If high- and low-α stars at $R > 10$ kpc are part of the same population, then the observations imply that high-α stars at large and small R may have different origins.

3.4 Scale Length of the High-α Population

The lack of high-α stars at large R suggests that the high-α population, which is typically associated with the thick disk, has a short radial extent. The similarity between the V_ϕ distributions of high- and low-α stars at large R also supports this idea. In this section, we estimate the scale length of the α-enhanced thick disk by quantifying the fraction of low- and high-α stars as a function of R and $|Z|$. We then compare the data to expected values based on different combinations of thin and thick disk scale lengths, $L_{\rm thin}$ and $L_{\rm thick}$. In addition, we require that the predicted total stellar density as a function of R and $|Z|$ is consistent with the total stellar density of the best-fit model obtained by Jurić et al. (2008). While it is possible that the data may be better fit by different analytical functions, we restrict our analysis to a radial exponential profile for the disk, for which we also have total stellar density measurements.

In using the fractions of high- and low-α stars to estimate the thin and thick disk scale lengths, we implicitly assume that high-α stars belong to the thick disk and low-α stars belong to the thin disk, as is observed in the solar neighborhood. We include the second constraint that the total stellar density match that of Jurić et al. (2008) because our data provide a poor constraint on the local normalization of the disk models we fit. In our fits, we fix the scale heights and the total normalization to the Jurić et al. (2008) values. We exclude the lowest $|Z|$ slice, where our sample does not cover a large range in R. In this section, we present the results of our analysis; details about the our procedure and the uncertainties in our estimates are provided in Appendix B.

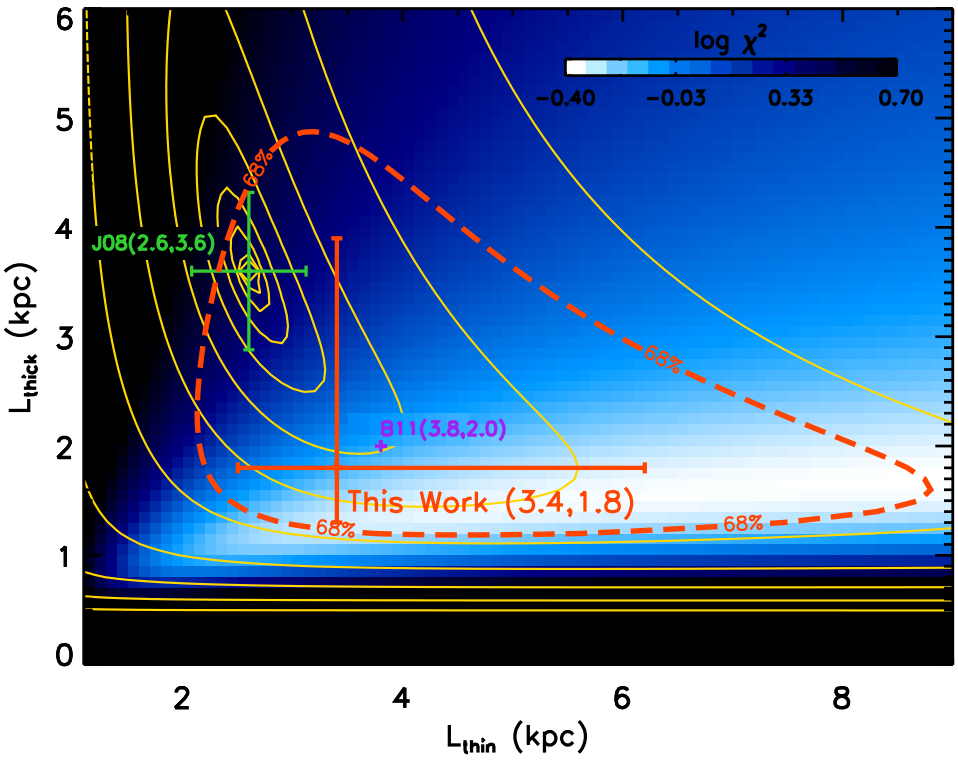

Figure 3.6: Best-fit thin and thick disk scale lengths. The blue shading shows the reduced χ^2 values using the fractions of high- and low-α stars as a function of R and $|Z|$ as a constraint. The thin yellow contours show the constraint of the total stellar density as determined by Jurić et al. (2008). Our best estimate of the thin and thick disk scale lengths using both constraints are $L_{\rm thin} = 3.4^{+2.8}_{-0.9}$ kpc and $L_{\rm thick} = 1.8^{+2.1}_{-0.5}$ kpc, marked by the large orange cross. The 68% contour for the combined constraint is shown as the thick dashed orange line. The published values of Jurić et al. (2008) and Bensby et al. (2011) are indicated in green and purple, respectively.

The blue shading in Figure 3.6 represents the reduced χ^2 values we obtain by comparing the observed and expected values of the high- and low-α fractions, as a function of R and $|Z|$, for different combinations of $L_{\rm thin}$ and $L_{\rm thick}$. The thin yellow contours show the discrepancy between the total stellar density predicted by each combination of scale lengths and the total density from the best-fit scale lengths reported by Jurić et al. (2008; see also their Figure 21). Combining both the constraints of total stellar density from Jurić et al. (2008) and the high- and low-α fractions from our sample, we find the best combination of thin and thick disk scale lengths to be $L_{\rm thin} = 3.4^{+2.8}_{-0.9}$ kpc, $L_{\rm thick} = 1.8^{+2.1}_{-0.5}$ kpc, marked by the large orange cross in

Figure 3.6. The best fit values and error bars are obtained by marginalizing over each axis and determining the 68% confidence interval for each scale length. The 68% contour in two dimensions for the combined constraint is shown as the thick dashed orange line. More details about the procedure and error analysis are given in Appendix B. The blue-shaded map shows that for any given thin disk scale length, the preferred thick disk scale length, as constrained by the high- and low-α fractions (i.e., the white regions), is always shorter thin disk scale length.

We note that our measurement of the thin and thick disk scale lengths is not well constrained, as we do not have data at large radius near the midplane. Our preferred value for the thin disk scale length is slightly larger, but consistent with values based on near-infrared photometry from the Spacelab Infrared Telescope (Kent et al. 1991; ~ 3.0 kpc) and the Cosmic Background Explorer (Freudenreich 1998; ~ 2.6 kpc). Other SDSS/SEGUE studies, which use detailed modeling to estimate disk structural parameters, are also consistent with these values for the thin disk scale length (Jurić et al. 2008, Bovy et al. 2011). While our sample's spatial coverage is not ideal for constraining the thick disk scale length, it is an improvement on earlier studies. Furthermore, our best-fit value does not change significantly when we vary the assumed Jurić et al. (2008) scale lengths or remove possible halo contaminants. See Appendix B for more details.

Figure 3.7 shows the weighted fractions of high- and low-α stars (blue and red squares, respectively), as a function of R in three $|Z|$ slices. The shaded regions indicate the errors on the measured fractions. Each column shows the same data compared to the expected fractions of thin (pink dotted lines) and thick (blue solid lines) disk stars for three different combinations of thin and thick disk scale lengths: (1) $L_{\rm thin} = 2.6$, $L_{\rm thick} = 3.6$ kpc in the left column (Jurić et al. 2008), (2) $L_{\rm thin} = 3.8$, $L_{\rm thick} = 2.0$ kpc in the middle column (Bensby et al. 2011), and (3) $L_{\rm thin} = 3.4$, $L_{\rm thick} = 1.8$ kpc in the right column (this work). For the Bensby et al. (2011) scale lengths, we show the predictions for both a constant thick disk scale height (thin, dark blue line) and one that varies as R_G/L (thick, light blue line), as described in their paper.

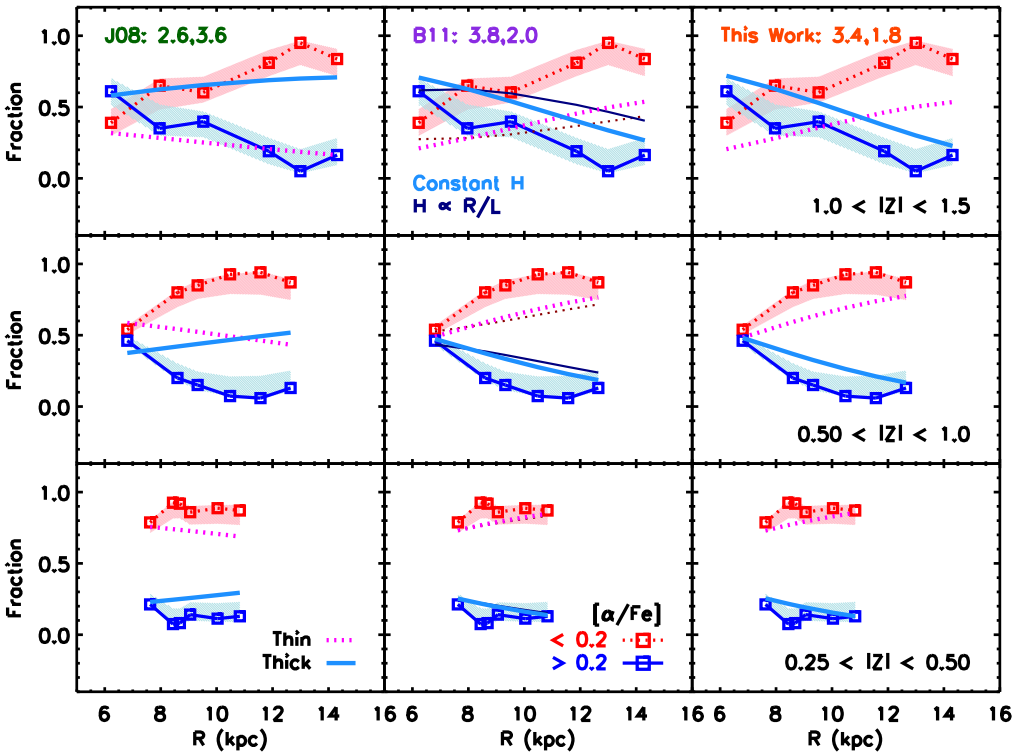

Figure 3.7: Weighted fractions of high- and low-α stars (blue and red squares, respectively) vs. Galactocentric radius R in three $|Z|$ slices. The shaded regions indicate the errors on the measured fractions. Pink dotted and blue solid lines show the expected contributions of the thin and thick disks, respectively, for different combinations of scale lengths: (1) $L_{\rm thin} = 2.6$, $L_{\rm thick} = 3.6$ kpc in the left column (Jurić et al. 2008), (2) $L_{\rm thin} = 3.8$, $L_{\rm thick} = 2.0$ kpc in the middle column (Bensby et al. 2011), and (3) $L_{\rm thin} = 3.4$, $L_{\rm thick} = 1.8$ kpc in the right column (this work). In the middle column, we also show the expected fractions if the scale height varies linearly with R_G/L, as discussed by Bensby et al. (2011; thinner lines). Our data support a shorter scale length for the high-α population, in agreement with the conclusion of Bensby et al. (2011).

As seen in Figures 3.1 and 3.2, Figure 3.7 shows that the fraction of high-α stars decreases at large R, in every $|Z|$ slice. If we assume that the thick disk is populated only by high-α stars, then the model of Jurić et al. (2008) vastly overpredicts the fraction of high-α stars at $|Z| > 0.5$ kpc; in our bin $R > 10$ kpc, $|Z| < 0.5$ kpc (Figure 3.2), we would expect $\sim 50\%$ of our sample (~ 700 stars) to be enhanced in [α/Fe] instead of the $\sim 10\%$ (~ 200 stars) that we observe. The data agree much better with a shorter thick disk scale length, consistent with the

results of Bensby et al. (2011; middle column). Using [α/Fe] as a proxy for membership in the thin and thick disks in our larger sample, we estimate that the thick disk has a shorter scale length than the thin disk (right column).

3.5 Discussion

3.5.1 The Thick Disk Scale Length

The results presented above show that the fraction of high-α stars drops off at large R and that the high-α populations at small and large R have different kinematic properties. Both of these results are consistent with the properties of the K-giant sample of Bensby et al. (2011), who found that the lack of high-α stars was consistent with the thick disk having a shorter scale length than the thin disk ($L_{\rm thin} = 3.8$, $L_{\rm thick} = 2.0$ kpc). Using our data, we estimate the scale lengths to be $L_{\rm thin} = 3.4^{+2.8}_{-0.9}$ and $L_{\rm thick} = 1.8^{+2.1}_{-0.5}$ kpc. While the scale lengths are not well constrained with our data, the thick disk scale length is consistently found to be shorter than 2 kpc (see Appendix B).

Independent analyses with other SDSS/SEGUE samples have also found similar scale lengths for stars with thick disk chemistry. Carollo et al. (2010), using the velocity ellipsoid of stars in a particular metallicity range and location in the disk ($-0.8 <$ [Fe/H] $< -0.6, 1 < |Z| < 2$ kpc), estimated the thick disk scale length to be 2.2 kpc. In recent work, Bovy et al. (2011) measured the scale length of their "α-old" population ($-1.5 <$ [Fe/H] $< -0.25, 0.25 <$ [α/Fe] < 0.50) to be 1.96 kpc. While the methods differ, these studies reach the same conclusion: the population of stars associated with a thick disk component in the solar neighborhood has a short radial scale length.

It is worth emphasizing, however, that the above results apply for stars with particular properties. The results presented in this work reflect the *fractions* of high- and low-α stars, and our scale length estimate reflects the radial extent of the high-α population, which we

associate with the thick disk based on studies of the solar neighborhood. Previous studies of external galaxies (Dalcanton & Bernstein 2002, Yoachim & Dalcanton 2006) and the Milky Way (Jurić et al. 2008, de Jong et al. 2010) have relied on surface brightness profiles and star counts, respectively, which follow the total stellar density, with no information about the stellar populations.

We now introduce terminology to distinguish between these two methods of identifying the two components of the disk. First, we will refer to the *structural* thin and thick disks to describe the components that are identified using the total stellar densities, either through star counts or surface brightness profiles (e.g., Gilmore & Reid 1983, Dalcanton & Bernstein 2002). Second, we will refer to the *chemical* thin and thick disks to describe the components that are identified using the chemical and/or kinematic properties of stars (e.g., Bensby et al. 2003; 2005, Lee et al. 2011b). In our work, we have found that the *chemical* thick disk has a shorter scale length than the *chemical* thin disk.

Whether *star counts* in the SEGUE imaging along our lines of sight support a short scale length for the *structural* thick disk remains an open question. Previous estimates of the scale length of the structural thick disk in the Milky Way have typically relied on star counts in higher latitude data and therefore do not have significant leverage in the radial direction (e.g., Jurić et al. 2008, Chang et al. 2011). Our lines of sight reach larger R at small $|Z|$ and may provide additional constraints on the scale lengths of the structural thin and thick disks. Comparing star counts in our low latitude lines of sight to different combinations of structural parameters, as well as exploring different radial profiles, will be the focus of future work.

If the structural thick disk is found to have a short scale length, in agreement with our result for the chemical thick disk, then we can compare these results to the scale lengths of structural thick disks seen in external galaxies. Observationally, structural thin and thick disk scale lengths have been found to be uncorrelated in external galaxies (Dalcanton & Bernstein 2002). For galaxies with circular velocities greater than $\sim$100 km s^{-1}, structural thin disks with

Table 3.2: Fraction of High-α Stars per Line of Sight

Plug-plates		l (°)	b (°)	$N_{\rm stars}$	$N_{\rm high-\alpha}$	$f_{\rm unweighted}$	$f_{\rm weighted}$
2534	2542	50.0	14.0	396	210	0.530	0.486
2536	2544	70.0	14.0	401	155	0.387	0.305
2554	2564	94.0	14.0	600	165	0.275	0.212
2555	2565	94.0	8.0	386	40	0.104	0.103
2556	2566	94.0	-8.0	526	68	0.129	0.092
2538	2546	110.0	16.0	553	92	0.166	0.143
2537	2545	110.0	10.5	467	56	0.120	0.093
2681	2699	178.0	-15.0	495	82	0.166	0.132
2668	2672	187.0	-12.0	670	81	0.121	0.094
2678	2696	187.0	8.0	580	67	0.116	0.080
2712	2727	203.0	8.0	546	93	0.170	0.142

larger scale lengths than structural thick disks have been reported (see Table 5 of Yoachim & Dalcanton 2006). Having a structural thick disk with a short scale length, then, would not make the Milky Way an unusual galaxy.

3.5.2 Possible Relation to the Hercules Thick Disk Cloud

In Table 3.2, we list the weighted fraction of high-α stars along each of the 11 lines of sight in our sample. Most of the 11 lines of sight have fewer than 15% of their stars with $[\alpha/\mathrm{Fe}] > +0.2$. Three lines of sight at $R < 10$ kpc, however, have $\sim 20\% - 50\%$ of their stars with $[\alpha/\mathrm{Fe}] > +0.2$. These lines of sight are directed toward the Hercules Thick Disk Cloud, a stellar overdensity in the disk, which has been studied in detail by Larsen et al. (2010; 2011) and Humphreys et al. (2011).

Larsen et al. (2010) detect this overdensity as an excess in star counts in the first quadrant (Q1, $0° < l < 90°$), compared to the fourth quadrant (Q4, $270° < l < 360°$), in particular, at Galactic coordinates $20° < l < 55°, 20° < b < 45°$. Stars associated with this overdensity in Q1 lag in rotation by 30 km s^{-1} compared to stars in Q4, but have metallicities similar to stars in analogous fields in Q4 (Parker et al. 2004, Humphreys et al. 2011). Their preferred scenario for the existence of the overdensity is that dynamical interactions with the

bar cause stars to pile up in a "gravitational wake" (e.g., Hernquist & Weinberg 1992). This feature may be related to the Hercules-Aquila Cloud seen in the SDSS (Belokurov et al. 2007, Jurić et al. 2008).

The rotation rates, ω, in our three high-α lines of sight ($22 - 31$ km s^{-1} kpc^{-1}) are slightly larger than the Q1 fields of Humphreys et al. (2011; $15 - 26$ km s^{-1} kpc^{-1}), which is not unexpected, since our lines of sight are at lower Galactic latitude. A direct comparison is not possible because our samples do not overlap spatially. Additionally, our sample does not cover a sufficiently large part of the Galaxy to fully test the presence of an asymmetry: all of our inner disk stars are in Q1, and we have no stars in Q4 with which to make a comparison. We do not currently have the necessary data to confirm or exclude the possibility that these three lines of sight are associated with this overdensity.

3.5.3 Implications for Thick Disk Formation

The short scale length of the chemical thick disk can be used to constrain various scenarios for thick disk formation, such as the four described in §4.1. In the following discussion, we will use the generic term "thick disk" to refer to both the structural and chemical thick disks. We assume these to be the same, as is done in all of the models discussed.

The lack of high-α stars at $R > 10, |Z| > 0.5$ kpc puts an upper limit on the strength of migration due to transient spiral structure (Scenario 4); the N-body simulation of Loebman et al. (2011), for example, predicts that this mechanism can transport many high-α stars from the inner disk to large R and $|Z|$. In this simulation, high-α stars are present at all R because they are old and have had more time to migrate to large R. The lack of high-α stars that we have observed at large R, then, implies that this mechanism cannot be very efficient.

If the stars we observe at large R and $|Z|$ reached their current positions through radial migration, the limited extent of the high-α population could be evidence that the mechanism must have some radial dependence on the strength of migration. One such mechanism relies

on the presence of a bar and a steady state spiral pattern, which leads to more efficient mixing at certain radii (e.g., Minchev & Famaey 2010, Brunetti et al. 2011). Brunetti et al. (2011), for example, find that stars that are close to the corotation radius of the bar are more likely to migrate. If the high-α stars in our sample were born in the bulge and have since migrated to where we observe them at $R < 10$ kpc, this would explain the similar abundance patterns that have been reported for thick disk and bulge stars (Meléndez et al. 2008, Bensby et al. 2009, Alves-Brito et al. 2010, Bensby et al. 2010b, Ryde et al. 2010, Gonzalez et al. 2011). One way to test this scenario is to examine whether the kinematic properties of stars in these simulations are different for those mixed in the inner and outer disks.

If the thick disk does indeed have a shorter scale length than the thin disk, as is suggested by both our data and the data of Bensby et al. (2011), and radial migration is not the dominant mechanism, our results may have implications on the formation and merger history of the Milky Way disk. A range of thick disk scale lengths can result from different merger histories. Brook et al. (2004; 2007) showed that chaotic gas accretion at early times (Scenario 3) results in a thick disk with a shorter scale length than the thin disk, while an early gas-rich 2:1 merger of two disks results in a thick disk with a longer scale length. The variation in merger histories would provide a possible explanation for the range of structural thin and thick disk scale lengths observed in nearby galaxies (Dalcanton & Bernstein 2002, Yoachim & Dalcanton 2006).

Scenarios involving minor mergers can also be constrained. If thick disk stars originated from an initially thin disk (Scenario 1) then any heating event must have occurred in a primordial disk with a short scale length. The predominantly low-α stars at large R and $|Z|$, then, should come from a more chemically evolved disk. Radial mixing induced by late minor mergers has been shown to be very efficient for stars in the outer disk (Bird et al. 2012) and could explain the presence of low-α stars at large R and $|Z|$. However, predictions can be dependent on the particular models being examined and their initial conditions (e.g., Di Matteo et al. 2011). If

thick disk stars originated from an accreted satellite (Scenario 2), then stars contributed by a single satellite should be located in a torus-like structure, and we should see the same abundance trends in Q1 and Q4. Our current sample is insufficient in spatial coverage to explore this possibility.

Finally, the radial gradients in [Fe/H] for high- and low-α stars (see Figures 3.3 and 3.4) also provide constraints on thick disk formation. Radial migration due to transient spiral structure (Scenario 4) could explain the flattening trend in the low-α stars, but the mechanism is too efficient in current simulations, resulting in too many high-α stars in the outer disk, especially at large $|Z|$. The observed distributions of [Fe/H] and [α/Fe] could be explained by the following: first, early gas-rich mergers (Scenario 3) created a chemically homogeneous, high-α population in a thick disk with a short scale length. Subsequently, a low-α thin disk forms and is heated by minor merger activity at later times (Scenario 1), mixing stars at large R (e.g., Bird et al. 2012) and flattening the radial metallicity gradient at large $|Z|$.

3.6 Summary

We have demonstrated, using a sample of 5620 main sequence turnoff stars from the SEGUE survey, that the high-α population, which is associated with the thick disk in the solar neighborhood, has a short scale length ($L_{\rm thick} \sim 1.8$ kpc) and a flat metallicity gradient at all $|Z|$. The abundance trends at $R < 10$ kpc show a dichotomy between high- and low-α stars similar to that seen between thick and thin disk stars observed in the solar neighborhood (Bensby et al. 2003; 2005). The fraction of high-α stars increases with $|Z|$, and these high-α stars lag in rotation compared to low-α stars (by $\sim$15 km s^{-1}), similar to the difference in kinematics seen for thin and thick disk stars in the solar neighborhood (Chiba & Beers 2000, Soubiran et al. 2003).

At $R > 10$ kpc, the fraction of high-α stars is lower than at small R and does not

increase with $|Z|$. High-α stars at large R also do not lag in rotation compared to low-α stars, with both populations having similar mean rotational velocities. These results suggest that the high-α stars in the outer disks may simply be the tail of the [α/Fe] distribution; the stars far from the plane in the outer disk ($R > 10, |Z| > 0.5$ kpc) likely have different origins than those far from the plane in the inner disk ($R < 10, |Z| > 0.5$ kpc).

The fractions of high- and low-α stars are consistent with the expected values for a thick disk with a short scale length as suggested by Bensby et al. (2011). Using the fractions of high- and low-α stars as a function of R and $|Z|$, we estimate the thick disk scale length to be $L_{\rm thick} \sim 1.8$ kpc. In addition, it is possible that the lines of sight in our sample with large fractions of high-α stars are related to the Hercules Thick Disk Cloud, a stellar overdensity studied by Humphreys et al. (2011). A sample of stars with better spatial coverage, particularly in Q4, is required to fully explore this possibility.

We find that the presence of a thick disk with a short scale length is consistent with the scenario of Brook et al. (2004; 2005), in which the thick disk formed during a turbulent disk phase at early times when gas accretion rates were high. In the outer disk, stars may have been moved to large R and $|Z|$ through radial mixing due to late minor mergers (e.g., Bird et al. 2012). The lack of high-α stars can be used to constrain the strength of radial migration of stars from the inner disk induced by transient spiral structure (e.g., Roškar et al. 2008b;a, Schönrich & Binney 2009a;b, Loebman et al. 2011). If stars in the outer disk arrived at their current locations through radial migration, some radially-dependent mechanisms may be responsible (e.g., Minchev & Famaey 2010, Brunetti et al. 2011).

Chapter 4

High Resolution Spectroscopy of In Situ Thick Disk Stars: α, Iron Peak, and Neutron Capture Elements

4.1 Introduction

The Milky Way disk is often described as the sum of two different populations. In addition to a thin disk of gas and young stars, there is a thick disk of old stars (Yoshii 1982, Gilmore & Reid 1983). Thick disk stars in the Milky Way are estimated to be ~ 10 Gyr (Bensby et al. 2005) and serve as a fossil record of the formation of the Galaxy at $z \sim 2$. Moreover, thick disks are a common feature of external galaxies and have been found to have similar structural properties, kinematics, and stellar populations to the thick disk of the Milky Way

(e.g., Dalcanton & Bernstein 2002, Yoachim & Dalcanton 2005; 2006; 2008b;a), indicating that thick disks form through some process important in the formation of all disks.

Many theories have been put forth to explain the existence of the thick disk, and its origin has been attributed to both external and internal galaxy formation processes. Four of these scenarios are: (1) vertical heating of a thin disk during a minor merger (e.g., Villalobos & Helmi 2008, Read et al. 2008, Kazantzidis et al. 2008; 2009, Purcell et al. 2009, Bird et al. 2012); (2) direct accretion of stars during a minor merger (e.g., Abadi et al. 2003); (3) star formation during a gravitationally unstable, clumpy disk phase (e.g., Brook et al. 2004; 2005, Bournaud et al. 2009); and (4) radial migration of stars due to transient spiral arms (e.g., Schönrich & Binney 2009a;b, Loebman et al. 2011) or a steady-state spiral and bar pattern (e.g., Minchev & Famaey 2010, Brunetti et al. 2010). Scenarios 1-3 fit within the context of hierarchical structure formation as predicted by ΛCDM, while Scenario 4 can occur in a disk in total isolation.

In the solar neighborhood, thick disk stars are typically identified by their "hotter" kinematics. These stars, which have larger random motions and slower rotation about the center of the Galaxy, are found to be more metal-poor and enhanced in α- and r-process elements compared to thin disk stars (e.g., Edvardsson et al. 1993, Prochaska et al. 2000, Mashonkina & Gehren 2000; 2001, Reddy et al. 2003; 2006, Bensby et al. 2003; 2005, Brewer & Carney 2006). The enhancement of these elements relative to iron provides information about the star formation history of the thin and thick disks (e.g., Tinsley 1979, McWilliam 1997). For example, α- and r-process elements are produced in Type II supernovae (SNe) and are returned early to the interstellar medium (ISM) because their progenitors are shortlived massive stars. Iron peak elements, however, are primarily produced in Type Ia SNe and are returned later to the ISM because their progenitors are white dwarfs: low mass stars at the end of their evolution. Stars that are α-enhanced, such as those in the thick disk, must have formed in a short period, before Type Ia SNe could contribute very much iron to the ISM. Using these arguments, the thick disk population has been estimated to have formed over a period of 1-3 Gyr (Gratton et al.

2000, Mashonkina et al. 2003, Bensby et al. 2004). In addition, some of the observed trends are extremely tight, with very little scatter, which indicates that the thick disk population formed in a well-mixed ISM.

The chemical properties of a stellar population can also be used to constrain the kinds of environments in which its stars could have been formed. Kirby et al. (2008), for example, argue that the presence of extremely metal-poor stars ([Fe/H] < -3.0) in dwarf spheroidals show that similar objects could have built up the Milky Way halo. Ruchti et al. (2010; 2011) argue that thick disk stars are too α-enhanced to have formed in objects like present-day dwarf galaxies, which had more extended star formation histories (e.g., Tolstoy et al. 2009). Thus the detailed elemental abundances of thick disk stars are a powerful tool that can advance our understanding of the origin of the thick disk. While significant work has been done to study thick disk stars in the solar neighborhood, less is known about in situ thick disk stars, i.e., those that are far from the midplane of the Galactic disk. In particular, how chemical abundances change as a function of location in the Galaxy can provide constraints on the likelihood of the four scenarios described above.

Our previous work used a large homogeneous sample of ~ 7000 main sequence turnoff (MSTO) stars from the Sloan Extension for Galactic Understanding and Exploration (SEGUE, Yanny et al. 2009, Eisenstein et al. 2011), part of the Sloan Digital Sky Survey (SDSS, York et al. 2000). This sample covers the region 6 kpc $< R <$ 16 kpc, 0.15 kpc $< |Z| <$ 1.5 kpc, where R is Galactocentric radius and $|Z|$ is distance from the plane, and has allowed us to explore trends in [Fe/H] and [α/Fe] in a larger volume than previous studies. Two main results have come out of this work. The first result is that the thick disk is chemically homogeneous. We find that the radial metallicity gradient Δ[Fe/H]/ΔR is flat for all stars far from the plane of the disk ($|Z| > 1.0$ kpc) (Chapter 2), as well as for high-α stars at *all* $|Z|$ (Chapter 3). The second result is that we find that the fraction of high-α stars as a function of R and $|Z|$ is consistent with the α-enhanced thick disk having a short radial scale length (Chapter 3).

The lack of a radial gradient at large $|Z|$ and a high-α population with a short scale length are consistent with the predictions of Scenario 3, in which the thick disk forms during a clumpy disk phase at early times. This phase has been studied in simulations (Brook et al. 2004; 2005, Bournaud et al. 2009) and observed in galaxies at high redshift (Elmegreen & Elmegreen 2005; 2006, Förster Schreiber et al. 2009). While this may explain the presence of stars far from the plane in the inner disk, those that are far from the plane in the outer disk are likely to have arrived at their current locations through other means, possibly through heating during minor mergers as in Scenario 1. The lack of high-α stars at large R and $|Z|$ also places strict constraints on Scenario 4, particularly the type of radial migration that is induced by transient spiral arms (e.g., Roškar et al. 2008b, Loebman et al. 2011).

The detailed chemical properties of in situ thick disk stars at a range of Galactocentric radius R can provide additional observational constraints. If stars far from the plane have the same chemical abundance trends as thick disk stars in the solar neighborhood (i.e., those that are kinematically hot), then the thick disk is truly chemically homogeneous, consistent with Scenario 3. If stars in the inner and outer thick disks differ in their chemical signatures, then two different mechanisms may be necessary to explain all of the stars that we observe far from the plane. Examining many more elements will shed light on where thick disk stars originated and whether cosmological or secular processes are more important in shaping the thick disk.

In this Chapter, we present individual α-, iron peak, and neutron capture elements of 37 stars observed using the High Resolution Echelle Spectrometer (HIRES, Vogt et al. 1994). The sample was chosen to span a large range in Galactocentric radius 6 kpc $< R <$ 11 kpc and to include stars located out of the plane of the Milky Way disk ($|Z| \gtrsim 0.5$ kpc) in order to explore the chemical properties of stars located where thick disk stars are expected to be a larger fraction than in the solar neighborhood. We present the observations and data in §4.2, followed by the results in §4.3. The implications are discussed in §4.4.

4.2 Data and Analysis

4.2.1 Observations

Our targets are drawn from the SEGUE survey, which has obtained spectra for over 240,000 stars at medium resolution ($R \sim 2000$). Stellar parameters effective temperature $T_{\rm eff}$, surface gravity log$g$, metallicity [Fe/H], and α-enhancement [α/Fe] have been derived using the SEGUE Stellar Parameter Pipeline (SSPP, Lee et al. 2008a;b, Allende Prieto et al. 2008b, Smolinski et al. 2011, Lee et al. 2011a). Distances for these stars were determined using photometric parallax methods, as described in Chapter 2. The R, $|Z|$ distribution of the sample is shown in Figure 4.1. The SEGUE sample is shown as gray dots, while the targets observed with HIRES are shown as larger symbols in blue. The light and dark blue symbols indicate objects at large and small R, respectively, where the division is set at $R = 9.5$ kpc. Open and filled circles indicate low- and high-α stars, respectively, where the division is set at [α/Fe] $= +0.2$ using [α/Fe] as determined by the SSPP. Both of these divisions are motivated by the properties of the MSTO sample that we observed in Chapter 3.

We obtained observations of 40 stars at $|Z| \gtrsim 0.5$ kpc, where two-component models (e.g., Jurić et al. 2008) predict that the contribution of the thick disk population is greater than in the solar neighborhood. Most of the stars we were able to observe are located at small R, and we were not able to observe any high-α stars in the outer disk. In Figure 4.1 we also plot the locations of inner and outer disk giants observed by Bensby et al. (2010a; 2011) and Carney et al. (2005), which to our knowledge are the only other high-resolution spectroscopic analysis of disk stars outside the solar neighborhood. These samples use K and red giants, respectively, and reach larger distances than our stars, so they are complementary in both the stellar tracers and spatial coverage.

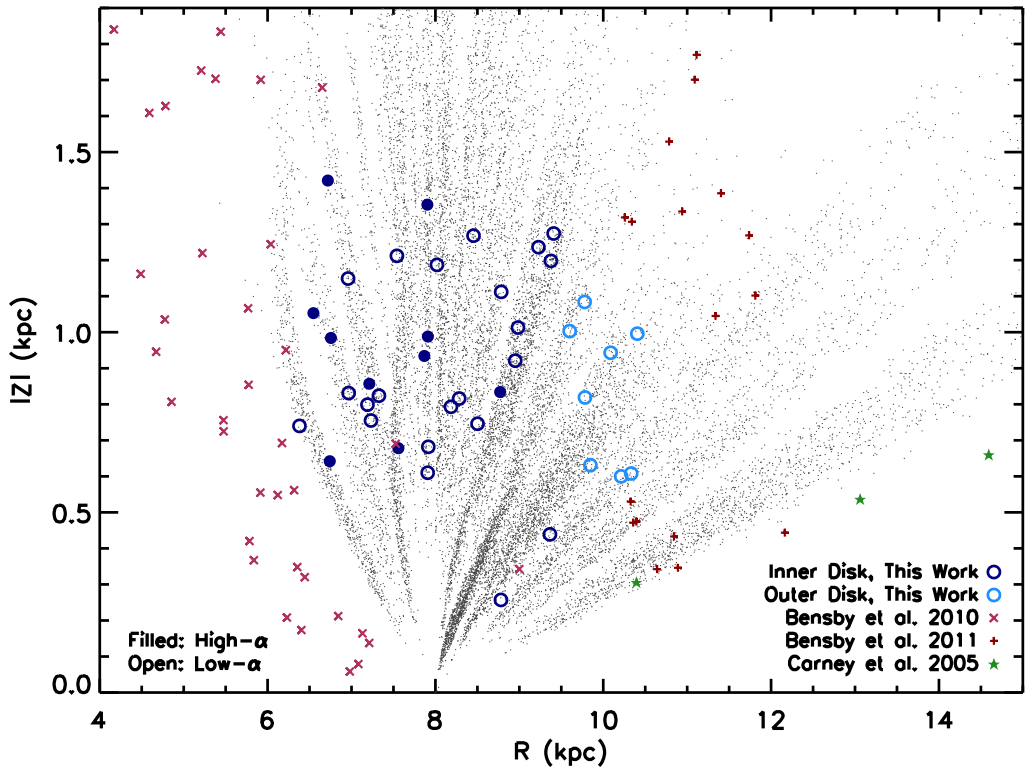

Figure 4.1: Spatial distribution of our sample in Galactic coordinates R and $|Z|$. The gray dots indicate potential targets in the SEGUE survey, while the blue circles indicate the stars observed with HIRES (Table 4.1). The light and dark blue symbols indicate objects at large and small R, respectively, where the division is set at $R = 9.5$ kpc. Open and filled circles indicate low- and high-α stars, respectively, where the division is set at $[\alpha/\mathrm{Fe}] = +0.2$. The sample consists of stars at $|Z| \gtrsim 0.5$ kpc, where the thick disk population has a greater contribution than in the solar neighborhood. Inner and outer disk K giants observed by Bensby et al. (2010a; 2011) are shown as red crosses and pluses. Outer disk red giants observed by Carney et al. (2005) are shown as green stars.

Table 4.1: Observations

SEGUE ID	r (mag)	$t_{\rm exp}$ (s)	Observation Date (UT)	Cross Disperser	Wavelength Coverage	RV_{SSPP} (km s^{-1})	RV_{HIRES} (km s^{-1})	d (kpc)	R (kpc)	Z (kpc)	S/N at 4150Å	S/N at 5150Å	S/N at 6150Å
1919-173	14.35	2700	2006 Oct 31	HIRESb	3500-6400Å	29.1	28.8	0.9	8.2	-0.8	43	50	86
1893-104	14.27	2700	2006 Oct 31	HIRESb	3500-6400Å	-12.4	-12.0	1.5	7.2	-0.8	32	41	82
1905-243	14.22	2700	2006 Oct 31	HIRESb	3500-6400Å	14.3	15.2	1.1	7.9	-0.7	40	62	82
2307-386	15.05	3600	2006 Oct 31	HIRESb	3500-6400Å	-4.6	-6.2	1.9	9.4	-1.2	42	52	76
2335-542	15.05	3600	2006 Oct 31	HIRESb	3500-6400Å	-9.2	-8.4	1.5	9.4	-0.4	50	76	74
2070-084	14.51	2700	2006 Oct 31	HIRESb	3500-6400Å	29.3	33.4	1.4	8.5	-1.3	49	69	90
2052-063	13.10	2700	2006 Oct 31	HIRESb	3500-6400Å	63.3	64.5	1.9	9.4	-1.3	64	70	99
2328-059	14.54	3600	2006 Nov 1	HIRESb	3500-6400Å	-26.1	-26.5	1.3	9.0	-0.9	31	44	79
2068-151	14.96	3600	2006 Nov 1	HIRESb	3500-6400Å	96.5	101.3	0.9	8.8	-0.3	43	56	94
2051-595	14.91	2700	2006 Nov 1	HIRESb	3500-6400Å	49.4	52.8	1.8	9.2	-1.2	49	68	82
2307-074	14.99	3300	2006 Nov 1	HIRESb	3500-6400Å	-27.8	-29.8	1.1	8.8	-0.8	43	46	62
2052-537	14.45	4500	2006 Nov 1	HIRESb	3500-6400Å	-9.4	-5.4	1.4	9.0	-1.0	46	54	69
2180-560	15.43	4200	2011 Jul 30,31	HIRESb	3500-6400Å	-61.1	-63.8	2.0	6.5	1.1	57	65	75
2797-017[a]	14.57	3600	2011 Jul 30	HIRESb	3500-6400Å	31.5	21.2	1.9	8.3	-0.8	44	53	74
2798-073	15.19	4800	2011 Jul 30	HIRESb	3500-6400Å	-20.2	-22.6	1.2	8.5	-0.7	66	64	70
1917-020	14.87	3600	2011 Jul 30	HIRESb	3500-6400Å	-3.0	-8.4	1.7	7.0	-0.8	39	45	64
2251-632	14.74	2700	2011 Jul 30	HIRESb	3500-6400Å	8.2	15.4	1.6	7.2	0.8	36	51	69
2310-312	14.56	2700	2011 Jul 30	HIRESb	3500-6400Å	-64.5	-73.2	1.5	7.2	-0.9	43	55	60
1903-096	14.88	3600	2011 Jul 30	HIRESb	3500-6400Å	-7.2	-9.9	2.1	6.4	0.7	32	56	63
2796-054	15.25	2700	2011 Jul 31	HIRESb	3500-6400Å	-18.0	-31.9	1.1	7.9	-1.0	42	60	64

Table 4.1: Observations, continued

SEGUE ID	r (mag)	$t_{\rm exp}$ (s)	Observation Date (UT)	Cross Disperser	Wavelength Coverage	$\rm RV_{SSPP}$ (km $\rm s^{-1}$)	$\rm RV_{HIRES}$ (km $\rm s^{-1}$)	d (kpc)	R (kpc)	Z (kpc)	S/N at 4150Å	S/N at 5150Å	S/N at 6150Å
2180-545	14.71	2100	2011 Jul 31	HIRESb	3500-6400Å	151.2	143.9	1.4	8.0	-1.2	56	97	77
2182-610[a]	14.44	1800	2011 Jul 31	HIRESb	3500-6400Å	-24.8	-23.4	2.0	7.0	1.1	51	65	79
2797-407	14.70	1800	2011 Jul 31	HIRESb	3500-6400Å	-17.1	-21.5	1.8	8.8	-1.1	43	55	62
1916-559	15.22	2700	2011 Jul 31	HIRESb	3500-6400Å	50.1	49.8	2.1	7.6	0.7	47	56	65
2305-365	15.26	2700	2011 Jul 31	HIRESb	3500-6400Å	-77.2	-83.6	1.7	6.7	0.6	38	54	64
2308-336[a]	14.78	2100	2011 Jul 31	HIRESb	3500-6400Å	-34.5	-44.2	2.1	6.8	-1.0	47	69	79
1891-140	15.06	2400	2011 Jul 31	HIRESb	3500-6400Å	1.2	-5.5	2.4	6.7	1.4	37	40	64
2311-476	14.94	2100	2011 Jul 31	HIRESb	3500-6400Å	-81.4	-75.2	1.9	7.3	-0.8	58	54	61
2311-208	14.67	1800	2011 Jul 31	HIRESb	3500-6400Å	-35.4	-37.5	2.0	7.5	-1.2	39	48	76
2621-215	14.71	2100	2011 Jul 31	HIRESb	3500-6400Å	-36.4	-40.7	1.5	7.9	-1.4	37	64	84
2038-050	14.69	1400	2011 Jul 31	HIRESb	3500-6400Å	-8.8	-11.3	1.3	7.9	-0.6	49	55	61
2038-226	13.77	900	2011 Jul 31	HIRESb	3500-6400Å	-2.8	-3.1	1.3	7.9	-0.9	60	78	93
2566-412	17.11	6000	2011 Oct 18	HIRESr	3800-8000Å	-71.3	-80.5	2.7	10.3	-0.6	7	13	25
2062-482	16.13	4800	2011 Oct 18	HIRESr	3800-8000Å	-23.4	-19.8	5.2	9.8	-0.6	28	46	65
2398-036	15.95	4800	2011 Oct 18	HIRESr	3800-8000Å	-59.7	-63.8	2.5	10.1	-0.9	21	36	55
2397-014	15.90	4800	2011 Oct 18	HIRESr	3800-8000Å	8.0	6.3	2.7	9.8	-1.1	21	38	53
2679-442	15.42	3000	2011 Oct 18	HIRESr	3800-8000Å	37.4	29.7	1.9	9.6	-1.0	11	24	33
2682-560	15.49	4500	2011 Oct 18	HIRESr	3800-8000Å	40.6	33.0	2.3	10.2	0.6	29	43	52
2057-001	15.65	10500	2011 Dec 4	HIRESb	3500-6400Å	70.6	69.2	2.6	10.4	1.0	50	55	61
2053-419	15.67	9600	2011 Dec 5	HIRESb	3500-6400Å	18.2	16.0	2.4	9.8	0.8	47	56	62

[a] Excluded from analysis due to lack of measurable lines.

The data were taken in 2006 and 2011 at the W. M. Keck Observatory using HIRES. All targets were observed using the C1 slit, which has dimensions $7.0'' \times 0.861''$ and gives a resolution of $R \sim 48,000$. Most targets were observed using the HIRESb setting and cover a wavelength range of 3500-6400Å; the exceptions are the six targets observed in October 2011, which were observed using the HIRESr setting and cover a slightly larger wavelength range of 3800-8000Å. The data were extracted using the reduction pipeline MAKEE[1] (MAuna Kea Echelle Extraction) and reduced using standard IRAF[2] procedures IMCOMBINE, SCOMBINE, CONTINUUM, FXCOR, and DOPCOR. Details about the observations are tabulated in Table 4.1. The radial velocities were determined using FXCOR; radial velocity standards (Udry et al. 1999b;a) are listed in Table 4.2. We obtain good agreement between our measured radial velocities and those in the literature.

Table 4.2: Radial Velocity Standards

Name	V (mag)	$t_{\rm exp}$ (s)	Observation Date (UT)	$\rm RV_{Ref}$ (km $\rm s^{-1}$)	$\rm RV_{HIRES}$ (km $\rm s^{-1}$)
HD37160	4.09	28	2006 Oct 31	99.0	98.1
HD42807	6.45	121	2006 Oct 31	6.0	5.8
HD182572	5.16	70	2006 Nov 1	-100.3	-100.7
HD190007	7.46	180	2006 Nov 1	-30.4	-29.9
HD35410	5.07	30	2006 Nov 1	20.7	19.9
HD139323	7.60	665	2011 Jul 30,31	-67.2	-68.2
HD140538	5.86	215	2011 Jul 30,31	19.0	18.1
HD144579	6.66	355	2011 Jul 30,31	-59.5	-60.5
HD38230	7.36	180	2011 Oct 18	-29.2	-30.0
HD32923	5.60	90	2011 Oct 18	20.5	20.1
HD50692	5.74	40	2011 Oct 18	-15.1	-16.2
HD42807	6.45	90	2011 Oct 18	6.0	6.3
HD73667	7.64	720	2011 Dec 4,5	-12.1	-12.1
HD82106	7.20	720	2011 Dec 4,5	29.8	30.2

[1] http://spider.ipac.caltech.edu/staff/tab/makee/index.html

[2] IRAF is distributed by the National Optical Astronomy Observatory, which is operated by the Association of Universities for Research in Astronomy, Inc., under cooperative agreement with the National Science Foundation.

4.2.2 Equivalent Widths

Our line list is compiled from the line lists of Lai et al. (2008; 2011) and Bensby et al. (2003; 2005) and references therein. Equivalent widths (EWs) were measured using SPECTRE (Fitzpatrick & Sneden 1987), which fits Gaussian profiles to absorption line features. Some lines were remeasured using SPLOT in IRAF. Three of the stars listed in Table 4.1 had few or no measurable lines and are excluded from the rest of the analysis. The lines and EWs measured for the remaining 37 stars are tabulated in Appendix C. For stellar parameter determinations (§4.2.3), we have excluded lines with EW > 100 mÅ or excitation potential EP < 0.2 eV, which may be saturated or have non-Gaussian line profiles.

4.2.3 Stellar Parameters

We use the grid of ATLAS9 (Kurucz 1993) model atmospheres computed by Kirby (2011), which includes atmospheres for metallicities in the range $-4.0 <$ [Fe/H] < 0.0 and α-enhancements in the range $-0.8 < [\alpha/\mathrm{Fe}] < +1.2$. For stars that have supersolar metallicities ([Fe/H] > 0.0), we use metal-rich atmospheres from the grid of Castelli & Kurucz (2003); this grid has only two [α/Fe] values available (0.0 and +0.4). All of these atmospheres are the 'ODFNEW' models, which have improved opacity distribution functions over preceding models.

For each star, we find the best fit solution of stellar parameters T_{eff}, log g, [Fe/H], and microturbulence ξ_{t} by minimizing three trends in the abundances derived for individual Fe I and Ti I lines: (1) Fe I abundance log ϵ(Fe) vs. EP, (2) log ϵ(Fe) vs. reduced equivalent width (log RW), and (3) Ti I abundance log ϵ(Ti) vs. EP. The abundance predicted by each line is generated using the `abfind` driver in the most recent version of MOOG (Sobeck et al. 2011), which accounts for Rayleigh scattering. For each solution (i.e., combination of stellar parameters), we calculate a goodness of fit, γ, by adding the slopes of these three trends in

quadrature:

$$\gamma \equiv \left(\frac{\partial \log \epsilon(\text{Fe I})}{\partial \text{ (EP)}} \right)^2 + \left(\frac{\partial \log \epsilon(\text{Fe I})}{\partial \text{ (logRW)}} \right)^2 + \beta \left(\frac{\partial \log \epsilon(\text{Ti I})}{\partial \text{ (EP)}} \right)^2, \tag{4.1}$$

where β is the ratio of the range of EPs covered by Ti I lines to the range of EPs covered by Fe I lines. When calculating the slopes, we exclude outliers that are $> 3\sigma$ from the mean abundance. In addition, we require any acceptable solution to fulfill the following criteria: (1) the input Fe abundance of the model atmosphere and the output Fe I abundance from MOOG match within 0.05 dex, (2) the output Fe I and Fe II abundances from MOOG match within 0.05 dex (i.e., ionization balance), and (3) the Ti I and Ti II abundances from MOOG match within 0.35 dex.

We determine the best fit solution using an automated script. Given an initial guess, we search the parameter space around it on a 5^4 grid, where the grid spacings for $T_{\rm eff}$, log g, [Fe/H], and $\xi_{\rm t}$ are 100 K, 0.1 dex, 0.1 dex, and 0.1 km s^{-1}. We do not vary [α/Fe] in this procedure. The script identifies the ten best solutions (i.e., those with the ten lowest values of γ) and calculates each best fit parameter to be the mean of the ten best. This best fit solution is the initial guess for the next iteration. The script continues until the best fit solution has converged, i.e., is the same for two consecutive iterations.

To lessen the possibility that we have found a local minimum, we search a larger 7^4 grid. If a different best fit solution is found, we return to searching on 5^4 grids, as described above. If the same best fit solution is found, we search a finer 5^4 grid, where the grid spacings for $T_{\rm eff}$ and $\xi_{\rm t}$ are 25 K and 0.05 km s^{-1}, respectively. The final parameter determinations are the best fit solution within the entire region of parameter space that has been searched. Figure 4.2 shows a schematic diagram of the steps taken by our automated script. For our analysis, the first initial guess for each star is the result from the SSPP. Because the SSPP does not have a value for $\xi_{\rm t}$, we arbitrarily start with $\xi_{\rm t}$ = 1.5 km s^{-1}; this choice does not affect the final solution.

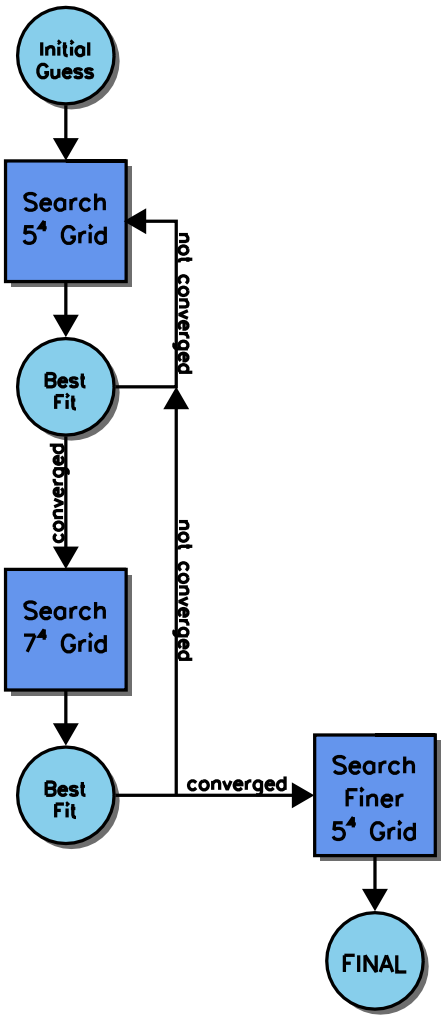

Figure 4.2: Schematic diagram of the parameter determination algorithm.

The resulting stellar parameters for the 37 stars are tabulated in Table 4.3. The SSPP values are the most recent results from Data Release 9 (DR9). The HIRES [α/Fe] is the mean of [Mg/Fe], [Si/Fe], [Ca/Fe] and [Ti/Fe], where each element is weighted by the number of lines measured. Although [α/Fe] is not varied in the parameter determination, the resulting abundances are in good agreement with the SSPP values. Figure 4.3 shows the comparison between the SSPP initial guesses and our HIRES determinations. Row 1 shows the discrepancy between

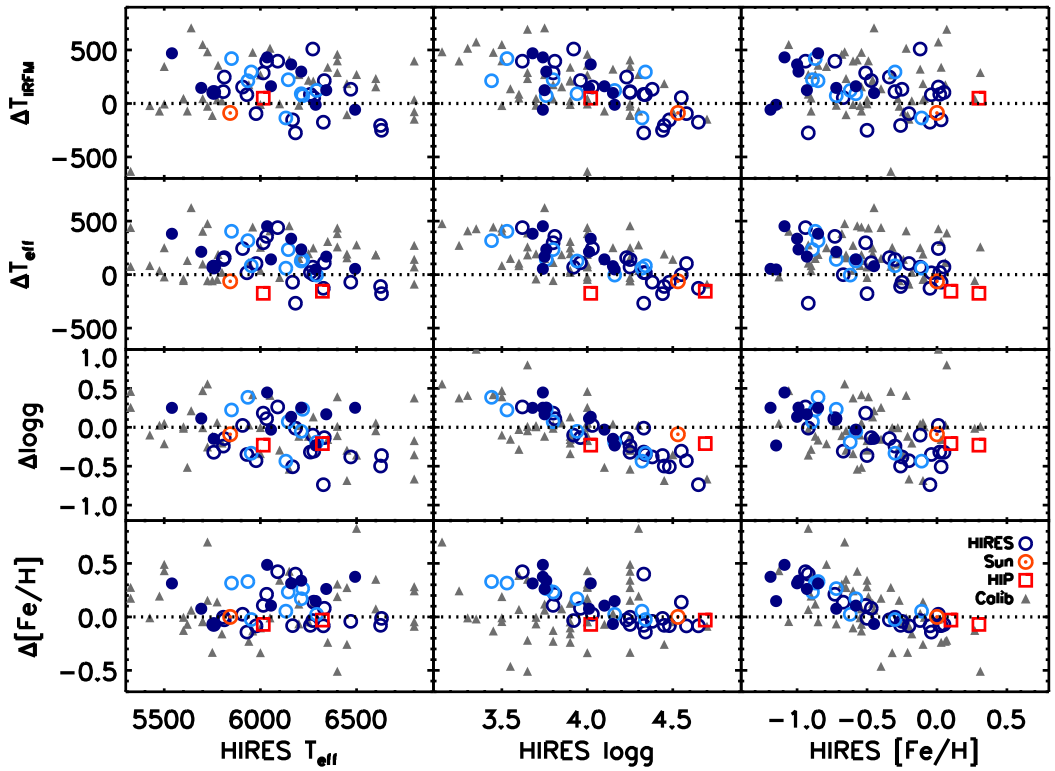

Figure 4.3: Comparison of SSPP and HIRES stellar parameters. Rows 1-4 show the difference between the SSPP and HIRES parameters (SSPP−HIRES), $T_{\rm IRFM}$, $T_{\rm eff}$, log g, and [Fe/H], as a function of the HIRES $T_{\rm eff}$, log g, and [Fe/H].

temperatures determined using the infrared flux method (Casagrande et al. 2010; IRFM) and our spectroscopic temperatures. Rows 2-4 show the discrepancy between SSPP $T_{\rm eff}$, log g, and [Fe/H] determinations and our spectroscopic determinations for MSTO stars (blue circles, as in Figure 4.1) and two HIPPARCOS stars (red squares, see §4.2.6). Gray triangles show a high-resolution spectroscopic calibration sample used to make improvements in the SSPP for DR9; in particular, we show the 48 stars that have properties similar to our turnoff stars ($T_{\rm eff} > 5000$ K, log $g > 3.0$, [Fe/H] > -1.5).

Table 4.3: Stellar Parameters

SEGUE	SSPP				HIRES				
ID	$T_{\rm eff}$ (K)	log g	[Fe/H]	[α/Fe]	$T_{\rm eff}$ (K)	log g	[Fe/H]	[α/Fe]	$\xi_{\rm t}$ (km s^{-1})
1919-173	6279	4.01	-0.06	+0.08	6260^{+40}_{-110}	$4.33^{+0.07}_{-0.13}$	$+0.02^{+0.08}_{-0.02}$	+0.08	$+1.18^{+0.02}_{-0.08}$
1893-104	5946	3.99	-0.18	+0.10	5930^{+45}_{-80}	$4.34^{+0.16}_{-0.14}$	$-0.04^{+0.04}_{-0.06}$	+0.10	$+0.98^{+0.07}_{-0.08}$
1905-243	5914	4.32	-0.52	+0.18	6182^{+117}_{-57}	$4.33^{+0.17}_{-0.03}$	$-0.92^{+0.02}_{-0.08}$	+0.18	$+0.11^{+0.08}_{-0.06}$
2307-386	6276	4.24	-0.53	+0.13	6277^{+122}_{-152}	$4.55^{+0.05}_{-0.25}$	$-0.67^{+0.07}_{-0.13}$	+0.13	$+1.83^{+0.17}_{-0.18}$
2335-542	6390	3.92	-0.52	+0.07	6032^{+167}_{-82}	$3.81^{+0.19}_{-0.11}$	$-0.73^{+0.03}_{-0.07}$	+0.07	$+1.17^{+0.03}_{-0.07}$
2070-084	6151	4.05	+0.03	+0.08	5907^{+92}_{-57}	$4.03^{+0.17}_{-0.13}$	$+0.01^{+0.09}_{-0.01}$	+0.08	$+1.35^{+0.05}_{-0.10}$
2052-063	6341	3.82	-0.15	+0.05	6272^{+102}_{-72}	$3.92^{+0.18}_{-0.12}$	$-0.12^{+0.02}_{-0.08}$	+0.05	$+1.38^{+0.07}_{-0.08}$
2328-059	6096	3.97	-0.05	+0.14	6167^{+82}_{-67}	$4.48^{+0.12}_{-0.08}$	$+0.03^{+0.07}_{-0.03}$	+0.14	$+1.05^{+0.05}_{-0.10}$
2068-151	5836	4.00	-0.52	+0.29	5757^{+92}_{-157}	$4.15^{+0.15}_{-0.25}$	$-0.45^{+0.05}_{-0.05}$	+0.29	$+0.88^{+0.07}_{-0.08}$
2051-595	6312	3.98	-0.40	+0.08	6015^{+85}_{-65}	$3.80^{+0.20}_{-0.10}$	$-0.51^{+0.01}_{-0.09}$	+0.08	$+1.04^{+0.06}_{-0.09}$
2307-074	5970	4.08	-0.37	+0.19	5812^{+62}_{-62}	$4.23^{+0.17}_{-0.13}$	$-0.34^{+0.04}_{-0.06}$	+0.19	$+1.05^{+0.05}_{-0.10}$
2052-537	6399	4.00	-0.29	+0.04	6470^{+30}_{-120}	$4.38^{+0.12}_{-0.18}$	$-0.25^{+0.05}_{-0.05}$	+0.04	$+1.42^{+0.08}_{-0.07}$
2180-560	6487	4.19	-0.60	+0.23	6035^{+165}_{-60}	$3.74^{+0.06}_{-0.14}$	$-1.09^{+0.09}_{-0.01}$	+0.23	$+1.20^{+0.20}_{-0.10}$
2798-073	6510	3.92	-0.67	+0.31	6342^{+107}_{-42}	$3.75^{+0.15}_{-0.15}$	$-0.93^{+0.03}_{-0.07}$	+0.31	$+1.49^{+0.06}_{-0.09}$
1917-020	6199	3.91	-0.13	+0.05	6327^{+47}_{-102}	$4.65^{+0.15}_{-0.15}$	$-0.05^{+0.05}_{-0.05}$	+0.05	$+1.34^{+0.06}_{-0.09}$
2251-632	6081	4.15	-0.28	+0.16	5977^{+97}_{-52}	$4.58^{+0.12}_{-0.18}$	$-0.20^{+0.10}_{-0.10}$	+0.16	$+0.72^{+0.08}_{-0.07}$
2310-312	6335	3.93	-1.00	+0.36	6287^{+87}_{-87}	$4.16^{+0.14}_{-0.16}$	$-1.15^{+0.05}_{-0.05}$	+0.36	$+1.14^{+0.06}_{-0.09}$
1903-096	5948	4.01	-0.30	+0.15	5807^{+67}_{-57}	$4.25^{+0.15}_{-0.15}$	$-0.30^{+0.10}_{-0.00}$	+0.15	$+0.87^{+0.08}_{-0.07}$
2796-054	6545	3.99	-0.82	+0.31	6492^{+82}_{-67}	$3.74^{+0.16}_{-0.14}$	$-1.19^{+0.09}_{-0.01}$	+0.31	$+1.79^{+0.01}_{-0.04}$
2180-545	6529	3.88	-0.52	+0.11	6090^{+310}_{-90}	$3.62^{+0.38}_{-0.12}$	$-0.94^{+0.14}_{-0.06}$	+0.11	$+1.40^{+0.10}_{-0.10}$
2797-407	6447	4.01	-0.65	+0.22	6212^{+62}_{-87}	$3.76^{+0.14}_{-0.16}$	$-0.99^{+0.09}_{-0.01}$	+0.22	$+1.52^{+0.08}_{-0.07}$
1916-559	6495	4.15	-0.69	+0.27	6160^{+115}_{-60}	$4.02^{+0.18}_{-0.12}$	$-1.00^{+0.10}_{-0.10}$	+0.27	$+1.12^{+0.08}_{-0.01}$
2305-365	5921	3.93	-0.54	+0.29	5540^{+160}_{-90}	$3.68^{+0.12}_{-0.18}$	$-0.85^{+0.15}_{-0.05}$	+0.29	$+1.01^{+0.09}_{-0.06}$
1891-140	5828	3.93	-0.02	+0.08	5757^{+67}_{-57}	$4.25^{+0.15}_{-0.15}$	$+0.05^{+0.05}_{-0.05}$	+0.08	$+1.04^{+0.11}_{-0.04}$
2311-476	6197	4.07	-0.47	+0.23	6055^{+95}_{-155}	$4.10^{+0.20}_{-0.30}$	$-0.58^{+0.08}_{-0.02}$	+0.23	$+1.04^{+0.06}_{-0.04}$
2311-208	5905	4.12	-0.64	+0.36	5692^{+82}_{-67}	$4.01^{+0.09}_{-0.11}$	$-0.72^{+0.02}_{-0.08}$	+0.36	$+0.98^{+0.06}_{-0.08}$
2621-215	6442	3.83	-0.39	+0.09	6332^{+42}_{-107}	$3.96^{+0.04}_{-0.16}$	$-0.47^{+0.07}_{-0.03}$	+0.09	$+1.39^{+0.05}_{-0.10}$
2038-050	6452	4.08	-0.51	+0.09	6630^{+70}_{-105}	$4.44^{+0.16}_{-0.14}$	$-0.50^{+0.10}_{-0.10}$	+0.09	$+1.41^{+0.09}_{-0.11}$
2038-226	6514	3.95	-0.34	+0.08	6625^{+50}_{-100}	$4.45^{+0.15}_{-0.25}$	$-0.26^{+0.06}_{-0.04}$	+0.08	$+1.47^{+0.08}_{-0.07}$
2566-412	6192	3.88	-0.06	+0.11	6132^{+67}_{-82}	$4.32^{+0.18}_{-0.12}$	$-0.11^{+0.01}_{-0.09}$	+0.11	$+1.01^{+0.09}_{-0.11}$
2062-482	6255	3.75	-0.55	+0.16	5850^{+50}_{-100}	$3.53^{+0.07}_{-0.23}$	$-0.87^{+0.07}_{-0.03}$	+0.16	$+1.16^{+0.09}_{-0.06}$
2398-036	6252	3.83	-0.52	+0.16	5935^{+65}_{-60}	$3.44^{+0.16}_{-0.14}$	$-0.85^{+0.05}_{-0.05}$	+0.16	$+1.33^{+0.07}_{-0.03}$
2397-014	6287	3.97	-0.60	+0.20	6292^{+82}_{-92}	$4.16^{+0.14}_{-0.16}$	$-0.62^{+0.02}_{-0.08}$	+0.20	$+1.13^{+0.07}_{-0.03}$
2679-442	6035	4.01	-0.32	+0.17	5952^{+122}_{-52}	$4.34^{+0.16}_{-0.14}$	$-0.30^{+0.10}_{-0.00}$	+0.17	$+0.52^{+0.08}_{-0.07}$
2682-560	6362	3.99	-0.46	+0.14	6220^{+80}_{-95}	$3.76^{+0.14}_{-0.16}$	$-0.72^{+0.02}_{-0.08}$	+0.14	$+1.55^{+0.04}_{-0.11}$
2057-001	6339	3.89	-0.41	+0.16	6212^{+62}_{-87}	$3.94^{+0.06}_{-0.14}$	$-0.58^{+0.08}_{-0.02}$	+0.16	$+1.39^{+0.06}_{-0.09}$
2053-419	6378	3.87	-0.66	+0.20	6145^{+80}_{-145}	$3.80^{+0.20}_{-0.10}$	$-0.89^{+0.09}_{-0.01}$	+0.20	$+1.33^{+0.07}_{-0.03}$

4.2.4 Abundances

The abundances we derive for α-, iron peak, and neutron capture elements are tabulated in Tables 4.4, 4.5, 4.6, 4.7. Fe abundances are given relative to H in Table 4.6. All other abundances are given relative to Fe (Fe I for neutral species and Fe II for ionized species), where the ratio of two elements X and Y is given by $[\mathrm{X/Y}] \equiv \log_{10}(\mathrm{X/Y}) - \log_{10}(\mathrm{X/Y})_{\odot}$. We have adopted the solar abundances of Grevesse & Sauval (1998), except for Fe and La, which have been revised to log ϵ(Fe)= 7.52 (Sneden et al. 1991) and log ϵ(La)= 1.13 (Lawler et al. 2001), respectively. For each species, we list the mean abundance, the standard deviation, and the number of individual lines measured in the spectrum.

For most of the lines, we obtain abundances using the `abfind` driver in MOOG. For Na, we have applied the line-by-line non-LTE corrections published by Gratton et al. (1999). For Sc, V, Mn, Co, Cu, Ba, and La, we account for hyperfine splitting using the `blends` driver. For iron peak elements Sc, V, Mn, Co, and Cu, we use hyperfine line lists from the Kurucz tables[3]. For neutron capture elements Ba and La, we use line lists from Gallagher et al. (2010) and Lawler et al. (2001), respectively. The full list of hyperfine lines is tabulated in Appendix D.

[3]http://kurucz.harvard.edu/linelists.html

Table 4.4: Abundances of Na, Mg, Si, Ca, Ti

ID	Na I	σ	N	Mg I	σ	N	Si I	σ	N	Si II	σ	N	Ca I	σ	N	Ti I	σ	N	Ti II	σ	N
Sun	0.03	0.07	2	0.07	0.07	3	0.10	0.07	15	0.36	0.08	2	0.06	0.10	8	-0.08	0.09	37	0.00	0.26	23
1919-173	-0.10	0.00	1	0.05	0.06	2	-0.01	0.07	7	-0.19	0.00	1	-0.04	0.15	10	0.13	0.19	22	0.09	0.25	16
1893-104	-0.15	0.06	3	0.00	0.00	1	-0.08	0.10	10	-0.37	0.00	1	-0.04	0.15	11	0.08	0.11	29	0.11	0.21	12
1905-243	1.16	0.00	1	...	...	...	0.24	0.00	1	...	...	...	-0.08	0.29	9	0.32	0.10	5	0.20	0.21	11
2307-386	...	...	...	0.38	0.00	1	...	...	...	0.05	0.00	1	0.09	0.00	1	0.29	0.05	2	0.39	0.15	5
2335-542	0.16	0.04	2	-0.09	0.03	2	0.07	0.20	2	0.23	0.00	1	0.04	0.12	13	-0.01	0.09	17	0.04	0.25	17
2070-084	...	...	...	...	...	...	0.03	0.07	9	-0.05	0.07	2	-0.11	0.17	3	0.05	0.18	11	0.00	0.20	9
2052-063	-0.10	0.10	3	-0.08	0.06	3	0.10	0.07	9	-0.04	0.01	2	0.05	0.14	13	0.05	0.10	24	-0.01	0.24	19
2328-059	-0.09	0.00	1	-0.07	0.00	1	0.09	0.11	12	0.02	0.00	1	0.00	0.14	9	0.19	0.11	20	0.18	0.25	14
2068-151	0.11	0.05	3	0.33	0.00	1	0.15	0.10	13	0.23	0.00	1	0.11	0.15	11	0.31	0.10	29	0.33	0.24	18
2051-595	...	...	...	-0.05	0.02	2	0.08	0.12	5	...	...	...	0.01	0.13	11	0.02	0.09	22	-0.03	0.20	18
2307-074	-0.07	0.05	3	...	...	...	0.03	0.12	10	0.02	0.00	1	0.08	0.13	11	0.04	0.10	22	0.12	0.21	17
2052-537	-0.02	0.03	2	0.04	0.03	2	0.17	0.00	1	-0.21	0.00	1	0.07	0.20	7	0.23	0.12	10	0.10	0.15	11
2180-560	0.26	0.00	1	0.32	0.19	3	0.36	0.14	3	0.35	0.00	1	0.28	0.21	10	0.34	0.12	17	0.31	0.20	15
2798-073	0.19	0.09	2	0.31	0.15	2	0.30	0.06	4	0.27	0.00	1	0.31	0.16	13	0.34	0.10	18	0.39	0.17	14
1917-020	-0.12	0.00	1	-0.05	0.17	2	-0.06	0.12	11	-0.41	0.00	1	-0.15	0.14	12	-0.05	0.09	20	0.11	0.24	13
2251-632	-0.18	0.10	3	-0.06	0.09	3	-0.06	0.09	11	...	...	...	-0.13	0.16	13	0.00	0.09	26	0.12	0.28	16
2310-312	...	...	...	0.25	0.02	2	0.04	0.08	2	0.20	0.00	1	0.25	0.12	13	0.38	0.12	12	0.41	0.17	15
1903-096	-0.24	0.01	2	0.04	0.02	3	-0.01	0.09	12	0.02	0.00	1	-0.06	0.17	12	0.05	0.11	28	0.10	0.30	16
2796-054	-0.11	0.00	1	0.24	0.00	1	0.37	0.00	1	...	...	...	0.43	0.17	9	0.56	0.05	6	0.44	0.18	16
2180-545	...	...	...	-0.05	0.04	2	0.20	0.09	3	...	...	...	0.11	0.21	10	0.11	0.11	18	0.14	0.21	16
2797-407	0.24	0.17	2	0.23	0.00	1	0.25	0.01	2	...	...	...	0.28	0.19	7	0.33	0.14	10	0.33	0.16	11
1916-559	0.19	0.23	2	0.14	0.00	1	...	...	...	...	...	...	0.11	0.16	11	0.18	0.14	16	0.31	0.19	16
2305-365	0.12	0.00	1	0.38	0.13	3	0.36	0.10	7	0.14	0.00	1	0.26	0.11	13	0.27	0.08	25	0.29	0.23	17
1891-140	-0.17	0.01	2	...	...	...	-0.02	0.09	11	-0.15	0.00	1	-0.13	0.12	10	0.03	0.12	28	0.07	0.23	15
2311-476	0.05	0.03	2	0.37	0.02	3	0.23	0.11	11	0.07	0.00	1	0.12	0.13	12	0.28	0.16	28	0.24	0.28	17
2311-208	0.16	0.10	4	0.32	0.12	3	0.20	0.08	10	0.19	0.00	1	0.16	0.11	13	0.23	0.11	29	0.27	0.23	16
2621-215	0.01	0.04	3	-0.05	0.03	2	-0.05	0.15	5	-0.05	0.00	1	0.01	0.10	11	0.01	0.12	18	0.14	0.25	17
2038-050	0.06	0.00	1	-0.02	0.00	1	...	...	...	...	...	...	...	...	...	0.14	0.07	6	0.17	0.20	6
2038-226	-0.10	0.00	1	...	...	...	...	...	...	...	...	...	-0.13	0.14	6	0.00	0.32	2	0.27	0.20	8

Table 4.4: Abundances of Na, Mg, Si, Ca, Ti, continued

ID	Na I	σ	N	Mg I	σ	N	Si I	σ	N	Si II	σ	N	Ca I	σ	N	Ti I	σ	N	Ti II	σ	N
2566-412	-0.15	0.08	2	-0.23	0.00	1	-0.03	0.13	10	-0.20	0.00	1	0.02	0.22	13	0.17	0.17	11	-0.04	0.26	6
2062-482	-0.02	0.19	3	0.03	0.08	3	0.05	0.19	13	0.04	0.06	2	0.05	0.13	29	0.01	0.11	16	0.05	0.24	22
2398-036	0.21	0.12	2	-0.08	0.05	2	0.10	0.13	11	-0.15	0.10	2	0.06	0.11	25	0.06	0.10	13	0.06	0.18	21
2397-014	0.10	0.04	3	0.12	0.14	2	-0.08	0.12	8	-0.19	0.12	2	0.04	0.12	25	0.08	0.14	14	0.21	0.21	18
2679-442	-0.23	0.10	2	-0.06	0.19	2	-0.04	0.15	16	-0.38	0.00	1	0.05	0.20	16	0.13	0.15	16	0.21	0.26	17
2682-560	0.20	0.00	1	-0.10	0.08	2	0.23	0.10	5	-0.09	0.00	1	0.06	0.21	11	0.02	0.20	6	0.04	0.14	8
2057-001	0.04	0.06	2	-0.06	0.11	2	0.03	0.00	1	-0.05	0.00	1	0.05	0.22	8	0.00	0.10	18	0.09	0.22	18
2053-419	0.08	0.17	3	0.08	0.24	2	0.10	0.12	5	-0.20	0.00	1	0.10	0.15	13	0.17	0.21	22	0.11	0.21	18

Table 4.5: Abundances of Sc, V, Co, Zn

ID	Sc II	σ	N	V I	σ	N	Co I	σ	N	Zn I	σ	N
Sun	0.08	0.05	6	-0.05	0.06	6	-0.14	0.01	2	0.07	0.04	2
1919-173	0.27	0.12	4	...	...	...	...	...	...	0.07	0.17	2
1893-104	0.16	0.12	6	-0.02	0.11	4	1.25	0.00	1	-0.01	0.15	2
1905-243	...	...	...	0.19	0.00	1	...	...	...	-0.31	0.00	1
2307-386	...	...	...	...	...	...	0.03	0.00	1	...	...	...
2335-542	-0.02	0.03	3	...	...	...	0.10	0.00	1	-0.05	0.13	2
2070-084	0.01	0.05	3	-0.02	0.07	3	...	...	...	0.08	0.14	2
2052-063	-0.03	0.07	6	...	...	...	0.03	0.00	1	-0.19	0.08	2
2328-059	0.21	0.10	5	0.11	0.00	1	...	...	...	0.16	0.14	2
2068-151	0.32	0.06	7	0.09	0.06	4	...	...	...	0.27	0.05	2
2051-595	-0.09	0.10	2	...	...	...	0.18	0.00	1	-0.08	0.05	2
2307-074	0.10	0.06	7	0.05	0.15	2	...	...	...	0.03	0.03	2
2052-537	0.03	0.03	3	...	...	...	0.10	0.00	1	-0.12	0.01	2
2180-560	0.05	0.11	2	0.07	0.13	2	0.22	0.00	1	-0.01	0.00	2
2798-073	0.21	0.15	4	...	...	...	0.17	0.00	1	0.01	0.05	2
1917-020	0.24	0.09	4	0.08	0.00	1	-0.02	0.00	1	-0.11	0.01	2
2251-632	0.07	0.17	5	0.08	0.23	4	...	...	...	0.05	0.00	1

Table 4.5: Abundances of Sc, V, Co, Zn, continued

ID	Sc II	σ	N	V I	σ	N	Co I	σ	N	Zn I	σ	N
2310-312	0.02	0.21	2	...	...	...	0.14	0.00	1	-0.15	0.00	1
1903-096	0.14	0.06	5	-0.08	0.17	5	...	...	...	0.01	0.13	2
2796-054	0.24	0.11	3	...	...	...	0.16	0.00	1	-0.02	0.00	1
2180-545	0.06	0.11	3	...	...	...	0.02	0.00	1	-0.02	0.02	2
2797-407	0.07	0.22	3	...	...	...	0.13	0.00	1	-0.06	0.16	2
1916-559	0.04	0.01	2	...	...	...	0.18	0.00	1	0.02	0.15	2
2305-365	0.17	0.08	5	...	...	...	0.41	0.00	1	0.22	0.15	2
1891-140	0.18	0.10	4	-0.01	0.05	7	...	...	...	0.03	0.09	2
2311-476	0.17	0.08	4	0.17	0.00	1	0.20	0.00	1	0.23	0.12	2
2311-208	0.16	0.04	5	0.09	0.17	4	0.16	0.00	1	0.13	0.09	2
2621-215	0.13	0.11	4	...	...	...	0.09	0.00	1	-0.08	0.06	2
2038-050	...	...	...	...	...	...	-0.06	0.00	1	...	...	...
2038-226	0.01	0.15	2	...	...	...	0.02	0.00	1	...	...	...
2566-412	-0.02	0.21	3	...	...	...	...	...	...	-0.08	0.00	1
2062-482	0.13	0.10	6	...	...	...	0.40	0.00	1	-0.12	0.13	2
2398-036	0.06	0.12	5	...	...	...	-0.07	0.00	1	-0.06	0.04	2
2397-014	-0.04	0.08	4	...	...	...	0.22	0.00	1	-0.16	0.11	2
2679-442	0.13	0.13	5	-0.14	0.09	3	0.56	0.00	1	0.20	0.00	1
2682-560	-0.25	0.09	2	...	...	...	0.06	0.00	1	-0.07	0.00	1
2057-001	0.06	0.09	3	...	...	...	0.08	0.00	1	-0.14	0.14	2
2053-419	0.06	0.08	6	...	...	...	0.15	0.00	1	-0.29	0.01	2

Table 4.6: Abundances of Cr, Mn, Fe, Ni, Cu

ID	Cr I	σ	N	Cr II	σ	N	Mn I	σ	N	Fe II	σ	N	Fe I	σ	N	Ni I	σ	N	Cu I	σ	N
Sun	-0.03	0.10	32	0.07	0.10	9	0.01	0.10	5	-0.05	0.14	178	-0.03	0.17	30	-0.03	0.11	43	-0.06	0.12	3
1919-173	0.12	0.19	19	0.05	0.11	9	-0.11	0.15	5	0.09	0.15	134	0.00	0.22	21	-0.04	0.13	25	-0.01	0.13	2
1893-104	0.02	0.14	25	0.01	0.11	9	-0.15	0.06	5	0.01	0.16	155	-0.01	0.20	22	-0.05	0.12	35	-0.06	0.00	1
1905-243	0.52	0.38	7	-0.02	0.11	3	...	...	...	-0.86	0.26	63	-0.93	0.33	12	0.19	0.26	3	0.16	0.00	1

Table 4.6: Abundances of Cr, Mn, Fe, Ni, Cu, continued

ID	Cr I	σ	N	Cr II	σ	N	Mn I	σ	N	Fe II	σ	N	Fe I	σ	N	Ni I	σ	N	Cu I	σ	N
2307-386	0.18	0.13	2	0.37	0.00	1	...	...	...	-0.61	0.19	45	-0.61	0.27	5	0.03	0.21	2	...	...	...
2335-542	-0.02	0.17	17	0.05	0.19	7	-0.13	0.12	4	-0.69	0.15	140	-0.72	0.17	19	-0.05	0.21	14	-0.18	0.00	1
2070-084	0.12	0.17	12	0.03	0.12	6	-0.08	0.10	3	0.07	0.15	83	0.02	0.23	11	0.01	0.20	17	-0.04	0.00	1
2052-063	0.02	0.10	21	-0.05	0.13	10	-0.15	0.06	4	-0.06	0.15	154	-0.09	0.13	23	-0.08	0.13	24	-0.19	0.00	1
2328-059	0.06	0.20	24	0.00	0.11	9	-0.12	0.12	4	0.09	0.15	161	0.08	0.13	21	-0.01	0.11	33	0.12	0.00	1
2068-151	0.04	0.15	21	0.04	0.16	7	-0.21	0.13	5	-0.40	0.16	148	-0.42	0.18	20	0.04	0.17	22	-0.09	0.12	2
2051-595	0.03	0.17	21	0.00	0.21	7	-0.21	0.12	4	-0.47	0.15	133	-0.48	0.14	19	-0.07	0.17	13	-0.11	0.00	1
2307-074	0.03	0.13	19	0.06	0.11	6	-0.21	0.08	6	-0.29	0.15	133	-0.32	0.14	16	-0.06	0.14	23	-0.03	0.00	1
2052-537	0.00	0.13	12	-0.01	0.14	6	-0.22	0.12	3	-0.20	0.14	84	-0.19	0.17	17	-0.06	0.08	8	-0.17	0.00	1
2180-560	-0.02	0.18	12	0.00	0.15	7	-0.29	0.15	2	-1.03	0.14	113	-1.05	0.09	15	-0.01	0.13	8	...	...	...
2798-073	-0.03	0.16	11	-0.01	0.20	7	-0.20	0.00	1	-0.88	0.13	114	-0.91	0.13	17	0.07	0.10	5	...	...	...
1917-020	0.04	0.15	23	0.04	0.11	9	-0.07	0.11	5	-0.01	0.14	141	-0.01	0.17	16	0.02	0.13	22	0.09	0.00	1
2251-632	0.03	0.12	27	0.13	0.11	9	-0.13	0.08	5	-0.14	0.15	162	-0.20	0.19	19	-0.02	0.15	30	0.04	0.00	1
2310-312	-0.12	0.19	11	-0.02	0.34	3	-0.42	0.18	2	-1.08	0.14	108	-1.05	0.11	16	-0.01	0.11	4	...	...	...
1903-096	0.00	0.18	25	0.14	0.16	9	-0.22	0.09	5	-0.26	0.16	167	-0.24	0.26	19	0.04	0.15	28	-0.11	0.11	2
2796-054	-0.03	0.10	2	0.21	0.06	3	-0.33	0.00	1	-1.14	0.16	84	-1.17	0.15	14	-0.02	0.15	2	...	...	...
2180-545	-0.09	0.18	14	0.14	0.18	8	-0.25	0.07	4	-0.89	0.14	111	-0.89	0.20	17	-0.01	0.16	8	-0.18	0.00	1
2797-407	0.05	0.21	9	-0.01	0.19	5	-0.39	0.00	1	-0.94	0.14	90	-0.96	0.15	11	0.07	0.13	3	...	...	...
1916-559	-0.08	0.13	10	0.10	0.14	5	-0.22	0.13	2	-0.95	0.15	104	-0.99	0.16	15	0.01	0.06	6	-0.18	0.00	1
2305-365	0.09	0.16	17	0.08	0.12	6	-0.24	0.07	4	-0.80	0.14	136	-0.81	0.15	17	0.04	0.17	18	-0.15	0.00	1
1891-140	0.05	0.19	27	0.09	0.18	9	-0.12	0.09	5	0.09	0.17	163	0.07	0.18	19	-0.02	0.13	39	0.15	0.00	1
2311-476	0.01	0.15	19	-0.01	0.17	10	-0.23	0.06	5	-0.54	0.12	151	-0.58	0.14	17	0.09	0.18	23	0.03	0.00	1
2311-208	0.05	0.16	23	-0.01	0.17	9	-0.35	0.08	6	-0.67	0.12	156	-0.71	0.12	19	0.03	0.17	19	-0.06	0.00	1
2621-215	0.02	0.21	14	0.00	0.12	9	-0.19	0.12	4	-0.41	0.15	127	-0.43	0.14	19	-0.01	0.12	11	-0.20	0.00	1
2038-050	0.00	0.08	5	0.26	0.06	2	...	...	...	-0.45	0.16	44	-0.48	0.15	10	-0.07	0.00	1	0.03	0.00	1
2038-226	0.10	0.24	8	0.05	0.15	6	-0.09	0.05	2	-0.20	0.14	50	-0.22	0.12	9	-0.11	0.00	1	-0.24	0.00	1
2566-412	0.02	0.21	15	-0.02	0.26	4	-0.12	0.20	5	-0.08	0.19	118	-0.12	0.27	13	0.05	0.25	18	0.03	0.00	1
2062-482	-0.08	0.14	20	0.02	0.13	7	-0.21	0.12	4	-0.80	0.15	170	-0.84	0.23	22	-0.04	0.17	18	-0.34	0.00	1
2398-036	-0.02	0.16	16	-0.08	0.16	7	-0.12	0.06	5	-0.80	0.15	158	-0.84	0.14	22	-0.05	0.28	18	...	...	...
2397-014	-0.02	0.19	12	-0.09	0.25	6	-0.35	0.21	2	-0.56	0.16	138	-0.59	0.18	22	0.00	0.21	11	-0.23	0.00	1
2679-442	0.00	0.23	22	0.00	0.25	6	-0.28	0.14	2	-0.25	0.18	171	-0.28	0.23	19	-0.07	0.20	31	0.13	0.00	1

Table 4.6: Abundances of Cr, Mn, Fe, Ni, Cu, continued

ID	Cr I	σ	N	Cr II	σ	N	Mn I	σ	N	Fe II	σ	N	Fe I	σ	N	Ni I	σ	N	Cu I	σ	N
2682-560	0.02	0.12	8	-0.11	0.08	4	0.05	0.00	1	-0.68	0.19	88	-0.69	0.19	11	-0.09	0.20	7	...	...	...
2057-001	0.01	0.23	20	0.05	0.16	8	-0.16	0.06	3	-0.53	0.16	109	-0.56	0.23	17	-0.02	0.11	8	-0.14	0.00	1
2053-419	-0.05	0.16	18	0.02	0.15	7	-0.28	0.19	4	-0.82	0.14	137	-0.87	0.22	19	0.00	0.14	11	-0.13	0.00	1

Table 4.7: Abundances of Y, Zr, Ba, La

ID	Y II	σ	N	Zr II	σ	N	Ba II	σ	N	La II	σ	N
Sun	-0.07	0.16	8	-0.10	0.06	3	0.00	0.00	1	-0.03	0.02	2
1919-173	0.02	0.07	6	0.14	0.08	2	0.42	0.00	1	0.14	0.00	1
1893-104	0.03	0.19	8	1.36	0.00	1	0.15	0.00	1	...	...	...
1905-243	0.21	0.46	4	...	...	...	0.14	0.30	2	...	...	...
2307-386	0.47	0.37	5	2.00	0.00	1	0.86	0.00	1	...	...	...
2335-542	-0.03	0.18	8	-0.15	0.00	1	0.05	0.00	1	-0.05	0.07	2
2070-084	-0.20	0.18	5	-0.02	0.00	1	0.14	0.00	1	0.03	0.00	1
2052-063	-0.01	0.04	6	0.00	0.13	2	0.33	0.00	1	0.02	0.00	1
2328-059	-0.10	0.11	9	0.09	0.00	1	0.28	0.00	1	0.16	0.00	1
2068-151	-0.02	0.16	7	0.19	0.14	3	0.23	0.00	1	0.09	0.00	1
2051-595	-0.16	0.23	8	-0.04	0.00	1	0.52	0.00	1	...	...	...
2307-074	-0.06	0.13	5	0.07	0.02	2	0.05	0.00	1	...	...	...
2052-537	0.05	0.08	4	...	...	...	0.46	0.00	1	...	...	...
2180-560	0.02	0.15	7	0.19	0.00	2	0.06	0.00	1	-0.05	0.00	1
2798-073	-0.02	0.14	5	0.25	0.10	2	0.07	0.00	1	...	...	...
1917-020	0.10	0.37	7	0.08	0.04	2	0.44	0.00	1	0.13	0.00	1
2251-632	0.25	0.13	8	0.26	0.04	3	0.56	0.00	1	0.35	0.00	1
2310-312	0.15	0.24	5	...	...	...	0.01	0.00	1	...	...	...
1903-096	-0.05	0.10	8	0.01	0.09	4	0.38	0.00	1	0.13	0.00	1
2796-054	0.44	0.07	6	0.78	0.08	2	0.38	0.00	1	...	...	...
2180-545	-0.09	0.09	8	0.14	0.29	2	-0.02	0.00	1	-0.12	0.00	1
2797-407	-0.03	0.08	5	...	...	...	-0.16	0.00	1	...	...	...

Table 4.7: Abundances of Y, Zr, Ba, La, continued

ID	Y II	σ	N	Zr II	σ	N	Ba II	σ	N	La II	σ	N
1916-559	-0.19	0.10	4	1.24	0.00	1	0.08	0.00	1	...	...	...
2305-365	-0.07	0.14	8	-0.04	0.22	2	0.16	0.00	1	0.06	0.00	1
1891-140	0.12	0.18	7	0.09	0.20	2	0.17	0.00	1	0.09	0.01	2
2311-476	-0.18	0.12	10	0.11	0.00	1	-0.02	0.00	1	0.09	0.00	1
2311-208	-0.02	0.11	6	0.24	0.00	1	0.00	0.00	1	-0.03	0.10	2
2621-215	-0.02	0.12	8	0.03	0.00	1	0.28	0.00	1	0.08	0.04	2
2038-050	-0.34	0.00	1	...	...	...	...	...	...	...	...	...
2038-226	-0.10	0.00	1	1.70	0.00	1	0.33	0.00	1	...	...	...
2566-412	-0.03	0.02	2	...	...	...	0.39	0.00	1	...	...	...
2062-482	-0.33	0.20	3	0.13	0.00	1	0.24	0.13	2	...	...	...
2398-036	-0.16	0.10	2	0.00	0.00	1	0.08	0.11	2	...	...	...
2397-014	0.00	0.24	3	-0.01	0.00	1	0.41	0.16	2	0.17	0.00	1
2679-442	0.03	0.25	4	0.46	0.00	1	0.36	0.06	2	...	...	...
2682-560	0.00	0.12	2	1.29	0.00	1	0.23	0.11	2	...	...	...
2057-001	-0.09	0.18	8	-0.05	0.00	1	0.13	0.00	1	-0.13	0.14	2
2053-419	-0.17	0.08	8	-0.06	0.00	1	...	...	...	0.10	0.00	1

For each species, we have calculated solar corrections from an analysis of the solar spectrum[4] (Delbouille et al. 1973). Using the same techniques described above, we obtain stellar parameters $T_{\rm eff}$= 5843^{+58}_{-93} K, log g= $4.53^{+0.17}_{-0.13}$, [Fe/H]= $0.0^{+0.10}_{-0.10}$, and $\xi_{\rm t}$= $0.79^{+0.06}_{-0.09}$ km s^{-1}, in good agreement with the accepted values: $T_{\rm eff}$= 5780 K, log g= 4.44, and [Fe/H]= 0.0. Our derived solar abundances are listed in the first row of each abundance table, and all of the species and the adopted solar values are compiled in Table 4.8. The corrections are made by subtracting our derived solar abundances from the abundances we obtain for our stars.

Table 4.8: Solar Abundances

Element	log$\epsilon_\odot$	logϵ	[X/Fe]	σ	N
Na I	6.33	6.31	0.03	0.07	2
Mg I	7.58	7.60	0.07	0.07	3
Si I	7.55	7.60	0.10	0.07	15
Si II	7.55	7.88	0.36	0.08	2
Ca I	6.36	6.37	0.06	0.10	8
Sc II	3.17	3.22	0.08	0.05	6
Ti I	5.02	4.89	-0.08	0.09	37
Ti II	5.02	4.99	0.00	0.26	23
V I	4.00	3.90	-0.05	0.06	6
Cr I	5.67	5.59	-0.03	0.10	32
Cr II	5.67	5.71	0.07	0.10	9
Mn I	5.39	5.35	0.01	0.10	5
Fe I	7.52	7.47	-0.05	0.14	178
Fe II	7.52	7.49	-0.03	0.17	30
Co I	4.92	4.73	-0.14	0.01	2
Ni I	6.25	6.17	-0.03	0.11	43
Cu I	4.21	4.10	-0.06	0.12	3
Zn I	4.60	4.62	0.07	0.04	2
Y II	2.24	2.14	-0.07	0.16	8
Zr II	2.60	2.47	-0.10	0.06	3
Ba II	2.13	2.10	0.00	0.00	1
La II	1.13	1.07	-0.03	0.02	2

4.2.5 Random Errors Due to Equivalent Width Measurements

We estimate errors in our stellar parameters by running 100 Monte Carlo realizations of our EW measurements. In each realization i, we use a simple bootstrapping method to generate a random subsample of the EW list and determine the goodness of fit, γ_i, for the same

[4]http://bass2000.obspm.fr/solar_spect.php

grids that we searched using the real data. Figure 4.4 shows how we can make two different estimates of the error from this exercise for one star. First, for each realization, we determine a best fit solution by minimizing γ_i using the same method described in §4.2.3. The distributions in $T_{\rm eff}$, log g, [Fe/H], and $\xi_{\rm t}$ of these 100 best fit solutions are given by the red histograms in Figure 4.4. The red vertical lines indicate the parameters for the best fit solution, where $\gamma = \gamma_0$, the minimum value of the goodness of fit using the real data.

Second, we can determine the errors due to degeneracies in the parameter space by calculating σ_γ, the error in γ_0. We find all of solutions that have $\gamma < \sigma_\gamma$ for the real data (i.e., those that are as good as the best fit solution, given the errors in the EWs). The distributions of these "good" solutions are given by the black histograms in Figure 4.4. The black vertical dotted lines indicate the 68% intervals for the black histograms. In general, for a given star, the two distributions are comparable. In cases where they are different, the second distribution tends to be wider, suggesting that degeneracies in the parameter space are the more dominant factor in the uncertainty of our stellar parameter determinations. We therefore adopt the 68% intervals of the second distribution (black histograms) as the errors on our stellar parameters.

We can then estimate the correlated errors on our stellar parameters and abundances by calculating how much they are affected for a given change in a single parameter. For example, if we fix a star's temperature to be $T_{\rm eff}+\Delta T_{\rm eff}$, where $\Delta T_{\rm eff}$ is the error bar derived above, how does this change the other parameters and the abundances? For each parameter ($T_{\rm eff}$, log g, [Fe/H], $\xi_{\rm t}$), we calculate the changes for both the upper and lower 68% confidence levels, and we tabulate the larger of the two values. In Table 4.9, we tabulate the changes in parameters, given perturbations $\Delta T_{\rm eff}$, Δlog g, Δ[Fe/H], and $\Delta\xi_{\rm t}$ for all of the stars in our sample. In Table 4.10, we tabulate the changes in the abundances for one star, 1893-104.

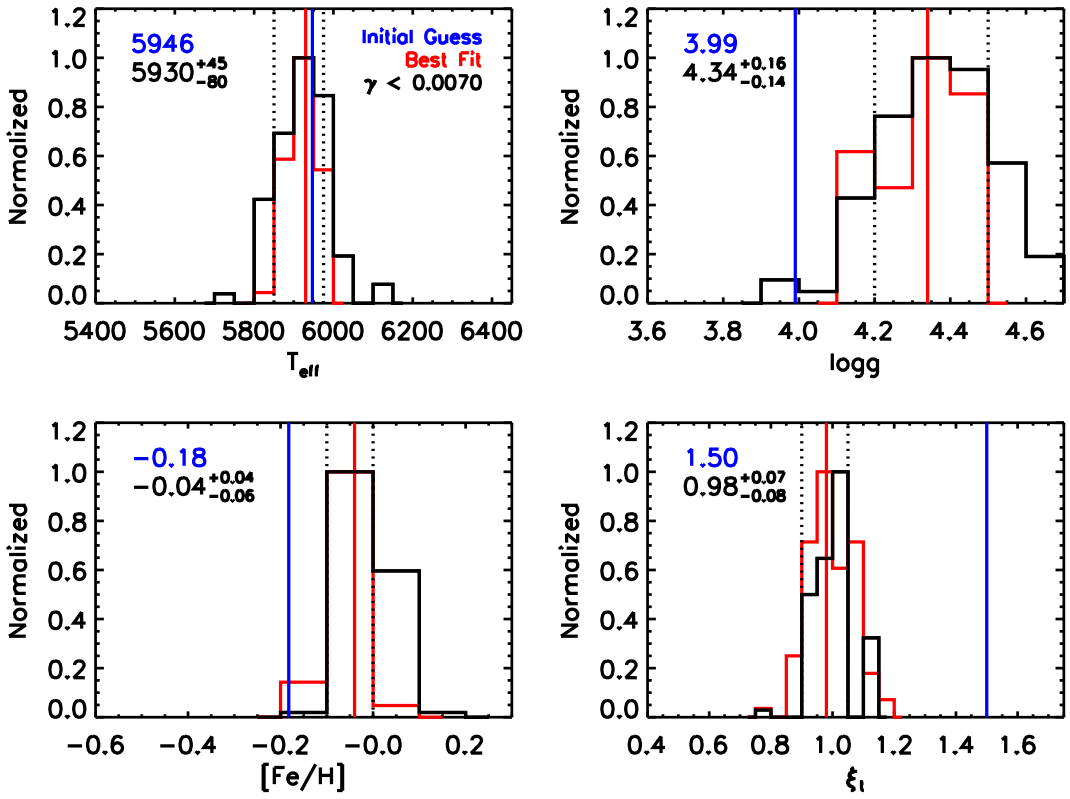

Figure 4.4: Random errors on stellar parameters $T_{\rm eff}$, log g, [Fe/H], and $\xi_{\rm t}$ for 1893-104. The red histograms show the distributions of parameters that are the best fit solutions for 100 Monte Carlo realizations. The red vertical lines show the best fit solution for the real data. The black histograms show the distributions of parameters that are as good as the best fit solution, given the errors in the EWs. The black vertical dotted lines indicate the 68% intervals determined by the black histograms.

Table 4.9: Correlated Errors on Stellar Parameters

ID	$\Delta T_{\rm eff}$			$\Delta\log g$			Δ[Fe/H]			$\Delta\xi_{\rm t}$		
	$\Delta\log g$	Δ[Fe/H]	$\Delta\xi_{\rm t}$	$\Delta T_{\rm eff}$	Δ[Fe/H]	$\Delta\xi_{\rm t}$	$\Delta T_{\rm eff}$	$\Delta\log g$	$\Delta\xi_{\rm t}$	$\Delta T_{\rm eff}$	$\Delta\log g$	Δ[Fe/H]
1919-173	0.10	0.05	0.05	98	0.05	0.03	65	0.12	0.01	15	0.08	0.01
1893-104	0.17	0.06	0.03	72	0.06	0.05	40	0.08	0.02	70	0.16	0.05
1905-243	0.19	0.08	0.03	118	0.07	0.03	62	0.07	0.09	35	0.03	0.03
2307-386	0.18	0.12	0.04	148	0.09	0.06	162	0.25	0.04	85	0.12	0.06
2335-542	0.17	0.09	0.11	150	0.07	0.09	82	0.08	0.07	72	0.08	0.05
2070-084	0.23	0.04	0.04	88	0.04	0.01	118	0.21	0.01	100	0.26	0.06
2052-063	0.13	0.07	0.04	122	0.08	0.03	90	0.14	0.02	155	0.20	0.09
2328-059	0.10	0.07	0.03	75	0.06	0.02	65	0.06	0.02	158	0.20	0.10
2068-151	0.30	0.10	0.11	135	0.07	0.09	65	0.10	0.02	82	0.16	0.05
2051-595	0.13	0.04	0.06	182	0.10	0.12	78	0.14	0.05	78	0.05	0.04
2307-074	0.12	0.05	0.06	68	0.06	0.09	40	0.05	0.02	40	0.12	0.03
2052-537	0.22	0.05	0.04	95	0.06	0.04	70	0.11	0.05	110	0.22	0.09
2180-560	0.14	0.09	0.14	70	0.02	0.03	95	0.07	0.08	202	0.12	0.12
2798-073	0.17	0.05	0.02	95	0.07	0.01	62	0.08	0.02	45	0.03	0.02
1917-020	0.23	0.06	0.07	112	0.05	0.03	40	0.06	0.04	125	0.18	0.07
2251-632	0.17	0.08	0.11	118	0.07	0.03	130	0.18	0.03	82	0.16	0.04
2310-312	0.18	0.07	0.06	162	0.10	0.03	65	0.09	0.04	20	0.03	0.03
1903-096	0.21	0.02	0.09	105	0.03	0.08	132	0.19	0.05	112	0.20	0.05
2796-054	0.13	0.05	0.00	170	0.10	0.05	170	0.30	0.07	130	0.18	0.09
2180-545	0.27	0.18	0.17	325	0.20	0.14	220	0.20	0.13	160	0.15	0.09

Table 4.9: Correlated Errors on Stellar Parameters, continued

ID	$\Delta T_{\rm eff}$			$\Delta\log g$			Δ[Fe/H]			$\Delta\xi_{\rm t}$		
	$\Delta\log g$	Δ[Fe/H]	$\Delta\xi_{\rm t}$	$\Delta T_{\rm eff}$	Δ[Fe/H]	$\Delta\xi_{\rm t}$	$\Delta T_{\rm eff}$	$\Delta\log g$	$\Delta\xi_{\rm t}$	$\Delta T_{\rm eff}$	$\Delta\log g$	Δ[Fe/H]
2797-407	0.12	0.05	0.04	128	0.09	0.05	82	0.12	0.02	90	0.06	0.06
1916-559	0.13	0.08	0.04	98	0.08	0.05	145	0.11	0.18	50	0.02	0.01
2305-365	0.18	0.15	0.17	130	0.13	0.19	142	0.13	0.20	238	0.36	0.19
1891-140	0.21	0.05	0.08	70	0.04	0.10	30	0.09	0.10	38	0.09	0.05
2311-476	0.21	0.10	0.08	170	0.11	0.07	80	0.08	0.07	82	0.07	0.04
2311-208	0.23	0.04	0.25	65	0.06	0.15	92	0.08	0.15	48	0.04	0.06
2621-215	0.13	0.05	0.04	82	0.03	0.02	62	0.06	0.02	192	0.24	0.10
2038-050	0.19	0.06	0.02	105	0.05	0.03	115	0.17	0.02	152	0.24	0.08
2038-226	0.18	0.05	0.08	138	0.07	0.04	70	0.08	0.07	192	0.29	0.12
2566-412	0.12	0.09	0.10	110	0.07	0.06	58	0.05	0.05	122	0.17	0.05
2062-482	0.22	0.05	0.05	90	0.04	0.07	38	0.07	0.02	110	0.27	0.05
2398-036	0.18	0.05	0.07	145	0.07	0.03	40	0.07	0.04	65	0.19	0.04
2397-014	0.17	0.06	0.10	160	0.09	0.08	95	0.05	0.09	38	0.05	0.05
2679-442	0.14	0.06	0.11	70	0.04	0.15	148	0.15	0.15	52	0.12	0.02
2682-560	0.15	0.06	0.07	108	0.07	0.06	75	0.15	0.03	130	0.16	0.07
2057-001	0.10	0.05	0.05	150	0.10	0.10	68	0.09	0.01	120	0.09	0.08
2053-419	0.10	0.07	0.14	118	0.07	0.09	72	0.09	0.02	80	0.06	0.06

Table 4.10: Effect of Parameter Errors on Abundances for 1893-104

Element	$\Delta T_{\rm eff}$	$\Delta\log g$	Δ[Fe/H]	$\Delta\xi_{\rm t}$
Fe I	0.06	0.01	0.01	0.00
Fe II	0.11	0.06	0.02	0.00
Na I	0.08	0.07	0.06	0.06
Si I	0.10	0.08	0.08	0.08
Si II	0.05	0.03	0.03	0.03
Ca I	1.30	1.21	1.16	1.16
Sc II	2.97	2.93	2.92	2.92
Ti I	1.60	1.67	1.65	1.63
Ti II	0.13	0.12	0.12	0.11
V I	1.19	1.16	1.09	1.09
V II	0.32	0.26	0.27	0.26
Cr I	1.38	1.49	1.50	1.47
Cr II	0.10	0.10	0.09	0.09
Mn I	0.41	0.37	0.30	0.30
Ni I	0.94	0.93	0.93	0.92
Cu I	1.42	1.40	1.39	1.39
Zn I	1.56	1.52	1.51	1.51
Y II	2.03	2.01	1.99	1.99
Zr II	0.89	0.81	0.80	0.80
Ba II	1.85	1.73	1.71	1.71

4.2.6 Analysis of Stars in Bensby et al. Sample

We identified two stars from the sample of Bensby et al. (2003; 2005) which had archival data in the Keck Observatory Archive[5]: HIP83601 and HIP86731. We perform the same analysis on these data following the procedures described in §4.2.3 and §4.2.4. In general, we find good agreement with their stellar parameters and abundances.

Figure 4.5 shows the comparison between the EWs measured by Bensby et al. (T. Bensby, private communication) and by our group. Our EWs are systematically lower and the discrepancy is larger for stronger lines; this is likely a result of differing determinations of the local continuum. In addition, for each star, we run our stellar parameter algorithm (§4.2.3) using the EWs measured by both groups. Table 4.11 shows the parameters published in Bensby

[5]http://www2.keck.hawaii.edu/koa/public/koa.php

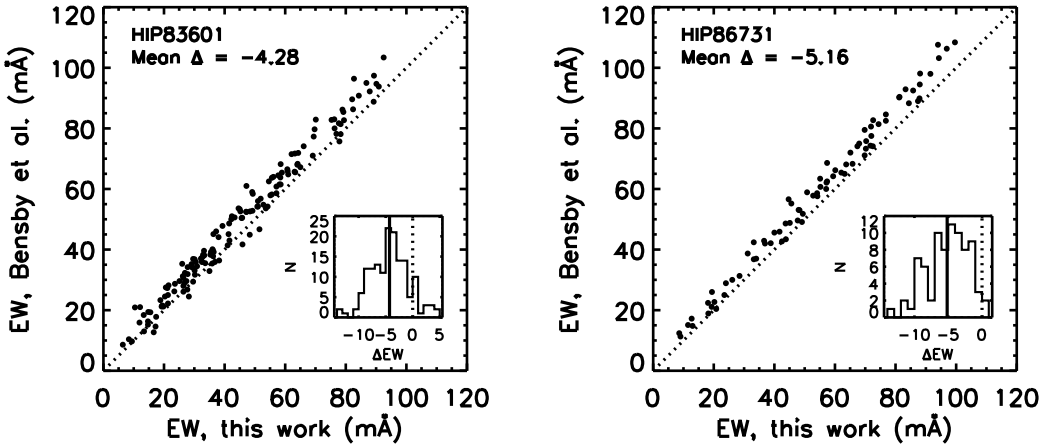

Figure 4.5: Equivalent width comparison between Bensby et al. (2003) and this work. Our measurements are systematically lower by a few mÅ, which is likely a result of differences in setting the local continuum.

et al. (2003) and the parameters determined in this work using both sets of EW measurements. Published values of parameters based on Strömgren photometry are also listed for each star (Feltzing et al. 2001, Casagrande et al. 2011). The results in Table 4.11 show that there is good general agreement with the Bensby et al. (2003) results, whether we use the EW measurements of Bensby et al. (2003) or our own measurements. These two stars are plotted as red squares in Figure 4.3.

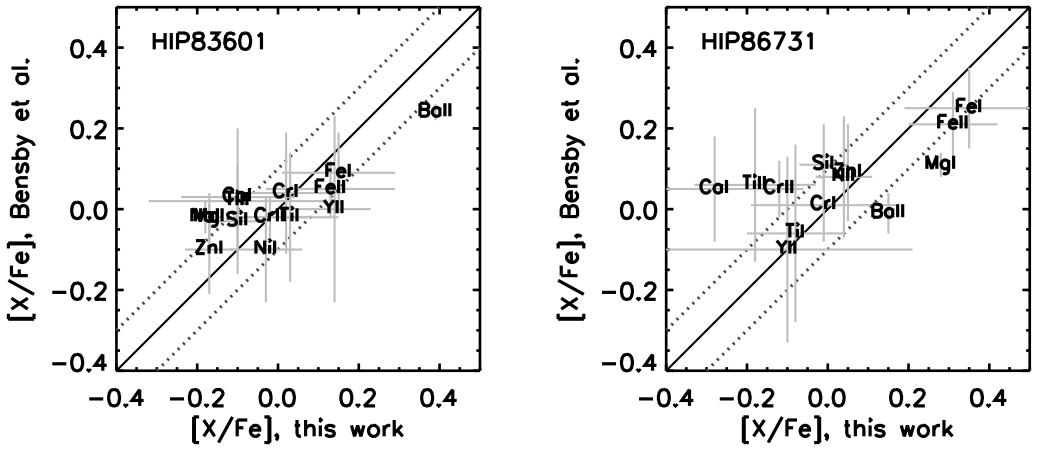

Figure 4.6: Abundance comparison between Bensby et al. (2003) and this work for two HIPPARCOS stars. We find good agreement between the two independent analyses for most elements, within 0.1 dex. The errors indicate the scatter in abundances between individual line measurements.

Table 4.11: Parameter Comparison for Two HIPPARCOS Stars

	$T_{\rm eff}$ (K)	log g	[Fe/H]	$\xi_{\rm t}$ (km s^{-1})	Comments
HIP83601					
Casagrande et al. (2011)	6064	4.4	-0.05	...	Strömgren photometry
Bensby et al. (2003)	6167	4.5	0.07	1.21	High-resolution spectroscopy
This Work (Bensby EWs)	6015	4.3	0.00	1.03	High-resolution spectroscopy
This Work (Cheng EWs)	6322	4.7	0.10	1.26	High-resolution spectroscopy
HIP86731					
Feltzing et al. (2001)	5754	...	0.23	...	Strömgren photometry
Bensby et al. (2003)	5840	3.8	0.23	1.43	High-resolution spectroscopy
This Work (Bensby EWs)	5875	3.7	0.25	1.49	High-resolution spectroscopy
This Work (Cheng EWs)	6015	4.0	0.30	1.28	High-resolution spectroscopy

Figure 4.6 shows the comparison between elemental abundances published by Bensby et al. (2003; 2005) and determined by our group using our EW measurements. The numerical values are tabulated in Table 4.12. Most elements are in good agreement, within 0.1 dex. We conclude from this comparison that we can compare our abundances to the sample of Bensby et al. (2003; 2005) without applying any corrections to either set of abundance measurements.

Table 4.12: Abundance Comparison for Two HIPPARCOS Stars

		Bensby et al.			This Work			
Element	Ion	[X/Fe]	σ	N	[X/Fe]	σ	N	Δ
HIP83601								
Fe I	26.0	+0.09	0.10	142	+0.15	0.14	166	+0.06
Fe II	26.1	+0.05	0.07	26	+0.13	0.16	24	+0.08
Na I	11.0	-0.02	0.04	4	-0.18	0.01	3	-0.16
Mg I	12.0	-0.02	0.06	4	-0.17	0.03	2	-0.15
Si I	14.0	-0.03	0.08	30	-0.10	0.07	12	-0.07
Ca I	20.0	+0.03	0.08	22	-0.10	0.14	9	-0.13
Ti I	22.0	-0.02	0.16	27	+0.03	0.12	31	+0.05
Ti II	22.1	+0.02	0.18	17	-0.10	0.22	17	-0.12
Cr I	24.0	+0.04	0.15	12	+0.02	0.14	26	-0.02
Cr II	24.1	-0.02	0.05	9	-0.02	0.09	10	+0.00
Ni I	28.0	-0.10	0.13	49	-0.03	0.09	35	+0.07
Zn I	30.0	-0.10	0.11	2	-0.17	0.06	2	-0.07
Y II	39.1	+0.00	0.23	6	+0.14	0.09	4	+0.14
Ba II	56.1	+0.24	0.02	4	+0.39	0.00	1	+0.15
HIP86731								
Fe I	26.0	+0.25	0.10	144	+0.35	0.16	95	+0.10
Fe II	26.1	+0.21	0.08	27	+0.31	0.11	6	+0.10
Mg I	12.0	+0.11	0.03	7	+0.28	0.00	1	+0.17
Si I	14.0	+0.11	0.10	31	-0.01	0.06	4	-0.12
Ca I	20.0	+0.05	0.13	22	-0.28	0.18	4	-0.33
Ti I	22.0	-0.06	0.22	29	-0.08	0.12	23	-0.02
Ti II	22.1	+0.06	0.19	18	-0.18	0.15	8	-0.24
Cr I	24.0	+0.01	0.09	13	-0.01	0.18	20	-0.02
Cr II	24.1	+0.05	0.07	9	-0.12	0.06	5	-0.17
Ni I	28.0	+0.08	0.15	54	+0.04	0.07	19	-0.04
Zn I	30.0	+0.09	0.12	2	+0.05	0.00	1	-0.04
Y II	39.1	-0.10	0.23	6	-0.10	0.31	5	-0.00
Ba II	56.1	-0.01	0.05	4	+0.15	0.00	1	+0.16

4.3 Results

In this section we present the abundance results for 17 elements: Na, Mg, Si, Ca, Sc, Ti, V, Cr, Mn, Co, Ni, Cu, Zn, Y, Zr, Ba, and La. We compare our abundances to published values from several studies: (1) 102 solar neighborhood thin and thick disk stars (Bensby et al. 2003; 2005); (2) ten thick disk stars (Prochaska et al. 2000) and 23 thin and thick disk stars (Brewer & Carney 2006), for which more elements were analyzed; (3) 117 thick disk stars, which extend to lower metallicities (Reddy et al. 2006, Reddy & Lambert 2008); (4) 62 inner and outer

disk giants, for which α-elements Mg, Si, and Ti were measured (Bensby et al. 2010a; 2011); and (5) three outer disk red giants (Carney et al. 2005). We have not made any corrections for systematic offsets between the various datasets. In the discussion of specific elements, we note differences in the analyses where appropriate.

For each element, we examine whether the high- and low-α stars look like solar neighborhood thick and thin disk stars, respectively. In particular, we discuss whether the distinct abundance trends in some elements for thick and thin disk stars also exist for high- and low-α stars. We find that high-α stars have abundances consistent with those of nearby thick disk stars in all elements; low-α stars, however, may exhibit small offsets in Na, Mg, Si, Ca, Zn, and Ba compared to nearby thin disk stars. Additionally, we note any trends with Galactocentric radius R.

4.3.1 Light and α-Elements: Na, Mg, Si, Ca, Ti

The production of the odd-Z light element Na and the α-elements Mg, Si, Ca, and Ti occurs in massive stars and their explosions (Woosley & Weaver 1995). Older stars tend to be enhanced in α-elements relative to iron because they formed at an early time when massive stars were the main contributors to the metal content of the ISM. In general the abundances of these elements track closely together; any differences may arise due to SNe of stars with different masses producing different mixtures of α-elements (Woosley & Weaver 1995, McWilliam 1997).

Figure 4.7 shows the abundance trends for Na, Mg, Si, Ca, and Ti, and their variation with Galactocentric radius R. Our stars are shown as open and filled blue circles, with the symbols indicating the same properties as in Figure 4.1. Smaller circles are plotted for stars where the abundance was measured using only one line. The horizontal and vertical dotted lines indicate the solar values. Where available, we have plotted measurements from Bensby et al. (2003; 2005; gray squares), Bensby et al. (2010a; 2011; dark red crosses and pluses), Prochaska et al. (2000; red asterisks), Brewer & Carney (2006; orange diamonds), Reddy et al. (2006)

and Reddy & Lambert (2008; pink stars), and Carney et al. (2005; green stars). For data from Bensby et al. (2003; 2005) and Brewer & Carney (2006), open and filled symbols indicate thin and thick disk membership, where these stars have been assigned by their kinematic properties. Typical error bars are shown in the top right corner and show the size of the scatter in the abundances derived from individual lines. The direction and magnitude of solar corrections (see Table 4.8) are shown in the bottom right corner if the correction changes the abundance by more than 0.05 dex.

The abundances of our stars are roughly consistent with those of previous studies, but there are some slight differences. While previous studies have found that Na plateaus at lower metallicity ([Fe/H] $\lesssim -1.0$), it is not clear whether our stars follow this trend. With the exception of one star, the stars at [Fe/H] ~ -1.0 are slightly enhanced in Na compared to those in the solar neighborhood. The discrepancy is about the size of the scatter, however, so our observations are still consistent with the previous studies. To account for non-LTE effects, we have applied the line-by-line corrections published by Gratton et al. (1999). None of the studies that we are comparing to have implemented corrections for non-LTE effects, although the authors argue that the effects should be small. For our stars, these corrections lead to a decrease in the abundances, but the effect is not large (< 0.1 dex).

The α-element abundances of high-α stars are consistent with thick disk stars in the solar neighborhood, which indicates that their star formation histories are not dramatically different. Low-α stars, however, are slightly underabundant in Na, Mg, Si, and Ca, relative to thin disk stars in the solar neighborhood. Ti does not show this offset, likely because it is both an iron peak and α-element and is thought to be produced in both Type Ia and Type II SNe (Woosley & Weaver 1995). We note that although we are looking far from the plane, low-α stars are still the dominant population at $|Z| \gtrsim 0.5$ kpc (see Chapter 3).

Like previous studies, we find that high- and low-α stars (filled and open circles, respectively) at the same [Fe/H] have similar abundances in Na, but show distinct trends in α-elements

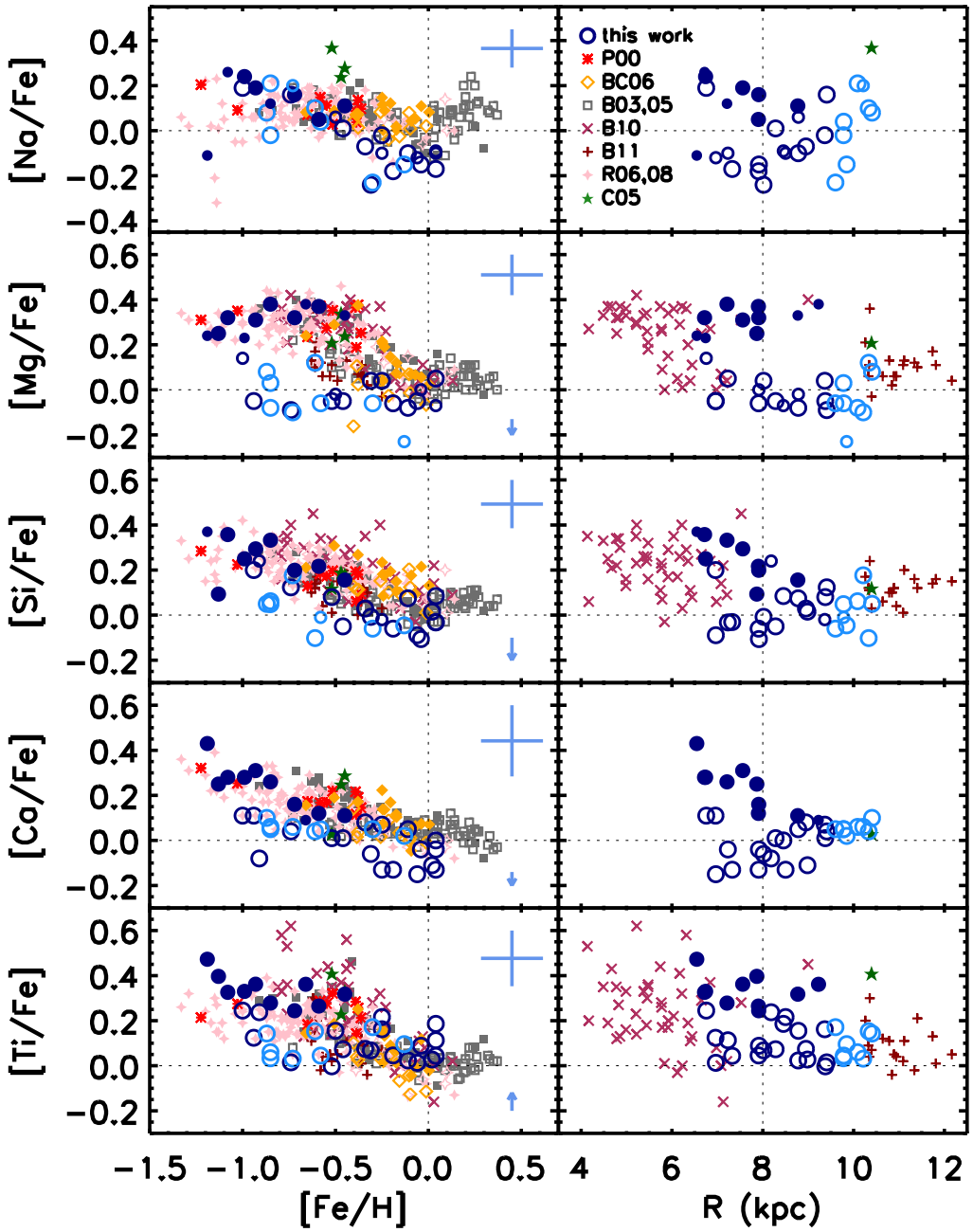

Figure 4.7: Light and α-element abundances, Na, Mg, Si, Ca, Ti, as a function of metallicity [Fe/H] and Galactocentric radius R.

Mg, Si, Ca, and Ti. High-α stars, as expected, are enhanced in all four α-elements. Bensby et al. (2003) identified the "knee" of the [α/Fe]-[Fe/H] relation for thick disk stars at [Fe/H] ≈ -0.4 as

a signature of the contribution from Type Ia SNe. We do not have enough high-α stars at higher metallicity to definitively confirm the location of the knee. In our sample, the gap between high- and low-α stars is most pronounced in Mg; this is likely because the SSPP [α/Fe], which we have used to identify high- and low-α targets for observation, is most sensitive to Mg.

For low-α stars, some of these elements show a slight increase with R. The chemical evolution model of Cescutti et al. (2007), in which the disk forms inside out, predicts flatter gradients for elements that are produced on longer timescales, i.e., those that are produced in Type Ia SNe. For example, they find slightly steeper slopes for [Si/H] and [Ca/H], which are partly produced in Type Ia SNe, and a flatter slope for [Mg/H], which is only produced in Type II SNe. This behavior will lead to more pronounced increases in [Si/Fe] and [Ca/Fe] with radius, which is consistent with what we observe for the low-α stars in our sample. Magrini et al. (2009) predict a similar enhancement of [α/Fe] in the outer disk.

4.3.2 Iron Peak Elements: Sc, V, Cr, Mn, Co, Ni, Cu, Zn

Iron peak elements are produced by both Type Ia and Type II SNe (Thielemann et al. 1986, Timmes et al. 1995, Woosley et al. 2002). Figures 4.8 and 4.9 show the abundance trends for Sc, V, Cr, Mn, Co, Ni, Cu, Zn, and their variation with Galactocentric radius R. Symbols are the same as in Figure 4.7.

Brewer & Carney (2006) found no differences between thin and thick disk stars for Mn, Cr, Ni, and Cu (Figure 4.8); Reddy et al. (2006) referred to these as "Ni-like" elements. In contrast, the abundances of "Mg-like" elements Sc, V, Co, and Zn (Figure 4.9) were significantly enhanced in thick disk stars. Our data show evidence of this separation—the high-α stars tend to be clustered together in abundance space—but the gap between high- and low-α stars is not as significant. If thin and thick disk stars have different abundance trends in these elements, the correlation with α-enhancement could indicate that Type II SNe contribute a non-negligible amount to the nucleosynthesis of Sc, V, Co, and Zn, while Mn, Cr, Ni, and Cu are almost

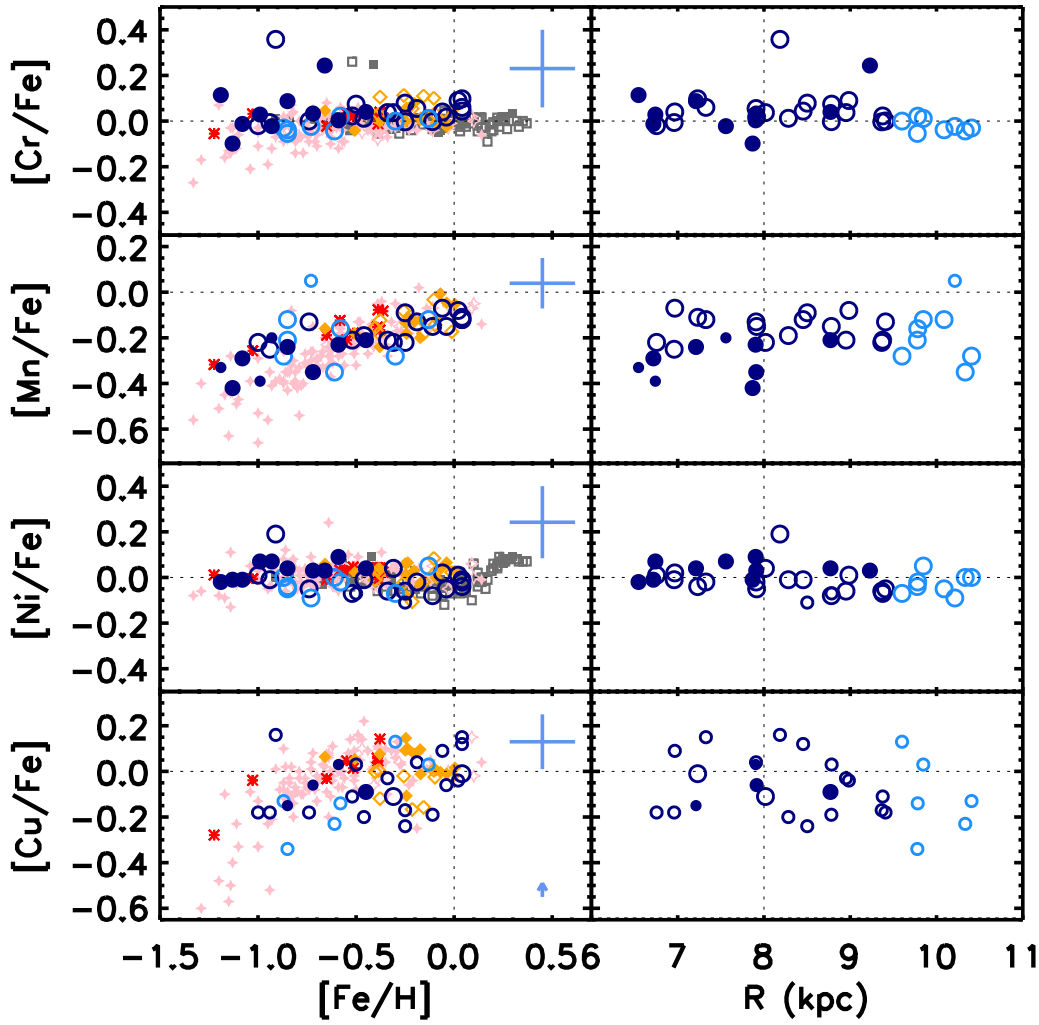

Figure 4.8: Iron peak element abundances, Cr, Mn, Ni, Cu, as a function of metallicity [Fe/H] and Galactocentric radius R. These elements were identified as "Ni-like" by Brewer & Carney (2006) and Reddy et al. (2006).

entirely made by Type Ia SNe.

In general there is good agreement between the abundances of our stars and those of previous studies. Even-Z elements Cr and Ni show tight relations that are close to solar, although Ni exhibits more variation. Zn is also an even-Z element, but its abundance relative to iron shows more scatter. Both Ni and Zn have upturns relative to solar at high metallicity, as seen in the Bensby et al. (2003; 2005) sample; we see possible evidence of this in Zn, but our

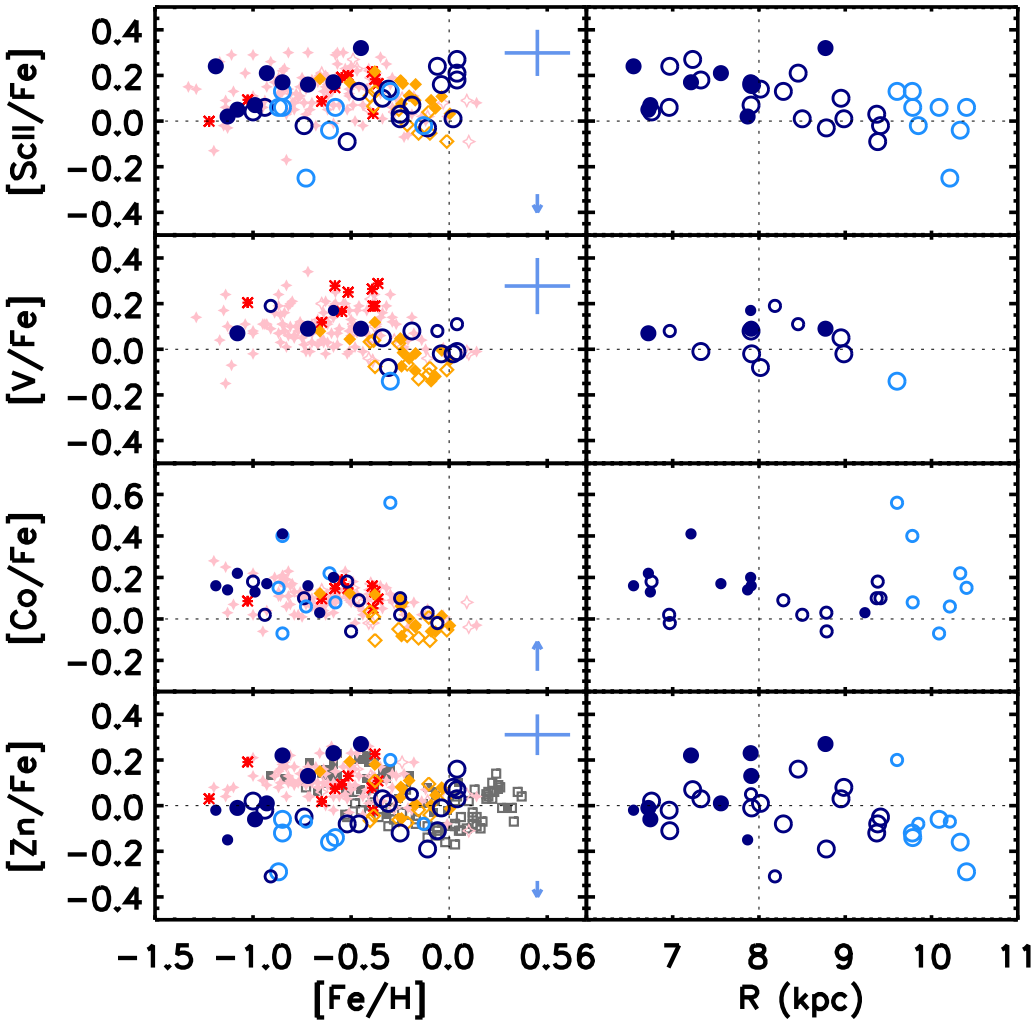

Figure 4.9: Iron peak element abundances, Sc, V, Co, Zn, as a function of metallicity [Fe/H] and Galactocentric radius R. These elements were identified as "Mg-like" by Brewer & Carney (2006) and Reddy et al. (2006).

sample does not reach high enough metallicity to confirm the trend. For low-α stars, we see a very slight underabundance in Zn, similar to what we saw for Na, Mg, Ca, and Si.

For odd-Z elements Sc, V, Mn, Co, and Cu, we also find good agreement between our stars and those of previous studies. Hyperfine splitting corrections are important for all of these elements and have been taken into account (see §4.2.4). Unlike Cr and Ni, the odd-Z elements deviate from solar and are not constant as a function of metallicity. Prochaska

et al. (2000) reported an overabundance of Sc at [Fe/H] ~ -0.5, with the abundance decreasing toward [Fe/H] ~ -1.0; the sample of Reddy et al. (2006) suggest a similar trend, and our data are consistent with this picture. We were not able to measure V for most of our sample, but the available measurements are in good agreement with previous work. Like previous work, we find that Co is supersolar and decreases with increasing metallicity, while Mn and Cu are both subsolar and increase with increasing metallicity.

All of the iron peak elements in the low-α stars appear to be roughly constant with R, in agreement with what is predicted by Magrini et al. (2009) for [Cr/Fe] and [Ni/Fe]. In elements where weak trends may be present, the abundance appears to be decreasing slightly with R.

4.3.3 Neutron Capture Elements: Y, Zr, Ba, La

"Slow" neutron capture, or s-process, elements are produced in neutron-rich environments when neutrons are added to iron nuclei faster than the rate of β-decay. While heavy s-process elements Ba and La are made in the main s-process in asymptotic giant branch (AGB) stars (Busso et al. 1999, Sneden et al. 2008), light s-process elements Y and Zr also have contributions from the weak s-process in massive stars (e.g., Pignatari et al. 2010). Rows 1-4 of Figure 4.10 show the abundance trends for Y, Zr, Ba, La, and their variation with Galactocentric radius R. Symbols are the same as in Figure 4.7. Row 5 of Figure 4.10 shows the ratio of Ba to Y, which is a indicator of the relative contributions of the main and weak components of the s-process. This ratio provides a constraint on the star formation history of the population, as metal-poor AGB stars make relatively more Ba than Y; in metal-poor AGB stars there are more available neutrons for each iron nucleus, leading to the production of heavier s-process elements.

In agreement with previous studies, we do not see any separation between high and low-α stars in the weak s-process element Y. Additionally, high-α stars tend to have lower

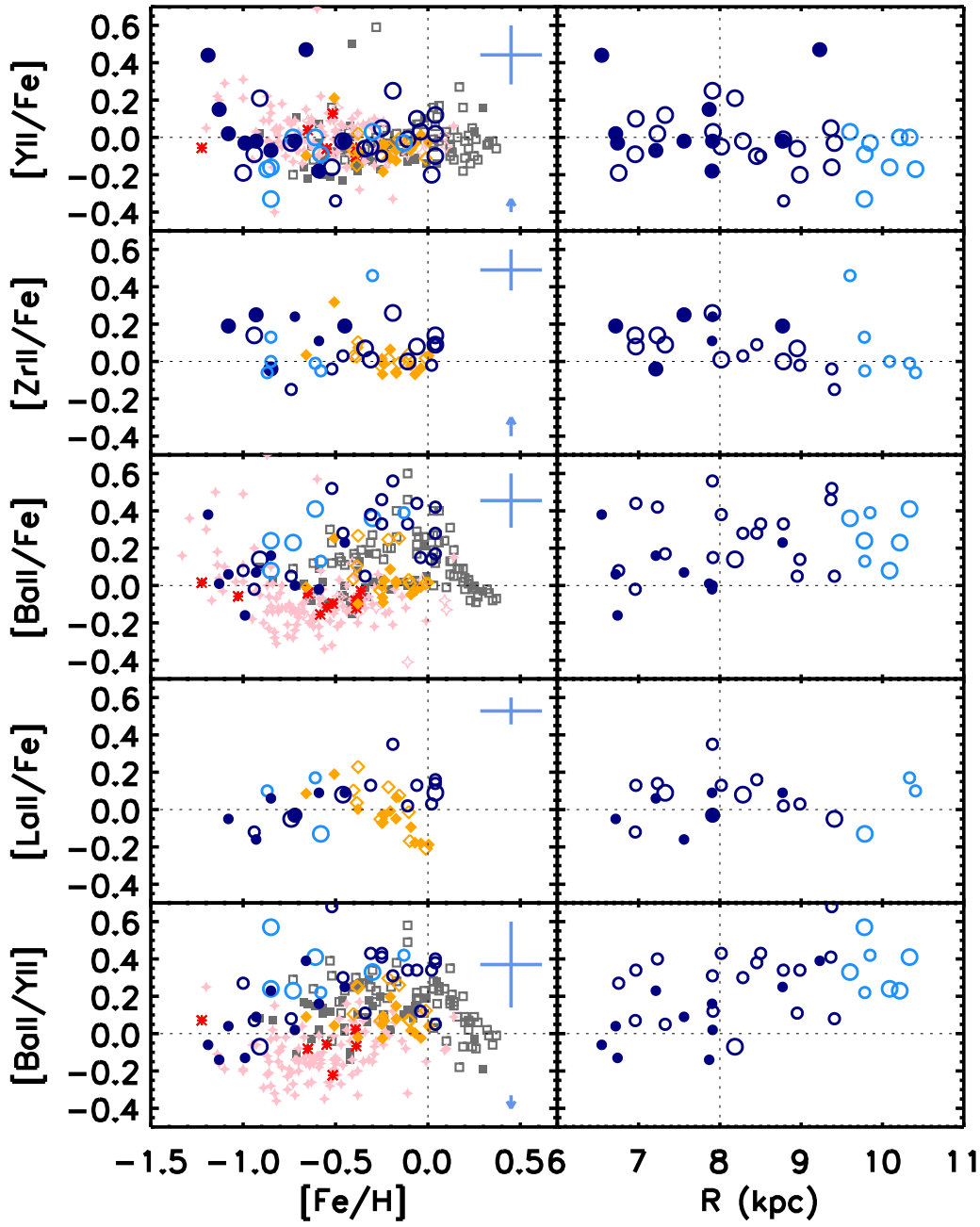

Figure 4.10: Neutron capture element abundances, Y, Zr, Ba, La, as a function of [Fe/H] and R. Row 5 shows the ratio of Ba, a main s-process element, to Y, a weak s-process element.

abundances in Ba, which is consistent with the picture where main s-process elements are made in metal-poor AGB stars. The populations are not as distinct in our sample as it is in other

studies. The low-α stars in our sample show a slight overabundance in Ba relative to thin disk stars in the solar neighborhood. This difference between our stars and the solar neighborhood sample is even more evident in [Ba/Y]. High [Ba/Y] is indicative of a more extended star formation history, as has been seen in some dwarf galaxies (e.g., Tolstoy et al. 2009, Colucci et al. 2012).

For low-α stars, the abundances of Y and Zr appear to decrease at large R, while the abundances of Ba and La appear to be roughly constant. The ratio [Ba/Y] increases with R, suggesting that metal-poor AGB stars have contributed more to the chemical enrichment in the outer disk than in the inner disk, consistent with an increase in α-element abundances with R

4.4 Discussion and Conclusions

In our analysis of 37 stars beyond the solar neighborhood, we find that the elemental abundances of high-α stars at $|Z| \gtrsim 0.5$ kpc are similar to thick disk stars observed in the solar neighborhood (Prochaska et al. 2000, Brewer & Carney 2006, Bensby et al. 2003; 2005; 2011, Reddy et al. 2006, Reddy & Lambert 2008). Previous studies have reported that thick disk stars exhibit distinct abundance trends in α-elements (Mg, Si, Ca, Ti), some iron peak elements (Sc, V, Co, Zn), and some s-process elements (Ba). Our high-α stars also appear to have high abundances in Sc, Co, Zn, and low abundances in Ba; we have only measured V in a few of our high-α stars. The scatter in our trends appears to be larger than in previous studies, however, and the high- and low-α stars are not as well separated in abundance space. This could be due to the different selection of targets in this work versus the previous studies. Thin and thick disk stars in the solar neighborhood were targeted if their kinematics indicated that they had a high probability of being in one of the components, leading to samples with more "extreme" kinematics and fewer stars with intermediate properties.

We see no significant trends in the elemental abundances of high-α stars with R in the

radial range 6.5 kpc $< R <$ 9.0 kpc. In Chapter 3, we found evidence that the canonical thick disk population (kinematically hot and enhanced in α-elements) is chemically homogeneous and has a flat radial metallicity gradient in [Fe/H]. The agreement between our high-α stars at $|Z| \gtrsim 0.5$ kpc and kinematically-selected thick disk stars in the solar neighborhood lend further support to this picture, extending the analysis to 17 elements. A chemically homogeneous thick disk is consistent with the thick disk having formed rapidly in a turbulent disk at early times (Scenario 3, described in §4.1). Another way to get a chemically homogeneous thick disk is to have very thorough mixing by minor mergers (Scenario 1) or internal radial migration processes (Scenario 4).

For low-α stars at $|Z| \gtrsim 0.5$ kpc, however, we find that some elements exhibit slight offsets relative to thin disk stars observed in the solar neighborhood. In comparison to thin disk stars in the solar neighborhood, these stars are deficient in Na, Mg, Si, Ca, and possibly Zn by ~ 0.1 dex. In addition, our low-α stars are enhanced in Ba relative to nearby thin disk stars by a similar amount. We see these offsets for low-α stars at all R and, if real, they are suggestive of a more extended star formation history for stars far from the plane of the disk.

The abundance trends we see for our low-α stars is reminiscent of the properties of some dwarf galaxies. The distinct behavior of Ti compared to the other α-elements is also seen in these galaxies (Kirby et al. 2011), and some of the abundance trends we see are intermediate between the trends for nearby disk stars and the those seen for the Sagittarius dwarf spheroidal galaxy, which exhibits low abundances in Na, Mg, and Ca and high abundances in Ba (Tolstoy et al. 2009). We do not, however, see the low abundances of Sc, V, Co, Ni, Cu, Zn, and Y reported for Sagittarius by Sbordone et al. (2007).

Why would low-α stars far from the plane have a star formation history similar to that of dwarf galaxies? If radial migration is responsible for the weaker gradient in [Fe/H] at large $|Z|$ (Scenario 4), then the stars at large $|Z|$ should be ones that were displaced from the inner parts of the galaxy and they should be older and more α-enhanced. The low abundances of Ma,

Ca, and Si, then, seem to disfavor radial migration in the low-α population. These stars also seem unlikely to have come from a destroyed satellite (Scenario 2) because we see the offsets for stars at all R, from 6 kpc to 12 kpc.

We see some weak trends in the elemental abundances of low-α stars with R. The slight increases in [α/Fe] and [Ba/Y] at large R suggest that the relative contribution of Type II SNe is higher in the outer disk. We note, however, that [Fe/H] is not constant as a function of R, and our outer disk stars are more metal-poor than the inner disk stars. A larger sample with better sampling of the metallicity distribution will yield more concrete results. Metal-rich high-α stars are needed to discern whether there are different trends for high- and low-α stars at all metallicities. More stars in the outer disk, particularly high-α stars, are needed to fully explore the origin of the canonical thick disk population. In this analysis, we have not considered any biases in our target selection that might have affected the radial trends.

Nevertheless, the results presented here represent a first exploration of the detailed chemical abundances of stars in a large volume of the Milky Way. Future high-resolution spectroscopic surveys of stars in the Milky Way such as APOGEE (Eisenstein et al. 2011) will provide the large samples needed to explore these questions more completely. Simulations of galaxy formation that follow the detailed chemical enrichment of the stellar populations (e.g., Kobayashi & Nakasato 2011) will provide explicit predictions that can be tested with these data.

Bibliography

Abadi, M. G., Navarro, J. F., Steinmetz, M., & Eke, V. R. 2003, *ApJ*, **597**, 21

Abazajian, K. N., Adelman-McCarthy, J. K., Agüeros, M. A., Allam, S. S., Allende Prieto, C., An, D., Anderson, K. S. J., Anderson, S. F., Annis, J., Bahcall, N. A., & et al. 2009, *ApJS*, **182**, 543

Aihara, H., Allende Prieto, C., An, D., Anderson, S. F., Aubourg, É., Balbinot, E., Beers, T. C., Berlind, A. A., Bickerton, S. J., Bizyaev, D., Blanton, M. R., Bochanski, J. J., Bolton, A. S., Bovy, J., Brandt, W. N., Brinkmann, J., Brown, P. J., Brownstein, J. R., Busca, N. G., Campbell, H., Carr, M. A., Chen, Y., Chiappini, C., Comparat, J., Connolly, N., Cortes, M., Croft, R. A. C., Cuesta, A. J., da Costa, L. N., Davenport, J. R. A., Dawson, K., Dhital, S., Ealet, A., Ebelke, G. L., Edmondson, E. M., Eisenstein, D. J., Escoffier, S., Esposito, M., Evans, M. L., Fan, X., Femenía Castellá, B., Font-Ribera, A., Frinchaboy, P. M., Ge, J., Gillespie, B. A., Gilmore, G., González Hernández, J. I., Gott, J. R., Gould, A., Grebel, E. K., Gunn, J. E., Hamilton, J., Harding, P., Harris, D. W., Hawley, S. L., Hearty, F. R., Ho, S., Hogg, D. W., Holtzman, J. A., Honscheid, K., Inada, N., Ivans, I. I., Jiang, L., Johnson, J. A., Jordan, C., Jordan, W. P., Kazin, E. A., Kirkby, D., Klaene, M. A., Knapp, G. R., Kneib, J., Kochanek, C. S., Koesterke, L., Kollmeier, J. A., Kron, R. G., Lampeitl, H., Lang, D., Le Goff, J., Lee, Y. S., Lin, Y., Long, D. C., Loomis, C. P., Lucatello, S., Lundgren, B., Lupton, R. H., Ma, Z., MacDonald, N., Mahadevan, S., Maia, M. A. G., Makler, M., Malanushenko, E., Malanushenko, V., Mandelbaum, R., Maraston, C., Margala, D., Masters, K. L., McBride, C. K., McGehee, P. M., McGreer, I. D., Ménard, B., Miralda-Escudé, J., Morrison, H. L., Mullally, F., Muna, D., Munn, J. A., Murayama, H., Myers, A. D., Naugle, T., Fausti Neto, A., Cuong Nguyen, D., Nichol, R. C., O'Connell, R. W., Ogando, R. L. C., Olmstead, M. D., Oravetz, D. J., Padmanabhan, N., Palanque-Delabrouille, N., Pan, K., Pandey, P., Pâris, I., Percival, W. J., Petitjean, P., Pfaffenberger, R., Pforr, J., Phleps, S., Pichon, C., Pieri, M. M., Prada, F., Price-Whelan, A. M., Raddick, M. J., Ramos, B. H. F., Reylé, C., Rich, J., Richards, G. T., Rix, H., Robin, A. C., Rocha-Pinto, H. J., Rockosi, C. M., Roe, N. A., Rollinde, E., Ross, A. J., Ross, N. P., Rossetto, B. M., Sánchez, A. G., Sayres, C., Schlegel, D. J., Schlesinger, K. J., Schmidt, S. J., Schneider, D. P., Sheldon, E., Shu, Y., Simmerer, J., Simmons, A. E., Sivarani, T., Snedden, S. A., Sobeck, J. S., Steinmetz, M., Strauss, M. A., Szalay, A. S., Tanaka, M., Thakar, A. R., Thomas, D., Tinker, J. L., Tofflemire, B. M., Tojeiro, R., Tremonti, C. A., Vandenberg, J., Vargas Magaña, M., Verde, L., Vogt, N. P., Wake, D. A., Wang, J., Weaver, B. A., Weinberg, D. H., White, M., White, S. D. M., Yanny, B., Yasuda, N., Yeche, C., & Zehavi, I. 2011, *ApJS*, **193**, 29

Allende Prieto, C., Beers, T. C., Wilhelm, R., Newberg, H. J., Rockosi, C. M., Yanny, B., & Lee, Y. S. 2006, *ApJ*, **636**, 804

Allende Prieto, C., Majewski, S. R., Schiavon, R., Cunha, K., Frinchaboy, P., Holtzman, J., Johnston, K., Shetrone, M., Skrutskie, M., Smith, V., & Wilson, J. 2008a, *Astronomische Nachrichten*, **329**, 1018

Allende Prieto, C., Sivarani, T., Beers, T. C., Lee, Y. S., Koesterke, L., Shetrone, M., Sneden, C., Lambert, D. L., Wilhelm, R., Rockosi, C. M., Lai, D. K., Yanny, B., Ivans, I. I., Johnson, J. A., Aoki, W., Bailer-Jones, C. A. L., & Re Fiorentin, P. 2008b, *AJ*, **136**, 2070

Alves-Brito, A., Meléndez, J., Asplund, M., Ramírez, I., & Yong, D. 2010, *A&A*, **513**, A35+

An, D., Pinsonneault, M. H., Masseron, T., Delahaye, F., Johnson, J. A., Terndrup, D. M., Beers, T. C., Ivans, I. I., & Ivezić, Ž. 2009, *ApJ*, **700**, 523

Anders, E. & Grevesse, N. 1989, *Geochim. Cosmochim. Acta*, **53**, 197

Andrievsky, S. M., Bersier, D., Kovtyukh, V. V., Luck, R. E., Maciel, W. J., Lépine, J. R. D., & Beletsky, Y. V. 2002a, *A&A*, **384**, 140

Andrievsky, S. M., Kovtyukh, V. V., Luck, R. E., Lépine, J. R. D., Bersier, D., Maciel, W. J., Barbuy, B., Klochkova, V. G., Panchuk, V. E., & Karpischek, R. U. 2002b, *A&A*, **381**, 32

Andrievsky, S. M., Kovtyukh, V. V., Luck, R. E., Lépine, J. R. D., Maciel, W. J., & Beletsky, Y. V. 2002c, *A&A*, **392**, 491

Andrievsky, S. M., Luck, R. E., Martin, P., & Lépine, J. R. D. 2004, *A&A*, **413**, 159

Aumer, M. & Binney, J. J. 2009, *MNRAS*, **397**, 1286

Belokurov, V., Evans, N. W., Irwin, M. J., Lynden-Bell, D., Yanny, B., Vidrih, S., Gilmore, G., Seabroke, G., Zucker, D. B., Wilkinson, M. I., Hewett, P. C., Bramich, D. M., Fellhauer, M., Newberg, H. J., Wyse, R. F. G., Beers, T. C., Bell, E. F., Barentine, J. C., Brinkmann, J., Cole, N., Pan, K., & York, D. G. 2007, *ApJ*, **658**, 337

Bensby, T., Alves-Brito, A., Oey, M. S., Yong, D., & Meléndez, J. 2010a, *A&A*, **516**, L13+

Bensby, T., Alves-Brito, A., Oey, M. S., Yong, D., & Meléndez, J. 2011, *ApJ*, **735**, L46+

Bensby, T., Feltzing, S., Johnson, J. A., Gould, A., Adén, D., Asplund, M., Meléndez, J., Gal-Yam, A., Lucatello, S., Sana, H., Sumi, T., Miyake, N., Suzuki, D., Han, C., Bond, I., & Udalski, A. 2010b, *A&A*, **512**, A41+

Bensby, T., Feltzing, S., & Lundström, I. 2003, *A&A*, **410**, 527

Bensby, T., Feltzing, S., & Lundström, I. 2004, *A&A*, **421**, 969

Bensby, T., Feltzing, S., Lundström, I., & Ilyin, I. 2005, *A&A*, **433**, 185

Bensby, T., Johnson, J. A., Cohen, J., Feltzing, S., Udalski, A., Gould, A., Huang, W., Thompson, I., Simmerer, J., & Adén, D. 2009, *A&A*, **499**, 737

Binney, J. & Merrifield, M. 1998, *Galactic Astronomy*, Princeton University Press

Binney, J. & Tremaine, S. 2008, *Galactic Dynamics: Second Edition*, Princeton University Press

Bird, J. C., Kazantzidis, S., & Weinberg, D. H. 2012, *MNRAS*, **420**, 913

Bochanski, J. J., Hawley, S. L., Covey, K. R., West, A. A., Reid, I. N., Golimowski, D. A., & Ivezić, Ž. 2010, *AJ*, **139**, 2679

Boesgaard, A. M., Jensen, E. E. C., & Deliyannis, C. P. 2009, *AJ*, **137**, 4949

Bournaud, F., Elmegreen, B. G., & Martig, M. 2009, *ApJ*, **707**, L1

Bovy, J., Rix, H.-W., Hogg, D. W., Beers, T. C., Lee, Y. S., & Zhang, L. 2012, *ArXiv e-prints*

Bovy, J., Rix, H.-W., Liu, C., Hogg, D. W., Beers, T. C., & Lee, Y. S. 2011, *ArXiv e-prints*

Bragaglia, A., Carretta, E., Gratton, R. G., Tosi, M., Bonanno, G., Bruno, P., Calì, A., Claudi, R., Cosentino, R., Desidera, S., Farisato, G., Rebeschini, M., & Scuderi, S. 2001, *AJ*, **121**, 327

Bragaglia, A., Sestito, P., Villanova, S., Carretta, E., Randich, S., & Tosi, M. 2008, *A&A*, **480**, 79

Brewer, M. & Carney, B. W. 2006, *AJ*, **131**, 431

Brook, C., Richard, S., Kawata, D., Martel, H., & Gibson, B. K. 2007, *ApJ*, **658**, 60

Brook, C. B., Gibson, B. K., Martel, H., & Kawata, D. 2005, *ApJ*, **630**, 298

Brook, C. B., Kawata, D., Gibson, B. K., & Freeman, K. C. 2004, *ApJ*, **612**, 894

Brooks, A. M., Governato, F., Quinn, T., Brook, C. B., & Wadsley, J. 2009, *ApJ*, **694**, 396

Brown, J. A., Wallerstein, G., Geisler, D., & Oke, J. B. 1996, *AJ*, **112**, 1551

Brunetti, M., Chiappini, C., & Pfenniger, D. 2010, *ArXiv e-prints*

Brunetti, M., Chiappini, C., & Pfenniger, D. 2011, *A&A*, **534**, A75

Busso, M., Gallino, R., & Wasserburg, G. J. 1999, *ARA&A*, **37**, 239

Caputo, F., Marconi, M., Musella, I., & Pont, F. 2001, *A&A*, **372**, 544

Carney, B. W., Yong, D., Teixera de Almeida, M. L., & Seitzer, P. 2005, *AJ*, **130**, 1111

Carollo, D., Beers, T. C., Chiba, M., Norris, J. E., Freeman, K. C., Lee, Y. S., Ivezić, Ž., Rockosi, C. M., & Yanny, B. 2010, *ApJ*, **712**, 692

Carraro, G., Bresolin, F., Villanova, S., Matteucci, F., Patat, F., & Romaniello, M. 2004, *AJ*, **128**, 1676

Carraro, G., de La Fuente Marcos, R., Villanova, S., Moni Bidin, C., de La Fuente Marcos, C., Baumgardt, H., & Solivella, G. 2007a, *A&A*, **466**, 931

Carraro, G., Geisler, D., Villanova, S., Frinchaboy, P. M., & Majewski, S. R. 2007b, *A&A*, **476**, 217

Carraro, G., Villanova, S., Demarque, P., McSwain, M. V., Piotto, G., & Bedin, L. R. 2006, *ApJ*, **643**, 1151

Carraro, G., Villanova, S., Demarque, P., Moni Bidin, C., & McSwain, M. V. 2008, *MNRAS*, **386**, 1625

Carrera, R. & Pancino, E. 2011, *A&A*, **535**, A30

Carretta, E., Bragaglia, A., & Gratton, R. G. 2007, *A&A*, **473**, 129

Carretta, E., Bragaglia, A., Gratton, R. G., & Tosi, M. 2004, *A&A*, **422**, 951

Carretta, E., Bragaglia, A., Gratton, R. G., & Tosi, M. 2005, *A&A*, **441**, 131

Casagrande, L., Ramírez, I., Meléndez, J., Bessell, M., & Asplund, M. 2010, *A&A*, **512**, A54

Casagrande, L., Schönrich, R., Asplund, M., Cassisi, S., Ramírez, I., Meléndez, J., Bensby, T., & Feltzing, S. 2011, *A&A*, **530**, A138+

Castelli, F. & Kurucz, R. L. 2003, in N. Piskunov, W. W. Weiss, & D. F. Gray (ed.), *Modelling of Stellar Atmospheres*, Vol. 210 of *IAU Symposium*, p. 20P

Cescutti, G., Matteucci, F., François, P., & Chiappini, C. 2007, *A&A*, **462**, 943

Chabrier, G. 2001, *ApJ*, **554**, 1274

Chang, C.-K., Ko, C.-M., & Peng, T.-H. 2011, *ApJ*, **740**, 34

Chen, L., Hou, J. L., & Wang, J. J. 2003, *AJ*, **125**, 1397

Cheng, J. Y., Rockosi, C. M., Morrison, H. L., Lee, Y. S., Beers, T. C., Bizyaev, D., Harding, P., Malanushenko, E., Malanushenko, V., Oravetz, D., Pan, K., Schlesinger, K. J., Schneider, D. P., Simmons, A., & Weaver, B. A. 2012a, *ApJ*, **752**, 51, Chapter 3

Cheng, J. Y., Rockosi, C. M., Morrison, H. L., Schönrich, R. A., Lee, Y. S., Beers, T. C., Bizyaev, D., Pan, K., & Schneider, D. P. 2012b, *ApJ*, **746**, 149, Chapter 2

Chiappini, C., Matteucci, F., & Gratton, R. 1997, *ApJ*, **477**, 765

Chiappini, C., Matteucci, F., & Romano, D. 2001, *ApJ*, **554**, 1044

Chiba, M. & Beers, T. C. 2000, *AJ*, **119**, 2843

Colucci, J. E., Bernstein, R. A., Cameron, S. A., & McWilliam, A. 2012, *ApJ*, **746**, 29

Cresci, G., Mannucci, F., Maiolino, R., Marconi, A., Gnerucci, A., & Magrini, L. 2010, *Nature*, **467**, 811

Dalcanton, J. J. & Bernstein, R. A. 2002, *AJ*, **124**, 1328

de Jong, J. T. A., Yanny, B., Rix, H., Dolphin, A. E., Martin, N. F., & Beers, T. C. 2010, *ApJ*, **714**, 663

De Silva, G. M., Freeman, K. C., Asplund, M., Bland-Hawthorn, J., Bessell, M. S., & Collet, R. 2007, *AJ*, **133**, 1161

Dekel, A., Sari, R., & Ceverino, D. 2009, *ApJ*, **703**, 785

Delbouille, L., Roland, G., & Neven, L. 1973, *Atlas photometrique DU spectre solaire de [lambda] 3000 a [lambda] 10000*

Di Matteo, P., Lehnert, M. D., Qu, Y., & van Driel, W. 2011, *A&A*, **525**, L3+

Dierickx, M., Klement, R., Rix, H.-W., & Liu, C. 2010, *ApJ*, **725**, L186

Dong, R., Gunn, J., Knapp, G., Rockosi, C., & Blanton, M. 2011, *AJ*, **142**, 116

Dotter, A., Chaboyer, B., Jevremović, D., Kostov, V., Baron, E., & Ferguson, J. W. 2008, *ApJS*, **178**, 89

Edvardsson, B., Andersen, J., Gustafsson, B., Lambert, D. L., Nissen, P. E., & Tomkin, J. 1993, *A&A*, **275**, 101

Edvardsson, B., Pettersson, B., Kharrazi, M., & Westerlund, B. 1995, *A&A*, **293**, 75

Eisenstein, D. J., Weinberg, D. H., Agol, E., Aihara, H., Allende Prieto, C., Anderson, S. F., Arns, J. A., Aubourg, É., Bailey, S., Balbinot, E., & et al. 2011, *AJ*, **142**, 72

Elmegreen, B. G. & Elmegreen, D. M. 2005, *ApJ*, **627**, 632

Elmegreen, B. G. & Elmegreen, D. M. 2006, *ApJ*, **650**, 644

Feltzing, S., Holmberg, J., & Hurley, J. R. 2001, *A&A*, **377**, 911

Fitzpatrick, M. J. & Sneden, C. 1987, in *Bulletin of the American Astronomical Society*, Vol. 19 of *Bulletin of the American Astronomical Society*, p. 1129

Ford, A., Jeffries, R. D., & Smalley, B. 2005, *MNRAS*, **364**, 272

Förster Schreiber, N. M., Genzel, R., Bouché, N., Cresci, G., Davies, R., Buschkamp, P., Shapiro, K., Tacconi, L. J., Hicks, E. K. S., Genel, S., Shapley, A. E., Erb, D. K., Steidel, C. C., Lutz, D., Eisenhauer, F., Gillessen, S., Sternberg, A., Renzini, A., Cimatti, A., Daddi, E., Kurk, J., Lilly, S., Kong, X., Lehnert, M. D., Nesvadba, N., Verma, A., McCracken, H., Arimoto, N., Mignoli, M., & Onodera, M. 2009, *ApJ*, **706**, 1364

Förster Schreiber, N. M., Shapley, A. E., Erb, D. K., Genzel, R., Steidel, C. C., Bouché, N., Cresci, G., & Davies, R. 2011, *ApJ*, **731**, 65

Freeman, K. & Bland-Hawthorn, J. 2002, *ARA&A*, **40**, 487

Freudenreich, H. T. 1998, *ApJ*, **492**, 495

Friedli, D., Benz, W., & Kennicutt, R. 1994, *ApJ*, **430**, L105

Friel, E. D. & Boesgaard, A. M. 1992, *ApJ*, **387**, 170

Friel, E. D., Jacobson, H. R., Barrett, E., Fullton, L., Balachandran, S. C., & Pilachowski, C. A. 2003, *AJ*, **126**, 2372

Friel, E. D., Jacobson, H. R., & Pilachowski, C. A. 2005, *AJ*, **129**, 2725

Friel, E. D., Jacobson, H. R., & Pilachowski, C. A. 2010, *AJ*, **139**, 1942

Friel, E. D., Janes, K. A., Tavarez, M., Scott, J., Katsanis, R., Lotz, J., Hong, L., & Miller, N. 2002, *AJ*, **124**, 2693

Frinchaboy, P. M., Marino, A. F., Villanova, S., Carraro, G., Majewski, S. R., & Geisler, D. 2008, *MNRAS*, **391**, 39

Fukugita, M., Ichikawa, T., Gunn, J. E., Doi, M., Shimasaku, K., & Schneider, D. P. 1996, *AJ*, **111**, 1748

Gallagher, A. J., Ryan, S. G., García Pérez, A. E., & Aoki, W. 2010, *A&A*, **523**, A24

Gilmore, G. & Reid, N. 1983, *MNRAS*, **202**, 1025

Gilmore, G., Wyse, R. F. G., & Jones, J. B. 1995, *AJ*, **109**, 1095

Girardi, L., Grebel, E. K., Odenkirchen, M., & Chiosi, C. 2004, *A&A*, **422**, 205

Goetz, M. & Koeppen, J. 1992, *A&A*, **262**, 455

Gonzalez, O. A., Rejkuba, M., Zoccali, M., Hill, V., Battaglia, G., Babusiaux, C., Minniti, D., Barbuy, B., Alves-Brito, A., Renzini, A., Gomez, A., & Ortolani, S. 2011, *A&A*, **530**, A54+

Gratton, R. G., Carretta, E., Eriksson, K., & Gustafsson, B. 1999, *A&A*, **350**, 955

Gratton, R. G., Carretta, E., Matteucci, F., & Sneden, C. 2000, *A&A*, **358**, 671

Gratton, R. G. & Contarini, G. 1994, *A&A*, **283**, 911

Grevesse, N. & Sauval, A. J. 1998, *Space Sci. Rev.*, **85**, 161

Guedes, J., Callegari, S., Madau, P., & Mayer, L. 2011, *ApJ*, **742**, 76

Gunn, J. E., Carr, M., Rockosi, C., Sekiguchi, M., Berry, K., Elms, B., de Haas, E., Ivezić, Ž., Knapp, G., Lupton, R., Pauls, G., Simcoe, R., Hirsch, R., Sanford, D., Wang, S., York, D., Harris, F., Annis, J., Bartozek, L., Boroski, W., Bakken, J., Haldeman, M., Kent, S., Holm, S., Holmgren, D., Petravick, D., Prosapio, A., Rechenmacher, R., Doi, M., Fukugita, M., Shimasaku, K., Okada, N., Hull, C., Siegmund, W., Mannery, E., Blouke, M., Heidtman, D., Schneider, D., Lucinio, R., & Brinkman, J. 1998, *AJ*, **116**, 3040

Gunn, J. E., Siegmund, W. A., Mannery, E. J., Owen, R. E., Hull, C. L., Leger, R. F., Carey, L. N., Knapp, G. R., York, D. G., Boroski, W. N., Kent, S. M., Lupton, R. H., Rockosi, C. M., Evans, M. L., Waddell, P., Anderson, J. E., Annis, J., Barentine, J. C., Bartoszek, L. M., Bastian, S., Bracker, S. B., Brewington, H. J., Briegel, C. I., Brinkmann, J., Brown, Y. J., Carr, M. A., Czarapata, P. C., Drennan, C. C., Dombeck, T., Federwitz, G. R., Gillespie, B. A., Gonzales, C., Hansen, S. U., Harvanek, M., Hayes, J., Jordan, W., Kinney, E., Klaene, M., Kleinman, S. J., Kron, R. G., Kresinski, J., Lee, G., Limmongkol, S., Lindenmeyer, C. W., Long, D. C., Loomis, C. L., McGehee, P. M., Mantsch, P. M., Neilsen, Jr., E. H., Neswold, R. M., Newman, P. R., Nitta, A., Peoples, Jr., J., Pier, J. R., Prieto, P. S., Prosapio, A., Rivetta, C., Schneider, D. P., Snedden, S., & Wang, S.-i. 2006, *AJ*, **131**, 2332

Hayashi, H. & Chiba, M. 2006, *PASJ*, **58**, 835

Haywood, M. 2008, *MNRAS*, **388**, 1175

Hernquist, L. & Weinberg, M. D. 1992, *ApJ*, **400**, 80

Hobbs, L. M. & Thorburn, J. A. 1992, *AJ*, **104**, 669

Humphreys, R. M., Beers, T. C., Cabanela, J. E., Grammer, S., Davidson, K., Lee, Y. S., & Larsen, J. A. 2011, *AJ*, **141**, 131

Ibata, R., Irwin, M., Lewis, G., Ferguson, A. M. N., & Tanvir, N. 2001, *Nature*, **412**, 49

Ivezić, Ž., Sesar, B., Jurić, M., Bond, N., Dalcanton, J., Rockosi, C. M., Yanny, B., Newberg, H. J., Beers, T. C., Allende Prieto, C., Wilhelm, R., Lee, Y. S., Sivarani, T., Norris, J. E., Bailer-Jones, C. A. L., Re Fiorentin, P., Schlegel, D., Uomoto, A., Lupton, R. H., Knapp, G. R., Gunn, J. E., Covey, K. R., Smith, J. A., Miknaitis, G., Doi, M., Tanaka, M., Fukugita, M., Kent, S., Finkbeiner, D., Munn, J. A., Pier, J. R., Quinn, T., Hawley, S., Anderson, S., Kiuchi, F., Chen, A., Bushong, J., Sohi, H., Haggard, D., Kimball, A., Barentine, J., Brewington, H., Harvanek, M., Kleinman, S., Krzesinski, J., Long, D., Nitta, A., Snedden, S., Lee, B., Harris, H., Brinkmann, J., Schneider, D. P., & York, D. G. 2008, *ApJ*, **684**, 287

Jacobson, H. R., Friel, E. D., & Pilachowski, C. A. 2007, *AJ*, **134**, 1216

Jacobson, H. R., Friel, E. D., & Pilachowski, C. A. 2008, *AJ*, **135**, 2341

Jacobson, H. R., Friel, E. D., & Pilachowski, C. A. 2009, *AJ*, **137**, 4753

Jacobson, H. R., Friel, E. D., & Pilachowski, C. A. 2011a, *AJ*, **141**, 58

Jacobson, H. R., Pilachowski, C. A., & Friel, E. D. 2011b, *AJ*, **142**, 59

Jenkins, A. 1992, *MNRAS*, **257**, 620

Jenkins, A. & Binney, J. 1990, *MNRAS*, **245**, 305

Jurić, M., Ivezić, Ž., Brooks, A., Lupton, R. H., Schlegel, D., Finkbeiner, D., Padmanabhan, N., Bond, N., Sesar, B., Rockosi, C. M., Knapp, G. R., Gunn, J. E., Sumi, T., Schneider, D. P., Barentine, J. C., Brewington, H. J., Brinkmann, J., Fukugita, M., Harvanek, M., Kleinman, S. J., Krzesinski, J., Long, D., Neilsen, Jr., E. H., Nitta, A., Snedden, S. A., & York, D. G. 2008, *ApJ*, **673**, 864

Katz, D., Soubiran, C., Cayrel, R., Barbuy, B., Friel, E., Bienaymé, O., & Perrin, M.-N. 2011, *A&A*, **525**, A90+

Kazantzidis, S., Bullock, J. S., Zentner, A. R., Kravtsov, A. V., & Moustakas, L. A. 2008, *ApJ*, **688**, 254

Kazantzidis, S., Zentner, A. R., Kravtsov, A. V., Bullock, J. S., & Debattista, V. P. 2009, *ApJ*, **700**, 1896

Kent, S. M., Dame, T. M., & Fazio, G. 1991, *ApJ*, **378**, 131

Kilic, M., Munn, J. A., Harris, H. C., Liebert, J., von Hippel, T., Williams, K. A., Metcalfe, T. S., Winget, D. E., & Levine, S. E. 2006, *AJ*, **131**, 582

Kirby, E. N. 2011, *PASP*, **123**, 531

Kirby, E. N., Cohen, J. G., Smith, G. H., Majewski, S. R., Sohn, S. T., & Guhathakurta, P. 2011, *ApJ*, **727**, 79

Kirby, E. N., Simon, J. D., Geha, M., Guhathakurta, P., & Frebel, A. 2008, *ApJ*, **685**, L43

Kobayashi, C. & Nakasato, N. 2011, *ApJ*, **729**, 16

Krumholz, M. & Burkert, A. 2010, *ApJ*, **724**, 895

Krumholz, M. R. & Dekel, A. 2010, *MNRAS*, **406**, 112

Kurucz, R. 1993, *ATLAS9 Stellar Atmosphere Programs and 2 km/s grid. Kurucz CD-ROM No. 13. Cambridge, Mass.: Smithsonian Astrophysical Observatory, 1993.*, 13

Lacey, C. G. & Fall, S. M. 1985, *ApJ*, **290**, 154

Lai, D. K., Bolte, M., Johnson, J. A., Lucatello, S., Heger, A., & Woosley, S. E. 2008, *ApJ*, **681**, 1524

Lai, D. K., Smith, G. H., Bolte, M., Johnson, J. A., Lucatello, S., Kraft, R. P., & Sneden, C. 2011, *AJ*, **141**, 62

Larsen, J. A., Cabanela, J. E., & Humphreys, R. M. 2011, *AJ*, **141**, 130

Larsen, J. A., Cabanela, J. E., Humphreys, R. M., & Haviland, A. P. 2010, *AJ*, **139**, 348

Larson, R. B. 1976, *MNRAS*, **176**, 31

Lawler, J. E., Bonvallet, G., & Sneden, C. 2001, *ApJ*, **556**, 452

Lee, Y. S., Beers, T. C., Allende Prieto, C., Lai, D. K., Rockosi, C. M., Morrison, H. L., Johnson, J. A., An, D., Sivarani, T., & Yanny, B. 2011a, *AJ*, **141**, 90

Lee, Y. S., Beers, T. C., An, D., Ivezić, Ž., Just, A., Rockosi, C. M., Morrison, H. L., Johnson, J. A., Schönrich, R., Bird, J., Yanny, B., Harding, P., & Rocha-Pinto, H. J. 2011b, *ApJ*, **738**, 187

Lee, Y. S., Beers, T. C., Sivarani, T., Allende Prieto, C., Koesterke, L., Wilhelm, R., Re Fiorentin, P., Bailer-Jones, C. A. L., Norris, J. E., Rockosi, C. M., Yanny, B., Newberg, H. J., Covey, K. R., Zhang, H., & Luo, A. 2008a, *AJ*, **136**, 2022

Lee, Y. S., Beers, T. C., Sivarani, T., Johnson, J. A., An, D., Wilhelm, R., Allende Prieto, C., Koesterke, L., Re Fiorentin, P., Bailer-Jones, C. A. L., Norris, J. E., Yanny, B., Rockosi, C., Newberg, H. J., Cudworth, K. M., & Pan, K. 2008b, *AJ*, **136**, 2050

Lemasle, B., François, P., Piersimoni, A., Pedicelli, S., Bono, G., Laney, C. D., Primas, F., & Romaniello, M. 2008, *A&A*, **490**, 613

Lewis, J. R. & Freeman, K. C. 1989, *AJ*, **97**, 139

Loebman, S. R., Roškar, R., Debattista, V. P., Ivezić, Ž., Quinn, T. R., & Wadsley, J. 2011, *ApJ*, **737**, 8

Luck, R. E., Gieren, W. P., Andrievsky, S. M., Kovtyukh, V. V., Fouqué, P., Pont, F., & Kienzle, F. 2003, *A&A*, **401**, 939

Luck, R. E., Kovtyukh, V. V., & Andrievsky, S. M. 2006, *AJ*, **132**, 902

Luck, R. E. & Lambert, D. L. 2011, *AJ*, **142**, 136

Maciel, W. J., Lago, L. G., & Costa, R. D. D. 2005, *A&A*, **433**, 127

Magrini, L., Randich, S., Zoccali, M., Jilkova, L., Carraro, G., Galli, D., Maiorca, E., & Busso, M. 2010, *A&A*, **523**, A11+

Magrini, L., Sestito, P., Randich, S., & Galli, D. 2009, *A&A*, **494**, 95

Martin, P. & Roy, J.-R. 1994, *ApJ*, **424**, 599

Martínez-Delgado, D., Gabany, R. J., Crawford, K., Zibetti, S., Majewski, S. R., Rix, H.-W., Fliri, J., Carballo-Bello, J. A., Bardalez-Gagliuffi, D. C., Peñarrubia, J., Chonis, T. S., Madore, B., Trujillo, I., Schirmer, M., & McDavid, D. A. 2010, *AJ*, **140**, 962

Martínez-Serrano, F. J., Serna, A., Doménech-Moral, M., & Domínguez-Tenreiro, R. 2009, *ApJ*, **705**, L133

Mashonkina, L. & Gehren, T. 2000, *A&A*, **364**, 249

Mashonkina, L. & Gehren, T. 2001, *A&A*, **376**, 232

Mashonkina, L., Gehren, T., Travaglio, C., & Borkova, T. 2003, *A&A*, **397**, 275

Matteucci, F. & Francois, P. 1989, *MNRAS*, **239**, 885

McWilliam, A. 1997, *ARA&A*, **35**, 503

Meléndez, J., Asplund, M., Alves-Brito, A., Cunha, K., Barbuy, B., Bessell, M. S., Chiappini, C., Freeman, K. C., Ramírez, I., Smith, V. V., & Yong, D. 2008, *A&A*, **484**, L21

Mikolaitis, Š., Tautvaišienė, G., Gratton, R., Bragaglia, A., & Carretta, E. 2011, *MNRAS*, **416**, 1092

Minchev, I. & Famaey, B. 2010, *ApJ*, **722**, 112

Munn, J. A., Monet, D. G., Levine, S. E., Canzian, B., Pier, J. R., Harris, H. C., Lupton, R. H., Ivezić, Ž., Hindsley, R. B., Hennessy, G. S., Schneider, D. P., & Brinkmann, J. 2004, *AJ*, **127**, 3034

Newberg, H. J., Yanny, B., Rockosi, C., Grebel, E. K., Rix, H., Brinkmann, J., Csabai, I., Hennessy, G., Hindsley, R. B., Ibata, R., Ivezić, Z., Lamb, D., Nash, E. T., Odenkirchen, M., Rave, H. A., Schneider, D. P., Smith, J. A., Stolte, A., & York, D. G. 2002, *ApJ*, **569**, 245

Nordström, B., Mayor, M., Andersen, J., Holmberg, J., Pont, F., Jørgensen, B. R., Olsen, E. H., Udry, S., & Mowlavi, N. 2004, *A&A*, **418**, 989

Origlia, L., Valenti, E., Rich, R. M., & Ferraro, F. R. 2006, *ApJ*, **646**, 499

Pace, G., Pasquini, L., & François, P. 2008, *A&A*, **489**, 403

Pancino, E., Carrera, R., Rossetti, E., & Gallart, C. 2010, *A&A*, **511**, A56+

Parker, J. E., Humphreys, R. M., & Beers, T. C. 2004, *AJ*, **127**, 1567

Pedicelli, S., Bono, G., Lemasle, B., François, P., Groenewegen, M., Lub, J., Pel, J. W., Laney, D., Piersimoni, A., Romaniello, M., Buonanno, R., Caputo, F., Cassisi, S., Castelli, F., Leurini, S., Pietrinferni, A., Primas, F., & Pritchard, J. 2009, *A&A*, **504**, 81

Peterson, R. C. & Green, E. M. 1998, *ApJ*, **502**, L39

Pignatari, M., Gallino, R., Heil, M., Wiescher, M., Käppeler, F., Herwig, F., & Bisterzo, S. 2010, *ApJ*, **710**, 1557

Portinari, L. & Chiosi, C. 2000, *A&A*, **355**, 929

Prantzos, N. & Boissier, S. 2000, *MNRAS*, **313**, 338

Prochaska, J. X., Naumov, S. O., Carney, B. W., McWilliam, A., & Wolfe, A. M. 2000, *AJ*, **120**, 2513

Purcell, C. W., Kazantzidis, S., & Bullock, J. S. 2009, *ApJ*, **694**, L98

Randich, S., Sestito, P., & Pallavicini, R. 2003, *A&A*, **399**, 133

Randich, S., Sestito, P., Primas, F., Pallavicini, R., & Pasquini, L. 2006, *A&A*, **450**, 557

Read, J. I., Lake, G., Agertz, O., & Debattista, V. P. 2008, *MNRAS*, **389**, 1041

Reddy, B. E. & Lambert, D. L. 2008, *MNRAS*, **391**, 95

Reddy, B. E., Lambert, D. L., & Allende Prieto, C. 2006, *MNRAS*, **367**, 1329

Reddy, B. E., Tomkin, J., Lambert, D. L., & Allende Prieto, C. 2003, *MNRAS*, **340**, 304

Reid, I. N., Gizis, J. E., & Hawley, S. L. 2002, *AJ*, **124**, 2721

Roškar, R., Debattista, V. P., Quinn, T. R., Stinson, G. S., & Wadsley, J. 2008a, *ApJ*, **684**, L79

Roškar, R., Debattista, V. P., Stinson, G. S., Quinn, T. R., Kaufmann, T., & Wadsley, J. 2008b, *ApJ*, **675**, L65

Ruchti, G. R., Fulbright, J. P., Wyse, R. F. G., Gilmore, G. F., Bienaymé, O., Binney, J., Bland-Hawthorn, J., Campbell, R., Freeman, K. C., Gibson, B. K., Grebel, E. K., Helmi, A., Munari, U., Navarro, J. F., Parker, Q. A., Reid, W., Seabroke, G. M., Siebert, A., Siviero, A., Steinmetz, M., Watson, F. G., Williams, M., & Zwitter, T. 2010, *ApJ*, **721**, L92

Ruchti, G. R., Fulbright, J. P., Wyse, R. F. G., Gilmore, G. F., Bienaymé, O., Bland-Hawthorn, J., Gibson, B. K., Grebel, E. K., Helmi, A., Munari, U., Navarro, J. F., Parker, Q. A., Reid, W., Seabroke, G. M., Siebert, A., Siviero, A., Steinmetz, M., Watson, F. G., Williams, M., & Zwitter, T. 2011, *ApJ*, **737**, 9

Ryde, N., Gustafsson, B., Edvardsson, B., Meléndez, J., Alves-Brito, A., Asplund, M., Barbuy, B., Hill, V., Käufl, H. U., Minniti, D., Ortolani, S., Renzini, A., & Zoccali, M. 2010, *A&A*, **509**, A20+

Sales, L. V., Helmi, A., Abadi, M. G., Brook, C. B., Gómez, F. A., Roškar, R., Debattista, V. P., House, E., Steinmetz, M., & Villalobos, Á. 2009, *MNRAS*, **400**, L61

Sánchez-Blázquez, P., Courty, S., Gibson, B. K., & Brook, C. B. 2009, *MNRAS*, **398**, 591

Santos, N. C., Lovis, C., Pace, G., Melendez, J., & Naef, D. 2009, *A&A*, **493**, 309

Sbordone, L., Bonifacio, P., Buonanno, R., Marconi, G., Monaco, L., & Zaggia, S. 2007, *A&A*, **465**, 815

Schlegel, D. J., Finkbeiner, D. P., & Davis, M. 1998, *ApJ*, **500**, 525

Schönrich, R. & Binney, J. 2009a, *MNRAS*, **396**, 203

Schönrich, R. & Binney, J. 2009b, *MNRAS*, **399**, 1145

Schwarzkopf, U. & Dettmar, R. 2000, *A&A*, **361**, 451

Sellwood, J. A. & Binney, J. J. 2002, *MNRAS*, **336**, 785

Sestito, P., Bragaglia, A., Randich, S., Carretta, E., Prisinzano, L., & Tosi, M. 2006, *A&A*, **458**, 121

Sestito, P., Bragaglia, A., Randich, S., Pallavicini, R., Andrievsky, S. M., & Korotin, S. A. 2008, *A&A*, **488**, 943

Sestito, P., Randich, S., & Bragaglia, A. 2007, *A&A*, **465**, 185

Sestito, P., Randich, S., & Pallavicini, R. 2004, *A&A*, **426**, 809

Siegel, M. H., Majewski, S. R., Reid, I. N., & Thompson, I. B. 2002, *ApJ*, **578**, 151

Smiljanic, R., Gauderon, R., North, P., Barbuy, B., Charbonnel, C., & Mowlavi, N. 2009, *A&A*, **502**, 267

Smolinski, J. P., Lee, Y. S., Beers, T. C., An, D., Bickerton, S. J., Johnson, J. A., Loomis, C. P., Rockosi, C. M., Sivarani, T., & Yanny, B. 2011, *AJ*, **141**, 89

Sneden, C., Cowan, J. J., & Gallino, R. 2008, *ARA&A*, **46**, 241

Sneden, C., Kraft, R. P., Prosser, C. F., & Langer, G. E. 1991, *AJ*, **102**, 2001

Sobeck, J. S., Kraft, R. P., Sneden, C., Preston, G. W., Cowan, J. J., Smith, G. H., Thompson, I. B., Shectman, S. A., & Burley, G. S. 2011, *AJ*, **141**, 175

Soubiran, C., Bienaymé, O., & Siebert, A. 2003, *A&A*, **398**, 141

Spagna, A., Lattanzi, M. G., Re Fiorentin, P., & Smart, R. L. 2010, *A&A*, **510**, L4

Spitoni, E. & Matteucci, F. 2011, *A&A*, **531**, A72+

Stanghellini, L. & Haywood, M. 2010, *ApJ*, **714**, 1096

Steinmetz, M., Zwitter, T., Siebert, A., Watson, F. G., Freeman, K. C., Munari, U., Campbell, R., Williams, M., Seabroke, G. M., Wyse, R. F. G., Parker, Q. A., Bienaymé, O., Roeser, S., Gibson, B. K., Gilmore, G., Grebel, E. K., Helmi, A., Navarro, J. F., Burton, D., Cass, C. J. P., Dawe, J. A., Fiegert, K., Hartley, M., Russell, K. S., Saunders, W., Enke, H., Bailin, J., Binney, J., Bland-Hawthorn, J., Boeche, C., Dehnen, W., Eisenstein, D. J., Evans, N. W., Fiorucci, M., Fulbright, J. P., Gerhard, O., Jauregi, U., Kelz, A., Mijović, L., Minchev, I., Parmentier, G., Peñarrubia, J., Quillen, A. C., Read, M. A., Ruchti, G., Scholz, R.-D., Siviero, A., Smith, M. C., Sordo, R., Veltz, L., Vidrih, S., von Berlepsch, R., Boyle, B. J., & Schilbach, E. 2006, *AJ*, **132**, 1645

Stewart, K. R., Bullock, J. S., Wechsler, R. H., Maller, A. H., & Zentner, A. R. 2008, *ApJ*, **683**, 597

Stinson, G. S., Bailin, J., Couchman, H., Wadsley, J., Shen, S., Nickerson, S., Brook, C., & Quinn, T. 2010, *MNRAS*, **408**, 812

Tautvaišiene, G., Edvardsson, B., Tuominen, I., & Ilyin, I. 2000, *A&A*, **360**, 499

Thielemann, F.-K., Nomoto, K., & Yokoi, K. 1986, *A&A*, **158**, 17

Timmes, F. X., Woosley, S. E., & Weaver, T. A. 1995, *ApJS*, **98**, 617

Tinsley, B. M. 1979, *ApJ*, **229**, 1046

Tolstoy, E., Hill, V., & Tosi, M. 2009, *ARA&A*, **47**, 371

Twarog, B. A., Ashman, K. M., & Anthony-Twarog, B. J. 1997, *AJ*, **114**, 2556

Udry, S., Mayor, M., Maurice, E., Andersen, J., Imbert, M., Lindgren, H., Mermilliod, J.-C., Nordström, B., & Prévot, L. 1999a, in J. B. Hearnshaw & C. D. Scarfe (ed.), *IAU Colloq. 170: Precise Stellar Radial Velocities*, Vol. 185 of *Astronomical Society of the Pacific Conference Series*, p. 383

Udry, S., Mayor, M., & Queloz, D. 1999b, in J. B. Hearnshaw & C. D. Scarfe (ed.), *IAU Colloq. 170: Precise Stellar Radial Velocities*, Vol. 185 of *Astronomical Society of the Pacific Conference Series*, p. 367

Venn, K. A., Irwin, M., Shetrone, M. D., Tout, C. A., Hill, V., & Tolstoy, E. 2004, *AJ*, **128**, 1177

Villalobos, Á. & Helmi, A. 2008, *MNRAS*, **391**, 1806

Villanova, S., Baume, G., & Carraro, G. 2007, *MNRAS*, **379**, 1089

Villanova, S., Carraro, G., Bresolin, F., & Patat, F. 2005, *AJ*, **130**, 652

Villanova, S., Geisler, D., & Piotto, G. 2010, *ApJ*, **722**, L18

Vogt, S. S., Allen, S. L., Bigelow, B. C., Bresee, L., Brown, B., Cantrall, T., Conrad, A., Couture, M., Delaney, C., Epps, H. W., Hilyard, D., Hilyard, D. F., Horn, E., Jern, N., Kanto, D., Keane, M. J., Kibrick, R. I., Lewis, J. W., Osborne, J., Pardeilhan, G. H., Pfister, T., Ricketts, T., Robinson, L. B., Stover, R. J., Tucker, D., Ward, J., & Wei, M. Z. 1994, in D. L. Crawford & E. R. Craine (ed.), *Society of Photo-Optical Instrumentation Engineers (SPIE) Conference Series*, Vol. 2198 of *Society of Photo-Optical Instrumentation Engineers (SPIE) Conference Series*, pp 362–+

Wilson, M. L., Helmi, A., Morrison, H. L., Breddels, M. A., Bienaymé, O., Binney, J., Bland-Hawthorn, J., Campbell, R., Freeman, K. C., Fulbright, J. P., Gibson, B. K., Gilmore, G., Grebel, E. K., Munari, U., Navarro, J. F., Parker, Q. A., Reid, W., Seabroke, G., Siebert, A., Siviero, A., Steinmetz, M., Williams, M. E. K., Wyse, R. F. G., & Zwitter, T. 2011, *MNRAS*, **413**, 2235

Woosley, S. E., Heger, A., & Weaver, T. A. 2002, *Reviews of Modern Physics*, **74**, 1015

Woosley, S. E. & Weaver, T. A. 1995, *ApJS*, **101**, 181

Yanny, B., Rockosi, C., Newberg, H. J., Knapp, G. R., Adelman-McCarthy, J. K., Alcorn, B., Allam, S., Allende Prieto, C., An, D., Anderson, K. S. J., Anderson, S., Bailer-Jones, C. A. L., Bastian, S., Beers, T. C., Bell, E., Belokurov, V., Bizyaev, D., Blythe, N., Bochanski, J. J., Boroski, W. N., Brinchmann, J., Brinkmann, J., Brewington, H., Carey, L., Cudworth, K. M., Evans, M., Evans, N. W., Gates, E., Gänsicke, B. T., Gillespie, B., Gilmore, G., Gomez-Moran, A. N., Grebel, E. K., Greenwell, J., Gunn, J. E., Jordan, C., Jordan, W., Harding, P., Harris, H., Hendry, J. S., Holder, D., Ivans, I. I., Ivezič, Ž., Jester, S., Johnson, J. A., Kent, S. M., Kleinman, S., Kniazev, A., Krzesinski, J., Kron, R., Kuropatkin, N., Lebedeva, S., Lee, Y. S., Leger, R. F., Lépine, S., Levine, S., Lin, H., Long, D. C., Loomis, C., Lupton, R., Malanushenko, O., Malanushenko, V., Margon, B., Martinez-Delgado, D., McGehee, P., Monet, D., Morrison, H. L., Munn, J. A., Neilsen, E. H., Nitta, A., Norris, J. E., Oravetz, D., Owen, R., Padmanabhan, N., Pan, K., Peterson, R. S., Pier, J. R., Platson, J., Fiorentin, P. R., Richards, G. T., Rix, H., Schlegel, D. J., Schneider, D. P., Schreiber, M. R., Schwope, A., Sibley, V., Simmons, A., Snedden, S. A., Smith, J. A., Stark, L., Stauffer, F., Steinmetz, M., Stoughton, C., Subba Rao, M., Szalay, A., Szkody, P., Thakar, A. R., Thirupathi, S., Tucker, D., Uomoto, A., Vanden Berk, D., Vidrih, S., Wadadekar, Y., Watters, S., Wilhelm, R., Wyse, R. F. G., Yarger, J., & Zucker, D. 2009, *AJ*, **137**, 4377

Yoachim, P. & Dalcanton, J. J. 2005, *ApJ*, **624**, 701

Yoachim, P. & Dalcanton, J. J. 2006, *AJ*, **131**, 226

Yoachim, P. & Dalcanton, J. J. 2008a, *ApJ*, **683**, 707

Yoachim, P. & Dalcanton, J. J. 2008b, *ApJ*, **682**, 1004

Yong, D., Carney, B. W., & Teixera de Almeida, M. L. 2005, *AJ*, **130**, 597

Yong, D., Carney, B. W., Teixera de Almeida, M. L., & Pohl, B. L. 2006, *AJ*, **131**, 2256

York, D. G., Adelman, J., Anderson, Jr., J. E., Anderson, S. F., Annis, J., Bahcall, N. A., Bakken, J. A., Barkhouser, R., Bastian, S., Berman, E., Boroski, W. N., Bracker, S., Briegel, C., Briggs, J. W., Brinkmann, J., Brunner, R., Burles, S., Carey, L., Carr, M. A., Castander, F. J., Chen, B., Colestock, P. L., Connolly, A. J., Crocker, J. H., Csabai, I., Czarapata, P. C., Davis, J. E., Doi, M., Dombeck, T., Eisenstein, D., Ellman, N., Elms, B. R., Evans, M. L., Fan, X., Federwitz, G. R., Fiscelli, L., Friedman, S., Frieman, J. A., Fukugita, M., Gillespie, B., Gunn, J. E., Gurbani, V. K., de Haas, E., Haldeman, M., Harris, F. H., Hayes, J., Heckman,

T. M., Hennessy, G. S., Hindsley, R. B., Holm, S., Holmgren, D. J., Huang, C.-h., Hull, C., Husby, D., Ichikawa, S.-I., Ichikawa, T., Ivezić, Ž., Kent, S., Kim, R. S. J., Kinney, E., Klaene, M., Kleinman, A. N., Kleinman, S., Knapp, G. R., Korienek, J., Kron, R. G., Kunszt, P. Z., Lamb, D. Q., Lee, B., Leger, R. F., Limmongkol, S., Lindenmeyer, C., Long, D. C., Loomis, C., Loveday, J., Lucinio, R., Lupton, R. H., MacKinnon, B., Mannery, E. J., Mantsch, P. M., Margon, B., McGehee, P., McKay, T. A., Meiksin, A., Merelli, A., Monet, D. G., Munn, J. A., Narayanan, V. K., Nash, T., Neilsen, E., Neswold, R., Newberg, H. J., Nichol, R. C., Nicinski, T., Nonino, M., Okada, N., Okamura, S., Ostriker, J. P., Owen, R., Pauls, A. G., Peoples, J., Peterson, R. L., Petravick, D., Pier, J. R., Pope, A., Pordes, R., Prosapio, A., Rechenmacher, R., Quinn, T. R., Richards, G. T., Richmond, M. W., Rivetta, C. H., Rockosi, C. M., Ruthmansdorfer, K., Sandford, D., Schlegel, D. J., Schneider, D. P., Sekiguchi, M., Sergey, G., Shimasaku, K., Siegmund, W. A., Smee, S., Smith, J. A., Snedden, S., Stone, R., Stoughton, C., Strauss, M. A., Stubbs, C., SubbaRao, M., Szalay, A. S., Szapudi, I., Szokoly, G. P., Thakar, A. R., Tremonti, C., Tucker, D. L., Uomoto, A., Vanden Berk, D., Vogeley, M. S., Waddell, P., Wang, S.-i., Watanabe, M., Weinberg, D. H., Yanny, B., & Yasuda, N. 2000, *AJ*, **120**, 1579

Yoshii, Y. 1982, *PASJ*, **34**, 365

Appendix A

Calculating Weights

As discussed in §2.4, we assign weights to each of the MSTO stars to reconstruct the properties of the underlying parent population. There are three major ways in which the spectroscopic sample is different from the full population along each line of sight: (1) the photometric objects in regions with the highest extinction were not considered for spectroscopy. (2) Not all candidates for spectroscopy are observed. (3) We observe only MSTO stars using a color cut which is biased against redder metal-rich stars.

Each star in our sample is given three weights which correspond with the three differences listed above: (1) the *area weight*, $W_{\rm A}$, which depends on the coverage on the plane of the sky in each line of sight; (2) the *CMD weight*, $W_{\rm CMD}$, which depends on the target's location in the CMD; (3) the *LF weight*, $W_{\rm LF}$, which depends on the target's $T_{\rm eff}$, [Fe/H], and location in the CMD. The total weight, W, is the product of the three weights $W_{\rm A}$, $W_{\rm CMD}$, and $W_{\rm LF}$.

A.1 Area Weight

The *area weight*, $W_{\rm A}$, corrects for the area not covered by the spectroscopic survey because the 25% most extincted photometric objects were not considered for spectroscopy. These

objects were removed using the cut described in steps 2 and 3 of §2.2.1. The right-hand panel of Figure 2.4 shows an example of how the missing area is distributed in the field. Since the missing area along each line of sight is slightly different, this weight is needed to ensure that every line of sight effectively probes the same volume of the Galaxy and has equal influence on the final gradient measurement. Since the dust is mainly in the foreground and our sample is primarily distant stars, we assume that the volume of the Galaxy behind the high-extinction patches is the same as the rest of the volume probed by stars along the same line of sight.

We use the extinction map of SFD98 to calculate the area with extinction lower than the cut. $W_{\rm A}$ is the ratio of the total area (7 deg^2) to the low-extinction area. We note that the angular resolution of the SFD98 maps is 6.1 arcmin, so that the most extincted regions are always in irregular, contiguous patches on the sky.

A.2 Color-Magnitude Weight

The *CMD weight*, $W_{\rm CMD}$, normalizes between the different lines of sight; while each field has roughly the same number of spectra, the total number of photometric objects varies a great deal due to the structure of the Galaxy. This weight also accounts for any uneven sampling due to the stochastic nature of the random selection of spectroscopic targets, especially at the faint and red limits, where targets are less likely to end up in our sample because they have low-quality spectra. We divide the CMD into bins of $g_{\rm SFD}$ and $(g-r)_{\rm SFD}$, as shown in Figure A.1 (black lines). We use the SFD98 colors and magnitudes because this is the CMD in which the $g-r$ cut was applied, meaning that the randomly selected spectra are an unbiased sample of the underlying CMD; this procedure does not depend on whether the SFD98 colors and magnitudes are correct. Since the sampling is a smooth function of color and magnitude and changes slowly, the bins are sufficiently small that we can assume the sampling is constant within each bin.

The magnitude bins are 0.5 mag wide and span the entire range of the sample. Because

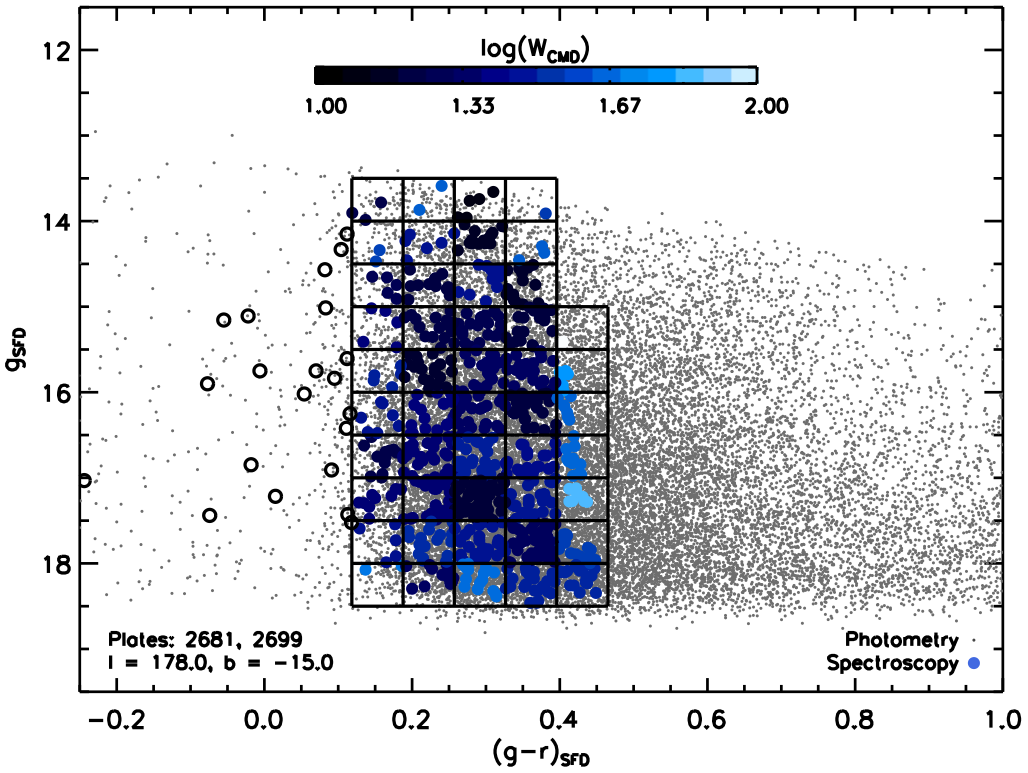

Figure A.1: Weighting for CMD sampling along one line of sight. For each bin (black lines) the CMD weight $W_{\rm CMD}$ is calculated by taking the ratio of the number of photometric (gray) to spectroscopic (blue) objects. Outliers bluer or redder than 2σ from the mean value of $(g-r)_{\rm SFD}$ are given a weight of zero (open circles). The values of $W_{\rm CMD}$ vary by less than a factor of 10, with the highest values in the reddest and faintest bins. This correction accounts for uneven sampling of the CMD, and provides the normalization for the variation in the number of objects between different lines of sight.

the CMD bins use corrections from SFD98, which can be affected by reddening, the color bins are different for each line of sight. To determine the color bins, we calculate the mean and standard deviation of the $(g-r)_{\rm SFD}$ colors of stars in each line of sight. Spectra with colors more than 2σ from the mean have $W_{\rm CMD}=0$; this removes 217 stars from the sample (open circles). Most of these are very blue objects (hotter stars that are likely not on the main sequence), although some red objects are removed as well. The remaining sample in the line of sight is divided into five equal-sized color bins. In each CMD bin, $W_{\rm CMD}$ is the ratio of the number of photometric objects (small gray dots) to the number of spectroscopic objects (blue circles) and is shown by

the color coding in Figure A.1. The highest values of $W_{\rm CMD}$ are found in the reddest and faintest bins, while the variation in the middle of CMD is relatively small. The difference between the smallest and largest values is less than a factor of 10.

A.3 Luminosity Function Weight

The *LF weight*, $W_{\rm LF}$, allows us to use the MSTO sample as tracers for the total underlying population. The CMD bins used to calculate $W_{\rm LF}$ use the isochrone extinction-corrected g_0 and $(g-r)_0$ (see §2.3) and are different than those used to calculate $W_{\rm CMD}$. For $W_{\rm CMD}$, we had to account for the random sampling from the total photometric sample using the SFD98 corrections, but for $W_{\rm LF}$, we use the isochrone extinction corrections because they provide the best estimates of the absolute magnitude and $g-r$ colors. The color bins are 0.1 mag wide in the range $0.05 < (g-r)_0 < 0.85$, while the magnitude bins are 0.5 mag wide in the range $12 < g_0 < 20$; these bins apply for all 11 lines of sight.

In each CMD bin, we find the fraction of the luminosity function that is observed in the given $(g-r)_0$ range. The weight is simply the reciprocal of the fraction. We use luminosity functions assuming a Chabrier (2001) lognormal initial mass function, generated by the Padova group (Girardi et al. 2004), where we have modified the faint end of the theoretical luminosity functions to more closely reflect the shapes of the luminosity functions for disk field stars reported by Reid et al. (2002) and Bochanski et al. (2010). The modifications are made at magnitudes fainter than the peak of the luminosity function. The luminosity function used depends on the age and metallicity of the target.

The derived values for $W_{\rm LF}$ are shown in Figure A.2 for the entire sample; each panel shows a different range in metallicity. For a given $(g-r)_0$ color, $W_{\rm LF}$ is roughly constant as a function of magnitude. Within a given color bin, the change in $W_{\rm LF}$ corresponds to different MSTOs for isochrones of different ages, which are assigned based on the temperatures of the

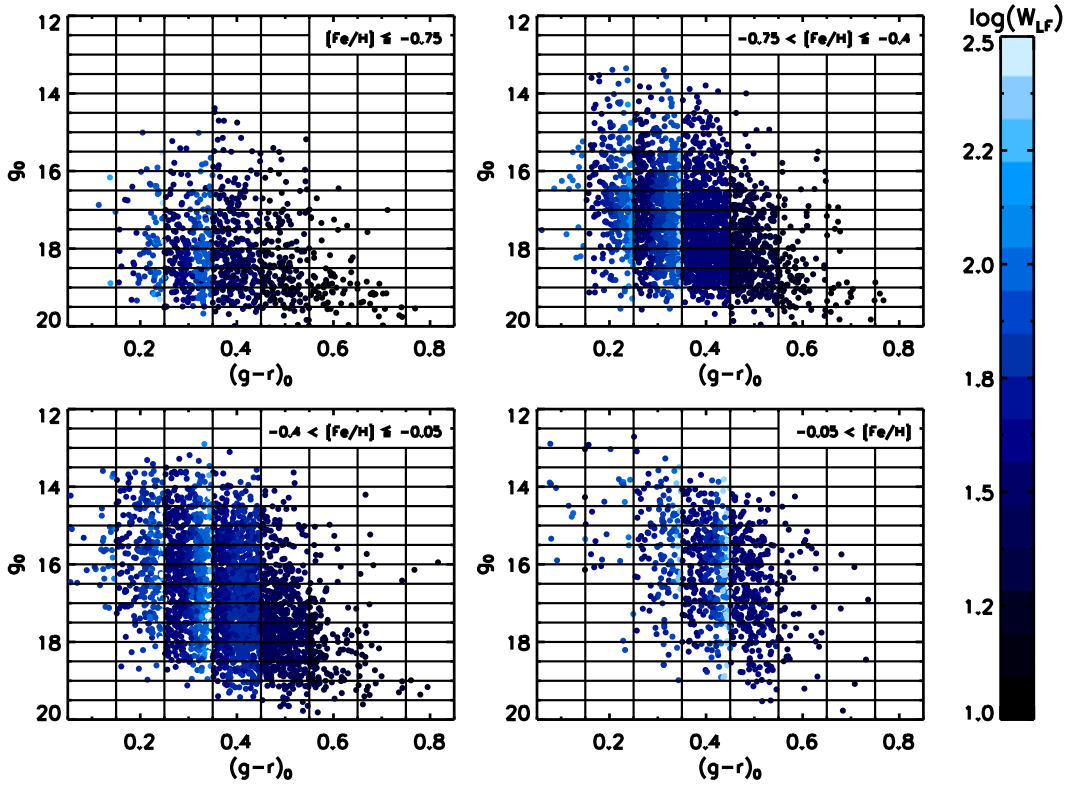

Figure A.2: Weighting for LF coverage for the total sample. For each isochrone extinction-corrected CMD bin (black lines) the LF weight $W_{\rm LF}$ corrects for the fraction of the luminosity function that is observed. The luminosity function used varies with both metallicity (shown in four separate panels) and age, which depends on the temperature. This correction accounts for the bias against redder, metal-rich stars that results from the $(g-r)_{\rm SFD}$ color selection.

targets as described in §2.3 and Figure 2.3. In a given CMD bin, stars with older ages have larger LF weights because a smaller fraction of the luminosity function is observable within the bin. This accounts for the vertical striping pattern seen in the four panels. We assign $W_{\rm LF} = 0$ to the three spectra that fall outside the bounds of the CMD bins.

Using the luminosity functions to correct for the fraction of unobserved stars represented by the stars in each CMD bin corrects for the bias against selecting metal-rich stars for the spectroscopic sample. The identification of MSTO stars relies on a cut in $(g-r)_{\rm SFD}$, which preferentially removes metal-rich stars that fall on isochrones with redder turnoff colors. Thus, for metal-rich stars, more of the population is removed by the color cut, and a smaller fraction

of the luminosity function is observed. Consequently, metal-rich targets have larger values of $W_{\rm LF}$ (lighter blue circles) at the same $(g-r)_0$ in the four panels in Figure A.2. In order for $W_{\rm LF}$ to make the proper corrections, we need to have a sufficient number of metal-rich stars in our sample to which we can apply the weights. Based on the arguments presented in §2.6.1, our sample should satisfy this requirement.

Appendix B

Scale Length Estimates

B.1 Procedure

To determine the scale lengths of the thin and thick disks, we follow the prescription of Jurić et al. (2008) and model the Galaxy as two double exponential disks plus a two-axial power-law ellipsoid halo (their Equations 21-24):

$$\rho(R,Z) = \rho_{\rm D}(R,Z;L_{\rm thin},H_{\rm thin}) + f\rho_{\rm D}(R,Z;L_{\rm thick},H_{\rm thick}) + \rho_{\rm H}(R,Z) \tag{B.1}$$

where

$$\rho_{\rm D}(R,Z;L,H) = \rho_{\rm D}(R_\odot,0) \times \exp\left(\frac{R_\odot}{L}\right) \times \exp\left(-\frac{R}{L} - \frac{Z+Z_\odot}{H}\right) \tag{B.2}$$

and

$$\rho_{\rm H}(R,Z) = \rho_{\rm D}(R_\odot,0) f_{\rm H} \left[\frac{R_\odot}{\sqrt{R^2+(Z/q_{\rm H})^2}}\right]^{n_{\rm H}} \tag{B.3}$$

The definitions of the parameters and the values used (the bias-corrected parameters in their Table 10) are listed in Table B.1. We vary the thin and thick disk scale lengths and fix

the remaining parameters (including the scale heights and the total normalization) to the Jurić et al. (2008) values, which are constrained using their photometric sample. Our spectroscopic sample is not well suited for determining the total stellar density because of the smaller sample size and the pencil-beam nature of the observations.

For each combination of scale lengths, we calculate a reduced χ^2 statistic to indicate how well the predicted fractions of high- and low-α stars as a function of R and $|Z|$ reproduce what we see in our SEGUE sample; these values are indicated by the blue-shaded map in Figure 3.6. In addition, we calculate how well the sum of the two exponential disks matches the total density measured by Jurić et al. (2008); these values are indicated by the thin yellow contours in Figure 3.6. This second constraint is not strictly a χ^2 statistic, as we are comparing two smooth models. We normalize the second constraint such that it has the same 10th and 90th percentile levels as the χ^2 values from the first constraint.

We determine our best-fit scale lengths by calculating a probability for each combination of scale lengths, where the probability is proportional to $e^{-\chi^2/2}$. All probabilities are normalized such that the total probability in the parameter space 1 kpc $< L_{\rm thin} <$ 10 kpc, 0 kpc $< L_{\rm thick} <$ 8 kpc is equal to one. The thick dashed orange contour in Figure 3.6 shows the contour that encompasses 68% of the volume under the surface defined by the probabilities. The best fit value of each scale length is obtained by marginalizing the probabilities over each axis and determining the peak in one dimension. The error bars indicate the 68% confidence interval in one dimension. This exercise yields our final results for the scale lengths: $L_{\rm thin} = 3.4^{+2.8}_{-0.9}$ kpc, $L_{\rm thick} = 1.8^{+2.1}_{-0.5}$ kpc.

B.2 Additional Sources of Error

In this section, we estimate the errors in our scale length estimates due to (1) random errors in the stellar parameters, (2) systematic errors in the Jurić et al. (2008) scale lengths,

Table B.1: Bias-Corrected Structural Parameters Measured by Jurić et al. (2008)

Parameter	Error	Definition
$Z_\odot = 25$ pc	20%	Solar offset from the Galactic plane
$L_{\rm thin} = 2600$ pc	20%	Thin disk scale length
$H_{\rm thin} = 300$ pc	20%	Thin disk scale height
$f = 0.12$	10%	Thick disk normalization relative to thin disk at $R = R_\odot, Z = 0$
$L_{\rm thick} = 3600$ pc	20%	Thick disk scale length
$H_{\rm thick} = 900$ pc	20%	Thick disk scale height
$f_{\rm H} = 0.0051$	25%	Halo normalization relative to thin disk at $R = R_\odot, Z = 0$
$q_{\rm H} = 0.64$	< 0.1	Halo ellipticity
$n_{\rm H} = 2.77$	$\lesssim 0.2$	Halo power law

and (3) contamination by halo stars. First, we estimate the random errors on the scale lengths using the same method as in Chapter 2, where we generate 500 Monte Carlo realizations of our data (see Chapter 2 for more details). In each realization, we perturb the stellar parameters $T_{\rm eff}$, [Fe/H], and [α/Fe] by the typical errors (200 K, 0.3 dex and 0.1 dex, respectively). We find that errors in the stellar parameters only change the scale lengths by 0.1 kpc.

Second, to estimate the errors in the assumed total density (i.e., the thin yellow contours in Figure 3.6), we repeat the calculation, varying the Jurić et al. (2008) scale lengths and scale heights by their reported errors (20%). The purpose of this exercise is to simulate the effect of systematic errors between the distances of Jurić et al. (2008) and the present work, which will cause the structural parameters to increase or decrease together. When we increase the Jurić et al. (2008) values by 20%, we obtain $L_{\rm thin} = 8.1^{+1.3}_{-2.7}$ kpc, $L_{\rm thick} = 1.8^{+3.7}_{-0.6}$ kpc; for a 20% decrease, we obtain $L_{\rm thin} = 2.5^{+1.8}_{-0.6}$ kpc, $L_{\rm thick} = 1.7^{+1.4}_{-0.5}$ kpc.

Lastly, to test the robustness of our results, we repeat the calculation after removing stars that may belong to the halo. Halo stars also have a short scale length and are enhanced in [α/Fe]. We adopt the three criteria to identify probable halo stars: (1) a metallicity cut that removes all stars with [Fe/H] < -0.7, (2) a kinematic cut, which removes all stars with $V_\phi < 150$ km s^{-1}, and (3) a kinematic cut that removes all stars with $V_{\rm Gal} < 100$ km s^{-1} to remove stars with the largest velocity offset relative to the projection of the local standard of rest, where $V_{\rm Gal} = V_R + 220 \cdot \cos b \cdot \sin l$ and V_R is the line-of-sight velocity measured from the SEGUE spectra. We only remove stars with $V_{\rm Gal} < 100$ km s^{-1} along lines of sight with

$50^\circ < l < 130^\circ$. We do not include the lines of sight directed toward the Galactic anticenter because the local standard of rest is tangent to those directions, and the projection does not give a meaningful velocity. For all three criteria we obtain the same scale lengths, which suggests that halo contamination does not affect our scale length measurements.

The above analysis shows that the best-fit thick disk scale length is not significantly affected by errors in the stellar parameters, our assumptions of the total stellar density, and possible contamination from halo stars. The thin disk scale length, however, is not well-constrained because we are limited by the lack of coverage in R and $|Z|$, particularly in the plane of the Galaxy. Future surveys such as APOGEE (Eisenstein et al. 2011) will be able to provide stricter constraints on both scale lengths.

Appendix C

Equivalent Width Measurements

We present below the equivalent width measurements for the 37 stars discussed in Chapter 4. Each table shows the equivalent width measurements for 6-8 stars in units of mÅ. The stars are presented in the order they were observed, except those in Table C.5. These six stars were observed using the HIRESr setting and cover a larger wavelength range than the rest of the sample.

Table C.1: Equivalent Width Measurements, Table 1 of 5

λ (Å)	Ion	loggf	EP	1919-173	1893-104	1905-243	2307-386	2335-542	2070-084	2052-063	2328-059
5682.65	11.0	-0.699	2.100	...	98.4	...	...	56.7	...	82.3	...
5688.19	11.0	-0.420	2.100	...	...	...	...	72.0	...	...	...
6154.23	11.0	-1.530	2.100	...	27.8	...	...	...	...	19.5	...
6160.75	11.0	-1.230	2.100	45.7	46.6	64.4	...	...	...	34.8	49.6
4571.10	12.0	-5.570	0.000	94.3	...	...	...	57.4	...	75.6	...
4730.04	12.0	-2.347	4.350	...	57.0	...	...	...	...	35.5	...
5711.09	12.0	-1.630	4.340	98.0	...	...	85.2	54.9	...	83.7	94.3
5665.55	14.0	-2.040	4.920	38.3	39.3	...	...	...	48.5	31.2	41.7
5684.49	14.0	-1.420	4.950	...	59.4	...	...	...	...	...	...
5690.43	14.0	-1.870	4.930	...	47.1	...	...	...	56.3	43.6	57.8
5701.10	14.0	-2.050	4.930	...	...	...	...	...	...	34.5	...
5772.15	14.0	-1.750	5.080	...	52.2	...	...	...	61.2	47.0	51.6
5793.07	14.0	-2.060	4.930	...	...	...	...	...	...	...	46.5
5948.54	14.0	-1.230	5.080	85.0	78.6	37.8	...	52.1	...	75.3	83.5
6125.03	14.0	-1.570	5.610	31.5	29.8	...	...	...	42.5	28.3	28.8
6142.49	14.0	-1.480	5.620	34.0	27.5	...	...	...	43.8	33.5	32.8
6145.02	14.0	-1.370	5.610	43.6	36.4	...	...	...	47.3	32.2	36.3
6155.13	14.0	-0.760	5.620	76.9	78.3	...	...	36.9	...	...	88.2
6237.32	14.0	-1.010	5.620	...	57.9	...	...	...	66.0	55.3	67.1
6243.82	14.0	-1.300	5.616	46.6	...	...	...	...	60.3	...	57.0
6244.48	14.0	-1.320	5.616	...	...	...	...	...	56.1	...	57.1
6347.09	14.1	0.260	8.120	...	...	...	42.8	57.2	73.4	73.2	70.2
6371.35	14.1	-0.050	8.120	48.4	33.0	...	...	...	53.1	57.5	...
4318.66	20.0	-0.210	1.900	...	...	53.0	...	94.8	...	...	...
4512.27	20.0	-2.030	2.520	...	...	...	...	...	...	...	20.8
4526.93	20.0	-0.420	2.710	79.1	80.8	...	...	44.8	...	66.4	85.8
4578.56	20.0	-0.558	2.520	78.5	...	29.1	...	51.3	82.8	69.9	75.0
4685.27	20.0	-0.940	2.930	...	...	...	...	...	...	45.1	...
5260.39	20.0	-1.780	2.520	...	29.7	...	...	...	...	23.5	...
5261.71	20.0	-0.730	2.520	87.0	94.9	...	...	58.0	...	82.3	89.9

Table C.1: Equivalent Width Measurements, Table 1 of 5, continued

λ (Å)	Ion	loggf	EP	1919-173	1893-104	1905-243	2307-386	2335-542	2070-084	2052-063	2328-059
5349.47	20.0	-0.310	2.710	...	94.1	52.7	...	...	...	...	...
5512.99	20.0	-0.266	2.930	81.6	74.3	...	...	48.3	...	75.6	...
5588.76	20.0	0.358	2.510	...	...	89.8	...	...	...	...	...
5590.13	20.0	-0.710	2.510	89.2	87.5	...	...	57.1	...	75.7	80.6
5601.28	20.0	-0.438	2.520	...	...	...	...	60.3	...	88.8	...
5857.46	20.0	0.240	2.930	...	...	...	...	84.5	...	...	...
5867.57	20.0	-1.610	2.930	...	21.3	...	...	...	...	...	...
6102.73	20.0	-0.790	1.880	...	...	52.2	...	81.9	...	...	...
6122.23	20.0	-0.320	1.890	...	...	68.3	...	...	...	...	...
6161.30	20.0	-1.270	2.520	56.5	57.7	...	...	...	69.9	42.1	52.6
6166.44	20.0	-1.140	2.520	55.4	64.7	...	...	31.1	68.9	49.2	60.9
6169.04	20.0	-0.800	2.520	80.3	89.9	48.7	...	51.0	...	77.2	85.0
6169.56	20.0	-0.480	2.520	92.1	...	38.1	...	62.6	...	91.0	98.1
5239.82	21.1	-0.765	1.450	56.5	58.2	...	...	34.7	66.1	52.8	61.6
5526.82	21.1	0.020	1.770	95.2	84.7	...	...	66.3	94.1	86.8	84.1
5640.99	21.1	-1.130	1.500	...	...	...	...	...	...	48.1	47.9
5657.88	21.1	-0.600	1.510	82.5	71.7	...	...	49.3	83.1	74.9	80.0
5667.15	21.1	-1.360	1.500	...	44.7	...	...	...	...	30.6	...
5669.04	21.1	-1.120	1.500	49.4	40.2	...	...	...	...	41.1	49.1
5684.20	21.1	-1.080	1.507	...	59.4	...	...	...	...	...	...
3924.53	22.0	-0.940	0.020	70.3	...	...	...	35.0	...	...	...
3958.22	22.0	-0.176	0.050	...	...	...	...	65.5	...	...	...
3998.64	22.0	-0.060	0.050	...	...	...	...	79.1	...	...	...
4008.93	22.0	-1.072	0.021	86.5	...	...	...	...	...	...	...
4512.74	22.0	-0.480	0.840	53.7	61.4	28.2	...	25.3	...	44.4	54.2
4518.03	22.0	-0.325	0.830	57.0	75.3	30.1	...	32.5	...	50.6	61.9
4533.25	22.0	0.476	0.850	...	98.4	...	...	...	...	...	...
4534.78	22.0	0.280	0.840	89.5	91.9	...	78.8	60.1	...	78.6	92.1
4548.77	22.0	-0.354	0.830	63.4	69.6	...	...	30.1	73.8	48.9	63.9
4555.49	22.0	-0.490	0.850	53.7	58.7	...	...	...	65.8	44.2	55.4
4617.28	22.0	0.390	1.750	...	67.0	...	...	...	66.9	46.5	63.5

Table C.1: Equivalent Width Measurements, Table 1 of 5, continued

λ (Å)	Ion	loggf	EP	1919-173	1893-104	1905-243	2307-386	2335-542	2070-084	2052-063	2328-059
4623.10	22.0	0.170	1.740	44.3	50.2	...	...	...	...	31.7	45.3
4758.12	22.0	0.425	2.250	34.6	32.2	...	...	...	37.1	24.2	37.4
4759.28	22.0	0.514	2.250	33.8	38.6	...	...	...	43.6	28.1	40.7
4778.26	22.0	-0.210	2.240	...	12.4	...	...	...	...	...	...
4820.41	22.0	-0.439	1.500	28.9	33.5	...	...	...	37.8	20.6	35.4
4840.88	22.0	-0.450	0.900	55.6	68.4	...	...	24.8	69.0	41.0	59.1
4913.62	22.0	0.220	1.870	...	51.5	...	...	...	...	28.5	44.8
4981.74	22.0	0.504	0.850	...	...	59.6	88.2	69.6	...	99.1	...
4997.10	22.0	-2.118	0.000	...	31.2	...	...	...	...	...	...
4999.51	22.0	0.250	0.830	92.9	...	...	...	59.3	...	91.6	...
5016.17	22.0	-0.574	0.850	52.3	60.9	...	...	16.1	...	40.1	55.7
5022.87	22.0	-0.430	0.830	54.9	66.3	...	...	32.9	...	48.9	64.0
5024.85	22.0	-0.600	0.820	...	63.2	...	...	20.5	...	43.8	...
5039.96	22.0	-1.130	0.020	...	76.0	...	...	38.0	85.4	57.1	...
5064.66	22.0	-0.990	0.050	75.7	...	...	...	38.4	...	62.4	...
5145.47	22.0	-0.574	1.460	...	27.7	...	...	...	...	...	...
5192.98	22.0	-1.006	0.020	77.4	76.0	31.4	...	44.1	86.2	56.6	79.6
5210.39	22.0	-0.884	0.050	78.9	87.3	43.6	...	47.5	98.7	67.1	81.8
5866.45	22.0	-0.840	1.070	37.4	45.1	...	...	...	...	...	46.3
5953.16	22.0	-0.329	1.890	...	26.8	...	...	...	...	...	...
5965.83	22.0	-0.409	1.880	...	27.4	...	...	...	...	...	...
5978.54	22.0	-0.496	1.870	...	20.4	...	...	...	...	...	...
6258.10	22.0	-0.355	1.440	33.8	47.1	...	...	...	...	30.6	42.3
6258.71	22.0	-0.240	1.460	50.9	61.1	...	...	...	81.2	36.9	63.0
6261.11	22.0	-0.480	1.430	34.9	39.0	...	...	...	...	23.3	40.6
3987.61	22.1	-2.730	0.610	48.6	...	38.5	...	43.8	...	58.1	...
4028.35	22.1	-1.000	1.890	87.0	86.9	41.2	69.0	72.0	...	92.1	94.4
4395.84	22.1	-1.970	1.240	...	66.5	...	...	...	74.4	...	...
4417.72	22.1	-1.430	1.160	...	...	56.7	...	90.7	...	...	...
4418.33	22.1	-1.990	1.240	79.7	77.3	...	...	54.9	89.2	79.7	84.8
4544.02	22.1	-2.410	1.240	...	44.9	22.6	...	25.0	...	49.0	43.5

Table C.1: Equivalent Width Measurements, Table 1 of 5, continued

λ (Å)	Ion	loggf	EP	1919-173	1893-104	1905-243	2307-386	2335-542	2070-084	2052-063	2328-059
4563.77	22.1	-0.960	1.220	...	...	63.7	...	...	...	...	...
4568.33	22.1	-2.650	1.220	29.8	...	...	...	...	...	30.3	36.5
4571.98	22.1	-0.530	1.570	...	...	77.8	...	...	...	...	...
4583.42	22.1	-2.720	1.160	39.3	...	...	...	20.0	...	32.6	34.7
4589.95	22.1	-1.790	1.240	90.0	86.9	36.1	75.8	71.5	99.1	93.9	93.3
4636.32	22.1	-3.020	1.165	22.5	...	...	...	...	24.8	14.9	21.4
4708.67	22.1	-2.210	1.240	64.0	...	...	...	40.6	65.4	55.8	64.3
4779.98	22.1	-1.370	2.048	70.2	65.7	32.2	56.7	58.0	82.9	76.8	75.3
4805.09	22.1	-1.120	2.061	...	...	53.7	79.2	79.1	...	...	...
4874.01	22.1	-0.790	3.090	...	36.3	...	...	...	45.3	42.1	...
4911.20	22.1	-0.330	3.120	57.2	54.0	...	...	38.8	...	56.0	59.8
5005.17	22.1	-2.540	1.570	...	...	...	...	...	...	22.8	...
5154.07	22.1	-1.920	1.570	77.7	76.1	...	...	52.6	...	81.0	...
5185.91	22.1	-1.350	1.890	...	...	...	...	50.9	...	75.6	70.3
5211.53	22.1	-1.160	2.590	38.3	...	...	...	15.0	...	37.1	40.8
5336.79	22.1	-1.630	1.580	82.4	75.9	28.9	70.8	62.8	87.9	80.4	83.1
5381.01	22.1	-1.970	1.570	67.6	66.4	26.7	...	50.5	...	69.6	...
5418.78	22.1	-2.110	1.580	62.6	51.6	...	...	41.1	61.7	58.0	57.7
5490.69	22.1	-2.430	1.566	26.0	...	...	...	...	...	...	...
4115.18	23.0	0.070	0.290	...	68.7	25.2	...	...	...	...	...
4875.49	23.0	-0.810	0.040	...	...	...	...	...	39.5	...	...
5670.86	23.0	-0.420	1.080	...	15.8	...	...	...	...	...	...
5703.59	23.0	-0.210	1.050	...	...	...	...	...	27.1	...	...
5727.06	23.0	-0.010	1.080	...	26.3	...	...	...	33.3	...	29.1
6039.73	23.0	-0.650	1.060	...	11.6	...	...	...	...	...	...
3592.03	23.1	-0.370	1.100	92.7	87.8	48.9	...	70.4	88.7	86.4	83.9
3951.97	23.1	-0.744	1.480	...	67.9	...	...	49.0	72.4	...	...
3732.02	24.0	-2.570	0.000	54.9	...	...	...	...	...	53.3	61.5
3768.74	24.0	-0.920	2.544	...	...	...	...	...	...	...	44.5
4272.90	24.0	-0.980	2.900	23.3	...	...	...	...	...	...	...
4351.05	24.0	-1.430	0.968	...	...	...	...	35.6	...	...	...

Table C.1: Equivalent Width Measurements, Table 1 of 5, continued

λ (Å)	Ion	loggf	EP	1919-173	1893-104	1905-243	2307-386	2335-542	2070-084	2052-063	2328-059
4412.23	24.0	-2.670	1.030	...	19.9	...	...	...	...	...	...
4496.84	24.0	-1.140	0.941	...	...	...	...	69.6	...	...	...
4511.90	24.0	-0.343	3.090	29.6	34.8	...	...	...	...	27.5	29.4
4545.95	24.0	-1.370	0.941	72.2	78.6	57.9	...	46.8	88.4	65.6	75.6
4580.04	24.0	-1.660	0.941	73.6	...	...	...	45.7	...	66.8	...
4591.39	24.0	-1.740	0.968	81.0	...	...	...	...	...	...	86.6
4616.12	24.0	-1.190	0.983	84.3	83.6	45.5	...	48.3	97.8	74.7	79.9
4626.17	24.0	-1.330	0.968	70.0	74.6	...	...	41.8	...	64.2	71.1
4646.15	24.0	-0.740	1.030	...	...	...	...	66.2	...	...	...
4651.28	24.0	-1.460	0.983	79.1	70.4	...	...	33.5	87.5	59.0	70.3
4652.15	24.0	-1.040	1.004	86.8	93.7	51.6	68.6	56.0	...	79.2	89.5
4689.38	24.0	-0.400	3.125	...	...	...	...	...	59.8	...	...
4708.02	24.0	0.070	3.168	53.4	48.6	...	...	25.2	57.7	40.3	44.8
4718.43	24.0	0.240	3.195	54.7	60.0	28.6	...	32.1	68.4	48.0	55.5
4724.41	24.0	-0.733	3.090	28.9	...	...	...	...	36.0	20.0	27.1
4730.72	24.0	-0.192	3.080	...	40.1	...	...	...	...	...	...
4737.35	24.0	-0.100	3.090	...	46.4	...	...	...	...	42.0	55.2
4789.34	24.0	-0.330	2.544	56.2	79.1	...	...	...	...	48.7	52.1
4801.03	24.0	-0.130	3.120	38.8	41.0	...	...	...	...	...	36.4
4814.28	24.0	-1.220	3.087	...	15.2	...	...	...	...	...	...
4936.34	24.0	-0.250	3.113	34.7	...	...	...	...	49.0	31.0	34.9
4964.93	24.0	-2.526	0.940	...	29.3	31.0	...	...	...	...	20.9
5067.72	24.0	-1.070	2.709	29.2	...	...	...	...	...	...	...
5247.57	24.0	-1.590	0.961	65.6	77.1	24.6	...	33.2	...	55.2	65.7
5296.69	24.0	-1.360	0.983	76.2	83.9	...	...	45.9	97.8	69.7	77.7
5297.39	24.0	0.000	2.900	...	80.1	...	...	...	96.2	62.8	71.4
5300.74	24.0	-2.000	0.983	...	52.9	...	...	14.4	...	...	46.6
5345.80	24.0	-0.950	1.004	...	...	...	87.0	71.9	...	89.3	...
5348.31	24.0	-1.210	1.004	...	90.4	...	...	55.7	...	75.8	81.7
5409.77	24.0	-0.670	1.030	...	...	88.2	...	85.5	...	...	...
5702.32	24.0	-0.670	3.449	...	18.3	...	...	...	...	...	...

Table C.1: Equivalent Width Measurements, Table 1 of 5, continued

λ (Å)	Ion	loggf	EP	1919-173	1893-104	1905-243	2307-386	2335-542	2070-084	2052-063	2328-059
5783.09	24.0	-0.500	3.320	...	25.7	...	...	...	...	17.6	...
5783.89	24.0	-0.295	3.320	...	29.9	...	...	...	39.0	...	31.8
5787.93	24.0	-0.083	3.320	...	35.4	...	...	...	44.5	31.7	40.8
6330.09	24.0	-2.900	0.940	...	22.3	...	...	...	...	...	...
4554.99	24.1	-1.373	4.070	55.7	49.4	...	...	38.2	...	63.2	54.4
4558.65	24.1	-0.656	4.070	88.1	83.0	37.2	...	74.6	...	...	85.7
4588.20	24.1	-0.826	4.070	74.0	71.4	28.8	71.8	66.3	88.9	82.1	73.7
4592.06	24.1	-1.419	4.070	53.8	49.1	...	...	29.9	58.3	58.5	50.6
4616.63	24.1	-1.210	4.073	53.7	48.7	...	...	33.6	65.4	58.1	52.9
4848.23	24.1	-0.999	3.870	...	...	...	...	54.3	...	72.1	...
5237.33	24.1	-1.155	4.070	60.9	55.1	25.3	...	36.2	60.6	58.2	53.7
5305.86	24.1	-2.060	3.830	...	35.6	...	...	...	42.3	...	...
5308.42	24.1	-1.790	4.070	27.6	25.7	...	...	...	...	30.9	30.0
5310.69	24.1	-2.240	4.070	16.3	...	...	...	...	...	17.3	13.3
5313.59	24.1	-1.640	4.070	39.3	34.4	...	...	...	44.4	40.4	37.1
5502.09	24.1	-1.970	4.168	...	...	...	...	...	...	25.1	...
4055.55	25.0	-0.080	2.140	...	...	...	...	78.5	...	...	...
4709.72	25.0	-0.339	2.890	49.5	57.2	...	...	...	65.9	43.0	51.7
4739.11	25.0	-0.490	2.940	37.1	48.2	...	...	...	59.6	39.4	...
4761.53	25.0	-0.138	2.950	57.6	62.3	...	...	28.5	...	51.1	57.1
4783.43	25.0	0.042	2.300	...	...	47.8	93.6	82.4	...	...	...
4823.51	25.0	0.144	2.320	...	...	43.5	92.2	73.2	...	...	...
6013.50	25.0	-0.252	3.070	67.9	70.8	...	...	18.9	...	...	76.4
6021.80	25.0	0.030	3.080	82.3	81.4	...	...	39.6	95.2	63.2	74.7
3916.74	26.0	-0.604	3.237	...	92.0	...	...	61.6	...	81.9	78.1
3917.18	26.0	-2.155	0.990	...	...	...	99.6	96.2	...	...	...
3949.96	26.0	-1.251	2.176	...	99.8	...	84.9	79.5	...	92.3	95.3
4114.45	26.0	-1.303	2.832	78.5	83.1	36.2	...	65.4	92.3	78.5	83.9
4132.91	26.0	-1.006	2.845	...	...	...	...	79.8	...	...	...
4139.94	26.0	-3.629	0.990	57.2	61.8	21.8	35.3	36.2	73.9	54.2	63.8
4157.79	26.0	-0.403	3.417	...	...	81.2	94.5	78.9	...	...	...

Table C.1: Equivalent Width Measurements, Table 1 of 5, continued

λ (Å)	Ion	loggf	EP	1919-173	1893-104	1905-243	2307-386	2335-542	2070-084	2052-063	2328-059
4174.92	26.0	-2.969	0.915	...	...	...	97.8	...	...	...	...
4175.64	26.0	-0.827	2.845	99.6	...	85.3	...	76.9	...	99.3	...
4184.91	26.0	-0.869	2.832	91.0	...	53.3	78.2	71.6	...	91.7	...
4216.19	26.0	-3.356	0.000	...	...	...	...	79.1	...	...	...
4217.56	26.0	-0.484	3.430	...	...	...	...	76.8	...	...	...
4222.22	26.0	-0.967	2.450	...	...	...	...	95.1	...	...	...
4238.81	26.0	-0.233	3.397	...	...	...	...	87.3	...	...	...
4347.24	26.0	-5.503	0.000	...	30.0	...	...	...	30.9	...	26.8
4375.94	26.0	-3.031	0.000	...	...	...	...	95.8	...	...	...
4388.41	26.0	-0.682	3.603	...	...	...	...	61.1	...	...	84.7
4389.25	26.0	-4.583	0.052	57.7	63.8	...	...	25.5	60.9	...	55.2
4489.75	26.0	-3.966	0.121	83.0	93.6	50.5	...	63.2	...	76.8	87.5
4494.57	26.0	-1.136	2.198	...	...	...	...	98.7	...	...	...
4517.52	26.0	-1.860	3.071	59.1	65.7	31.1	...	23.6	72.8	50.6	59.9
4523.41	26.0	-1.960	3.654	28.6	32.7	...	...	...	...	22.6	34.1
4547.85	26.0	-1.010	3.546	74.9	80.7	...	...	57.5	87.8	74.6	76.8
4551.65	26.0	-2.030	3.943	20.3	17.9	...	...	...	...	...	...
4556.93	26.0	-2.660	3.251	...	25.5	...	...	...	...	...	14.6
4566.52	26.0	-2.380	3.300	31.2	...	...	...	...	...	27.4	35.9
4574.23	26.0	-2.450	3.211	23.5	30.3	...	...	...	34.2	19.2	24.7
4587.13	26.0	-1.740	3.573	47.1	...	...	...	...	65.0	40.1	46.1
4593.53	26.0	-2.030	3.943	19.3	22.2	...	...	...	...	...	18.8
4602.01	26.0	-3.154	1.608	63.8	65.4	...	...	32.5	68.9	56.7	59.8
4602.95	26.0	-2.220	1.485	...	...	57.6	...	81.9	...	98.3	...
4630.12	26.0	-2.587	2.279	60.1	66.4	36.9	...	28.5	78.2	53.2	65.6
4632.92	26.0	-2.913	1.608	96.3	...	48.8	66.7	48.7	...	...	...
4635.85	26.0	-2.360	2.840	39.7	45.7	...	...	...	...	34.7	41.7
4647.43	26.0	-1.351	2.949	...	...	...	...	60.4	...	...	...
4672.84	26.0	-4.240	1.610	...	...	...	...	...	...	24.2	19.1
4683.56	26.0	-2.320	2.832	44.5	49.3	...	...	...	56.5	33.0	42.3
4690.14	26.0	-1.640	3.687	43.3	...	...	...	25.9	54.5	38.1	47.4

Table C.1: Equivalent Width Measurements, Table 1 of 5, continued

λ (Å)	Ion	loggf	EP	1919-173	1893-104	1905-243	2307-386	2335-542	2070-084	2052-063	2328-059
4733.59	26.0	-2.990	1.485	69.6	77.2	34.0	...	52.6	94.0	70.0	76.5
4741.53	26.0	-1.760	2.830	64.7	65.5	...	...	38.7	78.8	60.0	66.2
4745.80	26.0	-1.270	3.654	63.6	70.5	26.7	...	34.3	76.7	58.7	68.7
4779.45	26.0	-2.020	3.415	28.5	34.9	...	...	...	38.7	24.7	33.8
4787.83	26.0	-2.600	2.998	29.0	30.2	...	...	...	43.5	23.7	31.6
4788.76	26.0	-1.763	3.237	57.7	58.8	...	...	30.9	67.7	48.4	58.1
4789.65	26.0	-0.910	3.547	74.0	79.1	40.4	...	54.2	...	72.0	76.6
4802.52	26.0	-1.820	4.610	...	...	...	...	...	...	...	12.9
4802.88	26.0	-1.510	3.642	53.5	55.0	...	23.9	28.3	67.0	49.0	57.1
4808.16	26.0	-2.740	3.251	...	...	...	...	...	25.3	...	19.5
4809.94	26.0	-2.680	3.573	...	12.6	...	...	...	19.2	...	...
4835.87	26.0	-1.470	4.103	33.1	42.4	...	...	...	...	30.9	40.6
4839.52	26.0	-1.820	3.270	49.7	61.6	...	...	24.1	...	44.6	51.9
4844.01	26.0	-2.050	3.547	36.4	41.2	...	...	...	...	23.0	31.1
4882.14	26.0	-1.640	3.420	...	70.3	22.6	...	29.1	...	58.7	60.1
4892.87	26.0	-1.290	4.220	...	50.3	...	...	...	55.5	31.3	41.8
4903.32	26.0	-0.926	2.882	...	...	...	...	87.2	...	...	...
4905.14	26.0	-2.020	3.929	...	29.1	...	...	...	...	17.8	21.4
4917.24	26.0	-1.160	4.191	55.5	60.5	...	...	29.8	71.6	48.5	56.5
4924.77	26.0	-2.114	2.279	80.6	85.0	47.4	47.5	52.5	...	79.9	89.5
4938.82	26.0	-1.077	2.875	...	...	54.1	...	81.8	...	95.2	...
4939.69	26.0	-3.340	0.859	...	90.0	62.6	...	56.0	...	85.7	87.9
4961.92	26.0	-2.250	3.634	...	...	...	...	...	25.6	14.4	...
4962.58	26.0	-1.182	4.178	48.8	43.9	...	...	21.8	55.9	40.0	45.7
4966.09	26.0	-0.871	3.332	...	...	...	83.6	72.9	...	98.3	...
4994.14	26.0	-3.080	0.915	92.4	...	44.1	75.4	75.4	...	81.5	98.5
5001.87	26.0	-0.010	3.882	...	...	...	...	88.7	...	...	...
5014.94	26.0	-0.303	3.943	97.5	98.8	...	...	72.8	...	87.1	99.1
5044.21	26.0	-2.060	2.850	59.8	78.4	28.1	...	32.0	69.8	52.9	61.9
5049.83	26.0	-1.355	2.279	...	...	58.6	...	91.8	...	...	...
5051.64	26.0	-2.795	0.915	...	...	55.8	98.9	91.5	...	...	...

Table C.1: Equivalent Width Measurements, Table 1 of 5, continued

λ (Å)	Ion	loggf	EP	1919-173	1893-104	1905-243	2307-386	2335-542	2070-084	2052-063	2328-059
5054.64	26.0	-1.920	3.640	25.5	33.3	...	...	...	...	18.4	32.8
5067.16	26.0	-0.970	4.220	57.8	65.5	...	...	35.2	69.8	51.2	61.5
5068.77	26.0	-1.042	2.940	...	...	49.4	...	74.4	...	96.9	...
5074.75	26.0	-0.230	4.220	...	...	...	...	79.7	...	...	...
5079.74	26.0	-3.220	0.990	...	...	...	79.0	...	...	...	...
5083.35	26.0	-2.958	0.958	96.6	...	51.3	72.4	75.7	...	89.2	98.1
5088.16	26.0	-1.680	4.150	...	27.4	...	...	...	...	19.1	26.6
5090.78	26.0	-0.400	4.260	79.8	77.4	25.4	54.6	53.4	89.3	68.9	77.1
5109.66	26.0	-0.980	4.300	74.8	68.6	24.7	...	41.4	80.4	62.2	69.2
5123.73	26.0	-3.068	1.011	90.6	...	...	71.2	62.0	...	85.4	89.9
5125.12	26.0	-0.080	4.220	...	...	...	98.7	85.1	...	...	...
5127.37	26.0	-3.307	0.915	80.7	87.3	29.3	63.5	57.8	89.8	76.0	80.7
5131.48	26.0	-2.515	2.223	...	80.0	...	...	48.3	...	60.5	73.4
5133.69	26.0	0.200	4.180	...	...	50.9	...	90.6	...	...	...
5141.74	26.0	-2.238	2.424	73.3	72.7	...	...	38.2	83.6	61.0	68.2
5145.09	26.0	-2.876	2.198	31.8	45.4	...	...	...	...	28.9	39.4
5150.85	26.0	-3.037	0.990	...	...	...	72.3	62.8	...	95.0	...
5151.92	26.0	-3.322	1.011	81.5	90.9	...	54.6	52.6	...	75.2	83.4
5162.28	26.0	0.020	4.180	...	...	48.5	98.0	79.3	...	...	...
5166.28	26.0	-4.195	0.000	...	...	...	...	59.6	...	86.9	...
5187.92	26.0	-1.371	4.143	50.4	47.9	...	...	24.2	...	38.2	41.3
5191.47	26.0	-0.551	3.038	...	...	...	...	99.4	...	...	...
5192.35	26.0	-0.421	2.998	...	...	...	...	99.9	...	...	...
5194.95	26.0	-2.090	1.557	...	...	69.2	93.1	79.3	...	93.7	...
5198.72	26.0	-2.135	2.223	80.6	89.9	40.8	54.1	57.0	99.8	78.4	83.7
5202.34	26.0	-1.838	2.176	...	...	58.1	...	93.3	...	...	...
5216.28	26.0	-2.150	1.608	...	...	...	84.8	82.5	...	...	...
5217.40	26.0	-1.162	3.211	90.7	99.9	55.2	62.8	62.9	...	87.4	91.6
5225.53	26.0	-4.789	0.110	56.7	...	...	...	...	...	...	...
5242.46	26.0	-0.967	3.634	71.5	81.8	...	48.8	48.6	88.5	70.1	74.7
5243.78	26.0	-1.120	4.256	48.5	57.7	...	...	23.3	...	43.0	50.6

Table C.1: Equivalent Width Measurements, Table 1 of 5, continued

λ (Å)	Ion	loggf	EP	1919-173	1893-104	1905-243	2307-386	2335-542	2070-084	2052-063	2328-059
5247.06	26.0	-4.946	0.087	...	63.2	...	...	...	...	...	50.3
5250.22	26.0	-4.938	0.121	48.0	...	...	...	...	...	...	53.2
5266.56	26.0	-0.385	2.998	...	...	82.6	...	...	...	...	...
5281.80	26.0	-0.834	3.038	...	...	48.3	...	83.2	...	...	...
5283.63	26.0	-0.525	3.241	...	...	...	...	97.8	...	...	...
5288.53	26.0	-1.510	3.680	46.3	52.0	...	...	21.6	55.4	40.6	51.9
5295.32	26.0	-1.670	4.415	19.3	21.2	...	...	...	...	...	20.6
5302.31	26.0	-0.720	3.283	...	...	...	90.9	75.8	...	...	...
5307.37	26.0	-2.987	1.608	...	85.9	...	...	47.3	96.8	75.1	83.8
5321.11	26.0	-1.090	4.435	31.2	32.2	...	...	...	38.4	...	28.2
5322.01	26.0	-2.803	2.279	44.3	53.2	...	...	...	...	32.3	48.7
5324.19	26.0	-0.103	3.211	...	...	83.8	...	...	...	...	...
5332.92	26.0	-2.776	1.557	...	...	32.6	62.7	49.6	...	...	...
5339.94	26.0	-0.720	3.266	...	...	...	91.7	79.7	...	...	...
5364.87	26.0	0.228	4.446	...	...	46.1	...	78.4	...	...	...
5365.40	26.0	-1.020	3.573	73.6	72.4	28.6	...	42.4	...	67.8	70.1
5367.47	26.0	0.443	4.415	...	...	...	87.8	75.4	...	...	...
5369.97	26.0	0.536	4.371	...	...	...	...	82.6	...	...	...
5373.70	26.0	-0.760	4.470	56.1	54.5	15.5	...	25.9	62.9	47.8	56.9
5379.58	26.0	-1.514	3.695	46.1	51.5	...	...	28.2	59.8	41.9	51.3
5383.38	26.0	0.645	4.312	...	...	...	...	99.6	...	...	...
5386.34	26.0	-1.740	4.154	25.5	28.1	...	...	...	...	23.5	...
5389.49	26.0	-0.400	4.410	71.8	75.7	23.6	56.4	46.5	79.6	68.0	72.3
5393.18	26.0	-0.715	3.241	...	...	...	94.5	76.3	...	...	...
5395.22	26.0	-2.150	4.446	...	13.0	...	...	...	...	...	...
5397.14	26.0	-1.993	0.915	...	...	80.4	...	...	...	...	...
5398.29	26.0	-0.710	4.446	60.6	63.4	...	...	34.0	75.6	57.0	59.6
5401.27	26.0	-1.890	4.320	...	17.1	...	...	...	...	...	...
5405.36	26.0	-1.390	4.390	32.4	...	...	...	...	...	...	34.4
5406.78	26.0	-1.720	4.370	...	25.2	...	...	...	...	22.2	25.4
5409.14	26.0	-1.200	4.370	43.3	48.1	...	...	...	65.0	42.9	39.4

Table C.1: Equivalent Width Measurements, Table 1 of 5, continued

λ (Å)	Ion	loggf	EP	1919-173	1893-104	1905-243	2307-386	2335-542	2070-084	2052-063	2328-059
5410.91	26.0	0.398	4.473	...	...	62.4	90.1	96.1	...	...	...
5415.20	26.0	0.642	4.386	...	...	63.8	...	84.0	...	...	...
5417.04	26.0	-1.660	4.415	...	22.0	...	...	...	29.7	16.0	26.8
5424.08	26.0	0.520	4.320	...	...	59.9	...	90.4	...	...	...
5483.10	26.0	-1.410	4.150	40.7	...	...	...	...	...	...	...
5487.14	26.0	-1.430	4.410	29.3	29.1	...	...	...	...	28.9	27.7
5487.77	26.0	-0.620	4.140	81.3	...	38.0	...	48.2	...	78.7	...
5497.52	26.0	-2.830	1.010	...	...	42.9	...	82.1	...	...	...
5501.48	26.0	-3.047	0.958	...	...	47.6	...	80.8	...	96.2	99.5
5506.79	26.0	-2.797	0.990	...	...	...	...	93.8	...	...	...
5522.45	26.0	-1.520	4.209	33.2	36.5	...	...	...	39.3	24.9	33.3
5525.55	26.0	-1.080	4.230	44.6	50.2	...	...	...	55.9	38.3	48.0
5546.51	26.0	-1.210	4.372	37.3	46.6	...	...	...	51.3	34.9	36.8
5547.00	26.0	-1.880	4.218	...	22.5	...	...	...	...	...	18.2
5553.58	26.0	-1.310	4.430	36.8	54.8	...	...	...	...	35.7	46.8
5554.88	26.0	-0.350	4.550	83.7	91.3	...	...	37.0	95.7	74.2	85.2
5560.22	26.0	-1.160	4.435	41.0	50.2	...	...	...	...	40.7	41.0
5567.39	26.0	-2.670	2.610	36.7	63.3	...	...	...	67.5	40.5	56.5
5569.63	26.0	-0.486	3.417	...	...	53.1	...	81.1	...	...	...
5576.10	26.0	-0.940	3.430	77.2	...	39.4	...	68.4	...	86.5	97.3
5587.58	26.0	-1.840	4.140	...	45.0	...	...	...	...	...	...
5618.64	26.0	-1.276	4.209	43.6	42.8	...	...	16.5	50.0	34.2	40.8
5619.61	26.0	-1.670	4.386	...	29.2	...	...	...	...	...	...
5620.49	26.0	-1.810	4.150	...	43.7	...	...	...	...	26.8	33.8
5624.04	26.0	-1.220	4.390	43.3	...	19.1	...	...	...	38.6	46.7
5624.54	26.0	-0.755	3.420	...	...	50.3	91.9	64.8	...	98.8	...
5635.83	26.0	-1.860	4.256	...	...	...	...	...	...	18.1	24.6
5641.44	26.0	-1.080	4.260	...	...	...	...	...	...	48.6	54.7
5650.00	26.0	-0.920	5.100	28.4	35.2	...	...	...	...	...	...
5650.70	26.0	-0.860	4.550	36.6	33.7	...	...	...	41.0	...	31.9
5651.48	26.0	-2.000	4.470	13.0	...	...	...	...	...	...	...

Table C.1: Equivalent Width Measurements, Table 1 of 5, continued

λ (Å)	Ion	loggf	EP	1919-173	1893-104	1905-243	2307-386	2335-542	2070-084	2052-063	2328-059
5652.33	26.0	-1.920	4.260	22.1	23.4	...	...	...	26.9	...	17.5
5653.89	26.0	-1.540	4.390	30.7	34.3	...	...	...	37.7	...	31.5
5662.52	26.0	-0.573	4.178	88.4	90.2	30.4	...	43.0	...	71.6	80.6
5667.52	26.0	-1.500	4.480	39.8	44.7	...	...	...	...	27.6	37.9
5679.02	26.0	-0.820	4.650	38.1	55.9	18.8	...	...	66.5	37.7	49.1
5686.53	26.0	-0.446	4.548	...	...	...	...	27.5	...	60.0	...
5701.56	26.0	-2.216	2.559	69.8	76.1	29.0	...	51.0	87.3	65.8	75.9
5705.47	26.0	-1.360	4.300	29.4	28.8	...	...	...	44.0	25.3	32.3
5705.98	26.0	-0.490	4.610	77.3	87.1	...	...	...	...	76.0	83.2
5717.84	26.0	-1.100	4.284	54.2	52.9	...	...	...	...	54.7	61.3
5731.77	26.0	-1.270	4.256	44.5	50.2	...	...	19.4	60.4	44.5	50.9
5741.86	26.0	-1.673	4.256	22.7	26.9	...	...	...	28.9	...	21.6
5752.04	26.0	-0.940	4.550	43.3	46.4	...	...	18.7	58.2	44.8	49.3
5753.12	26.0	-0.688	4.260	66.3	71.5	...	...	40.6	75.6	67.9	71.6
5762.99	26.0	-0.410	4.210	...	...	...	90.6	66.2	...	90.2	...
5775.09	26.0	-1.298	4.220	51.1	48.8	...	...	...	62.7	51.1	52.6
5793.92	26.0	-1.660	4.220	31.3	34.6	...	...	...	...	...	27.4
5806.73	26.0	-1.030	4.608	...	...	...	...	...	...	43.4	44.1
5809.22	26.0	-1.740	3.880	...	41.3	...	...	...	...	31.0	41.1
5814.81	26.0	-1.940	4.283	...	11.6	...	...	...	...	...	13.9
5816.38	26.0	-0.601	4.548	...	70.1	...	...	27.9	...	51.0	70.4
5852.23	26.0	-1.300	4.548	...	30.8	...	...	...	44.6	22.9	31.7
5855.09	26.0	-1.478	4.608	...	14.8	...	...	...	...	...	18.0
5856.10	26.0	-1.328	4.294	...	24.3	...	...	...	...	16.6	28.3
5858.78	26.0	-2.260	4.220	...	11.2	...	...	...	...	...	...
5859.60	26.0	-0.550	4.550	60.5	59.7	22.0	...	26.4	75.9	53.9	61.9
5862.35	26.0	-0.330	4.550	80.6	70.9	27.7	63.1	44.3	91.5	67.4	76.6
5883.81	26.0	-1.260	3.960	62.8	60.4	...	...	...	...	44.6	51.0
5902.48	26.0	-1.810	4.590	...	...	...	...	...	...	...	19.1
5905.68	26.0	-0.770	4.652	...	58.2	...	...	24.4	62.5	43.2	61.0
5927.80	26.0	-1.070	4.652	29.3	28.9	...	...	...	50.3	...	35.9

Table C.1: Equivalent Width Measurements, Table 1 of 5, continued

λ (Å)	Ion	loggf	EP	1919-173	1893-104	1905-243	2307-386	2335-542	2070-084	2052-063	2328-059
5929.68	26.0	-1.380	4.548	26.6	...	...	...	...	39.0	28.4	33.3
5930.19	26.0	-0.140	4.650	75.9	80.1	...	...	59.1	91.4	70.7	80.7
5934.67	26.0	-1.120	3.929	68.5	71.3	...	...	28.4	69.3	55.4	62.9
5952.72	26.0	-1.340	3.980	49.6	54.9	...	...	...	...	42.5	...
5956.71	26.0	-4.608	0.859	35.2	43.9	...	...	...	48.5	...	36.9
5976.79	26.0	-1.330	3.940	66.7	62.8	...	...	23.3	...	54.7	59.0
5983.69	26.0	-0.660	4.550	65.7	64.7	...	...	...	71.6	61.0	...
5984.83	26.0	-0.260	4.730	70.2	85.0	...	...	49.2	94.2	66.6	74.5
6003.02	26.0	-1.110	3.880	69.2	...	...	...	40.2	...	66.8	75.3
6024.05	26.0	0.030	4.550	97.1	97.3	41.5	74.2	60.0	...	86.5	96.5
6027.06	26.0	-1.089	4.076	55.2	60.3	21.7	...	34.9	67.6	46.5	61.6
6055.99	26.0	-0.370	4.730	63.2	68.7	20.5	...	27.4	79.8	54.8	62.9
6065.49	26.0	-1.530	2.608	...	...	40.0	69.0	73.6	...	91.3	...
6078.50	26.0	-0.330	4.790	...	68.4	...	...	35.2	82.2	54.9	70.3
6079.02	26.0	-1.100	4.652	...	37.0	...	...	16.2	...	...	40.4
6082.72	26.0	-3.573	2.223	...	27.4	...	...	...	...	13.1	...
6085.26	26.0	-2.710	2.759	...	35.8	...	...	...	...	...	33.7
6094.38	26.0	-1.920	4.652	...	18.7	...	...	...	...	...	...
6096.67	26.0	-1.880	3.984	25.7	30.0	...	...	...	29.2	22.8	32.7
6127.90	26.0	-1.400	4.140	34.1	45.7	...	...	...	...	30.1	41.7
6136.62	26.0	-1.400	2.453	...	...	...	...	83.8	...	...	...
6137.00	26.0	-2.950	2.198	...	63.3	...	...	...	...	...	...
6137.70	26.0	-1.403	2.588	...	...	55.5	77.4	75.6	...	...	...
6151.62	26.0	-3.299	2.176	34.9	42.0	...	...	...	...	28.9	35.0
6157.73	26.0	-1.220	4.076	53.0	52.1	17.7	...	25.2	65.0	46.4	53.0
6165.36	26.0	-1.474	4.143	35.0	41.4	...	...	...	45.8	27.0	37.7
6173.34	26.0	-2.880	2.223	55.0	60.1	...	...	...	71.0	50.5	63.7
6180.20	26.0	-2.650	2.730	39.5	47.8	...	...	...	...	35.0	47.9
6188.00	26.0	-1.670	3.943	30.1	44.0	...	...	...	...	27.3	37.7
6191.57	26.0	-1.416	2.433	...	...	...	...	91.4	...	...	...
6200.32	26.0	-2.437	2.608	...	...	...	...	...	...	54.5	...

Table C.1: Equivalent Width Measurements, Table 1 of 5, continued

λ (Å)	Ion	loggf	EP	1919-173	1893-104	1905-243	2307-386	2335-542	2070-084	2052-063	2328-059
6213.44	26.0	-2.482	2.223	73.3	83.9	...	...	46.9	83.0	62.0	73.5
6219.29	26.0	-2.433	2.198	80.6	85.3	...	...	46.8	88.0	67.0	85.9
6226.74	26.0	-2.200	3.880	...	22.0	...	...	...	...	...	20.7
6229.23	26.0	-2.805	2.845	...	33.8	...	...	...	...	...	22.6
6230.74	26.0	-1.281	2.559	...	...	...	97.3	85.6	...	...	...
6240.65	26.0	-3.173	2.223	28.6	...	...	...	...	...	22.5	35.4
6246.33	26.0	-0.877	3.603	93.4	...	...	66.4	63.5	...	87.6	98.3
6252.56	26.0	-1.687	2.404	98.2	...	...	...	82.7	...	97.7	...
6254.26	26.0	-2.430	2.280	...	...	...	67.2	64.6	...	...	...
6265.14	26.0	-2.550	2.176	67.6	79.7	...	41.4	39.6	82.0	62.4	76.8
6270.23	26.0	-2.609	2.858	38.6	49.1	...	...	...	...	31.2	35.8
6271.28	26.0	-2.700	3.330	16.7	...	...	...	...	...	...	...
6290.97	26.0	-0.730	4.730	69.9	57.4	...	...	...	...	...	58.9
6297.80	26.0	-2.740	2.223	...	72.6	...	...	...	...	...	...
6301.51	26.0	-0.718	3.654	...	...	...	...	63.8	...	...	...
6302.50	26.0	-1.110	3.690	78.1	98.4	...	...	...	...	65.0	...
6315.31	26.0	-1.230	4.140	...	61.3	...	...	...	...	45.6	70.8
6315.81	26.0	-1.660	4.076	...	29.3	...	...	...	...	...	...
6322.69	26.0	-2.426	2.588	70.3	70.2	...	...	...	78.3	58.6	73.3
6330.85	26.0	-1.720	4.733	...	30.2	...	...	...	...	...	27.0
6335.33	26.0	-2.177	2.198	86.5	90.2	...	69.2	51.1	...	78.6	85.0
6344.15	26.0	-2.923	2.433	...	57.5	...	...	27.9	...	...	...
6355.04	26.0	-2.291	2.845	...	72.1	...	...	32.0	78.3	57.2	66.9
6358.69	26.0	-4.468	0.859	...	...	...	...	...	76.9	51.8	67.5
4178.86	26.1	-2.443	2.583	87.6	82.2	46.2	69.4	72.2	95.1	96.8	88.9
4416.82	26.1	-2.600	2.778	88.3	80.9	...	...	61.3	94.2	96.5	83.2
4491.40	26.1	-2.640	2.856	77.6	77.6	...	56.5	66.6	...	85.6	75.1
4508.30	26.1	-2.350	2.856	92.9	86.6	42.2	86.9	76.6	...	99.0	90.2
4520.23	26.1	-2.620	2.807	83.4	79.2	35.2	...	69.5	...	92.3	82.7
4541.52	26.1	-2.970	2.856	...	...	...	...	...	...	84.5	...
4576.34	26.1	-2.920	2.844	70.3	64.9	24.7	...	54.4	72.8	74.2	64.1

Table C.1: Equivalent Width Measurements, Table 1 of 5, continued

λ (Å)	Ion	loggf	EP	1919-173	1893-104	1905-243	2307-386	2335-542	2070-084	2052-063	2328-059
4582.83	26.1	-3.062	2.844	67.4	59.3	...	...	46.7	71.1	66.1	62.2
4583.84	26.1	-1.740	2.807	...	...	66.7	...	...	...	...	...
4620.52	26.1	-3.188	2.828	58.0	52.7	...	...	42.5	63.5	62.1	58.6
4629.34	26.1	-2.480	2.810	...	92.9	42.7	92.7	75.5	...	...	...
4635.31	26.1	-1.580	5.956	...	14.8	...	...	...	...	22.5	21.9
4670.17	26.1	-4.070	2.583	...	57.3	...	...	...	...	...	...
4833.19	26.1	-4.790	2.657	9.8	...	...	...	...	...	...	...
4893.82	26.1	-4.270	2.828	18.7	...	11.2	...	...	24.9	15.8	...
4993.35	26.1	-3.680	2.807	41.5	49.8	...	...	26.9	48.3	49.7	42.1
5018.45	26.1	-1.350	2.891	...	...	94.9	...	...	...	...	...
5132.67	26.1	-4.090	2.807	25.4	...	...	...	...	...	27.5	22.7
5197.58	26.1	-2.054	3.230	83.2	80.6	66.2	...	64.2	...	94.9	86.3
5234.63	26.1	-2.210	3.221	91.3	83.9	34.2	78.7	71.6	...	91.8	85.4
5264.81	26.1	-3.233	3.230	51.3	46.9	...	...	38.1	...	57.1	45.5
5276.00	26.1	-1.900	3.199	...	...	...	...	90.3	...	...	...
5284.11	26.1	-3.200	2.891	72.8	59.6	24.0	...	43.2	...	68.8	62.4
5325.56	26.1	-2.570	3.221	42.6	...	...	...	...	...	...	...
5414.08	26.1	-3.482	3.221	38.5	27.0	...	...	24.2	...	...	33.4
5534.85	26.1	-2.860	3.245	73.5	62.6	...	...	54.3	81.5	75.9	63.0
5627.50	26.1	-4.078	3.387	...	...	...	...	...	...	15.4	...
5991.38	26.1	-3.650	3.153	...	...	...	...	...	59.4	40.8	...
6084.10	26.1	-3.880	3.199	...	18.5	...	...	...	...	...	29.0
6149.25	26.1	-2.840	3.889	45.3	37.4	...	...	34.3	44.4	50.0	42.2
6247.56	26.1	-2.430	3.892	61.7	60.1	35.2	...	47.0	79.4	60.7	56.1
6369.46	26.1	-4.360	2.891	...	22.2	...	...	...	...	27.7	26.1
4121.33	27.0	-0.320	0.920	...	...	...	85.3	84.1	...	100.0	...
5352.05	27.0	0.060	3.560	...	16.9	...	...	...	...	...	...
3807.15	28.0	-1.180	0.420	...	...	...	...	92.8	...	...	...
4686.22	28.0	-0.580	3.600	54.2	56.0	32.5	...	30.2	62.2	43.1	54.7
4831.18	28.0	-0.320	3.610	62.0	...	...	...	34.1	...	...	...
4857.40	28.0	-0.830	3.740	42.0	39.9	...	...	...	44.7	...	36.2

Table C.1: Equivalent Width Measurements, Table 1 of 5, continued

λ (Å)	Ion	loggf	EP	1919-173	1893-104	1905-243	2307-386	2335-542	2070-084	2052-063	2328-059
4866.27	28.0	-0.210	3.539	61.1	...	...	...	33.3	75.5	...	70.9
4904.42	28.0	-0.190	3.540	80.3	79.4	...	...	42.8	87.5	67.1	79.8
4913.98	28.0	-0.630	3.740	46.7	49.3	...	...	...	...	36.2	47.2
4935.83	28.0	-0.380	3.940	53.7	56.8	...	...	...	66.8	41.9	56.7
4953.21	28.0	-0.580	3.740	40.3	47.4	...	...	18.4	52.3	38.1	45.1
4998.22	28.0	-0.690	3.606	41.9	45.2	...	...	...	55.7	39.3	50.9
5010.94	28.0	-0.900	3.630	32.5	37.0	...	...	...	43.2	30.0	40.1
5035.37	28.0	0.290	3.630	93.5	87.7	53.8	68.1	68.7	...	79.5	90.8
5048.85	28.0	-0.390	3.850	52.7	55.9	...	...	29.0	66.4	46.6	61.9
5082.35	28.0	-0.540	3.660	51.5	54.5	...	...	22.8	54.2	41.1	55.5
5084.11	28.0	-0.060	3.680	77.4	81.2	...	62.0	55.1	85.4	71.7	82.2
5088.54	28.0	-1.080	3.850	...	22.5	...	...	...	...	...	21.7
5088.96	28.0	-1.290	3.680	15.9	...	...	...	...	...	...	...
5094.42	28.0	-1.120	3.830	...	...	...	...	...	...	...	22.6
5102.97	28.0	-2.660	1.680	...	38.7	...	...	...	...	22.9	39.6
5115.40	28.0	-0.140	3.830	59.5	65.3	23.2	...	41.1	74.2	61.6	68.1
5578.72	28.0	-2.640	1.680	33.1	43.2	...	...	...	...	26.9	36.2
5587.86	28.0	-2.140	1.930	...	50.2	...	...	...	...	...	43.8
5589.36	28.0	-1.140	3.900	15.7	21.7	...	...	...	...	...	17.8
5593.74	28.0	-0.840	3.900	29.9	32.6	...	...	...	42.7	23.2	28.6
5625.32	28.0	-0.701	4.090	...	34.7	...	...	...	...	...	...
5682.20	28.0	-0.469	4.100	42.7	...	...	...	21.9	...	35.9	41.6
5748.35	28.0	-3.260	1.680	...	22.2	...	...	...	...	...	...
5754.67	28.0	-1.850	1.930	56.1	65.8	...	...	24.8	...	48.1	...
5760.83	28.0	-0.805	4.100	...	28.6	...	...	...	...	19.6	24.5
5805.22	28.0	-0.638	4.170	...	36.2	...	...	...	...	27.2	34.8
5846.99	28.0	-3.210	1.680	...	16.2	...	...	...	...	...	14.7
5892.87	28.0	-2.340	1.990	...	...	...	...	...	84.7	...	...
5996.74	28.0	-1.010	4.236	...	16.2	...	...	...	...	...	20.1
6007.32	28.0	-3.410	1.677	...	21.8	...	...	...	...	...	...
6086.28	28.0	-0.515	4.260	...	...	...	...	...	...	...	41.8

Table C.1: Equivalent Width Measurements, Table 1 of 5, continued

λ (Å)	Ion	loggf	EP	1919-173	1893-104	1905-243	2307-386	2335-542	2070-084	2052-063	2328-059
6108.12	28.0	-2.430	1.680	45.0	60.5	...	...	33.4	64.3	48.3	53.8
6111.08	28.0	-0.820	4.090	24.6	29.7	...	...	...	31.8	18.8	28.7
6128.97	28.0	-3.330	1.680	...	16.5	...	...	...	...	...	...
6175.37	28.0	-0.535	4.090	...	41.2	...	...	...	...	33.1	41.7
6176.81	28.0	-0.529	4.090	52.9	56.2	...	...	...	71.7	43.7	58.7
6186.71	28.0	-0.965	4.100	24.7	...	...	...	...	...	...	...
6223.98	28.0	-0.910	4.106	...	29.8	...	...	...	...	...	21.6
6314.66	28.0	-1.770	1.930	...	70.1	...	...	...	...	48.1	68.1
6327.60	28.0	-3.060	1.680	...	34.8	...	...	...	...	...	...
5105.54	29.0	-3.720	1.380	63.5	...	30.3	...	29.5	87.2	51.4	78.2
5782.12	29.0	-1.780	1.642	60.9	65.9	...	...	...	...	...	...
4722.16	30.0	-0.390	4.030	74.9	69.8	...	...	47.6	85.2	61.3	76.7
4810.54	30.0	-0.170	4.080	72.5	68.9	24.8	...	47.1	84.6	63.9	76.0
4607.34	38.0	0.280	0.000	32.2	82.7	...	...	...	...	27.0	33.4
3549.01	39.1	-0.280	0.130	...	70.8	45.9	...	58.7	65.2	63.9	59.2
3600.74	39.1	0.280	0.180	76.0	74.9	39.2	...	61.2	72.8	79.2	71.3
3747.55	39.1	-0.910	0.100	...	...	...	...	...	53.3	...	41.8
3774.33	39.1	0.210	0.130	...	86.7	49.6	...	68.8	...	...	72.6
3788.70	39.1	-0.070	0.100	...	...	...	78.0	59.6	...	...	...
3818.34	39.1	-0.980	0.130	...	...	...	...	42.0	...	...	...
3950.36	39.1	-0.490	0.100	62.9	62.5	...	68.5	51.6	75.2	72.2	62.2
4398.01	39.1	-1.000	0.130	48.1	...	...	...	...	...	...	37.6
4883.69	39.1	0.070	1.080	59.6	58.4	...	50.4	40.7	65.1	63.8	54.8
4900.12	39.1	-0.090	1.030	...	...	...	87.3	...	...	...	...
5087.43	39.1	-0.170	1.080	44.0	39.2	11.1	44.5	29.7	...	52.6	39.6
5123.22	39.1	-0.830	0.990	...	29.9	...	...	...	...	...	...
5200.41	39.1	-0.570	0.990	33.6	30.3	...	...	...	...	39.9	30.2
3607.38	40.1	-0.700	1.240	...	52.0	...	...	...	...	...	...
3714.78	40.1	-0.960	0.530	28.2	...	...	...	...	...	26.8	...
4208.99	40.1	-0.510	0.710	45.8	...	...	...	22.2	50.2	48.8	41.4
4496.97	40.1	-0.890	0.710	...	...	...	95.1	...	...	...	...

Table C.1: Equivalent Width Measurements, Table 1 of 5, continued

λ (Å)	Ion	loggf	EP	1919-173	1893-104	1905-243	2307-386	2335-542	2070-084	2052-063	2328-059
3692.36	45.0	0.173	0.000	28.7	...	...	...	...	...	...	...
4554.04	56.1	0.140	0.000	...	...	83.2	...	...	...	...	...
5853.69	56.1	-0.910	0.600	71.5	62.3	28.7	82.1	45.0	77.2	75.6	65.9
3988.51	57.1	0.210	0.170	43.0	45.2	...	...	19.7	60.3	44.9	41.8
3995.75	57.1	-0.060	0.170	...	...	...	...	19.8	...	...	...
4086.71	57.1	-0.070	0.000	39.6	...	...	...	19.8	48.8	40.9	40.5

Table C.2: Equivalent Width Measurements, Table 2 of 5

λ (Å)	Ion	loggf	EP	2068-151	2051-595	2307-074	2052-537	2180-560	2798-073	1917-020	2251-632
5682.65	11.0	-0.699	2.100	78.0	...	79.2	65.5	...	33.2	...	80.9
5688.19	11.0	-0.420	2.100	...	...	...	93.2	63.4	58.1	...	...
6154.23	11.0	-1.530	2.100	27.1	...	19.8	...	...	...	24.2	18.9
6160.75	11.0	-1.230	2.100	41.7	...	39.1	...	...	...	...	43.5
4571.10	12.0	-5.570	0.000	...	70.5	...	67.0	48.9	48.1	89.0	89.1
4730.04	12.0	-2.347	4.350	55.3	...	...	...	25.5	...	...	51.3
5711.09	12.0	-1.630	4.340	...	68.3	...	74.6	56.2	61.6	86.0	87.6
5665.55	14.0	-2.040	4.920	28.5	...	...	...	...	...	34.8	32.6
5684.49	14.0	-1.420	4.950	49.4	...	43.8	...	...	...	...	...
5690.43	14.0	-1.870	4.930	39.7	35.0	40.3	...	...	...	40.5	30.2
5701.10	14.0	-2.050	4.930	26.8	...	30.0	...	...	...	30.8	30.6
5708.40	14.0	-1.470	4.950	...	48.6	...	...	35.0	37.4	...	...
5772.15	14.0	-1.750	5.080	35.6	...	38.2	...	...	...	45.4	39.2
5793.07	14.0	-2.060	4.930	36.9	...	31.2	...	...	...	40.0	37.6
5948.54	14.0	-1.230	5.080	69.2	...	63.3	64.6	45.3	37.1	73.8	68.4
6125.03	14.0	-1.570	5.610	24.5	...	...	...	...	9.9	19.5	26.2

Table C.2: Equivalent Width Measurements, Table 2 of 5, continued

λ (Å)	Ion	loggf	EP	2068-151	2051-595	2307-074	2052-537	2180-560	2798-073	1917-020	2251-632
6142.49	14.0	-1.480	5.620	18.8	...	...	...	...	...	26.8	...
6145.02	14.0	-1.370	5.610	28.7	...	...	...	...	...	26.2	34.7
6155.13	14.0	-0.760	5.620	61.1	...	64.4	...	31.2	37.1	73.2	...
6237.32	14.0	-1.010	5.620	50.8	41.5	45.8	...	...	...	...	47.1
6243.82	14.0	-1.300	5.616	...	21.0	40.7	...	...	...	...	36.4
6244.48	14.0	-1.320	5.616	33.4	32.6	33.0	...	...	...	38.5	33.4
6347.09	14.1	0.260	8.120	42.0	...	42.0	...	46.3	54.3	49.2	...
6371.35	14.1	-0.050	8.120	...	...	...	42.7	...	...	...	...
4318.66	20.0	-0.210	1.900	...	...	...	...	93.2	97.1	...	...
4526.93	20.0	-0.420	2.710	74.6	61.1	86.0	55.1	40.9	38.0	64.2	65.5
4578.56	20.0	-0.558	2.520	67.5	53.5	78.3	62.1	41.1	39.4	72.6	68.1
4685.27	20.0	-0.940	2.930	43.5	32.4	41.6	...	...	23.2	...	44.6
5260.39	20.0	-1.780	2.520	...	...	...	...	...	...	20.8	15.8
5261.71	20.0	-0.730	2.520	81.2	65.6	85.7	74.3	50.7	51.8	82.6	80.6
5512.99	20.0	-0.266	2.930	70.0	...	...	...	33.7	44.7	72.9	73.6
5590.13	20.0	-0.710	2.510	82.3	66.2	73.5	73.0	49.4	51.5	72.3	84.0
5594.47	20.0	0.050	2.510	...	...	...	...	96.6	94.8	...	...
5601.28	20.0	-0.438	2.520	82.6	70.7	79.5	...	51.9	55.6	89.3	89.2
6102.73	20.0	-0.790	1.880	...	93.9	...	...	...	...	...	...
6161.30	20.0	-1.270	2.520	49.7	...	53.6	...	...	21.2	44.7	47.1
6166.44	20.0	-1.140	2.520	47.6	36.0	66.7	...	16.3	...	47.4	50.4
6169.04	20.0	-0.800	2.520	78.1	55.1	87.5	63.8	...	40.8	75.9	76.9
6169.56	20.0	-0.480	2.520	90.4	68.9	95.7	84.2	...	56.1	99.3	97.0
5001.47	20.1	-0.520	7.500	...	...	...	...	...	...	15.3	...
5239.82	21.1	-0.765	1.450	48.7	39.2	46.1	43.2	...	33.3	53.8	47.3
5526.82	21.1	0.020	1.770	80.9	73.6	71.5	78.3	60.0	57.2	84.9	67.8
5640.99	21.1	-1.130	1.500	42.0	...	34.9	...	...	...	...	38.6
5657.88	21.1	-0.600	1.510	66.6	...	61.1	58.9	35.5	52.2	76.3	55.2
5667.15	21.1	-1.360	1.500	30.2	...	31.3	...	...	...	...	14.0
5669.04	21.1	-1.120	1.500	31.8	...	29.4	...	...	25.5	42.1	...
5684.20	21.1	-1.080	1.507	39.8	...	33.0	...	...	...	...	...

Table C.2: Equivalent Width Measurements, Table 2 of 5, continued

λ (Å)	Ion	loggf	EP	2068-151	2051-595	2307-074	2052-537	2180-560	2798-073	1917-020	2251-632
3924.53	22.0	-0.940	0.020	61.2	47.1	...	...	29.5	30.4	50.5	55.1
3958.22	22.0	-0.176	0.050	...	...	91.7	86.9	66.3	62.0	...	...
3998.64	22.0	-0.060	0.050	...	...	...	92.4	78.0	73.1	...	...
4008.93	22.0	-1.072	0.021	...	...	...	...	38.4	39.4	...	...
4512.74	22.0	-0.480	0.840	62.5	34.6	48.9	32.5	20.1	23.3	45.6	50.6
4518.03	22.0	-0.325	0.830	66.8	42.7	57.4	...	...	...	...	52.7
4534.78	22.0	0.280	0.840	90.2	73.1	87.8	70.4	60.8	55.0	78.6	83.1
4548.77	22.0	-0.354	0.830	61.1	47.0	60.5	40.7	32.0	27.3	48.1	53.7
4555.49	22.0	-0.490	0.850	56.5	34.9	53.7	...	25.1	17.8	41.6	53.1
4617.28	22.0	0.390	1.750	59.5	40.7	54.4	...	...	...	50.7	53.8
4623.10	22.0	0.170	1.740	51.3	30.5	31.7	...	14.7	...	34.4	43.8
4758.12	22.0	0.425	2.250	35.4	14.9	28.3	...	...	...	26.5	30.4
4759.28	22.0	0.514	2.250	36.9	21.4	32.2	...	15.2	12.4	28.9	33.8
4820.41	22.0	-0.439	1.500	31.4	15.5	29.1	...	...	...	19.5	27.1
4840.88	22.0	-0.450	0.900	59.3	32.7	52.4	...	19.8	...	45.7	50.8
4913.62	22.0	0.220	1.870	42.2	20.5	44.1	...	...	14.9	...	35.3
4981.74	22.0	0.504	0.850	...	82.1	...	92.1	73.0	68.1	93.8	96.8
4999.51	22.0	0.250	0.830	96.8	74.2	...	...	61.0	61.2	84.6	91.8
5016.17	22.0	-0.574	0.850	58.5	31.7	48.2	...	...	21.5	39.6	47.2
5022.87	22.0	-0.430	0.830	64.3	37.1	61.5	38.4	25.2	20.9	49.3	51.5
5024.85	22.0	-0.600	0.820	59.0	27.9	60.0	40.5	21.1	23.3	...	...
5039.96	22.0	-1.130	0.020	73.9	43.5	...	...	...	30.7	59.7	...
5064.66	22.0	-0.990	0.050	73.4	...	72.3	...	...	...	...	...
5087.06	22.0	-0.780	1.430	17.8	...	...	...	...	...	...	12.6
5113.45	22.0	-0.780	1.440	22.3	...	...	...	...	...	...	...
5192.98	22.0	-1.006	0.020	72.3	49.0	74.5	...	30.7	34.9	60.5	69.3
5210.39	22.0	-0.884	0.050	86.2	51.1	72.1	60.8	49.0	46.6	65.7	63.1
5219.71	22.0	-2.292	0.020	22.2	...	...	...	...	...	...	15.4
5662.16	22.0	-0.110	2.320	20.5	...	...	...	...	...	...	...
5866.45	22.0	-0.840	1.070	40.9	...	29.1	...	...	...	34.4	28.6
5922.11	22.0	-1.470	1.050	...	...	...	...	...	...	...	10.7

Table C.2: Equivalent Width Measurements, Table 2 of 5, continued

λ (Å)	Ion	loggf	EP	2068-151	2051-595	2307-074	2052-537	2180-560	2798-073	1917-020	2251-632
6258.10	22.0	-0.355	1.440	44.5	...	33.5	...	...	...	25.1	46.0
6258.71	22.0	-0.240	1.460	58.7	33.4	35.4	31.0	...	...	...	44.5
6261.11	22.0	-0.480	1.430	37.5	...	...	...	...	...	...	36.9
3987.61	22.1	-2.730	0.610	57.8	42.5	49.0	43.0	35.0	38.8	47.0	...
4028.35	22.1	-1.000	1.890	89.6	80.8	82.1	79.2	66.4	74.3	86.5	76.1
4394.06	22.1	-1.770	1.220	...	74.6	...	...	63.9	72.2	...	...
4395.84	22.1	-1.970	1.240	67.9	62.2	...	61.8	48.2	58.8	...	56.5
4399.77	22.1	-1.270	1.240	...	...	...	...	85.4	95.2	...	...
4417.72	22.1	-1.430	1.160	...	...	93.4	93.4	...	...	...	...
4418.33	22.1	-1.990	1.240	71.0	63.6	69.5	64.3	...	...	...	...
4544.02	22.1	-2.410	1.240	38.6	33.1	29.5	...	...	...	...	31.7
4568.33	22.1	-2.650	1.220	23.5	23.3	21.9	21.8	...	...	28.6	22.3
4583.42	22.1	-2.720	1.160	27.6	21.0	29.0	...	16.0	...	24.3	23.9
4589.95	22.1	-1.790	1.240	82.1	79.4	81.4	79.3	75.4	73.7	91.6	79.6
4636.32	22.1	-3.020	1.165	21.5	...	...	...	...	...	22.2	11.8
4708.67	22.1	-2.210	1.240	46.1	42.4	46.2	43.9	...	...	...	43.7
4779.98	22.1	-1.370	2.048	66.7	61.5	62.2	67.1	57.0	58.1	70.2	66.1
4798.54	22.1	-2.430	1.080	...	...	...	...	...	34.9	...	...
4805.09	22.1	-1.120	2.061	...	...	...	...	64.5	74.8	97.4	89.7
4865.62	22.1	-2.590	1.120	...	...	40.7	...	...	...	...	...
4874.01	22.1	-0.790	3.090	37.3	34.4	...	...	19.7	27.4	35.7	...
4911.20	22.1	-0.330	3.120	51.2	48.1	...	...	36.0	...	...	46.5
4981.36	22.1	-3.160	1.570	...	...	...	...	...	...	...	8.7
5005.17	22.1	-2.540	1.570	23.0	...	...	...	...	...	...	...
5154.07	22.1	-1.920	1.570	65.0	65.2	62.6	...	54.0	61.7	...	...
5185.91	22.1	-1.350	1.890	...	63.0	66.3	65.7	50.3	57.3	73.5	58.9
5211.53	22.1	-1.160	2.590	...	...	29.2	...	...	...	41.8	...
5336.79	22.1	-1.630	1.580	70.3	66.2	69.2	70.7	61.8	70.9	75.5	72.9
5381.01	22.1	-1.970	1.570	55.8	49.4	53.9	...	46.8	48.1	60.1	55.0
5418.78	22.1	-2.110	1.580	60.3	39.2	47.1	...	...	...	...	...
5490.69	22.1	-2.430	1.566	...	...	...	...	...	...	...	22.9

Table C.2: Equivalent Width Measurements, Table 2 of 5, continued

λ (Å)	Ion	loggf	EP	2068-151	2051-595	2307-074	2052-537	2180-560	2798-073	1917-020	2251-632
4115.18	23.0	0.070	0.290	66.9	...	63.6	...	15.3	...	...	...
4116.47	23.0	-0.310	0.280	45.5	...	...	...	...	...	...	...
4406.63	23.0	-0.190	0.300	...	...	70.3	...	13.8	...	46.8	62.5
4875.49	23.0	-0.810	0.040	32.6	...	...	...	...	...	...	21.0
5627.64	23.0	-0.370	1.080	...	...	...	...	...	...	...	23.1
5727.06	23.0	-0.010	1.080	19.8	...	...	...	...	...	...	...
6090.22	23.0	-0.060	1.080	...	...	...	...	...	...	...	21.5
3545.19	23.1	-0.390	1.100	76.1	75.7	...	...	...	73.1	...	72.2
3592.03	23.1	-0.370	1.100	78.6	80.4	79.0	79.3	62.3	69.8	70.2	65.5
3951.97	23.1	-0.744	1.480	63.7	63.4	55.1	57.5	41.2	51.7	52.5	55.3
3732.02	24.0	-2.570	0.000	51.4	...	...	...	...	...	...	55.2
3768.74	24.0	-0.920	2.544	...	...	...	...	...	...	42.1	29.4
3928.64	24.0	-1.310	1.004	...	...	...	...	28.3	...	...	...
4272.90	24.0	-0.980	2.900	...	...	...	...	...	...	17.5	16.5
4373.26	24.0	-2.300	0.983	...	...	...	...	...	...	...	22.0
4496.84	24.0	-1.140	0.941	91.8	76.2	...	76.0	...	57.7	...	...
4511.90	24.0	-0.343	3.090	19.8	14.4	23.7	...	...	...	24.0	28.4
4545.95	24.0	-1.370	0.941	62.0	60.1	73.2	48.9	30.3	...	67.9	69.4
4580.04	24.0	-1.660	0.941	62.1	46.0	69.9	52.1	25.8	26.6	...	...
4591.39	24.0	-1.740	0.968	63.8	55.0	71.8	...	...	...	...	...
4600.74	24.0	-1.250	1.004	...	50.1	...	...	...	...	...	...
4616.12	24.0	-1.190	0.983	74.8	61.7	79.5	63.2	36.4	...	76.2	80.4
4626.17	24.0	-1.330	0.968	63.9	53.6	72.2	54.5	...	31.9	70.6	72.2
4646.15	24.0	-0.740	1.030	...	75.3	96.6	82.0	50.4	51.5	...	...
4651.28	24.0	-1.460	0.983	62.3	43.8	65.1	50.8	29.0	23.1	66.9	62.5
4652.15	24.0	-1.040	1.004	80.6	66.7	86.7	69.3	40.0	42.1	86.2	84.8
4708.02	24.0	0.070	3.168	33.7	26.5	38.1	23.0	...	13.1	40.0	38.9
4718.43	24.0	0.240	3.195	45.3	36.4	51.4	38.3	21.3	...	43.5	47.6
4724.41	24.0	-0.733	3.090	...	...	...	...	...	...	20.5	24.3
4730.72	24.0	-0.192	3.080	26.4	...	...	...	18.5	...	...	...
4737.35	24.0	-0.100	3.090	35.8	...	41.7	...	...	...	...	43.4

Table C.2: Equivalent Width Measurements, Table 2 of 5, continued

λ (Å)	Ion	loggf	EP	2068-151	2051-595	2307-074	2052-537	2180-560	2798-073	1917-020	2251-632
4789.34	24.0	-0.330	2.544	41.8	34.9	48.2	...	...	...	42.5	48.0
4801.03	24.0	-0.130	3.120	...	...	...	...	...	...	...	36.7
4936.34	24.0	-0.250	3.113	31.4	...	29.9	...	...	...	35.1	33.6
4964.93	24.0	-2.526	0.940	17.9	...	...	...	...	...	...	...
5067.72	24.0	-1.070	2.709	...	...	...	...	...	...	20.5	22.3
5247.57	24.0	-1.590	0.961	56.1	44.2	60.5	...	...	...	61.0	54.7
5296.69	24.0	-1.360	0.983	74.1	55.5	72.6	56.4	...	21.7	76.6	76.9
5297.39	24.0	0.000	2.900	...	47.7	...	...	...	...	...	66.8
5300.74	24.0	-2.000	0.983	...	...	44.4	...	...	...	40.0	39.6
5312.87	24.0	-0.550	3.449	...	14.4	...	...	...	...	...	...
5345.80	24.0	-0.950	1.004	82.2	71.9	90.3	...	50.2	43.5	89.6	90.4
5348.31	24.0	-1.210	1.004	75.4	59.1	82.7	60.1	29.2	31.0	73.2	75.3
5409.77	24.0	-0.670	1.030	...	90.9	...	...	62.1	59.8	...	...
5712.75	24.0	-1.030	3.011	...	...	...	...	...	...	14.2	...
5783.09	24.0	-0.500	3.320	...	...	...	...	...	...	17.1	18.0
5783.89	24.0	-0.295	3.320	...	...	...	...	...	...	28.6	30.6
5787.93	24.0	-0.083	3.320	...	...	...	...	...	...	28.5	35.8
4554.99	24.1	-1.373	4.070	34.5	43.6	39.4	39.7	28.1	27.0	50.3	44.1
4558.65	24.1	-0.656	4.070	65.1	81.1	...	84.4	58.3	68.4	87.2	77.4
4588.20	24.1	-0.826	4.070	53.7	66.7	63.8	68.4	50.1	59.4	75.7	62.7
4592.06	24.1	-1.419	4.070	35.8	42.8	41.5	44.2	18.1	25.2	...	43.0
4616.63	24.1	-1.210	4.073	27.8	43.7	38.6	...	...	25.5	52.9	39.0
4848.23	24.1	-0.999	3.870	...	53.2	56.5	59.6	38.2	38.4	67.2	61.8
5237.33	24.1	-1.155	4.070	36.4	41.1	44.4	57.8	24.6	30.4	52.6	47.3
5305.86	24.1	-2.060	3.830	13.6	...	...	...	...	...	27.6	20.2
5308.42	24.1	-1.790	4.070	...	...	...	...	...	...	21.4	...
5313.59	24.1	-1.640	4.070	...	...	...	...	12.9	...	36.6	29.5
4055.55	25.0	-0.080	2.140	...	83.2	92.0	73.2	41.8	51.1	98.5	...
4709.72	25.0	-0.339	2.890	32.0	25.6	44.7	...	...	...	44.5	46.8
4739.11	25.0	-0.490	2.940	30.4	...	34.6	...	...	...	39.1	46.5
4761.53	25.0	-0.138	2.950	43.0	31.6	44.5	42.4	15.5	...	58.6	54.1

Table C.2: Equivalent Width Measurements, Table 2 of 5, continued

λ (Å)	Ion	loggf	EP	2068-151	2051-595	2307-074	2052-537	2180-560	2798-073	1917-020	2251-632
4783.43	25.0	0.042	2.300	99.2	87.9	...	95.0	45.6	49.4	...	...
4823.51	25.0	0.144	2.320	...	...	...	...	44.9	...	...	...
6013.50	25.0	-0.252	3.070	55.3	...	53.4	...	...	...	...	56.6
6021.80	25.0	0.030	3.080	56.0	47.2	68.0	41.7	...	...	77.1	69.0
3916.74	26.0	-0.604	3.237	71.6	64.3	89.9	74.7	...	55.1	...	...
3917.18	26.0	-2.155	0.990	...	95.4	...	99.4	...	79.9	...	...
3949.96	26.0	-1.251	2.176	88.1	79.1	...	84.9	77.2	78.4	86.6	90.2
4114.45	26.0	-1.303	2.832	73.6	66.1	80.1	69.1	49.8	45.8	82.2	74.4
4132.91	26.0	-1.006	2.845	80.0	...	...	...	63.4	...	...	...
4139.94	26.0	-3.629	0.990	58.4	40.1	64.9	43.3	...	21.6	54.2	57.7
4147.68	26.0	-2.104	1.485	...	84.7	...	...	61.5	65.0	...	...
4157.79	26.0	-0.403	3.417	...	82.2	97.3	87.4	64.5	75.2	...	99.4
4174.92	26.0	-2.969	0.915	...	81.9	...	...	56.4	55.6	...	...
4175.64	26.0	-0.827	2.845	93.0	83.0	...	92.1	67.8	72.6	...	...
4184.91	26.0	-0.869	2.832	91.3	83.6	93.0	87.7	59.7	60.9	93.4	88.2
4187.05	26.0	-0.548	2.450	...	...	...	...	99.6	88.2	...	...
4199.10	26.0	0.156	3.047	...	...	...	...	97.4	90.1	...	...
4216.19	26.0	-3.356	0.000	...	...	...	...	76.2	72.7	...	...
4217.56	26.0	-0.484	3.430	98.2	84.5	...	92.4	67.1	65.5	...	...
4222.22	26.0	-0.967	2.450	...	...	...	...	79.2	77.7	...	...
4233.61	26.0	-0.604	2.482	...	...	...	...	92.5	...	...	...
4238.81	26.0	-0.233	3.397	...	98.8	...	...	81.2	73.1	...	...
4250.13	26.0	-0.405	2.469	...	...	...	...	...	95.0	...	...
4282.41	26.0	-0.779	2.176	...	...	...	...	87.7	...	...	...
4347.24	26.0	-5.503	0.000	24.5	...	26.1	...	...	...	...	19.7
4375.94	26.0	-3.031	0.000	...	...	...	...	85.9	85.1	...	...
4388.41	26.0	-0.682	3.603	...	68.1	...	69.0	46.5	50.6	...	81.7
4389.25	26.0	-4.583	0.052	54.8	39.5	59.5	29.8	14.7	17.5	54.0	52.5
4489.75	26.0	-3.966	0.121	81.3	70.1	90.7	66.9	45.7	...	...	84.1
4494.57	26.0	-1.136	2.198	...	...	...	...	88.7	92.4	...	...
4517.52	26.0	-1.860	3.071	48.8	37.3	53.3	39.3	21.3	...	51.1	58.7

Table C.2: Equivalent Width Measurements, Table 2 of 5, continued

λ (Å)	Ion	loggf	EP	2068-151	2051-595	2307-074	2052-537	2180-560	2798-073	1917-020	2251-632
4523.41	26.0	-1.960	3.654	25.3	...	21.1	...	...	...	24.8	27.7
4547.85	26.0	-1.010	3.546	67.4	64.8	77.6	62.9	42.5	40.9	70.9	70.9
4551.65	26.0	-2.030	3.943	...	...	...	...	...	...	11.4	10.6
4566.52	26.0	-2.380	3.300	...	14.6	29.3	14.1	...	...	23.6	28.0
4574.23	26.0	-2.450	3.211	14.0	...	27.1	...	...	...	17.8	18.4
4587.13	26.0	-1.740	3.573	34.9	27.3	39.0	23.0	...	...	42.0	43.7
4593.53	26.0	-2.030	3.943	...	...	...	...	...	...	...	16.8
4602.01	26.0	-3.154	1.608	54.3	44.9	60.1	...	19.0	16.7	55.5	59.8
4602.95	26.0	-2.220	1.485	96.7	88.6	...	93.2	70.0	63.8	...	...
4630.12	26.0	-2.587	2.279	52.9	38.8	47.9	40.7	22.7	18.6	60.4	58.2
4632.92	26.0	-2.913	1.608	86.4	64.7	...	65.1	35.7	28.7	...	98.3
4635.85	26.0	-2.360	2.840	32.6	22.0	44.4	20.8	...	...	40.7	39.5
4647.43	26.0	-1.351	2.949	...	65.4	...	75.4	48.5	...	...	...
4658.30	26.0	-2.990	3.267	...	...	...	...	...	...	...	15.5
4672.84	26.0	-4.240	1.610	16.4	...	...	...	...	...	...	...
4683.56	26.0	-2.320	2.832	33.8	18.5	33.4	...	...	...	35.8	41.0
4690.14	26.0	-1.640	3.687	33.9	26.1	...	23.7	...	10.1	41.4	43.4
4733.59	26.0	-2.990	1.485	66.1	56.5	68.9	67.5	36.7	30.0	79.4	...
4741.53	26.0	-1.760	2.830	55.2	49.4	...	...	...	...	62.0	52.8
4745.80	26.0	-1.270	3.654	55.1	43.0	62.4	51.1	28.8	...	65.2	57.9
4779.45	26.0	-2.020	3.415	23.6	...	26.2	...	...	...	28.9	30.1
4787.83	26.0	-2.600	2.998	21.5	14.0	27.6	...	...	...	24.0	27.1
4788.76	26.0	-1.763	3.237	48.2	43.0	51.4	...	...	11.8	57.3	54.5
4789.65	26.0	-0.910	3.547	68.4	63.0	68.6	...	...	...	...	77.9
4802.88	26.0	-1.510	3.642	...	38.5	54.4	35.1	12.6	...	51.7	48.7
4808.16	26.0	-2.740	3.251	...	...	20.5	...	...	...	17.0	14.0
4809.94	26.0	-2.680	3.573	...	...	...	...	...	...	8.7	16.3
4835.87	26.0	-1.470	4.103	...	25.8	33.7	...	...	...	...	38.8
4839.52	26.0	-1.820	3.270	48.0	33.6	42.0	...	14.2	...	...	54.8
4844.01	26.0	-2.050	3.547	24.2	15.7	25.9	...	...	...	31.0	28.1
4871.33	26.0	-0.362	2.865	...	...	...	...	86.1	93.2	...	...

Table C.2: Equivalent Width Measurements, Table 2 of 5, continued

λ (Å)	Ion	loggf	EP	2068-151	2051-595	2307-074	2052-537	2180-560	2798-073	1917-020	2251-632
4872.14	26.0	-0.567	2.882	...	...	...	...	78.5	85.1	...	...
4882.14	26.0	-1.640	3.420	...	44.3	65.2	42.0	18.7	17.9	59.2	61.3
4890.76	26.0	-0.394	2.875	...	...	...	...	91.0	85.6	...	...
4892.87	26.0	-1.290	4.220	31.8	26.0	38.8	...	...	...	38.3	40.3
4903.32	26.0	-0.926	2.882	...	97.3	...	...	70.2	70.5	...	...
4905.14	26.0	-2.020	3.929	...	...	...	...	...	...	15.5	13.9
4917.24	26.0	-1.160	4.191	44.0	38.7	45.9	...	21.2	...	57.8	50.8
4924.77	26.0	-2.114	2.279	74.9	64.7	77.6	71.6	34.8	30.6	80.1	75.5
4938.82	26.0	-1.077	2.875	...	86.0	97.4	86.1	65.1	59.4	...	...
4939.69	26.0	-3.340	0.859	82.5	71.5	90.1	70.7	40.5	41.3	84.2	87.7
4961.92	26.0	-2.250	3.634	13.4	...	...	...	...	...	13.0	14.8
4962.58	26.0	-1.182	4.178	33.7	26.1	37.5	...	...	10.3	40.3	36.3
4966.09	26.0	-0.871	3.332	87.7	77.6	97.3	76.9	54.4	...	...	...
4994.14	26.0	-3.080	0.915	87.6	75.3	91.2	...	53.9	53.0	85.2	87.7
5001.87	26.0	-0.010	3.882	...	...	...	...	75.9	...	...	...
5014.94	26.0	-0.303	3.943	83.8	75.7	94.4	85.2	53.8	52.2	94.4	...
5044.21	26.0	-2.060	2.850	50.1	41.1	47.7	44.1	20.7	17.4	56.0	57.5
5049.83	26.0	-1.355	2.279	...	94.8	...	...	79.9	76.0	...	...
5051.64	26.0	-2.795	0.915	...	...	...	...	74.3	68.7	...	...
5054.64	26.0	-1.920	3.640	27.2	...	...	...	...	...	24.7	17.1
5067.16	26.0	-0.970	4.220	46.4	43.6	...	40.6	...	22.7	56.9	55.5
5068.77	26.0	-1.042	2.940	98.1	88.9	...	89.9	...	59.9	96.6	...
5074.75	26.0	-0.230	4.220	93.0	86.3	96.7	85.7	56.6	60.1	93.7	99.0
5079.74	26.0	-3.220	0.990	...	...	...	...	...	41.3	...	...
5083.35	26.0	-2.958	0.958	87.8	82.3	94.6	79.9	55.4	47.7	90.7	93.1
5088.16	26.0	-1.680	4.150	18.6	14.8	...	...	...	...	17.4	19.0
5090.78	26.0	-0.400	4.260	64.9	51.1	71.1	55.6	33.2	29.1	73.7	74.3
5109.66	26.0	-0.980	4.300	55.2	46.5	68.0	49.1	...	24.2	65.0	55.0
5123.73	26.0	-3.068	1.011	91.2	76.4	91.3	75.0	49.4	48.5	92.4	87.0
5125.12	26.0	-0.080	4.220	...	99.2	...	...	67.2	67.8	...	...
5127.37	26.0	-3.307	0.915	78.7	69.3	80.2	66.8	52.4	41.3	81.9	79.6

Table C.2: Equivalent Width Measurements, Table 2 of 5, continued

λ (Å)	Ion	loggf	EP	2068-151	2051-595	2307-074	2052-537	2180-560	2798-073	1917-020	2251-632
5131.48	26.0	-2.515	2.223	67.1	...	68.6	47.5	...	...	...	74.3
5133.69	26.0	0.200	4.180	...	96.2	...	...	71.6	76.6	...	...
5141.74	26.0	-2.238	2.424	64.9	50.4	67.5	50.1	...	...	70.2	70.1
5145.09	26.0	-2.876	2.198	36.6	...	39.2	...	...	...	...	34.9
5150.85	26.0	-3.037	0.990	88.8	73.9	...	86.3	52.0	51.3	...	96.6
5151.92	26.0	-3.322	1.011	79.8	69.0	85.2	68.7	40.5	...	...	83.7
5162.28	26.0	0.020	4.180	99.9	93.2	...	96.5	63.0	65.9	...	...
5166.28	26.0	-4.195	0.000	...	69.1	...	75.6	46.9	48.3	91.4	...
5171.61	26.0	-1.793	1.485	...	...	...	...	...	90.4	...	...
5187.92	26.0	-1.371	4.143	36.6	28.9	43.9	24.4	...	...	39.1	38.7
5191.47	26.0	-0.551	3.038	...	...	...	...	71.5	70.2	...	...
5192.35	26.0	-0.421	2.998	...	...	...	...	90.2	90.4	...	...
5194.95	26.0	-2.090	1.557	...	84.8	...	88.1	66.7	71.0	96.6	...
5198.72	26.0	-2.135	2.223	77.3	68.8	77.6	63.2	50.0	38.3	78.9	82.6
5202.34	26.0	-1.838	2.176	...	...	...	...	72.2	...	...	...
5216.28	26.0	-2.150	1.608	...	83.6	...	97.6	67.1	70.5	...	...
5217.40	26.0	-1.162	3.211	79.6	69.4	86.8	77.0	39.4	47.8	88.5	94.3
5225.53	26.0	-4.789	0.110	61.4	33.6	60.3	...	...	...	...	58.2
5242.46	26.0	-0.967	3.634	82.5	50.1	63.8	...	31.8	37.6	69.9	79.4
5243.78	26.0	-1.120	4.256	37.1	26.5	48.6	...	...	12.2	...	49.1
5247.06	26.0	-4.946	0.087	44.5	...	53.0	...	...	...	...	...
5250.22	26.0	-4.938	0.121	50.5	28.0	47.0	...	...	...	50.9	53.4
5253.03	26.0	-3.940	2.280	...	...	...	...	...	...	...	10.4
5254.95	26.0	-4.764	0.110	...	...	...	...	32.6	...	...	...
5266.56	26.0	-0.385	2.998	...	...	...	...	93.8	92.7	...	...
5281.80	26.0	-0.834	3.038	...	93.4	...	99.8	62.0	74.4	...	...
5283.63	26.0	-0.525	3.241	...	...	...	...	88.4	74.7	...	...
5288.53	26.0	-1.510	3.680	38.5	...	36.0	...	...	...	44.6	45.7
5295.32	26.0	-1.670	4.415	...	...	...	...	...	...	...	21.1
5302.31	26.0	-0.720	3.283	98.3	86.2	...	...	66.0	67.8	...	...
5307.37	26.0	-2.987	1.608	72.2	56.6	74.1	...	31.1	27.8	68.1	72.8

Table C.2: Equivalent Width Measurements, Table 2 of 5, continued

λ (Å)	Ion	loggf	EP	2068-151	2051-595	2307-074	2052-537	2180-560	2798-073	1917-020	2251-632
5321.11	26.0	-1.090	4.435	30.6	...	...	...	...	...	33.3	31.1
5322.01	26.0	-2.803	2.279	33.1	...	36.8	...	...	...	47.2	48.8
5324.19	26.0	-0.103	3.211	...	...	...	...	89.3	97.1	...	...
5332.92	26.0	-2.776	1.557	...	...	...	...	39.7	...	...	...
5339.94	26.0	-0.720	3.266	...	93.1	...	...	66.4	65.8	...	...
5364.87	26.0	0.228	4.446	...	83.2	99.9	...	63.0	57.0	...	...
5365.40	26.0	-1.020	3.573	59.8	49.7	71.7	57.5	35.7	27.5	62.2	67.8
5367.47	26.0	0.443	4.415	97.2	95.0	...	...	55.1	67.2	...	...
5369.97	26.0	0.536	4.371	...	94.4	...	...	69.7	70.3	...	...
5373.70	26.0	-0.760	4.470	39.2	...	45.2	35.1	18.0	...	51.8	51.3
5379.58	26.0	-1.514	3.695	44.7	27.9	39.4	36.1	...	...	48.0	42.5
5383.38	26.0	0.645	4.312	...	...	...	...	81.3	86.6	...	...
5386.34	26.0	-1.740	4.154	...	...	20.6	...	...	...	19.5	17.3
5389.49	26.0	-0.400	4.410	60.3	51.7	74.2	...	26.1	28.6	63.5	67.2
5393.18	26.0	-0.715	3.241	95.4	81.2	...	94.3	65.9	55.5	...	...
5397.14	26.0	-1.993	0.915	...	...	...	...	99.1	...	...	...
5398.29	26.0	-0.710	4.446	40.7	39.9	59.8	48.4	25.5	21.6	58.3	54.4
5401.27	26.0	-1.890	4.320	...	...	...	...	...	...	...	12.5
5406.78	26.0	-1.720	4.370	...	...	...	...	...	...	17.8	21.0
5409.14	26.0	-1.200	4.370	26.9	...	36.4	...	...	...	39.8	40.3
5410.91	26.0	0.398	4.473	83.5	79.7	96.9	...	65.5	62.2	...	...
5415.20	26.0	0.642	4.386	...	99.5	...	...	81.5	77.5	...	...
5417.04	26.0	-1.660	4.415	15.1	...	...	...	...	...	19.8	18.7
5483.10	26.0	-1.410	4.150	23.0	...	...	...	...	...	...	...
5487.14	26.0	-1.430	4.410	16.6	...	29.9	...	...	...	...	30.4
5487.77	26.0	-0.620	4.140	...	67.9	73.6	...	33.7	32.0	...	...
5497.52	26.0	-2.830	1.010	98.2	86.0	...	96.9	66.6	61.1	...	...
5501.48	26.0	-3.047	0.958	90.3	79.4	97.1	77.9	64.0	57.1	99.2	96.9
5506.79	26.0	-2.797	0.990	98.2	87.2	...	95.7	72.6	68.6	...	...
5522.45	26.0	-1.520	4.209	24.7	...	...	...	...	...	25.1	22.1
5525.55	26.0	-1.080	4.230	30.1	...	37.2	...	...	...	...	41.5

Table C.2: Equivalent Width Measurements, Table 2 of 5, continued

λ (Å)	Ion	loggf	EP	2068-151	2051-595	2307-074	2052-537	2180-560	2798-073	1917-020	2251-632
5546.51	26.0	-1.210	4.372	...	...	...	...	...	...	...	41.5
5547.00	26.0	-1.880	4.218	...	...	...	...	...	...	...	18.4
5553.58	26.0	-1.310	4.430	38.3	...	35.1	...	...	...	32.9	33.3
5554.88	26.0	-0.350	4.550	63.0	64.9	72.6	64.8	26.7	28.7	77.7	76.0
5560.22	26.0	-1.160	4.435	24.0	...	32.7	...	...	...	...	48.5
5567.39	26.0	-2.670	2.610	36.4	...	40.8	...	...	...	48.7	42.3
5569.63	26.0	-0.486	3.417	...	95.0	...	...	...	73.0	...	...
5572.85	26.0	-0.275	3.397	...	...	...	...	...	82.4	...	...
5576.10	26.0	-0.940	3.430	81.3	71.3	90.3	76.1	47.7	48.5	93.6	...
5586.77	26.0	-0.144	3.368	...	...	...	...	96.2	93.3	...	...
5618.64	26.0	-1.276	4.209	...	...	37.4	...	...	...	37.8	...
5619.61	26.0	-1.670	4.386	...	...	...	...	...	...	25.4	19.1
5620.49	26.0	-1.810	4.150	...	...	...	...	...	...	25.4	...
5624.04	26.0	-1.220	4.390	33.2	25.1	...	...	...	...	...	40.1
5624.54	26.0	-0.755	3.420	...	85.5	...	90.0	60.2	...	...	...
5635.83	26.0	-1.860	4.256	...	...	...	...	...	...	21.0	20.2
5636.70	26.0	-2.560	3.640	...	...	...	...	...	...	9.7	...
5641.44	26.0	-1.080	4.260	...	...	44.9	...	...	...	49.4	47.7
5652.33	26.0	-1.920	4.260	...	...	...	...	...	...	10.9	...
5661.35	26.0	-1.756	4.284	...	...	...	...	...	...	12.4	...
5662.52	26.0	-0.573	4.178	63.9	58.5	67.2	...	...	40.3	...	78.0
5667.52	26.0	-1.500	4.480	...	20.2	27.3	...	...	...	...	30.3
5679.02	26.0	-0.820	4.650	30.4	26.6	43.9	29.7	...	...	42.6	51.7
5686.53	26.0	-0.446	4.548	45.8	62.1	...	...	...	...	...	...
5701.56	26.0	-2.216	2.559	62.1	53.7	63.0	...	...	...	65.6	71.0
5705.47	26.0	-1.360	4.300	16.5	...	26.4	...	...	...	34.1	24.8
5705.98	26.0	-0.490	4.610	57.6	...	73.6	...	...	...	...	...
5717.84	26.0	-1.100	4.284	43.5	31.4	47.3	48.3	...	17.3	46.5	49.1
5731.77	26.0	-1.270	4.256	40.2	31.0	46.2	...	...	...	44.8	33.5
5741.86	26.0	-1.673	4.256	...	...	19.5	...	...	...	...	19.4
5752.04	26.0	-0.940	4.550	28.1	...	42.6	...	...	...	42.2	41.1

Table C.2: Equivalent Width Measurements, Table 2 of 5, continued

λ (Å)	Ion	loggf	EP	2068-151	2051-595	2307-074	2052-537	2180-560	2798-073	1917-020	2251-632
5753.12	26.0	-0.688	4.260	49.7	...	60.5	...	26.0	...	62.6	59.8
5760.36	26.0	-2.440	3.642	...	...	...	...	...	...	...	16.6
5762.99	26.0	-0.410	4.210	82.4	70.3	87.3	78.7	47.2	50.2	...	95.7
5775.09	26.0	-1.298	4.220	33.6	30.6	45.9	...	...	...	42.5	44.6
5793.92	26.0	-1.660	4.220	...	...	...	...	...	...	23.1	16.5
5806.73	26.0	-1.030	4.608	...	...	...	...	...	...	46.0	37.0
5809.22	26.0	-1.740	3.880	...	...	...	...	...	...	36.3	33.6
5814.81	26.0	-1.940	4.283	...	...	...	...	...	...	9.1	...
5816.38	26.0	-0.601	4.548	46.5	...	59.1	46.0	...	...	...	62.8
5852.23	26.0	-1.300	4.548	19.5	...	20.8	...	...	...	29.6	27.1
5855.09	26.0	-1.478	4.608	...	...	13.4	...	...	...	18.5	16.5
5856.10	26.0	-1.328	4.294	...	...	21.6	...	...	...	20.1	17.6
5858.78	26.0	-2.260	4.220	...	...	...	...	...	...	...	8.3
5859.60	26.0	-0.550	4.550	49.7	53.8	50.7	46.2	14.8	18.3	58.8	54.8
5862.35	26.0	-0.330	4.550	59.7	50.8	64.3	62.0	29.2	32.0	83.4	73.5
5883.81	26.0	-1.260	3.960	...	...	...	...	...	...	47.4	57.8
5905.68	26.0	-0.770	4.652	...	...	38.1	...	...	...	48.9	44.7
5927.80	26.0	-1.070	4.652	...	...	...	...	...	...	28.9	28.4
5929.68	26.0	-1.380	4.548	...	...	...	...	...	...	22.4	27.9
5930.19	26.0	-0.140	4.650	88.3	57.7	70.3	...	...	30.7	74.2	...
5934.67	26.0	-1.120	3.929	53.3	...	66.4	41.4	17.2	14.0	60.3	60.0
5940.99	26.0	-2.050	4.180	...	...	...	...	...	...	...	19.7
5952.72	26.0	-1.340	3.980	35.6	...	...	...	...	...	...	...
5956.71	26.0	-4.608	0.859	39.6	...	...	...	...	...	26.0	36.9
5976.79	26.0	-1.330	3.940	...	...	...	...	...	...	48.1	50.9
5983.69	26.0	-0.660	4.550	47.7	...	53.9	...	...	...	53.6	52.0
5984.83	26.0	-0.260	4.730	57.2	51.5	71.5	61.1	...	...	62.9	68.8
6003.02	26.0	-1.110	3.880	62.6	53.9	68.5	56.4	...	25.5	67.0	70.9
6024.05	26.0	0.030	4.550	80.9	75.9	92.1	83.4	47.0	51.4	91.7	93.2
6027.06	26.0	-1.089	4.076	44.1	40.1	49.7	43.0	...	...	60.3	51.9
6055.99	26.0	-0.370	4.730	...	47.2	57.9	49.2	...	...	60.7	50.2

Table C.2: Equivalent Width Measurements, Table 2 of 5, continued

λ (Å)	Ion	loggf	EP	2068-151	2051-595	2307-074	2052-537	2180-560	2798-073	1917-020	2251-632
6065.49	26.0	-1.530	2.608	97.9	84.2	98.2	84.4	69.8	60.3	97.2	93.2
6078.50	26.0	-0.330	4.790	52.0	...	64.1	...	...	...	62.8	70.8
6079.02	26.0	-1.100	4.652	30.4	...	36.9	...	...	...	25.5	...
6082.72	26.0	-3.573	2.223	...	...	...	...	...	...	15.7	26.8
6085.26	26.0	-2.710	2.759	...	...	...	...	...	...	21.1	30.4
6096.67	26.0	-1.880	3.984	...	...	...	...	...	...	24.5	...
6127.90	26.0	-1.400	4.140	28.1	...	...	...	...	...	36.0	38.1
6136.62	26.0	-1.400	2.453	99.8	82.2	...	...	64.7	67.4	...	...
6137.70	26.0	-1.403	2.588	94.6	80.3	...	95.9	66.9	65.5	...	...
6151.62	26.0	-3.299	2.176	31.3	...	30.1	...	...	...	28.5	33.4
6157.73	26.0	-1.220	4.076	41.7	30.9	47.6	...	...	...	46.9	44.1
6165.36	26.0	-1.474	4.143	...	...	24.9	...	...	...	33.5	...
6173.34	26.0	-2.880	2.223	47.5	29.6	51.3	...	...	16.9	48.7	52.5
6180.20	26.0	-2.650	2.730	...	17.8	41.1	...	...	...	35.7	36.9
6188.00	26.0	-1.670	3.943	...	...	...	...	...	...	...	32.8
6191.57	26.0	-1.416	2.433	...	98.6	...	...	60.7	...	...	...
6200.32	26.0	-2.437	2.608	55.2	...	...	...	...	...	...	60.1
6213.44	26.0	-2.482	2.223	71.7	...	...	53.3	33.2	25.0	63.9	66.0
6219.29	26.0	-2.433	2.198	75.2	58.6	81.3	61.3	43.6	36.2	77.3	78.4
6229.23	26.0	-2.805	2.845	21.8	...	22.8	...	...	...	...	24.5
6230.74	26.0	-1.281	2.559	...	98.5	...	...	75.2	75.4	...	...
6240.65	26.0	-3.173	2.223	27.4	...	23.8	...	...	...	...	37.8
6246.33	26.0	-0.877	3.603	86.2	68.2	88.4	75.6	...	48.1	93.5	...
6252.56	26.0	-1.687	2.404	89.7	89.0	96.8	86.1	59.6	57.4	...	92.3
6254.26	26.0	-2.430	2.280	95.3	...	93.4	...	...	40.6	...	95.7
6265.14	26.0	-2.550	2.176	68.5	59.9	67.1	...	30.7	...	70.0	70.0
6270.23	26.0	-2.609	2.858	32.9	...	34.2	...	...	...	...	38.8
6290.97	26.0	-0.730	4.730	51.8	...	...	...	...	...	...	...
6297.80	26.0	-2.740	2.223	...	...	59.8	55.6	...	...	54.8	43.9
6301.51	26.0	-0.718	3.654	85.7	...	98.5	...	...	...	94.9	90.0
6302.50	26.0	-1.110	3.690	60.3	...	...	...	...	...	...	...

Table C.2: Equivalent Width Measurements, Table 2 of 5, continued

λ (Å)	Ion	loggf	EP	2068-151	2051-595	2307-074	2052-537	2180-560	2798-073	1917-020	2251-632
6315.31	26.0	-1.230	4.140	...	...	...	...	...	...	57.2	46.0
6322.69	26.0	-2.426	2.588	60.7	52.1	70.1	...	...	...	56.3	59.6
6335.33	26.0	-2.177	2.198	74.0	60.4	88.9	66.3	39.3	44.2	87.3	78.3
6344.15	26.0	-2.923	2.433	38.5	22.4	49.6	...	...	...	46.5	45.2
6355.04	26.0	-2.291	2.845	47.4	33.6	51.6	...	...	20.9	50.0	51.6
6358.69	26.0	-4.468	0.859	46.5	30.6	62.1	...	...	...	60.6	55.1
4178.86	26.1	-2.443	2.583	79.6	88.2	75.8	92.3	70.3	75.2	83.2	75.6
4416.82	26.1	-2.600	2.778	63.1	71.6	67.4	76.4	54.0	63.8	...	...
4491.40	26.1	-2.640	2.856	59.7	68.4	69.8	73.1	55.3	59.5	...	...
4508.30	26.1	-2.350	2.856	74.2	85.8	77.3	84.8	68.5	76.7	85.7	79.9
4520.23	26.1	-2.620	2.807	67.4	79.9	72.4	84.2	58.2	65.5	...	...
4541.52	26.1	-2.970	2.856	52.5	66.5	...	66.4	44.7	41.8	...	...
4576.34	26.1	-2.920	2.844	45.7	59.8	53.9	62.1	44.9	42.5	73.4	58.6
4582.83	26.1	-3.062	2.844	42.0	53.5	53.7	52.8	36.9	38.5	63.7	50.5
4583.84	26.1	-1.740	2.807	...	...	...	...	92.5	...	...	...
4620.52	26.1	-3.188	2.828	42.9	52.3	43.7	54.7	29.3	32.9	61.2	43.7
4629.34	26.1	-2.480	2.810	80.9	85.8	77.6	85.9	68.6	78.0	95.9	80.7
4635.31	26.1	-1.580	5.956	...	...	...	...	...	...	20.5	...
4833.19	26.1	-4.790	2.657	...	...	...	...	...	...	...	8.8
4893.82	26.1	-4.270	2.828	...	...	...	...	...	...	18.4	11.8
4993.35	26.1	-3.680	2.807	20.0	26.9	30.9	...	...	16.9	38.0	26.5
5132.67	26.1	-4.090	2.807	...	18.6	...	...	...	...	...	15.3
5197.58	26.1	-2.054	3.230	64.0	76.7	71.3	80.8	65.4	68.5	85.8	68.3
5234.63	26.1	-2.210	3.221	69.3	76.3	83.2	85.2	63.2	63.7	80.4	74.8
5264.81	26.1	-3.233	3.230	32.4	34.5	...	44.6	24.1	28.5	44.4	33.1
5284.11	26.1	-3.200	2.891	44.5	52.2	47.0	...	...	37.9	...	...
5325.56	26.1	-2.570	3.221	32.9	...	...	...	...	...	52.5	34.2
5414.08	26.1	-3.482	3.221	15.2	31.0	...	...	...	...	34.2	20.1
5534.85	26.1	-2.860	3.245	48.9	56.6	58.0	69.9	...	47.8	...	57.6
5991.38	26.1	-3.650	3.153	...	...	...	30.7	...	...	...	24.4
6149.25	26.1	-2.840	3.889	22.6	...	30.2	40.0	...	...	36.3	27.2

Table C.2: Equivalent Width Measurements, Table 2 of 5, continued

λ (Å)	Ion	loggf	EP	2068-151	2051-595	2307-074	2052-537	2180-560	2798-073	1917-020	2251-632
6247.56	26.1	-2.430	3.892	41.0	60.2	41.6	65.2	32.4	39.5	53.1	40.1
4121.33	27.0	-0.320	0.920	...	94.5	...	91.4	76.1	71.2	99.3	...
4686.22	28.0	-0.580	3.600	42.7	31.5	49.0	31.6	...	...	46.7	44.0
4831.18	28.0	-0.320	3.610	55.7	...	56.5	44.3	18.5	23.1	...	...
4857.40	28.0	-0.830	3.740	...	...	33.6	...	...	...	34.8	33.3
4866.27	28.0	-0.210	3.539	...	...	56.8	...	...	...	...	70.2
4904.42	28.0	-0.190	3.540	73.8	54.3	73.9	59.7	40.6	...	69.8	63.9
4913.98	28.0	-0.630	3.740	...	31.4	38.2	...	...	...	41.2	37.5
4935.83	28.0	-0.380	3.940	40.8	31.0	45.8	...	...	...	49.5	45.3
4953.21	28.0	-0.580	3.740	35.8	24.1	40.1	...	...	...	41.8	38.1
4998.22	28.0	-0.690	3.606	34.8	24.6	35.1	...	13.8	...	42.6	39.4
5003.75	28.0	-3.130	1.680	19.5	...	...	...	...	...	21.6	21.6
5010.94	28.0	-0.900	3.630	23.6	16.1	25.9	...	...	...	35.6	28.3
5035.37	28.0	0.290	3.630	76.7	64.2	78.3	76.9	43.6	...	90.4	86.0
5048.85	28.0	-0.390	3.850	...	41.3	43.5	...	10.7	13.7	53.8	48.2
5082.35	28.0	-0.540	3.660	44.8	32.9	44.4	30.3	17.7	19.3	47.6	54.8
5084.11	28.0	-0.060	3.680	69.5	58.4	72.6	64.1	34.1	39.1	79.2	...
5088.54	28.0	-1.080	3.850	...	...	...	...	...	...	...	16.1
5094.42	28.0	-1.120	3.830	...	...	...	...	...	...	15.0	...
5102.97	28.0	-2.660	1.680	...	...	29.2	...	...	...	...	30.2
5115.40	28.0	-0.140	3.830	57.3	51.0	54.3	50.5	25.8	30.7	61.8	...
5197.17	28.0	-1.140	3.900	...	...	...	...	...	...	...	12.9
5578.72	28.0	-2.640	1.680	30.3	...	33.4	...	...	...	...	36.9
5587.86	28.0	-2.140	1.930	39.0	...	...	...	...	...	...	...
5589.36	28.0	-1.140	3.900	...	...	...	...	...	...	...	12.0
5593.74	28.0	-0.840	3.900	19.5	...	...	...	...	...	29.1	29.6
5625.32	28.0	-0.701	4.090	...	...	...	...	...	...	...	30.5
5682.20	28.0	-0.469	4.100	29.2	...	34.7	...	...	...	...	36.2
5754.67	28.0	-1.850	1.930	55.8	28.8	56.4	46.7	...	...	...	55.3
5760.83	28.0	-0.805	4.100	...	...	...	...	...	...	25.4	26.9
5805.22	28.0	-0.638	4.170	...	...	...	...	...	...	29.4	25.9

Table C.2: Equivalent Width Measurements, Table 2 of 5, continued

λ (Å)	Ion	loggf	EP	2068-151	2051-595	2307-074	2052-537	2180-560	2798-073	1917-020	2251-632
5846.99	28.0	-3.210	1.680	...	...	...	...	...	...	...	14.0
5892.87	28.0	-2.340	1.990	56.2	...	...	...	...	...	...	61.5
6007.32	28.0	-3.410	1.677	...	...	...	...	...	...	...	13.3
6086.28	28.0	-0.515	4.260	...	...	...	...	...	...	36.5	...
6108.12	28.0	-2.430	1.680	53.8	...	50.4	...	...	...	39.9	40.8
6175.37	28.0	-0.535	4.090	30.5	...	32.5	...	...	...	...	...
6176.81	28.0	-0.529	4.090	42.1	...	46.3	...	...	...	50.0	44.0
6204.60	28.0	-1.140	4.090	...	...	...	...	...	...	...	17.5
6314.66	28.0	-1.770	1.930	54.3	...	56.2	...	...	...	53.9	...
5105.54	29.0	-3.720	1.380	64.4	44.4	68.6	35.3	...	...	66.6	69.7
5218.21	29.0	0.300	3.800	29.9	...	...	...	...	...	...	...
4722.16	30.0	-0.390	4.030	61.8	51.0	57.0	50.8	32.7	33.0	59.2	58.5
4810.54	30.0	-0.170	4.080	66.0	55.0	65.9	59.2	40.1	43.8	66.3	...
4607.34	38.0	0.280	0.000	24.0	...	38.5	...	...	...	...	34.3
3549.01	39.1	-0.280	0.130	50.7	47.9	57.8	...	46.6	...	50.9	58.1
3600.74	39.1	0.280	0.180	63.2	74.5	71.1	74.0	64.0	61.5	75.1	80.1
3611.04	39.1	0.010	0.130	...	...	...	...	47.8	54.7	...	...
3774.33	39.1	0.210	0.130	81.9	...	...	...	...	...	72.6	74.5
3788.70	39.1	-0.070	0.100	58.5	71.9	...	...	61.9	52.6	...	...
3950.36	39.1	-0.490	0.100	...	54.7	51.6	62.5	40.9	51.6	61.1	53.7
4398.01	39.1	-1.000	0.130	...	37.6	...	...	...	...	...	...
4883.69	39.1	0.070	1.080	44.7	39.5	49.9	55.6	39.5	...	...	55.3
5087.43	39.1	-0.170	1.080	33.3	27.6	32.3	38.2	21.4	24.2	43.6	40.1
5123.22	39.1	-0.830	0.990	...	...	...	...	...	...	34.2	26.1
5200.41	39.1	-0.570	0.990	18.5	18.0	...	...	...	...	...	29.2
5509.91	39.1	-1.010	0.990	...	...	...	...	...	...	44.4	...
3714.78	40.1	-0.960	0.530	20.0	...	23.2	...	14.5	13.9	22.0	26.2
4050.33	40.1	-1.060	0.710	21.2	...	...	...	...	...	...	17.4
4208.99	40.1	-0.510	0.710	35.4	33.5	36.1	...	25.3	30.6	37.7	37.3
3692.36	45.0	0.173	0.000	37.0	...	...	...	...	...	...	...
4130.65	56.1	0.530	2.720	...	...	...	...	...	...	...	39.8

Table C.2: Equivalent Width Measurements, Table 2 of 5, continued

λ (Å)	Ion	loggf	EP	2068-151	2051-595	2307-074	2052-537	2180-560	2798-073	1917-020	2251-632
5853.69	56.1	-0.910	0.600	52.0	69.1	50.5	68.4	34.9	34.2	71.3	65.3
3988.51	57.1	0.210	0.170	28.3	27.3	29.6	...	...	10.4	37.3	43.6
4086.71	57.1	-0.070	0.000	30.1	...	...	...	13.6	...	33.0	37.6

Table C.3: Equivalent Width Measurements, Table 3 of 5

λ (Å)	Ion	loggf	EP	2310-312	1903-096	2796-054	2180-545	2797-407	1916-559	2305-365	1891-140
5682.65	11.0	-0.699	2.100	...	...	...	...	32.7	...	...	...
5688.19	11.0	-0.420	2.100	...	...	23.5	...	66.6	47.4	82.5	...
6154.23	11.0	-1.530	2.100	...	16.7	...	...	...	12.5	...	36.7
6160.75	11.0	-1.230	2.100	...	29.4	...	...	...	...	...	55.6
4571.10	12.0	-5.570	0.000	43.4	97.2	29.8	44.1	53.3	50.3	94.9	...
4730.04	12.0	-2.347	4.350	...	47.8	...	...	...	...	49.3	...
5711.09	12.0	-1.630	4.340	45.9	92.8	...	43.5	...	...	91.3	...
5665.55	14.0	-2.040	4.920	...	27.0	...	...	...	...	...	47.6
5690.43	14.0	-1.870	4.930	...	36.9	...	...	...	...	35.7	51.5
5701.10	14.0	-2.050	4.930	...	30.2	...	...	...	...	32.4	43.1
5772.15	14.0	-1.750	5.080	...	42.2	...	20.2	...	...	32.6	61.3
5793.07	14.0	-2.060	4.930	...	35.2	...	...	...	...	...	49.7
5948.54	14.0	-1.230	5.080	23.1	68.3	28.8	35.3	36.1	...	69.3	88.6
6125.03	14.0	-1.570	5.610	...	20.9	...	...	...	...	...	35.9
6142.49	14.0	-1.480	5.620	...	23.6	...	...	...	...	24.2	31.9
6145.02	14.0	-1.370	5.610	...	22.9	...	...	...	...	22.9	43.8
6155.13	14.0	-0.760	5.620	18.9	63.1	...	36.9	35.7	...	55.4	92.1
6237.32	14.0	-1.010	5.620	...	53.0	...	...	...	...	...	65.3
6244.48	14.0	-1.320	5.616	...	32.0	...	...	...	...	...	...

Table C.3: Equivalent Width Measurements, Table 3 of 5, continued

λ (Å)	Ion	loggf	EP	2310-312	1903-096	2796-054	2180-545	2797-407	1916-559	2305-365	1891-140
6347.09	14.1	0.260	8.120	35.6	44.2	...	...	...	...	30.9	47.3
4283.01	20.0	-0.224	1.890	88.6	...	90.1	...	...	...	...	...
4318.66	20.0	-0.210	1.900	79.3	...	88.9	85.4	93.0	85.5	...	...
4512.27	20.0	-2.030	2.520	...	13.7	...	...	...	...	...	26.9
4526.93	20.0	-0.420	2.710	...	61.6	34.5	32.1	...	31.3	64.7	87.4
4578.56	20.0	-0.558	2.520	32.2	72.5	37.9	38.1	41.5	37.7	71.8	87.2
4685.27	20.0	-0.940	2.930	...	...	...	22.2	...	...	...	...
5260.39	20.0	-1.780	2.520	...	21.4	...	9.6	...	...	15.5	35.7
5261.71	20.0	-0.730	2.520	45.6	87.6	...	54.4	52.1	39.7	76.6	...
5349.47	20.0	-0.310	2.710	42.5	...	54.4	...	...	...	...	...
5512.99	20.0	-0.266	2.930	...	...	30.8	33.5	...	...	64.8	87.9
5588.76	20.0	0.358	2.510	87.8	...	96.0	...	...	93.7	...	...
5590.13	20.0	-0.710	2.510	37.4	79.3	53.2	52.2	58.7	41.4	69.1	91.3
5594.47	20.0	0.050	2.510	...	...	...	...	...	87.8	...	...
5601.28	20.0	-0.438	2.520	44.0	91.3	...	56.7	52.3	44.4	79.2	...
5857.46	20.0	0.240	2.930	66.9	...	...	...	79.7	...	...	...
5867.57	20.0	-1.610	2.930	...	...	...	...	...	...	12.9	26.9
6102.73	20.0	-0.790	1.880	64.1	...	...	...	...	...	...	...
6122.23	20.0	-0.320	1.890	87.5	...	...	...	...	96.4	...	...
6161.30	20.0	-1.270	2.520	...	43.2	...	...	...	...	47.7	73.7
6166.44	20.0	-1.140	2.520	25.3	53.5	...	...	...	...	45.2	72.3
6169.04	20.0	-0.800	2.520	...	70.5	...	...	...	32.2	71.7	93.6
6169.56	20.0	-0.480	2.520	...	97.3	...	...	...	...	91.3	...
5001.47	20.1	-0.520	7.500	...	9.7	...	...	...	...	...	...
4400.39	21.1	-0.540	0.610	63.8	...	77.1	...	...	...	...	...
5239.82	21.1	-0.765	1.450	...	50.2	...	34.7	24.4	21.8	47.0	61.5
5526.82	21.1	0.020	1.770	33.4	76.4	50.7	62.0	50.2	49.5	75.9	91.3
5640.99	21.1	-1.130	1.500	...	39.6	...	...	...	...	32.0	...
5657.88	21.1	-0.600	1.510	...	62.1	42.0	55.6	53.0	...	53.1	85.2
5669.04	21.1	-1.120	1.500	...	28.3	...	...	...	...	29.1	44.2
3924.53	22.0	-0.940	0.020	20.0	61.7	...	24.2	...	25.6	57.2	69.1

Table C.3: Equivalent Width Measurements, Table 3 of 5, continued

λ (Å)	Ion	loggf	EP	2310-312	1903-096	2796-054	2180-545	2797-407	1916-559	2305-365	1891-140
3958.22	22.0	-0.176	0.050	62.8	...	63.4	66.8	72.8	...	83.1	...
3998.64	22.0	-0.060	0.050	66.6	...	...	67.1	...	70.6	95.5	...
4008.93	22.0	-1.072	0.021	29.4	...	24.8	32.6	43.4	33.4	...	...
4512.74	22.0	-0.480	0.840	16.7	52.3	...	19.0	...	15.2	55.4	70.3
4518.03	22.0	-0.325	0.830	...	58.6	...	...	...	...	...	78.5
4533.25	22.0	0.476	0.850	...	...	63.4	...	...	...	...	...
4534.78	22.0	0.280	0.840	55.6	82.4	52.3	58.4	57.6	51.2	87.6	...
4548.77	22.0	-0.354	0.830	24.1	59.2	...	30.2	...	18.5	58.1	76.2
4555.49	22.0	-0.490	0.850	...	52.7	...	15.8	19.0	...	52.7	64.5
4617.28	22.0	0.390	1.750	...	52.9	...	22.8	24.3	28.7	50.7	67.1
4623.10	22.0	0.170	1.740	...	40.7	...	12.1	...	10.9	35.2	65.2
4758.12	22.0	0.425	2.250	...	31.8	...	...	...	...	30.3	43.5
4759.28	22.0	0.514	2.250	...	34.4	...	...	...	10.4	31.7	51.6
4778.26	22.0	-0.210	2.240	...	...	...	...	...	...	...	19.7
4820.41	22.0	-0.439	1.500	...	27.9	...	...	...	...	29.6	48.3
4840.88	22.0	-0.450	0.900	22.8	59.0	...	...	...	...	48.6	73.4
4913.62	22.0	0.220	1.870	...	35.5	...	...	...	...	34.8	56.7
4981.74	22.0	0.504	0.850	60.3	...	68.7	74.2	74.1	69.2	98.0	...
4999.51	22.0	0.250	0.830	57.9	94.5	...	51.9	58.4	54.4	86.3	...
5009.66	22.0	-2.260	0.020	...	...	...	...	...	...	17.7	...
5016.17	22.0	-0.574	0.850	...	53.6	...	...	...	17.4	50.7	75.3
5022.87	22.0	-0.430	0.830	21.9	59.6	23.6	24.7	...	20.7	58.1	75.0
5024.85	22.0	-0.600	0.820	...	...	...	22.2	...	...	51.3	...
5039.96	22.0	-1.130	0.020	...	65.0	...	34.1	20.5	24.2	...	80.5
5043.59	22.0	-1.730	0.840	...	13.7	...	...	...	...	...	...
5087.06	22.0	-0.780	1.430	...	15.4	...	...	...	...	...	26.5
5173.75	22.0	-1.118	0.000	...	...	...	25.9	...	...	...	...
5192.98	22.0	-1.006	0.020	...	...	...	35.1	38.0	32.4	66.9	92.2
5210.39	22.0	-0.884	0.050	34.7	79.1	...	34.2	41.1	39.6	80.3	92.9
5219.71	22.0	-2.292	0.020	...	17.0	...	...	...	...	...	...
5866.45	22.0	-0.840	1.070	...	...	...	...	...	...	36.4	57.6

Table C.3: Equivalent Width Measurements, Table 3 of 5, continued

λ (Å)	Ion	loggf	EP	2310-312	1903-096	2796-054	2180-545	2797-407	1916-559	2305-365	1891-140
5922.11	22.0	-1.470	1.050	...	11.7	...	...	...	...	...	27.7
5941.75	22.0	-1.520	1.050	...	18.6	...	...	...	...	...	24.4
5965.83	22.0	-0.409	1.880	...	...	...	...	...	...	...	43.5
5978.54	22.0	-0.496	1.870	...	21.8	...	...	...	...	...	29.6
6126.22	22.0	-1.420	1.070	...	12.7	...	...	...	...	...	28.6
6258.10	22.0	-0.355	1.440	...	36.2	...	...	...	...	39.2	54.8
6258.71	22.0	-0.240	1.460	...	54.8	...	...	...	...	39.4	78.2
6261.11	22.0	-0.480	1.430	...	34.5	...	...	...	...	...	55.4
3987.61	22.1	-2.730	0.610	27.6	...	38.6	30.5	43.5	31.0	57.3	57.7
4012.39	22.1	-1.610	0.570	88.3	...	...	...	...	91.3	...	...
4028.35	22.1	-1.000	1.890	58.8	83.4	75.0	69.0	73.4	62.9	81.2	94.3
4312.86	22.1	-1.160	1.180	...	...	96.2	...	...	...	...	...
4394.06	22.1	-1.770	1.220	57.6	...	66.0	66.7	...	...	...	...
4395.84	22.1	-1.970	1.240	38.9	64.8	45.2	55.3	56.1	40.4	...	62.9
4399.77	22.1	-1.270	1.240	81.2	...	92.3	93.0	94.1	82.6	...	...
4544.02	22.1	-2.410	1.240	...	...	...	22.0	...	...	39.3	...
4563.77	22.1	-0.960	1.220	96.9	...	...	...	...	99.0	...	...
4568.33	22.1	-2.650	1.220	...	23.2	...	...	...	...	29.2	35.3
4583.42	22.1	-2.720	1.160	...	30.7	...	14.8	...	18.2	29.1	37.6
4589.95	22.1	-1.790	1.240	62.2	80.5	69.1	76.5	75.1	67.6	81.3	...
4609.27	22.1	-3.260	1.180	...	...	...	...	...	...	...	17.8
4636.32	22.1	-3.020	1.165	...	18.4	...	...	...	...	18.4	33.4
4708.67	22.1	-2.210	1.240	...	40.5	...	...	38.8	...	57.6	60.2
4779.98	22.1	-1.370	2.048	42.7	70.8	55.6	54.5	53.1	49.5	62.0	78.9
4798.54	22.1	-2.430	1.080	...	...	25.1	...	26.8	...	...	...
4805.09	22.1	-1.120	2.061	53.2	93.0	63.5	74.5	67.8	65.3	82.5	...
4865.62	22.1	-2.590	1.120	...	41.3	...	...	...	...	...	...
4874.01	22.1	-0.790	3.090	...	27.5	...	30.5	...	18.8	29.6	42.8
4911.20	22.1	-0.330	3.120	...	...	27.4	40.0	...	34.8	42.9	63.4
5129.16	22.1	-1.390	1.890	42.8	...	59.2	...	...	...	...	...
5154.07	22.1	-1.920	1.570	37.3	...	50.3	56.3	...	43.2	68.9	84.2

Table C.3: Equivalent Width Measurements, Table 3 of 5, continued

λ (Å)	Ion	loggf	EP	2310-312	1903-096	2796-054	2180-545	2797-407	1916-559	2305-365	1891-140
5185.91	22.1	-1.350	1.890	36.0	61.8	47.2	56.3	56.0	46.1	69.9	...
5211.53	22.1	-1.160	2.590	...	29.4	...	...	...	...	32.2	43.2
5336.79	22.1	-1.630	1.580	49.8	73.6	57.2	63.6	59.6	50.7	70.1	83.3
5381.01	22.1	-1.970	1.570	38.2	55.7	40.0	50.5	...	39.7	60.6	71.4
5490.69	22.1	-2.430	1.566	...	24.7	...	...	...	...	...	...
4115.18	23.0	0.070	0.290	...	55.6	...	...	...	...	...	...
4406.63	23.0	-0.190	0.300	...	66.0	...	...	...	...	...	...
4864.74	23.0	-0.960	0.020	...	...	...	...	...	...	...	43.9
4875.49	23.0	-0.810	0.040	...	21.8	...	...	...	...	...	50.9
5627.64	23.0	-0.370	1.080	...	15.3	...	...	...	...	...	...
5670.86	23.0	-0.420	1.080	...	...	...	...	...	...	...	21.5
5703.59	23.0	-0.210	1.050	...	...	...	...	...	...	...	33.1
5727.06	23.0	-0.010	1.080	...	17.1	...	...	...	...	...	42.9
6039.73	23.0	-0.650	1.060	...	...	...	...	...	...	...	17.2
6090.22	23.0	-0.060	1.080	...	...	...	...	...	...	...	41.6
3538.23	23.1	-1.640	1.070	...	...	...	22.8	...	...	...	...
3545.19	23.1	-0.390	1.100	54.0	79.6	56.0	68.2	63.2	...	71.4	87.9
3592.03	23.1	-0.370	1.100	57.2	70.7	59.4	59.4	62.5	59.7	72.7	88.4
3951.97	23.1	-0.744	1.480	...	46.5	40.7	...	...	...	57.7	57.7
3732.02	24.0	-2.570	0.000	...	51.2	...	...	...	...	...	76.6
3768.74	24.0	-0.920	2.544	...	34.5	...	...	...	...	...	...
3908.76	24.0	-1.050	1.004	20.5	...	...	...	50.6	...	...	...
3963.69	24.0	0.620	2.544	...	...	...	39.9	...	...	...	...
4272.90	24.0	-0.980	2.900	...	19.5	...	...	...	...	...	41.9
4274.80	24.0	-0.220	0.000	94.4	...	...	...	...	...	...	...
4373.26	24.0	-2.300	0.983	...	20.8	...	...	...	...	...	43.1
4496.84	24.0	-1.140	0.941	44.0	...	...	58.1	...	45.7	...	...
4511.90	24.0	-0.343	3.090	...	24.9	...	...	...	...	23.3	45.8
4545.95	24.0	-1.370	0.941	24.6	67.1	...	33.3	...	26.7	64.8	91.7
4580.04	24.0	-1.660	0.941	...	70.0	...	30.0	28.8	21.1	...	...
4591.39	24.0	-1.740	0.968	...	...	...	...	...	...	60.5	...

Table C.3: Equivalent Width Measurements, Table 3 of 5, continued

λ (Å)	Ion	loggf	EP	2310-312	1903-096	2796-054	2180-545	2797-407	1916-559	2305-365	1891-140
4600.74	24.0	-1.250	1.004	25.2	...	...	...	...	...	...	...
4613.36	24.0	-1.650	0.961	...	...	...	...	45.0	...	...	...
4616.12	24.0	-1.190	0.983	...	71.4	...	36.5	37.9	38.3	64.7	92.5
4626.17	24.0	-1.330	0.968	16.1	67.3	...	31.0	30.8	31.3	59.0	87.0
4646.15	24.0	-0.740	1.030	40.3	...	38.0	55.7	57.5	...	80.2	...
4651.28	24.0	-1.460	0.983	...	67.8	...	23.2	...	22.4	58.7	84.6
4652.15	24.0	-1.040	1.004	33.3	84.4	...	48.9	44.5	...	72.1	...
4663.82	24.0	-0.390	3.111	...	46.7	...	...	...	...	...	...
4689.38	24.0	-0.400	3.125	...	...	...	...	...	...	24.6	...
4700.62	24.0	-1.254	2.710	...	...	...	...	...	...	...	10.0
4708.02	24.0	0.070	3.168	...	38.3	...	...	...	12.9	28.8	55.6
4718.43	24.0	0.240	3.195	...	45.7	...	17.4	...	...	35.0	71.3
4724.41	24.0	-0.733	3.090	...	...	...	...	...	...	16.6	41.6
4730.72	24.0	-0.192	3.080	...	26.1	...	...	...	...	...	48.2
4801.03	24.0	-0.130	3.120	...	...	...	...	...	...	26.2	60.2
4936.34	24.0	-0.250	3.113	...	29.7	...	...	...	...	...	50.2
5065.92	24.0	-1.380	2.708	...	...	...	...	...	...	...	34.2
5067.72	24.0	-1.070	2.709	...	15.4	...	...	...	...	...	38.5
5247.57	24.0	-1.590	0.961	...	...	...	...	...	...	...	84.8
5287.20	24.0	-0.870	3.438	...	...	...	...	...	...	...	15.5
5296.69	24.0	-1.360	0.983	...	70.3	...	36.3	...	...	66.3	97.4
5297.39	24.0	0.000	2.900	...	62.1	...	32.7	...	...	...	96.1
5300.74	24.0	-2.000	0.983	...	42.0	...	...	...	...	...	...
5345.80	24.0	-0.950	1.004	39.9	89.5	...	56.1	45.7	46.2	86.8	...
5348.31	24.0	-1.210	1.004	16.0	75.5	...	41.2	...	23.0	62.1	96.9
5409.77	24.0	-0.670	1.030	48.1	...	49.5	...	63.3	59.6	97.5	...
5702.32	24.0	-0.670	3.449	...	14.0	...	...	...	...	...	25.8
5783.09	24.0	-0.500	3.320	...	...	...	...	...	...	...	33.0
5783.89	24.0	-0.295	3.320	...	23.9	...	...	...	...	...	44.2
5787.93	24.0	-0.083	3.320	...	23.5	...	...	...	...	...	42.1
6330.09	24.0	-2.900	0.940	...	...	...	...	...	...	...	25.4

Table C.3: Equivalent Width Measurements, Table 3 of 5, continued

λ (Å)	Ion	loggf	EP	2310-312	1903-096	2796-054	2180-545	2797-407	1916-559	2305-365	1891-140
4554.99	24.1	-1.373	4.070	...	49.3	...	33.5	26.2	23.5	33.0	58.9
4558.65	24.1	-0.656	4.070	50.0	80.0	62.1	74.8	62.8	54.2	64.1	87.3
4588.20	24.1	-0.826	4.070	39.0	65.5	53.3	69.1	52.2	46.9	54.1	69.7
4592.06	24.1	-1.419	4.070	...	40.1	21.2	43.6	...	22.8	26.0	53.3
4616.63	24.1	-1.210	4.073	...	40.0	...	35.2	...	...	29.9	52.7
4848.23	24.1	-0.999	3.870	19.4	57.5	...	53.6	34.7	34.8	...	...
5237.33	24.1	-1.155	4.070	...	46.9	...	41.9	28.5	...	35.4	54.2
5305.86	24.1	-2.060	3.830	...	19.9	...	...	...	...	...	27.3
5308.42	24.1	-1.790	4.070	...	21.7	...	...	...	...	...	22.5
5313.59	24.1	-1.640	4.070	...	...	...	19.6	...	...	...	47.2
3577.87	25.0	-0.010	2.110	29.6	...	...	...	...	...	...	...
4055.55	25.0	-0.080	2.140	36.5	...	27.0	54.2	42.2	45.8	80.5	...
4709.72	25.0	-0.339	2.890	...	39.0	...	14.8	...	...	27.8	67.4
4739.11	25.0	-0.490	2.940	...	34.4	...	...	...	...	...	59.4
4761.53	25.0	-0.138	2.950	...	52.5	...	19.2	...	17.5	32.5	77.6
4783.43	25.0	0.042	2.300	36.0	...	37.2	68.1	46.8	54.0	89.9	...
4823.51	25.0	0.144	2.320	33.0	...	32.2	65.1	56.6	49.7	...	...
6013.50	25.0	-0.252	3.070	...	54.3	...	...	...	...	...	82.8
6021.80	25.0	0.030	3.080	...	65.1	...	18.3	...	...	47.7	94.7
3891.93	26.0	-0.734	3.415	45.8	...	...	...	...	54.7	...	...
3916.74	26.0	-0.604	3.237	47.0	...	39.3	...	...	51.6	...	...
3917.18	26.0	-2.155	0.990	72.3	...	62.1	80.8	84.2	81.8	...	...
3949.96	26.0	-1.251	2.176	67.9	92.1	72.9	84.5	79.7	68.1	88.2	...
4114.45	26.0	-1.303	2.832	38.5	74.2	30.5	54.7	46.7	45.4	73.5	89.1
4132.91	26.0	-1.006	2.845	56.8	...	44.4	67.3	58.2	60.8	...	...
4139.94	26.0	-3.629	0.990	...	57.1	...	21.0	18.9	17.8	52.6	71.0
4147.68	26.0	-2.104	1.485	53.0	...	53.3	67.3	66.3	67.7	85.5	...
4157.79	26.0	-0.403	3.417	51.5	...	51.2	76.1	67.0	65.9	90.3	...
4174.92	26.0	-2.969	0.915	51.7	...	47.8	...	68.2	58.2	...	...
4175.64	26.0	-0.827	2.845	60.8	91.2	60.0	75.8	71.9	70.0	87.1	...
4184.91	26.0	-0.869	2.832	53.0	93.0	43.3	66.7	65.8	62.0	77.6	...

Table C.3: Equivalent Width Measurements, Table 3 of 5, continued

λ (Å)	Ion	loggf	EP	2310-312	1903-096	2796-054	2180-545	2797-407	1916-559	2305-365	1891-140
4187.05	26.0	-0.548	2.450	88.2	...	82.3	...	...	87.6	...	...
4199.10	26.0	0.156	3.047	91.3	...	94.1	99.7	...	95.6	...	...
4216.19	26.0	-3.356	0.000	67.3	...	67.0	75.9	72.2	67.6	...	...
4217.56	26.0	-0.484	3.430	47.8	84.1	55.2	71.5	70.3	59.9	85.6	...
4222.22	26.0	-0.967	2.450	63.2	...	68.3	78.7	85.1	78.9	...	...
4233.61	26.0	-0.604	2.482	89.7	...	81.6	98.7	94.4	95.6	...	...
4238.81	26.0	-0.233	3.397	60.7	...	62.3	82.0	68.4	72.7	...	...
4250.13	26.0	-0.405	2.469	92.1	...	97.8	...	...	...	...	...
4271.16	26.0	-0.349	2.450	...	...	98.3	...	...	...	...	...
4282.41	26.0	-0.779	2.176	82.4	...	85.2	...	...	...	...	...
4347.24	26.0	-5.503	0.000	...	19.9	...	...	...	...	15.4	39.7
4375.94	26.0	-3.031	0.000	79.2	...	72.0	87.5	87.3	78.4	...	...
4388.41	26.0	-0.682	3.603	42.5	84.7	36.9	54.0	48.6	...	...	98.3
4389.25	26.0	-4.583	0.052	...	56.6	...	20.0	...	21.1	...	68.1
4471.68	26.0	-5.995	0.110	...	15.3	...	...	...	...	...	...
4489.75	26.0	-3.966	0.121	33.8	83.0	...	47.1	...	42.6	82.4	...
4494.57	26.0	-1.136	2.198	81.6	...	78.7	98.5	97.4	86.8	...	...
4517.52	26.0	-1.860	3.071	...	55.4	...	18.9	...	17.2	46.6	82.2
4523.41	26.0	-1.960	3.654	...	23.0	...	...	...	...	18.3	42.7
4547.85	26.0	-1.010	3.546	32.6	73.4	35.7	50.5	40.8	43.2	62.2	88.1
4551.65	26.0	-2.030	3.943	...	15.1	...	...	...	...	...	25.4
4556.93	26.0	-2.660	3.251	...	15.4	...	...	...	...	...	24.4
4566.52	26.0	-2.380	3.300	...	24.6	...	...	...	...	...	43.8
4574.23	26.0	-2.450	3.211	...	22.9	...	...	...	...	13.1	...
4587.13	26.0	-1.740	3.573	...	42.7	...	...	...	...	25.3	60.0
4592.66	26.0	-2.449	1.557	...	...	49.7	...	...	...	...	...
4593.53	26.0	-2.030	3.943	...	18.9	...	...	...	...	...	30.4
4602.01	26.0	-3.154	1.608	22.5	56.5	...	19.2	...	21.3	48.8	74.6
4602.95	26.0	-2.220	1.485	67.1	96.9	54.5	75.0	64.1	67.4	95.4	...
4630.12	26.0	-2.587	2.279	14.0	55.6	...	26.1	17.5	16.3	46.4	77.3
4632.92	26.0	-2.913	1.608	22.4	98.1	...	...	33.4	...	80.6	...

Table C.3: Equivalent Width Measurements, Table 3 of 5, continued

λ (Å)	Ion	loggf	EP	2310-312	1903-096	2796-054	2180-545	2797-407	1916-559	2305-365	1891-140
4635.85	26.0	-2.360	2.840	...	35.8	...	...	...	...	...	54.8
4647.43	26.0	-1.351	2.949	36.8	...	31.2	51.7	53.4	49.0	...	...
4672.84	26.0	-4.240	1.610	...	...	...	...	...	...	...	38.9
4683.56	26.0	-2.320	2.832	...	38.1	...	...	...	...	26.7	57.1
4690.14	26.0	-1.640	3.687	...	39.6	...	...	...	...	27.4	57.5
4726.15	26.0	-3.190	2.998	...	14.4	...	...	...	...	...	...
4733.59	26.0	-2.990	1.485	30.1	74.1	...	38.4	40.1	38.0	67.4	89.8
4741.53	26.0	-1.760	2.830	16.1	60.4	17.6	...	...	...	48.5	69.8
4745.80	26.0	-1.270	3.654	20.8	65.6	...	27.0	23.3	22.3	44.0	81.3
4779.45	26.0	-2.020	3.415	...	24.7	...	...	...	...	16.9	45.1
4787.83	26.0	-2.600	2.998	...	28.5	...	...	...	...	17.2	44.9
4788.76	26.0	-1.763	3.237	...	55.8	...	...	...	...	43.2	67.8
4789.65	26.0	-0.910	3.547	...	...	...	...	...	...	63.4	86.7
4802.52	26.0	-1.820	4.610	...	...	...	...	...	...	...	17.1
4802.88	26.0	-1.510	3.642	...	44.6	...	16.2	...	...	45.2	62.4
4808.16	26.0	-2.740	3.251	...	13.5	...	...	...	...	...	24.5
4809.94	26.0	-2.680	3.573	...	...	...	...	...	...	...	25.6
4835.87	26.0	-1.470	4.103	...	...	...	...	...	...	19.0	59.8
4839.52	26.0	-1.820	3.270	...	47.4	...	15.9	...	...	38.3	65.2
4844.01	26.0	-2.050	3.547	...	28.4	...	...	...	...	19.3	49.0
4871.33	26.0	-0.362	2.865	84.3	...	79.0	...	...	93.3	...	...
4872.14	26.0	-0.567	2.882	77.5	...	71.4	92.5	82.9	84.6	...	...
4882.14	26.0	-1.640	3.420	14.4	61.0	...	24.5	26.0	24.6	47.8	81.1
4890.76	26.0	-0.394	2.875	84.2	...	83.6	...	...	...	...	...
4891.50	26.0	-0.112	2.851	...	...	92.5	...	...	...	...	...
4892.87	26.0	-1.290	4.220	...	32.1	...	...	...	...	24.8	59.3
4903.32	26.0	-0.926	2.882	56.2	...	54.3	79.9	70.0	68.1	...	...
4905.14	26.0	-2.020	3.929	...	22.1	...	...	...	...	...	37.5
4917.24	26.0	-1.160	4.191	...	46.0	...	...	...	16.9	38.8	71.3
4919.00	26.0	-0.342	2.865	88.8	...	90.1	...	99.6	...	...	...
4924.77	26.0	-2.114	2.279	28.5	81.6	16.5	47.0	...	40.0	70.3	97.2

Table C.3: Equivalent Width Measurements, Table 3 of 5, continued

λ (Å)	Ion	loggf	EP	2310-312	1903-096	2796-054	2180-545	2797-407	1916-559	2305-365	1891-140
4938.82	26.0	-1.077	2.875	51.5	...	...	72.1	...	...	93.9	...
4939.69	26.0	-3.340	0.859	41.7	86.3	27.5	48.5	45.9	...	81.6	...
4961.92	26.0	-2.250	3.634	...	11.6	...	...	...	...	...	28.7
4962.58	26.0	-1.182	4.178	...	39.7	...	...	...	...	25.0	55.5
4966.09	26.0	-0.871	3.332	43.2	...	37.6	64.6	63.6	58.7	83.9	...
4994.14	26.0	-3.080	0.915	48.7	91.2	40.3	56.5	52.2	47.9	85.4	...
5001.87	26.0	-0.010	3.882	...	...	58.9	78.0	67.3	70.9	87.8	...
5014.94	26.0	-0.303	3.943	42.4	93.3	45.7	63.5	54.9	53.3	77.0	...
5016.48	26.0	-1.680	4.260	...	...	...	...	...	...	...	30.5
5044.21	26.0	-2.060	2.850	...	55.1	...	26.3	...	...	50.1	73.3
5049.83	26.0	-1.355	2.279	71.0	...	68.7	79.5	71.6	75.9	...	...
5051.64	26.0	-2.795	0.915	59.5	...	64.0	81.6	79.4	75.3	...	...
5054.64	26.0	-1.920	3.640	...	25.4	...	...	...	...	16.5	41.6
5058.49	26.0	-2.830	3.640	...	5.6	...	...	...	...	...	...
5067.16	26.0	-0.970	4.220	10.3	54.7	...	25.6	...	27.4	47.5	77.1
5068.77	26.0	-1.042	2.940	55.7	99.9	45.9	69.0	57.2	56.4	83.1	...
5074.75	26.0	-0.230	4.220	45.1	95.5	42.3	64.0	53.0	53.6	86.0	...
5079.74	26.0	-3.220	0.990	...	...	...	51.5	...	...	...	...
5083.35	26.0	-2.958	0.958	42.8	92.5	48.0	60.0	53.9	54.3	87.0	...
5088.16	26.0	-1.680	4.150	...	20.4	...	...	...	...	...	39.0
5090.78	26.0	-0.400	4.260	20.6	69.4	19.0	39.9	33.5	34.3	58.6	89.6
5104.44	26.0	-1.590	4.280	...	23.0	...	...	...	...	...	...
5109.66	26.0	-0.980	4.300	...	62.4	...	31.1	23.5	22.3	36.7	74.0
5123.73	26.0	-3.068	1.011	42.2	89.3	33.9	58.7	56.3	59.3	83.1	...
5125.12	26.0	-0.080	4.220	53.3	...	47.7	64.1	66.2	70.7	...	...
5127.37	26.0	-3.307	0.915	...	81.4	25.1	52.1	47.5	53.6	71.6	98.9
5133.69	26.0	0.200	4.180	61.3	...	59.0	82.9	85.6	81.2	98.4	...
5141.74	26.0	-2.238	2.424	21.8	70.1	...	35.9	30.1	...	59.7	94.3
5145.09	26.0	-2.876	2.198	...	31.5	...	...	...	...	24.4	58.3
5150.85	26.0	-3.037	0.990	41.1	92.5	32.9	56.3	53.1	...	85.3	...
5151.92	26.0	-3.322	1.011	28.4	...	25.1	44.7	49.0	33.7	...	...

Table C.3: Equivalent Width Measurements, Table 3 of 5, continued

λ (Å)	Ion	loggf	EP	2310-312	1903-096	2796-054	2180-545	2797-407	1916-559	2305-365	1891-140
5162.28	26.0	0.020	4.180	56.6	...	44.2	80.3	67.0	71.8	87.6	...
5166.28	26.0	-4.195	0.000	32.5	98.7	...	51.4	...	...	...	...
5171.61	26.0	-1.793	1.485	80.0	...	69.0	98.3	...	...	...	...
5187.92	26.0	-1.371	4.143	...	38.1	...	...	...	...	20.5	63.5
5191.47	26.0	-0.551	3.038	63.7	...	...	90.8	86.0	82.1	...	...
5192.35	26.0	-0.421	2.998	78.7	...	74.0	...	97.1	...	...	...
5194.95	26.0	-2.090	1.557	65.2	...	56.3	78.3	...	74.1	91.2	...
5198.72	26.0	-2.135	2.223	30.8	88.4	...	49.0	52.2	43.9	65.1	...
5202.34	26.0	-1.838	2.176	59.5	...	56.4	...	74.0	...	...	...
5216.28	26.0	-2.150	1.608	62.2	...	54.1	69.8	71.8	...	91.5	...
5217.40	26.0	-1.162	3.211	33.3	95.9	33.2	49.3	48.5	47.4	70.1	...
5223.19	26.0	-1.783	3.635	...	...	...	...	...	...	...	27.8
5225.53	26.0	-4.789	0.110	...	52.2	...	...	...	...	40.6	76.3
5232.95	26.0	-0.057	2.940	96.7	...	99.8	...	...	...	...	...
5242.46	26.0	-0.967	3.634	...	68.7	...	37.3	39.9	36.5	58.1	78.1
5243.78	26.0	-1.120	4.256	...	41.7	...	14.7	...	...	23.5	63.3
5247.06	26.0	-4.946	0.087	...	...	...	...	...	...	39.6	...
5250.22	26.0	-4.938	0.121	...	52.2	...	...	...	...	41.9	80.7
5253.03	26.0	-3.940	2.280	...	...	...	...	...	...	...	16.5
5254.95	26.0	-4.764	0.110	22.8	...	22.7	...	...	...	...	...
5266.56	26.0	-0.385	2.998	83.0	...	85.4	94.8	95.5	82.9	...	...
5281.80	26.0	-0.834	3.038	62.5	...	57.9	74.2	64.2	...	96.6	...
5283.63	26.0	-0.525	3.241	74.3	...	...	84.6	81.8	78.6	...	...
5288.53	26.0	-1.510	3.680	...	42.0	...	...	...	13.6	38.8	61.8
5295.32	26.0	-1.670	4.415	...	12.6	...	...	...	...	...	35.7
5302.31	26.0	-0.720	3.283	52.4	...	55.3	69.9	53.6	58.6	97.5	...
5307.37	26.0	-2.987	1.608	20.3	71.0	...	35.1	...	28.3	62.0	94.0
5321.11	26.0	-1.090	4.435	...	27.8	...	...	...	...	...	40.8
5322.01	26.0	-2.803	2.279	...	46.8	...	...	...	...	27.9	64.9
5324.19	26.0	-0.103	3.211	85.3	...	88.6	...	99.5	95.1	...	...
5332.92	26.0	-2.776	1.557	33.5	...	...	...	...	34.4	...	...

Table C.3: Equivalent Width Measurements, Table 3 of 5, continued

λ (Å)	Ion	loggf	EP	2310-312	1903-096	2796-054	2180-545	2797-407	1916-559	2305-365	1891-140
5339.94	26.0	-0.720	3.266	56.5	...	46.7	76.0	64.2	55.8	94.9	...
5364.87	26.0	0.228	4.446	54.9	95.1	51.1	71.9	...	42.8	84.6	...
5365.40	26.0	-1.020	3.573	21.0	60.5	...	29.6	...	...	53.3	74.5
5367.47	26.0	0.443	4.415	53.3	...	55.3	82.8	71.3	64.7	92.5	...
5369.97	26.0	0.536	4.371	60.9	...	64.7	85.6	80.8	69.7	...	...
5373.70	26.0	-0.760	4.470	...	50.1	...	...	...	...	32.2	66.8
5379.58	26.0	-1.514	3.695	...	47.6	...	15.9	...	...	38.5	63.9
5383.38	26.0	0.645	4.312	72.3	...	67.6	83.5	...	86.1	...	...
5386.34	26.0	-1.740	4.154	...	18.7	...	...	...	...	...	35.5
5389.49	26.0	-0.400	4.410	...	67.4	19.2	34.4	...	28.1	50.0	82.3
5393.18	26.0	-0.715	3.241	56.7	...	51.1	72.6	73.1	61.8	90.8	...
5397.14	26.0	-1.993	0.915	93.7	...	...	...	...	98.1	...	...
5398.29	26.0	-0.710	4.446	15.3	55.5	...	32.2	...	22.0	40.6	79.4
5401.27	26.0	-1.890	4.320	...	12.8	...	...	...	...	...	31.9
5405.78	26.0	-1.844	0.990	98.4	...	...	...	...	...	...	...
5406.78	26.0	-1.720	4.370	...	27.0	...	...	...	...	...	39.7
5409.14	26.0	-1.200	4.370	...	39.8	...	...	...	...	...	56.8
5410.91	26.0	0.398	4.473	...	...	...	64.6	...	58.0	...	...
5415.20	26.0	0.642	4.386	61.3	...	66.6	...	78.2	70.6	...	...
5417.04	26.0	-1.660	4.415	...	18.8	...	...	...	...	...	32.7
5487.14	26.0	-1.430	4.410	...	24.5	...	...	...	...	...	51.5
5487.77	26.0	-0.620	4.140	17.8	...	...	46.8	31.2	39.8	51.5	...
5497.52	26.0	-2.830	1.010	51.8	...	52.8	72.3	66.7	61.0	93.6	...
5501.48	26.0	-3.047	0.958	47.6	...	...	64.6	62.8	57.2	84.8	...
5506.79	26.0	-2.797	0.990	58.8	...	...	72.6	68.0	66.4	91.3	...
5522.45	26.0	-1.520	4.209	...	29.8	...	...	...	...	...	49.4
5525.55	26.0	-1.080	4.230	...	41.0	...	...	...	...	29.5	69.6
5546.51	26.0	-1.210	4.372	...	32.2	...	...	...	...	...	49.9
5547.00	26.0	-1.880	4.218	...	...	...	...	...	...	...	23.6
5553.58	26.0	-1.310	4.430	...	...	...	...	...	...	...	58.5
5554.88	26.0	-0.350	4.550	...	70.9	...	...	...	27.6	52.1	90.3

Table C.3: Equivalent Width Measurements, Table 3 of 5, continued

λ (Å)	Ion	loggf	EP	2310-312	1903-096	2796-054	2180-545	2797-407	1916-559	2305-365	1891-140
5560.22	26.0	-1.160	4.435	...	45.3	...	...	...	...	...	54.2
5567.39	26.0	-2.670	2.610	...	49.1	...	...	...	...	34.2	68.5
5569.63	26.0	-0.486	3.417	53.6	...	54.3	79.4	54.7	68.4	96.7	...
5572.85	26.0	-0.275	3.397	76.7	...	...	...	98.3	82.0	...	...
5576.10	26.0	-0.940	3.430	38.9	93.4	...	61.0	53.0	47.4	79.6	...
5586.77	26.0	-0.144	3.368	81.2	...	71.1	...	97.9	88.3	...	...
5618.64	26.0	-1.276	4.209	...	...	...	...	...	...	...	56.5
5619.61	26.0	-1.670	4.386	...	20.3	...	...	...	...	...	41.3
5620.49	26.0	-1.810	4.150	...	23.1	...	...	...	...	...	47.3
5624.04	26.0	-1.220	4.390	...	35.8	...	10.2	...	...	18.4	50.4
5624.54	26.0	-0.755	3.420	...	...	36.1	66.3	49.8	53.4	...	...
5635.83	26.0	-1.860	4.256	...	22.3	...	...	...	...	...	40.9
5636.70	26.0	-2.560	3.640	...	11.9	...	...	...	...	...	...
5641.44	26.0	-1.080	4.260	...	48.9	...	...	...	...	30.1	68.0
5650.00	26.0	-0.920	5.100	...	...	...	...	...	...	...	33.6
5650.70	26.0	-0.860	4.550	...	...	...	...	...	...	...	39.5
5652.33	26.0	-1.920	4.260	...	17.6	...	...	...	...	...	28.3
5653.89	26.0	-1.540	4.390	...	...	...	...	...	...	...	38.2
5662.52	26.0	-0.573	4.178	30.6	...	...	...	...	...	59.4	...
5679.02	26.0	-0.820	4.650	...	42.6	...	...	...	...	26.2	62.3
5686.53	26.0	-0.446	4.548	...	...	...	...	...	...	40.9	...
5701.56	26.0	-2.216	2.559	...	71.9	...	...	...	...	55.5	87.1
5705.47	26.0	-1.360	4.300	...	24.7	...	...	...	...	38.1	36.9
5705.98	26.0	-0.490	4.610	...	65.5	...	...	...	...	...	...
5717.84	26.0	-1.100	4.284	...	45.0	...	...	14.8	...	36.1	64.7
5731.77	26.0	-1.270	4.256	...	39.8	...	18.9	...	...	35.5	55.7
5741.86	26.0	-1.673	4.256	...	16.3	...	...	...	...	...	32.2
5752.04	26.0	-0.940	4.550	...	37.6	...	...	...	...	20.6	55.9
5753.12	26.0	-0.688	4.260	...	60.5	...	...	...	24.7	...	77.3
5762.99	26.0	-0.410	4.210	...	93.9	34.9	59.1	50.5	42.6	68.8	...
5775.09	26.0	-1.298	4.220	...	40.4	...	15.8	...	...	20.8	62.2

Table C.3: Equivalent Width Measurements, Table 3 of 5, continued

λ (Å)	Ion	loggf	EP	2310-312	1903-096	2796-054	2180-545	2797-407	1916-559	2305-365	1891-140
5793.92	26.0	-1.660	4.220	...	24.2	...	...	...	...	...	36.8
5805.76	26.0	-1.490	5.030	...	...	...	...	...	...	...	15.1
5806.73	26.0	-1.030	4.608	...	41.8	...	...	...	...	...	59.1
5809.22	26.0	-1.740	3.880	...	...	...	...	...	...	...	55.3
5814.81	26.0	-1.940	4.283	...	14.5	...	...	...	...	...	19.3
5816.38	26.0	-0.601	4.548	...	...	...	22.5	...	...	36.0	83.6
5838.37	26.0	-2.240	3.940	...	...	...	...	...	...	...	23.1
5852.23	26.0	-1.300	4.548	...	30.6	...	...	...	...	...	36.8
5855.09	26.0	-1.478	4.608	...	...	...	...	...	...	...	17.7
5856.10	26.0	-1.328	4.294	...	23.2	...	...	...	...	...	37.1
5858.78	26.0	-2.260	4.220	...	...	...	...	...	...	...	9.7
5859.60	26.0	-0.550	4.550	...	53.7	...	19.9	...	23.1	33.6	73.7
5862.35	26.0	-0.330	4.550	...	73.7	...	38.9	32.9	...	55.3	85.7
5883.81	26.0	-1.260	3.960	...	48.5	...	...	...	...	...	68.5
5905.68	26.0	-0.770	4.652	...	43.9	...	...	...	...	22.8	59.3
5927.80	26.0	-1.070	4.652	...	28.7	...	...	...	...	...	43.0
5929.68	26.0	-1.380	4.548	...	29.3	...	...	...	...	...	41.9
5930.19	26.0	-0.140	4.650	24.2	71.1	26.8	...	27.9	33.5	57.5	88.7
5934.67	26.0	-1.120	3.929	...	61.5	...	30.7	...	...	...	77.9
5940.99	26.0	-2.050	4.180	...	11.0	...	...	...	...	...	...
5952.72	26.0	-1.340	3.980	...	...	...	...	...	...	...	64.5
5956.71	26.0	-4.608	0.859	...	33.1	...	...	...	...	24.8	57.3
5976.79	26.0	-1.330	3.940	...	46.1	...	...	...	...	38.6	69.4
5983.69	26.0	-0.660	4.550	...	57.1	...	...	...	...	39.2	74.6
5984.83	26.0	-0.260	4.730	...	56.2	...	...	...	...	46.4	87.5
6003.02	26.0	-1.110	3.880	...	65.8	...	22.9	...	...	42.4	84.9
6024.05	26.0	0.030	4.550	36.8	88.7	28.8	52.8	45.5	52.1	72.0	...
6027.06	26.0	-1.089	4.076	...	51.4	...	...	...	...	40.1	68.0
6055.99	26.0	-0.370	4.730	...	56.5	...	...	...	...	37.2	76.9
6065.49	26.0	-1.530	2.608	49.3	94.2	42.2	60.9	...	...	86.0	...
6078.50	26.0	-0.330	4.790	...	55.3	...	...	...	...	35.3	80.8

Table C.3: Equivalent Width Measurements, Table 3 of 5, continued

λ (Å)	Ion	loggf	EP	2310-312	1903-096	2796-054	2180-545	2797-407	1916-559	2305-365	1891-140
6079.02	26.0	-1.100	4.652	...	24.7	...	...	...	...	10.7	47.2
6082.72	26.0	-3.573	2.223	...	16.5	...	...	...	...	...	42.6
6085.26	26.0	-2.710	2.759	...	28.4	...	...	...	...	...	53.6
6089.57	26.0	-0.900	5.020	...	22.2	...	...	...	...	...	35.9
6093.65	26.0	-1.470	4.608	...	...	...	...	...	...	...	35.4
6096.67	26.0	-1.880	3.984	...	17.1	...	...	...	...	...	44.4
6098.25	26.0	-1.880	4.560	...	...	...	...	...	...	...	28.6
6127.90	26.0	-1.400	4.140	...	30.2	...	...	...	...	24.9	47.9
6136.62	26.0	-1.400	2.453	54.7	...	...	...	64.1	68.2	...	...
6137.70	26.0	-1.403	2.588	50.8	...	...	60.8	56.9	53.1	85.6	...
6151.62	26.0	-3.299	2.176	...	34.6	...	...	...	...	20.6	49.6
6157.73	26.0	-1.220	4.076	...	52.5	...	...	...	...	38.8	71.4
6165.36	26.0	-1.474	4.143	...	30.3	...	...	...	...	...	46.8
6173.34	26.0	-2.880	2.223	...	60.0	...	...	...	...	39.9	75.0
6180.20	26.0	-2.650	2.730	...	37.5	...	...	...	...	...	57.7
6188.00	26.0	-1.670	3.943	...	37.8	...	...	...	...	...	51.4
6200.32	26.0	-2.437	2.608	...	57.6	...	...	...	...	...	74.3
6213.44	26.0	-2.482	2.223	...	62.6	...	32.2	...	20.1	66.1	89.2
6219.29	26.0	-2.433	2.198	...	79.2	...	40.8	...	36.1	67.3	91.7
6226.74	26.0	-2.200	3.880	...	...	...	...	...	...	...	35.8
6229.23	26.0	-2.805	2.845	...	21.8	...	...	...	...	...	44.5
6230.74	26.0	-1.281	2.559	62.9	...	69.2	81.1	65.8	82.2	...	...
6240.65	26.0	-3.173	2.223	...	28.5	...	...	...	...	...	54.8
6246.33	26.0	-0.877	3.603	...	93.7	...	52.1	43.5	47.0	74.7	...
6252.56	26.0	-1.687	2.404	49.0	99.4	...	67.6	58.3	56.6	91.4	...
6254.26	26.0	-2.430	2.280	36.3	94.5	35.6	54.9	48.4	41.1	...	...
6265.14	26.0	-2.550	2.176	21.7	65.6	...	37.3	26.7	22.2	66.7	88.0
6270.23	26.0	-2.609	2.858	...	33.3	...	...	...	...	...	57.4
6271.28	26.0	-2.700	3.330	...	...	...	...	...	...	...	26.1
6290.97	26.0	-0.730	4.730	...	56.7	...	...	...	...	...	68.4
6297.80	26.0	-2.740	2.223	...	...	...	...	...	...	61.1	83.0

Table C.3: Equivalent Width Measurements, Table 3 of 5, continued

λ (Å)	Ion	loggf	EP	2310-312	1903-096	2796-054	2180-545	2797-407	1916-559	2305-365	1891-140
6302.50	26.0	-1.110	3.690	...	...	...	...	...	...	...	86.5
6315.31	26.0	-1.230	4.140	...	...	...	...	...	...	...	82.4
6315.81	26.0	-1.660	4.076	...	...	...	...	...	...	...	44.0
6322.69	26.0	-2.426	2.588	...	64.4	...	...	23.5	...	47.6	...
6330.85	26.0	-1.720	4.733	...	...	...	...	...	...	...	36.1
6335.33	26.0	-2.177	2.198	28.1	82.4	...	57.4	35.8	42.2	75.0	97.3
6344.15	26.0	-2.923	2.433	...	51.0	...	...	...	...	33.6	71.3
6355.04	26.0	-2.291	2.845	...	55.5	...	...	...	...	41.1	79.8
6358.69	26.0	-4.468	0.859	...	63.0	...	...	...	...	42.0	87.4
4178.86	26.1	-2.443	2.583	59.0	63.0	68.5	72.8	72.6	63.8	73.2	89.1
4233.17	26.1	-1.809	2.583	86.0	...	99.5	...	...	...	...	...
4416.82	26.1	-2.600	2.778	49.5	59.4	...	...	...	...	62.1	77.4
4491.40	26.1	-2.640	2.856	41.0	69.1	47.3	65.1	57.7	48.4	58.7	84.1
4508.30	26.1	-2.350	2.856	57.5	80.0	69.9	80.9	68.7	69.4	74.7	93.5
4520.23	26.1	-2.620	2.807	47.1	...	61.0	69.7	62.2	61.9	69.5	91.0
4541.52	26.1	-2.970	2.856	32.8	...	...	57.3	44.6	41.7	54.6	...
4576.34	26.1	-2.920	2.844	28.8	61.1	38.6	60.5	42.5	39.3	48.8	72.1
4582.83	26.1	-3.062	2.844	27.9	58.4	25.8	40.6	...	29.2	40.1	64.5
4583.84	26.1	-1.740	2.807	...	...	92.7	...	...	95.0	...	...
4620.52	26.1	-3.188	2.828	...	41.4	20.1	38.3	...	29.0	31.8	59.2
4629.34	26.1	-2.480	2.810	58.9	89.9	74.5	80.5	76.7	68.5	79.7	...
4635.31	26.1	-1.580	5.956	...	10.8	...	...	...	...	...	...
4893.82	26.1	-4.270	2.828	...	...	...	...	...	...	...	21.1
4923.93	26.1	-1.206	2.891	96.1	...	...	...	...	...	...	...
4993.35	26.1	-3.680	2.807	...	33.5	...	22.4	...	...	23.9	41.7
5132.67	26.1	-4.090	2.807	...	14.0	...	11.1	...	...	...	32.4
5197.58	26.1	-2.054	3.230	50.8	79.2	62.5	76.6	62.7	61.8	65.8	86.7
5234.63	26.1	-2.210	3.221	46.3	76.4	65.3	73.5	69.9	51.7	57.9	83.1
5264.81	26.1	-3.233	3.230	14.4	35.7	...	29.1	24.3	14.9	27.4	46.9
5276.00	26.1	-1.900	3.199	72.1	...	85.0	...	92.1	...	...	...
5284.11	26.1	-3.200	2.891	26.0	...	...	...	...	...	46.5	...

Table C.3: Equivalent Width Measurements, Table 3 of 5, continued

λ (Å)	Ion	loggf	EP	2310-312	1903-096	2796-054	2180-545	2797-407	1916-559	2305-365	1891-140
5325.56	26.1	-2.570	3.221	...	35.2	...	32.8	...	27.8	...	47.1
5414.08	26.1	-3.482	3.221	...	20.5	...	...	...	...	...	...
5534.85	26.1	-2.860	3.245	...	59.6	36.9	57.8	...	27.8	37.9	59.2
5991.38	26.1	-3.650	3.153	...	26.0	...	...	...	...	...	37.9
6149.25	26.1	-2.840	3.889	...	...	...	...	...	...	...	37.6
6247.56	26.1	-2.430	3.892	...	52.9	...	46.8	...	...	39.5	53.8
4121.33	27.0	-0.320	0.920	59.6	...	54.3	73.2	72.4	71.3	...	...
5369.56	27.0	-1.590	1.740	...	...	...	...	...	...	20.7	...
3807.15	28.0	-1.180	0.420	93.2	...	...	...	...	...	...	...
3858.30	28.0	-0.970	0.420	...	...	96.5	...	...	...	...	...
4686.22	28.0	-0.580	3.600	...	44.0	...	18.4	...	15.0	35.9	61.7
4857.40	28.0	-0.830	3.740	...	30.4	...	...	...	...	34.7	55.8
4866.27	28.0	-0.210	3.539	...	61.9	...	...	...	...	49.2	80.8
4904.42	28.0	-0.190	3.540	20.8	68.5	23.4	40.5	...	28.2	62.0	80.0
4913.98	28.0	-0.630	3.740	...	41.9	...	...	...	...	28.1	54.0
4935.83	28.0	-0.380	3.940	...	47.4	...	...	19.4	14.1	40.2	62.0
4953.21	28.0	-0.580	3.740	...	35.7	...	...	...	12.5	26.1	52.6
4998.22	28.0	-0.690	3.606	...	38.1	...	...	...	...	...	57.0
5003.75	28.0	-3.130	1.680	...	...	...	...	...	...	...	37.7
5010.94	28.0	-0.900	3.630	...	28.6	...	...	...	...	27.9	49.5
5035.37	28.0	0.290	3.630	37.4	82.9	...	54.3	49.8	51.1	...	...
5048.85	28.0	-0.390	3.850	...	46.0	...	24.0	...	...	33.5	72.7
5082.35	28.0	-0.540	3.660	...	45.2	...	19.1	...	...	36.3	65.6
5084.11	28.0	-0.060	3.680	...	74.6	...	43.5	...	...	57.9	88.2
5088.54	28.0	-1.080	3.850	...	...	...	...	...	...	...	30.1
5088.96	28.0	-1.290	3.680	...	14.9	...	...	...	...	...	28.0
5094.42	28.0	-1.120	3.830	...	16.6	...	...	...	...	...	30.3
5102.97	28.0	-2.660	1.680	...	33.3	...	...	...	...	26.1	51.8
5115.40	28.0	-0.140	3.830	21.3	58.2	...	31.1	27.6	27.3	48.6	73.2
5197.17	28.0	-1.140	3.900	...	...	...	...	...	...	...	21.8
5578.72	28.0	-2.640	1.680	...	45.3	...	...	...	...	...	56.8

Table C.3: Equivalent Width Measurements, Table 3 of 5, continued

λ (Å)	Ion	loggf	EP	2310-312	1903-096	2796-054	2180-545	2797-407	1916-559	2305-365	1891-140
5587.86	28.0	-2.140	1.930	...	...	...	...	...	...	28.1	...
5589.36	28.0	-1.140	3.900	...	23.9	...	...	...	...	...	23.3
5593.74	28.0	-0.840	3.900	...	35.9	...	...	...	...	...	38.5
5754.67	28.0	-1.850	1.930	...	...	...	17.4	...	...	49.7	...
5760.83	28.0	-0.805	4.100	...	23.4	...	...	...	...	...	...
5805.22	28.0	-0.638	4.170	...	...	...	...	...	...	...	36.8
5846.99	28.0	-3.210	1.680	...	...	...	...	...	...	...	20.3
5892.87	28.0	-2.340	1.990	...	58.9	...	...	...	...	42.1	...
5996.74	28.0	-1.010	4.236	...	...	...	...	...	...	...	21.9
6007.32	28.0	-3.410	1.677	...	15.2	...	...	...	...	...	37.8
6086.28	28.0	-0.515	4.260	...	...	...	...	...	...	...	44.8
6108.12	28.0	-2.430	1.680	...	47.3	...	...	...	...	37.5	65.6
6111.08	28.0	-0.820	4.090	...	...	...	...	...	...	...	32.1
6128.97	28.0	-3.330	1.680	...	18.7	...	...	...	...	...	27.4
6175.37	28.0	-0.535	4.090	...	35.3	...	...	...	...	...	42.9
6176.81	28.0	-0.529	4.090	...	52.0	...	...	...	...	...	65.3
6186.71	28.0	-0.965	4.100	...	...	...	...	...	...	...	22.6
6204.60	28.0	-1.140	4.090	...	...	...	...	...	...	...	19.9
6223.98	28.0	-0.910	4.106	...	...	...	...	...	...	...	38.5
6314.66	28.0	-1.770	1.930	...	...	...	...	...	...	51.2	85.9
6322.17	28.0	-1.210	4.154	...	...	...	...	...	...	...	22.5
6327.60	28.0	-3.060	1.680	...	...	...	...	...	...	...	42.1
6360.82	28.0	-1.150	4.170	...	...	...	...	...	...	...	28.0
5105.54	29.0	-3.720	1.380	...	68.6	...	19.6	...	15.2	50.9	99.2
5218.21	29.0	0.300	3.800	...	34.5	...	...	...	...	...	...
4722.16	30.0	-0.390	4.030	...	58.7	...	39.2	27.1	36.5	58.6	73.2
4810.54	30.0	-0.170	4.080	25.2	58.6	28.7	45.9	44.8	35.2	57.5	75.7
4607.34	38.0	0.280	0.000	...	...	...	...	...	...	18.0	44.7
3549.01	39.1	-0.280	0.130	...	53.8	49.2	45.2	43.5	...	53.8	77.3
3600.74	39.1	0.280	0.180	47.5	65.8	71.9	63.0	59.7	49.7	71.5	81.3
3611.04	39.1	0.010	0.130	42.9	...	62.4	62.1	55.0	...	...	...

Table C.3: Equivalent Width Measurements, Table 3 of 5, continued

λ (Å)	Ion	loggf	EP	2310-312	1903-096	2796-054	2180-545	2797-407	1916-559	2305-365	1891-140
3774.33	39.1	0.210	0.130	...	69.3	...	...	...	52.9	68.1	83.9
3788.70	39.1	-0.070	0.100	61.3	...	76.1	62.5	66.1	41.5	58.4	...
3818.34	39.1	-0.980	0.130	...	...	28.6	...	...	...	...	...
3950.36	39.1	-0.490	0.100	31.0	52.5	56.0	55.3	44.2	35.6	59.3	73.2
4398.01	39.1	-1.000	0.130	...	40.8	...	...	...	...	...	...
4883.69	39.1	0.070	1.080	33.5	48.1	...	37.7	...	...	46.1	59.3
5087.43	39.1	-0.170	1.080	...	32.4	...	26.0	...	...	...	54.3
5119.12	39.1	-1.360	0.990	...	...	...	...	...	...	...	18.1
5123.22	39.1	-0.830	0.990	...	23.1	...	...	...	...	12.8	...
5200.41	39.1	-0.570	0.990	...	...	...	16.0	...	...	19.9	...
3714.78	40.1	-0.960	0.530	...	21.6	27.4	...	...	...	14.1	38.8
4050.33	40.1	-1.060	0.710	...	13.3	...	...	...	...	...	...
4161.21	40.1	-0.590	0.710	...	...	...	35.6	...	...	...	...
4208.99	40.1	-0.510	0.710	...	32.5	37.3	22.4	...	...	34.8	41.4
4317.32	40.1	-1.450	0.710	...	10.0	...	...	...	...	...	...
4496.97	40.1	-0.890	0.710	...	...	...	...	...	45.7	...	...
3692.36	45.0	0.173	0.000	...	38.0	...	...	...	...	...	50.2
5853.69	56.1	-0.910	0.600	20.6	62.7	36.2	39.4	25.1	29.5	52.1	68.3
3988.51	57.1	0.210	0.170	...	38.8	...	18.0	...	...	31.9	73.4
3995.75	57.1	-0.060	0.170	...	...	...	...	...	...	...	49.6
4086.71	57.1	-0.070	0.000	...	35.4	...	16.2	...	...	31.3	45.0

Table C.4: Equivalent Width Measurements, Table 4 of 5

λ (Å)	Ion	loggf	EP	2311-476	2311-208	2621-215	2038-050	2038-226	2057-001	2053-419
5682.65	11.0	-0.699	2.100	57.6	64.4	53.8	...	...	48.8	37.0

Table C.4: Equivalent Width Measurements, Table 4 of 5, continued

λ (Å)	Ion	loggf	EP	2311-476	2311-208	2621-215	2038-050	2038-226	2057-001	2053-419
5688.19	11.0	-0.420	2.100	83.3	76.5	75.9	71.2	82.1	74.8	68.2
6154.23	11.0	-1.530	2.100	...	21.5	...	...	...	...	...
6160.75	11.0	-1.230	2.100	...	29.2	25.8	...	...	...	10.7
4571.10	12.0	-5.570	0.000	84.0	90.1	57.8	42.4	...	56.8	45.2
4730.04	12.0	-2.347	4.350	41.0	41.2	25.5	...	...	...	...
5711.09	12.0	-1.630	4.340	85.7	92.2	...	...	...	64.9	61.0
5665.55	14.0	-2.040	4.920	16.8	20.2	17.1	...	...	17.2	...
5690.43	14.0	-1.870	4.930	28.6	23.3	...	...	...	...	12.5
5701.10	14.0	-2.050	4.930	19.0	25.4	...	...	...	...	...
5708.40	14.0	-1.470	4.950	...	...	...	...	...	...	39.4
5772.15	14.0	-1.750	5.080	29.5	31.1	18.0	...	...	...	16.1
5793.07	14.0	-2.060	4.930	27.2	...	...	...	...	...	...
5948.54	14.0	-1.230	5.080	64.6	58.5	58.7	...	...	...	34.7
6125.03	14.0	-1.570	5.610	19.0	17.6	...	...	...	...	...
6142.49	14.0	-1.480	5.620	...	21.7	...	...	...	...	...
6145.02	14.0	-1.370	5.610	22.0	...	18.1	...	...	...	...
6155.13	14.0	-0.760	5.620	52.2	47.8	...	...	...	...	32.4
6237.32	14.0	-1.010	5.620	44.9	38.4	25.8	...	...	...	...
6243.82	14.0	-1.300	5.616	...	23.9	...	...	...	...	...
6244.48	14.0	-1.320	5.616	36.5	...	...	...	...	...	...
6347.09	14.1	0.260	8.120	47.4	31.0	58.6	...	...	52.2	30.8
4318.66	20.0	-0.210	1.900	...	...	...	...	...	...	90.3
4512.27	20.0	-2.030	2.520	8.6	...	...	...	...	...	...
4526.93	20.0	-0.420	2.710	64.4	60.0	57.6	...	...	45.6	...
4578.56	20.0	-0.558	2.520	55.2	64.2	59.1	...	49.8	50.2	41.5
4685.27	20.0	-0.940	2.930	30.6	28.6	...	...	...	...	17.7
5260.39	20.0	-1.780	2.520	...	15.1	...	...	...	...	...
5261.71	20.0	-0.730	2.520	64.2	69.5	61.6	...	...	60.9	50.8
5349.47	20.0	-0.310	2.710	...	...	...	...	...	...	45.2
5512.99	20.0	-0.266	2.930	56.8	59.8	54.9	...	53.8	56.2	41.2
5588.76	20.0	0.358	2.510	...	...	...	...	...	...	95.7

Table C.4: Equivalent Width Measurements, Table 4 of 5, continued

λ (Å)	Ion	loggf	EP	2311-476	2311-208	2621-215	2038-050	2038-226	2057-001	2053-419
5590.13	20.0	-0.710	2.510	68.8	67.8	54.7	...	60.9	71.4	57.2
5601.28	20.0	-0.438	2.520	71.4	77.0	71.4	...	62.8	71.9	55.4
6102.73	20.0	-0.790	1.880	...	...	...	...	...	82.1	81.2
6161.30	20.0	-1.270	2.520	...	39.2	27.2	...	...	...	...
6166.44	20.0	-1.140	2.520	36.9	43.5	30.0	...	38.0	...	23.4
6169.04	20.0	-0.800	2.520	53.3	70.9	58.0	...	...	...	...
6169.56	20.0	-0.480	2.520	71.4	82.5	70.8	...	...	...	52.5
5001.47	20.1	-0.520	7.500	...	...	...	...	...	...	8.0
4400.39	21.1	-0.540	0.610	...	...	...	...	...	84.9	73.8
5239.82	21.1	-0.765	1.450	45.7	37.4	42.6	...	44.9	41.3	37.1
5526.82	21.1	0.020	1.770	75.4	62.1	84.4	...	67.3	76.5	62.5
5640.99	21.1	-1.130	1.500	...	26.1	...	...	...	...	21.5
5657.88	21.1	-0.600	1.510	52.8	45.8	58.2	...	...	...	45.0
5669.04	21.1	-1.120	1.500	24.1	22.6	31.9	...	...	...	14.7
3924.53	22.0	-0.940	0.020	41.1	52.0	30.8	...	25.7	36.5	31.4
3958.22	22.0	-0.176	0.050	72.8	...	...	...	78.9	...	61.4
3998.64	22.0	-0.060	0.050	89.0	94.0	77.2	...	...	84.1	70.9
4008.93	22.0	-1.072	0.021	70.2	...	...	...	...	...	46.6
4512.74	22.0	-0.480	0.840	41.7	49.8	29.3	...	...	22.9	19.4
4518.03	22.0	-0.325	0.830	...	61.0	...	...	...	33.1	29.4
4533.25	22.0	0.476	0.850	...	...	...	...	...	...	64.4
4534.78	22.0	0.280	0.840	73.6	81.9	61.8	...	...	62.7	56.8
4548.77	22.0	-0.354	0.830	41.7	52.8	30.8	28.8	...	34.8	27.7
4555.49	22.0	-0.490	0.850	37.5	51.0	...	...	...	21.6	19.2
4617.28	22.0	0.390	1.750	43.1	44.8	31.5	29.0	...	30.4	23.9
4623.10	22.0	0.170	1.740	27.1	37.5	17.5	...	...	20.5	...
4758.12	22.0	0.425	2.250	22.5	23.7	15.8	10.6	...	12.7	...
4759.28	22.0	0.514	2.250	22.3	34.0	19.9	...	...	20.3	...
4820.41	22.0	-0.439	1.500	21.9	24.7	...	...	...	...	...
4840.88	22.0	-0.450	0.900	42.2	47.3	28.4	25.6	...	34.5	...
4913.62	22.0	0.220	1.870	27.9	31.1	...	...	...	...	11.6

Table C.4: Equivalent Width Measurements, Table 4 of 5, continued

λ (Å)	Ion	loggf	EP	2311-476	2311-208	2621-215	2038-050	2038-226	2057-001	2053-419
4981.74	22.0	0.504	0.850	90.6	89.4	77.2	66.0	...	78.2	72.2
4999.51	22.0	0.250	0.830	82.3	86.4	74.3	...	...	69.2	64.7
5016.17	22.0	-0.574	0.850	38.8	43.8	16.4	...	...	...	...
5022.87	22.0	-0.430	0.830	38.8	54.2	32.5	...	...	...	25.5
5024.85	22.0	-0.600	0.820	38.1	48.1	24.6	...	...	20.9	21.5
5039.96	22.0	-1.130	0.020	49.7	56.3	...	...	...	40.1	27.3
5064.66	22.0	-0.990	0.050	...	...	...	...	...	...	35.9
5087.06	22.0	-0.780	1.430	...	8.7	...	...	...	...	...
5113.45	22.0	-0.780	1.440	...	18.3	...	...	...	...	...
5147.48	22.0	-2.012	0.000	...	19.3	7.7	...	...	...	...
5192.98	22.0	-1.006	0.020	55.1	67.5	44.6	...	...	42.0	37.0
5210.39	22.0	-0.884	0.050	62.2	75.1	54.3	37.2	...	49.7	34.2
5644.14	22.0	0.050	2.270	16.6	...	...	...	...	...	...
5662.16	22.0	-0.110	2.320	...	9.4	...	...	...	...	...
5866.45	22.0	-0.840	1.070	19.6	...	...	...	...	...	...
5941.75	22.0	-1.520	1.050	...	...	...	...	...	...	12.3
6258.10	22.0	-0.355	1.440	22.5	39.5	...	...	...	...	14.8
6258.71	22.0	-0.240	1.460	30.3	43.7	...	...	...	...	...
6261.11	22.0	-0.480	1.430	20.9	32.1	...	...	...	...	...
3987.61	22.1	-2.730	0.610	49.3	44.0	52.8	...	...	48.9	41.4
4028.35	22.1	-1.000	1.890	76.5	74.1	83.8	64.2	72.8	77.2	70.3
4394.06	22.1	-1.770	1.220	...	...	76.6	...	...	62.9	59.0
4395.84	22.1	-1.970	1.240	...	59.2	67.6	44.7	...	54.6	48.8
4399.77	22.1	-1.270	1.240	...	...	98.4	96.9	...	91.5	84.7
4544.02	22.1	-2.410	1.240	30.3	36.6	29.3	27.4	...	31.9	...
4563.77	22.1	-0.960	1.220	...	...	...	98.6	...	...	...
4568.33	22.1	-2.650	1.220	...	17.2	...	...	...	20.0	...
4583.42	22.1	-2.720	1.160	18.8	24.8	23.7	...	...	24.4	12.3
4589.95	22.1	-1.790	1.240	81.9	77.4	86.3	...	88.1	80.6	72.2
4636.32	22.1	-3.020	1.165	12.6	13.7	12.6	...	...	...	...
4708.67	22.1	-2.210	1.240	45.2	44.9	44.2	...	...	44.3	32.8

Table C.4: Equivalent Width Measurements, Table 4 of 5, continued

λ (Å)	Ion	loggf	EP	2311-476	2311-208	2621-215	2038-050	2038-226	2057-001	2053-419
4779.98	22.1	-1.370	2.048	60.6	58.1	66.2	...	68.6	65.4	53.8
4798.54	22.1	-2.430	1.080	...	...	...	...	...	...	30.3
4805.09	22.1	-1.120	2.061	85.8	76.4	88.1	69.0	88.1	82.2	69.0
4874.01	22.1	-0.790	3.090	34.0	28.5	...	...	...	32.9	17.7
4911.20	22.1	-0.330	3.120	47.0	38.7	...	...	...	43.4	33.7
5005.17	22.1	-2.540	1.570	14.8	...	...	...	...	...	...
5154.07	22.1	-1.920	1.570	64.8	55.3	60.7	...	67.6	67.5	44.8
5185.91	22.1	-1.350	1.890	57.9	...	64.9	...	69.3	63.2	53.7
5211.53	22.1	-1.160	2.590	32.8	...	...	...	...	...	19.4
5336.79	22.1	-1.630	1.580	76.8	64.3	72.4	...	68.8	72.1	63.9
5381.01	22.1	-1.970	1.570	41.7	46.4	61.6	...	50.6	60.9	43.9
5490.69	22.1	-2.430	1.566	...	...	14.1	...	...	...	...
4115.18	23.0	0.070	0.290	...	48.2	...	...	...	...	...
4389.98	23.0	0.200	0.280	...	...	...	...	...	...	29.1
4406.63	23.0	-0.190	0.300	34.7	57.4	...	...	...	...	...
4875.49	23.0	-0.810	0.040	...	16.3	...	...	...	...	...
6090.22	23.0	-0.060	1.080	...	17.5	...	...	...	...	...
3538.23	23.1	-1.640	1.070	52.0	...	...	...	...	...	...
3545.19	23.1	-0.390	1.100	73.2	70.6	81.7	...	...	60.5	56.3
3592.03	23.1	-0.370	1.100	72.1	66.1	75.9	...	55.6	66.9	65.5
3951.97	23.1	-0.744	1.480	48.3	46.3	58.8	45.1	...	52.0	48.3
3941.48	24.0	-1.390	1.030	...	...	...	...	...	...	22.4
3963.69	24.0	0.620	2.544	...	...	...	...	...	...	43.9
4272.90	24.0	-0.980	2.900	...	15.4	...	...	...	...	...
4496.84	24.0	-1.140	0.941	75.6	...	84.9	...	82.3	...	62.5
4511.90	24.0	-0.343	3.090	13.0	...	...	...	...	...	...
4545.95	24.0	-1.370	0.941	56.3	59.4	45.8	37.4	...	54.4	38.0
4580.04	24.0	-1.660	0.941	...	45.7	...	...	...	41.9	37.0
4591.39	24.0	-1.740	0.968	42.8	52.8	37.6	...	...	39.3	26.7
4600.74	24.0	-1.250	1.004	...	...	...	...	...	54.1	...
4613.36	24.0	-1.650	0.961	...	...	...	...	...	70.9	...

Table C.4: Equivalent Width Measurements, Table 4 of 5, continued

λ (Å)	Ion	loggf	EP	2311-476	2311-208	2621-215	2038-050	2038-226	2057-001	2053-419
4616.12	24.0	-1.190	0.983	60.1	66.1	60.3	...	...	50.2	49.0
4626.17	24.0	-1.330	0.968	48.8	55.1	47.6	...	54.4	38.9	38.7
4646.15	24.0	-0.740	1.030	...	77.1	68.6	64.9	...	69.6	64.8
4651.28	24.0	-1.460	0.983	46.2	53.5	43.5	...	36.2	41.7	33.7
4652.15	24.0	-1.040	1.004	67.0	70.8	63.5	...	63.5	67.3	54.5
4708.02	24.0	0.070	3.168	23.5	23.6	...	...	...	14.7	16.5
4718.43	24.0	0.240	3.195	29.8	32.2	25.6	...	...	35.4	20.1
4737.35	24.0	-0.100	3.090	...	...	...	...	...	17.0	...
4789.34	24.0	-0.330	2.544	31.1	36.5	...	...	...	...	...
4936.34	24.0	-0.250	3.113	13.8	21.6	...	...	...	14.6	...
5065.92	24.0	-1.380	2.708	...	10.1	...	...	...	...	...
5067.72	24.0	-1.070	2.709	...	12.9	...	...	...	...	...
5247.57	24.0	-1.590	0.961	37.0	44.2	39.4	...	...	37.0	21.7
5296.69	24.0	-1.360	0.983	52.9	60.8	53.4	...	...	46.3	35.9
5297.39	24.0	0.000	2.900	41.7	48.4	...	...	...	44.2	...
5300.74	24.0	-2.000	0.983	19.2	25.0	...	...	...	...	...
5345.80	24.0	-0.950	1.004	77.2	74.5	75.9	53.1	73.4	65.4	53.8
5348.31	24.0	-1.210	1.004	54.5	65.8	47.3	43.8	48.1	54.6	38.6
5409.77	24.0	-0.670	1.030	87.9	90.0	90.2	74.6	98.7	83.8	64.4
5787.93	24.0	-0.083	3.320	...	19.5	...	...	...	...	...
4554.99	24.1	-1.373	4.070	32.5	26.5	43.5	...	50.7	40.8	25.8
4558.65	24.1	-0.656	4.070	73.7	59.2	...	77.4	82.3	82.5	69.6
4588.20	24.1	-0.826	4.070	60.8	46.7	70.7	66.7	77.5	64.7	51.9
4592.06	24.1	-1.419	4.070	36.5	24.8	43.8	...	...	42.7	...
4616.63	24.1	-1.210	4.073	30.2	21.4	42.7	...	...	38.1	30.5
4848.23	24.1	-0.999	3.870	49.2	36.3	58.8	...	63.2	57.5	44.0
5237.33	24.1	-1.155	4.070	36.4	26.3	48.8	...	53.1	46.3	33.1
5305.86	24.1	-2.060	3.830	13.5	10.6	24.9	...	...	...	...
5308.42	24.1	-1.790	4.070	15.0	7.8	19.1	...	...	...	...
5313.59	24.1	-1.640	4.070	19.7	...	...	...	27.0	24.9	19.0
5502.09	24.1	-1.970	4.168	...	...	16.7	...	...	...	...

Table C.4: Equivalent Width Measurements, Table 4 of 5, continued

λ (Å)	Ion	loggf	EP	2311-476	2311-208	2621-215	2038-050	2038-226	2057-001	2053-419
3577.87	25.0	-0.010	2.110	...	...	...	...	...	...	50.3
4055.55	25.0	-0.080	2.140	71.5	75.8	79.1	...	82.5	71.8	58.2
4709.72	25.0	-0.339	2.890	24.3	20.3	...	...	...	...	...
4739.11	25.0	-0.490	2.940	21.1	18.2	...	...	...	18.7	...
4761.53	25.0	-0.138	2.950	28.9	25.2	27.3	...	...	...	15.8
4783.43	25.0	0.042	2.300	83.9	...	83.4	79.4	81.2	81.2	69.4
4823.51	25.0	0.144	2.320	82.3	...	...	72.4	92.2	86.3	70.8
6013.50	25.0	-0.252	3.070	...	22.7	31.2	...	...	...	...
6021.80	25.0	0.030	3.080	38.2	38.1	32.5	...	44.0	40.2	31.8
3891.93	26.0	-0.734	3.415	...	...	...	...	...	...	53.5
3916.74	26.0	-0.604	3.237	63.3	64.4	...	...	...	63.2	57.6
3917.18	26.0	-2.155	0.990	97.6	...	98.5	85.1	...	91.9	80.8
3949.96	26.0	-1.251	2.176	80.0	85.7	84.4	...	...	77.8	76.8
4114.45	26.0	-1.303	2.832	65.3	69.3	57.8	49.3	65.7	56.8	50.8
4132.91	26.0	-1.006	2.845	...	...	...	...	...	...	66.8
4139.94	26.0	-3.629	0.990	40.0	50.2	33.4	...	...	34.5	28.6
4147.68	26.0	-2.104	1.485	...	...	...	...	...	...	73.2
4157.79	26.0	-0.403	3.417	87.9	...	76.6	69.7	94.1	84.1	72.3
4174.92	26.0	-2.969	0.915	...	...	...	...	...	...	63.8
4175.64	26.0	-0.827	2.845	82.3	85.4	90.0	80.2	...	84.9	73.4
4184.91	26.0	-0.869	2.832	75.1	80.6	77.9	...	83.8	73.7	63.7
4199.10	26.0	0.156	3.047	...	...	...	...	...	...	99.5
4216.19	26.0	-3.356	0.000	88.4	...	...	...	...	...	78.6
4217.56	26.0	-0.484	3.430	83.9	83.0	83.9	...	...	84.6	66.2
4222.22	26.0	-0.967	2.450	...	...	...	86.0	...	95.2	89.8
4233.61	26.0	-0.604	2.482	...	...	...	...	...	...	91.7
4238.81	26.0	-0.233	3.397	94.6	...	95.1	87.8	...	93.7	74.4
4282.41	26.0	-0.779	2.176	...	...	...	...	...	...	94.9
4375.94	26.0	-3.031	0.000	93.8	...	...	...	...	96.4	87.9
4388.41	26.0	-0.682	3.603	...	...	65.3	...	...	59.7	57.6
4389.25	26.0	-4.583	0.052	34.7	...	27.7	23.0	...	25.3	26.5

Table C.4: Equivalent Width Measurements, Table 4 of 5, continued

λ (Å)	Ion	loggf	EP	2311-476	2311-208	2621-215	2038-050	2038-226	2057-001	2053-419
4489.75	26.0	-3.966	0.121	69.2	74.1	57.5	...	...	56.4	50.6
4494.57	26.0	-1.136	2.198	...	...	...	98.6	...	...	89.2
4517.52	26.0	-1.860	3.071	31.4	36.2	30.0	...	...	27.6	...
4523.41	26.0	-1.960	3.654	12.2	12.7	...	...	...	...	...
4547.85	26.0	-1.010	3.546	59.2	59.4	54.7	...	52.3	61.7	49.2
4566.52	26.0	-2.380	3.300	...	18.4	...	...	...	...	...
4574.23	26.0	-2.450	3.211	10.4	...	...	...	...	...	...
4587.13	26.0	-1.740	3.573	23.1	27.4	25.6	...	...	...	...
4593.53	26.0	-2.030	3.943	...	6.6	...	...	...	...	...
4602.01	26.0	-3.154	1.608	42.2	43.7	34.6	...	...	36.6	23.1
4602.95	26.0	-2.220	1.485	86.0	87.1	85.6	70.1	84.6	92.1	71.9
4630.12	26.0	-2.587	2.279	42.9	42.5	42.8	...	...	36.3	28.2
4632.92	26.0	-2.913	1.608	61.8	67.1	65.6	...	57.6	63.7	38.7
4635.85	26.0	-2.360	2.840	24.5	...	...	...	...	22.8	15.9
4647.43	26.0	-1.351	2.949	68.1	...	...	...	...	61.9	60.4
4672.84	26.0	-4.240	1.610	9.3	...	...	...	...	...	...
4683.56	26.0	-2.320	2.832	18.0	27.4	...	...	...	...	...
4690.14	26.0	-1.640	3.687	24.0	27.8	...	15.2	...	18.9	12.9
4733.59	26.0	-2.990	1.485	59.4	62.6	55.2	40.2	...	54.5	44.7
4741.53	26.0	-1.760	2.830	44.8	42.3	39.4	...	...	38.8	32.0
4745.80	26.0	-1.270	3.654	46.0	43.5	42.7	34.0	39.6	42.3	28.4
4779.45	26.0	-2.020	3.415	15.5	15.5	...	...	...	...	...
4787.83	26.0	-2.600	2.998	...	11.2	...	...	...	...	...
4788.76	26.0	-1.763	3.237	33.5	35.2	32.6	...	...	39.6	21.7
4789.65	26.0	-0.910	3.547	...	61.1	...	...	...	54.5	...
4802.88	26.0	-1.510	3.642	34.3	...	25.4	...	...	...	...
4835.87	26.0	-1.470	4.103	18.9	...	...	...	...	...	...
4839.52	26.0	-1.820	3.270	28.9	31.9	25.5	...	...	29.6	22.0
4844.01	26.0	-2.050	3.547	17.5	16.6	...	...	...	...	...
4872.14	26.0	-0.567	2.882	...	...	...	...	...	...	88.9
4882.14	26.0	-1.640	3.420	36.0	36.4	36.3	...	...	34.2	23.7

Table C.4: Equivalent Width Measurements, Table 4 of 5, continued

λ (Å)	Ion	loggf	EP	2311-476	2311-208	2621-215	2038-050	2038-226	2057-001	2053-419
4892.87	26.0	-1.290	4.220	27.0	24.2	20.1	...	...	...	10.7
4903.32	26.0	-0.926	2.882	93.3	...	92.5	84.4	...	90.6	82.0
4917.24	26.0	-1.160	4.191	33.7	36.8	36.9	22.6	...	28.2	23.1
4924.77	26.0	-2.114	2.279	60.0	63.5	50.8	38.4	59.1	53.7	46.3
4938.82	26.0	-1.077	2.875	85.5	89.2	...	...	...	80.3	72.6
4939.69	26.0	-3.340	0.859	71.5	74.9	61.1	38.1	...	61.0	52.2
4962.58	26.0	-1.182	4.178	23.1	...	...	...	...	...	...
4966.09	26.0	-0.871	3.332	79.5	77.7	82.0	...	87.4	73.3	66.2
4994.14	26.0	-3.080	0.915	76.5	72.4	74.8	...	...	74.1	60.4
5001.87	26.0	-0.010	3.882	92.5	90.8	...	...	...	89.7	77.9
5006.12	26.0	-0.615	2.833	...	...	...	...	...	...	98.5
5014.94	26.0	-0.303	3.943	68.3	74.1	73.1	...	80.0	79.5	64.9
5044.21	26.0	-2.060	2.850	38.1	38.8	34.1	...	...	39.5	29.9
5049.83	26.0	-1.355	2.279	97.5	...	96.7	79.4	95.1	94.2	81.3
5051.64	26.0	-2.795	0.915	...	...	...	84.9	...	91.1	82.3
5054.64	26.0	-1.920	3.640	...	18.6	...	...	...	...	...
5067.16	26.0	-0.970	4.220	31.8	36.8	37.2	28.8	37.8	28.4	...
5068.77	26.0	-1.042	2.940	83.4	90.1	83.1	...	87.0	76.3	78.6
5074.75	26.0	-0.230	4.220	80.3	76.3	79.5	71.6	78.4	72.8	61.4
5079.74	26.0	-3.220	0.990	...	...	...	...	...	...	55.1
5083.35	26.0	-2.958	0.958	73.6	78.2	72.2	...	71.8	72.6	62.3
5090.78	26.0	-0.400	4.260	49.7	55.6	53.1	45.9	55.8	49.2	40.0
5109.66	26.0	-0.980	4.300	41.9	43.9	40.3	...	43.0	32.1	...
5123.73	26.0	-3.068	1.011	73.1	82.9	69.6	...	...	63.7	59.5
5125.12	26.0	-0.080	4.220	96.1	91.8	90.1	82.5	96.1	86.4	74.8
5127.37	26.0	-3.307	0.915	60.3	69.7	58.8	...	59.6	58.0	50.2
5131.48	26.0	-2.515	2.223	50.1	51.3	...	...	...	...	32.0
5133.69	26.0	0.200	4.180	...	95.5	...	99.7	...	90.6	82.3
5141.74	26.0	-2.238	2.424	50.1	53.3	44.0	...	41.3	40.7	31.4
5150.85	26.0	-3.037	0.990	74.1	83.1	76.8	...	...	71.3	58.2
5151.92	26.0	-3.322	1.011	64.1	69.1	60.1	...	53.0	50.8	46.5

Table C.4: Equivalent Width Measurements, Table 4 of 5, continued

λ (Å)	Ion	loggf	EP	2311-476	2311-208	2621-215	2038-050	2038-226	2057-001	2053-419
5162.28	26.0	0.020	4.180	90.8	90.5	90.8	...	...	87.4	70.6
5166.28	26.0	-4.195	0.000	...	...	65.3	...	66.1	69.8	54.5
5171.61	26.0	-1.793	1.485	...	...	...	...	...	...	93.3
5187.92	26.0	-1.371	4.143	21.6	23.0	22.0	...	...	...	...
5191.47	26.0	-0.551	3.038	...	...	...	93.4	...	...	90.8
5192.35	26.0	-0.421	2.998	...	...	...	...	...	...	96.7
5194.95	26.0	-2.090	1.557	87.4	91.5	81.2	...	...	84.6	76.4
5198.72	26.0	-2.135	2.223	62.2	71.7	65.1	...	61.5	66.4	53.6
5202.34	26.0	-1.838	2.176	...	...	...	...	...	...	87.2
5216.28	26.0	-2.150	1.608	...	94.1	84.5	...	86.1	84.2	73.8
5217.40	26.0	-1.162	3.211	68.4	73.7	66.8	54.8	73.9	69.2	55.1
5225.53	26.0	-4.789	0.110	...	42.6	...	...	...	24.7	...
5242.46	26.0	-0.967	3.634	55.2	51.9	57.4	...	...	53.5	40.6
5243.78	26.0	-1.120	4.256	28.1	29.1	...	...	...	28.9	...
5247.06	26.0	-4.946	0.087	...	40.6	...	...	...	...	...
5250.22	26.0	-4.938	0.121	31.6	34.5	...	...	...	20.1	...
5254.95	26.0	-4.764	0.110	...	...	...	...	...	53.0	43.3
5266.56	26.0	-0.385	2.998	...	...	...	...	...	...	99.3
5281.80	26.0	-0.834	3.038	98.0	90.5	84.8	76.9	88.5	84.5	78.2
5283.63	26.0	-0.525	3.241	...	...	97.8	...	...	...	89.4
5288.53	26.0	-1.510	3.680	26.9	30.1	24.0	...	...	...	17.7
5295.32	26.0	-1.670	4.415	10.9	...	15.5	...	...	...	...
5302.31	26.0	-0.720	3.283	89.3	97.0	82.4	...	87.5	90.6	78.4
5307.37	26.0	-2.987	1.608	54.4	58.0	46.1	...	...	...	38.9
5321.11	26.0	-1.090	4.435	12.2	...	15.6	...	...	...	...
5322.01	26.0	-2.803	2.279	21.6	25.8	...	...	...	...	16.3
5332.92	26.0	-2.776	1.557	...	...	...	...	...	...	40.6
5339.94	26.0	-0.720	3.266	88.6	95.1	84.5	77.6	91.3	81.8	70.5
5364.87	26.0	0.228	4.446	83.1	80.3	79.2	...	...	82.9	67.5
5365.40	26.0	-1.020	3.573	48.0	44.2	43.2	...	...	42.9	36.8
5367.47	26.0	0.443	4.415	83.3	88.9	90.0	...	97.0	78.8	72.3

Table C.4: Equivalent Width Measurements, Table 4 of 5, continued

λ (Å)	Ion	loggf	EP	2311-476	2311-208	2621-215	2038-050	2038-226	2057-001	2053-419
5369.97	26.0	0.536	4.371	...	...	...	...	...	...	80.8
5373.70	26.0	-0.760	4.470	27.5	32.8	25.4	...	...	31.9	18.9
5379.58	26.0	-1.514	3.695	27.7	28.4	31.9	...	...	28.5	...
5383.38	26.0	0.645	4.312	...	...	...	...	...	...	86.8
5389.49	26.0	-0.400	4.410	45.2	47.7	44.8	34.5	44.4	51.3	37.5
5393.18	26.0	-0.715	3.241	86.3	89.5	84.1	73.9	90.6	91.8	68.3
5398.29	26.0	-0.710	4.446	41.8	38.9	38.9	...	...	41.2	...
5409.14	26.0	-1.200	4.370	25.2	20.3	...	...	...	...	...
5410.91	26.0	0.398	4.473	85.5	81.9	93.5	...	...	75.4	61.7
5415.20	26.0	0.642	4.386	99.1	98.9	...	91.2	...	...	...
5417.04	26.0	-1.660	4.415	...	10.0	...	...	...	...	...
5483.10	26.0	-1.410	4.150	...	...	18.2	...	...	...	...
5487.14	26.0	-1.430	4.410	10.3	...	...	...	...	...	...
5487.77	26.0	-0.620	4.140	52.3	48.3	55.7	...	...	58.9	39.0
5497.52	26.0	-2.830	1.010	82.7	90.6	79.2	70.7	83.9	91.0	80.5
5501.48	26.0	-3.047	0.958	73.9	83.2	66.0	...	72.1	76.9	61.2
5506.79	26.0	-2.797	0.990	85.5	90.4	81.9	...	79.9	91.6	72.7
5522.45	26.0	-1.520	4.209	...	17.9	...	...	...	...	...
5525.55	26.0	-1.080	4.230	22.2	24.5	22.6	...	...	...	...
5546.51	26.0	-1.210	4.372	22.3	...	23.1	...	...	...	...
5553.58	26.0	-1.310	4.430	...	...	15.8	...	...	...	...
5554.88	26.0	-0.350	4.550	47.1	47.5	51.1	50.2	...	...	...
5560.22	26.0	-1.160	4.435	21.7	20.6	28.1	...	...	...	...
5567.39	26.0	-2.670	2.610	24.2	27.8	28.4	...	...	...	...
5569.63	26.0	-0.486	3.417	88.9	93.1	96.3	80.2	89.9	87.7	80.5
5576.10	26.0	-0.940	3.430	70.2	77.7	72.2	64.6	78.3	69.8	56.3
5586.77	26.0	-0.144	3.368	...	...	...	...	...	...	97.2
5618.64	26.0	-1.276	4.209	15.2	23.5	...	...	...	...	...
5619.61	26.0	-1.670	4.386	12.0	...	...	...	...	...	...
5624.04	26.0	-1.220	4.390	16.8	15.2	16.7	...	...	...	...
5624.54	26.0	-0.755	3.420	81.2	87.7	82.9	...	...	85.9	58.2

Table C.4: Equivalent Width Measurements, Table 4 of 5, continued

λ (Å)	Ion	loggf	EP	2311-476	2311-208	2621-215	2038-050	2038-226	2057-001	2053-419
5641.44	26.0	-1.080	4.260	...	...	...	...	...	...	15.4
5662.52	26.0	-0.573	4.178	52.3	54.3	...	...	...	60.8	37.8
5679.02	26.0	-0.820	4.650	27.6	26.4	23.7	...	...	...	...
5686.53	26.0	-0.446	4.548	...	39.9	41.6	...	...	48.1	...
5701.56	26.0	-2.216	2.559	44.5	55.6	39.8	...	...	49.0	31.6
5705.47	26.0	-1.360	4.300	...	13.0	...	...	...	...	...
5705.98	26.0	-0.490	4.610	42.0	42.0	53.2	...	...	...	28.9
5717.84	26.0	-1.100	4.284	24.7	37.9	28.3	...	...	...	15.7
5731.77	26.0	-1.270	4.256	...	25.1	24.4	...	27.5	...	...
5752.04	26.0	-0.940	4.550	21.1	20.8	...	...	...	...	...
5753.12	26.0	-0.688	4.260	47.4	52.0	...	...	...	42.5	36.2
5762.99	26.0	-0.410	4.210	61.5	69.4	75.4	60.6	82.8	71.6	52.6
5775.09	26.0	-1.298	4.220	26.9	27.0	...	...	...	...	...
5793.92	26.0	-1.660	4.220	...	16.2	...	...	...	...	...
5806.73	26.0	-1.030	4.608	17.1	...	...	...	...	...	...
5809.22	26.0	-1.740	3.880	...	20.6	...	...	...	...	...
5816.38	26.0	-0.601	4.548	35.9	39.0	37.3	...	40.7	...	...
5852.23	26.0	-1.300	4.548	...	17.1	...	...	...	...	...
5859.60	26.0	-0.550	4.550	34.9	42.3	43.4	28.3	...	35.9	26.8
5862.35	26.0	-0.330	4.550	52.1	52.7	35.6	...	58.2	47.5	34.8
5883.81	26.0	-1.260	3.960	35.4	29.4	31.9	...	...	...	...
5905.68	26.0	-0.770	4.652	26.4	24.0	24.4	...	...	...	...
5927.80	26.0	-1.070	4.652	19.3	17.1	19.7	...	...	...	...
5929.68	26.0	-1.380	4.548	...	15.0	...	...	...	...	...
5930.19	26.0	-0.140	4.650	55.3	55.7	50.7	...	...	53.0	44.2
5934.67	26.0	-1.120	3.929	43.6	46.1	36.6	...	...	...	...
5956.71	26.0	-4.608	0.859	15.1	...	...	...	...	...	...
5976.79	26.0	-1.330	3.940	40.8	31.2	...	26.1	...	...	...
5983.69	26.0	-0.660	4.550	40.6	40.7	...	...	...	...	23.0
5984.83	26.0	-0.260	4.730	...	52.1	46.2	43.5	...	45.6	...
6003.02	26.0	-1.110	3.880	44.7	41.6	41.2	...	54.7	41.9	36.3

Table C.4: Equivalent Width Measurements, Table 4 of 5, continued

λ (Å)	Ion	loggf	EP	2311-476	2311-208	2621-215	2038-050	2038-226	2057-001	2053-419
6024.05	26.0	0.030	4.550	75.3	71.3	67.0	67.2	76.1	62.8	53.9
6027.06	26.0	-1.089	4.076	35.2	36.3	31.4	21.8	35.2	...	25.5
6055.99	26.0	-0.370	4.730	37.1	37.3	39.4	...	...	...	30.5
6065.49	26.0	-1.530	2.608	75.5	83.9	74.6	...	89.2	85.8	71.8
6078.50	26.0	-0.330	4.790	36.3	40.3	41.8	...	...	...	30.2
6079.02	26.0	-1.100	4.652	22.9	...	...	...	...	...	...
6127.90	26.0	-1.400	4.140	...	19.5	19.2	...	...	...	...
6136.62	26.0	-1.400	2.453	...	96.6	...	...	...	...	82.5
6137.00	26.0	-2.950	2.198	...	31.5	...	...	...	...	16.8
6137.70	26.0	-1.403	2.588	85.6	92.9	88.8	74.5	84.4	91.3	73.6
6151.62	26.0	-3.299	2.176	17.9	18.1	...	...	...	...	...
6157.73	26.0	-1.220	4.076	32.8	36.3	25.9	...	...	...	...
6165.36	26.0	-1.474	4.143	20.5	19.4	...	...	...	...	...
6173.34	26.0	-2.880	2.223	34.6	38.4	29.6	...	...	...	11.8
6180.20	26.0	-2.650	2.730	23.4	24.1	...	...	...	...	...
6200.32	26.0	-2.437	2.608	...	46.5	...	...	...	...	30.6
6213.44	26.0	-2.482	2.223	50.2	54.9	43.8	...	...	37.3	34.3
6219.29	26.0	-2.433	2.198	59.0	59.3	51.3	...	...	62.0	45.5
6230.74	26.0	-1.281	2.559	94.9	...	93.4	87.7	98.7	91.9	86.8
6240.65	26.0	-3.173	2.223	...	24.3	...	...	...	...	11.1
6246.33	26.0	-0.877	3.603	68.5	77.9	63.5	...	...	66.5	56.8
6252.56	26.0	-1.687	2.404	78.9	86.0	81.2	...	...	77.3	69.7
6254.26	26.0	-2.430	2.280	...	...	70.5	...	69.5	66.4	54.8
6265.14	26.0	-2.550	2.176	54.2	59.7	42.1	...	...	48.8	32.8
6270.23	26.0	-2.609	2.858	...	19.9	...	...	...	17.7	...
6290.97	26.0	-0.730	4.730	...	...	...	37.5	...	...	...
6301.51	26.0	-0.718	3.654	...	73.6	...	...	65.7	...	58.6
6302.50	26.0	-1.110	3.690	...	45.3	...	...	...	...	...
6322.69	26.0	-2.426	2.588	...	39.1	39.0	...	...	...	...
6330.85	26.0	-1.720	4.733	...	...	14.2	...	...	...	...
6335.33	26.0	-2.177	2.198	62.8	69.9	67.3	...	66.2	63.8	47.9

Table C.4: Equivalent Width Measurements, Table 4 of 5, continued

λ (Å)	Ion	loggf	EP	2311-476	2311-208	2621-215	2038-050	2038-226	2057-001	2053-419
6344.15	26.0	-2.923	2.433	23.7	25.3	...	...	...	...	...
6355.04	26.0	-2.291	2.845	...	30.1	37.3	...	...	...	...
6358.69	26.0	-4.468	0.859	23.7	39.6	32.1	...	...	...	...
4178.86	26.1	-2.443	2.583	73.1	67.6	84.3	74.3	...	76.8	71.0
4233.17	26.1	-1.809	2.583	...	...	...	...	...	...	99.7
4416.82	26.1	-2.600	2.778	64.6	55.5	72.5	...	80.9	...	...
4491.40	26.1	-2.640	2.856	63.0	54.1	74.9	62.6	71.8	68.9	60.8
4508.30	26.1	-2.350	2.856	73.5	65.4	83.4	78.8	92.0	84.7	77.3
4520.23	26.1	-2.620	2.807	...	64.4	82.8	76.8	80.6	70.3	57.0
4541.52	26.1	-2.970	2.856	57.5	...	64.8	55.1	66.7	63.5	52.0
4576.34	26.1	-2.920	2.844	57.6	46.4	62.9	52.0	67.2	62.2	47.7
4582.83	26.1	-3.062	2.844	50.7	35.1	56.7	...	52.9	50.6	38.9
4583.84	26.1	-1.740	2.807	...	91.9	...	...	...	...	...
4620.52	26.1	-3.188	2.828	40.0	28.7	49.1	...	...	39.7	31.7
4629.34	26.1	-2.480	2.810	80.7	70.7	92.1	87.5	96.2	88.9	78.0
4635.31	26.1	-1.580	5.956	...	...	13.2	...	...	...	...
4993.35	26.1	-3.680	2.807	29.1	15.3	...	...	...	30.8	21.8
5197.58	26.1	-2.054	3.230	67.3	58.0	77.3	78.5	...	...	67.9
5234.63	26.1	-2.210	3.221	73.6	56.4	77.3	69.7	81.1	88.4	71.4
5264.81	26.1	-3.233	3.230	32.2	24.6	39.2	...	...	37.1	33.2
5284.11	26.1	-3.200	2.891	40.0	31.8	48.6	...	...	57.1	47.0
5325.56	26.1	-2.570	3.221	...	...	...	...	...	34.7	27.7
5414.08	26.1	-3.482	3.221	11.9	...	23.7	...	...	...	13.4
5534.85	26.1	-2.860	3.245	51.8	29.8	64.5	41.9	...	57.1	46.9
5991.38	26.1	-3.650	3.153	...	15.3	...	...	...	...	...
6149.25	26.1	-2.840	3.889	...	16.9	29.1	...	...	23.5	...
6247.56	26.1	-2.430	3.892	41.4	28.7	58.0	...	...	54.7	51.9
4121.33	27.0	-0.320	0.920	92.2	97.8	85.7	65.7	81.6	85.6	79.4
4686.22	28.0	-0.580	3.600	28.8	34.7	30.1	...	...	26.7	15.5
4831.18	28.0	-0.320	3.610	42.5	...	...	...	...	38.4	30.2
4857.40	28.0	-0.830	3.740	21.2	...	...	...	...	...	...

Table C.4: Equivalent Width Measurements, Table 4 of 5, continued

λ (Å)	Ion	loggf	EP	2311-476	2311-208	2621-215	2038-050	2038-226	2057-001	2053-419
4904.42	28.0	-0.190	3.540	57.8	59.2	55.1	...	51.1	53.6	41.5
4913.98	28.0	-0.630	3.740	27.8	...	27.1	...	...	...	...
4935.83	28.0	-0.380	3.940	36.6	35.2	22.9	18.8	...	34.2	22.2
4953.21	28.0	-0.580	3.740	26.3	...	...	...	...	22.7	14.4
4998.22	28.0	-0.690	3.606	...	20.1	...	...	...	...	...
5010.94	28.0	-0.900	3.630	18.8	18.0	13.8	...	...	...	...
5035.37	28.0	0.290	3.630	73.3	73.2	71.1	...	...	60.5	62.3
5048.85	28.0	-0.390	3.850	34.8	34.0	28.9	...	...	...	...
5082.35	28.0	-0.540	3.660	31.3	33.4	23.4	...	...	...	...
5084.11	28.0	-0.060	3.680	64.5	56.4	57.1	...	...	51.9	43.2
5102.97	28.0	-2.660	1.680	19.5	19.4	...	...	...	...	...
5115.40	28.0	-0.140	3.830	44.8	47.9	...	...	...	40.2	30.2
5578.72	28.0	-2.640	1.680	...	...	...	...	...	...	15.4
5587.86	28.0	-2.140	1.930	...	20.9	...	...	...	...	...
5589.36	28.0	-1.140	3.900	13.7	...	...	...	...	...	...
5593.74	28.0	-0.840	3.900	22.5	15.5	...	...	...	...	...
5682.20	28.0	-0.469	4.100	26.7	...	...	...	...	...	...
5754.67	28.0	-1.850	1.930	36.6	46.5	...	...	...	...	20.4
5805.22	28.0	-0.638	4.170	...	18.2	...	...	...	...	...
5892.87	28.0	-2.340	1.990	40.2	...	...	...	...	...	...
6086.28	28.0	-0.515	4.260	...	21.0	...	...	...	...	...
6108.12	28.0	-2.430	1.680	28.9	38.8	...	...	...	...	...
6175.37	28.0	-0.535	4.090	22.9	25.0	20.7	...	...	...	...
6176.81	28.0	-0.529	4.090	36.5	27.8	25.3	...	...	...	13.4
6314.66	28.0	-1.770	1.930	36.0	...	...	...	...	...	...
5105.54	29.0	-3.720	1.380	46.7	50.9	29.5	26.8	25.2	31.9	22.5
4722.16	30.0	-0.390	4.030	60.0	50.5	46.8	...	...	48.3	27.5
4810.54	30.0	-0.170	4.080	60.4	52.1	57.5	...	...	47.1	35.5
4607.34	38.0	0.280	0.000	...	21.0	...	...	...	...	...
3549.01	39.1	-0.280	0.130	47.4	46.4	47.5	31.2	...	52.0	37.1
3600.74	39.1	0.280	0.180	56.1	62.8	67.9	...	65.0	64.3	57.0

Table C.4: Equivalent Width Measurements, Table 4 of 5, continued

λ (Å)	Ion	loggf	EP	2311-476	2311-208	2621-215	2038-050	2038-226	2057-001	2053-419
3611.04	39.1	0.010	0.130	...	...	...	...	...	69.9	...
3747.55	39.1	-0.910	0.100	26.7	...	...	...	...	...	...
3774.33	39.1	0.210	0.130	65.0	61.5	80.8	...	...	69.9	63.9
3788.70	39.1	-0.070	0.100	52.0	...	...	...	...	58.5	54.5
3950.36	39.1	-0.490	0.100	47.7	48.6	61.1	...	...	53.7	45.5
4398.01	39.1	-1.000	0.130	...	...	...	...	...	...	26.1
4883.69	39.1	0.070	1.080	43.9	43.4	53.1	...	...	51.2	35.6
5087.43	39.1	-0.170	1.080	24.1	27.6	36.5	...	...	31.6	21.9
5123.22	39.1	-0.830	0.990	10.1	...	20.0	...	...	...	...
5200.41	39.1	-0.570	0.990	14.4	...	21.5	...	...	...	...
4687.81	40.0	0.550	0.730	...	10.8	...	...	...	...	...
4208.99	40.1	-0.510	0.710	30.4	32.0	31.9	...	...	26.9	19.2
4496.97	40.1	-0.890	0.710	...	...	...	...	82.3	...	...
4130.65	56.1	0.530	2.720	...	...	...	...	...	...	20.2
5853.69	56.1	-0.910	0.600	40.0	37.8	58.1	...	58.1	50.7	...
3988.51	57.1	0.210	0.170	...	23.5	...	...	...	...	...
3995.75	57.1	-0.060	0.170	...	14.4	...	...	...	...	...
4086.71	57.1	-0.070	0.000	25.5	22.4	27.0	...	...	22.9	20.3
4333.75	57.1	-0.060	0.170	...	...	27.8	...	...	13.2	...

Table C.5: Equivalent Width Measurements, Table 5 of 5

λ (Å)	Ion	loggf	EP	2566-412	2062-482	2398-036	2397-014	2679-442	2682-560
5682.65	11.0	-0.699	2.100	...	37.5	43.3	51.1	...	...
5688.19	11.0	-0.420	2.100	94.8	65.6	74.1	77.9	92.3	75.7
6160.75	11.0	-1.230	2.100	40.1	9.5	...	23.1	25.0	...

Table C.5: Equivalent Width Measurements, Table 5 of 5, continued

λ (Å)	Ion	loggf	EP	2566-412	2062-482	2398-036	2397-014	2679-442	2682-560
4571.10	12.0	-5.570	0.000	74.1	64.3	58.1	65.1	86.4	42.9
4730.04	12.0	-2.347	4.350	...	23.5	...	...	...	...
5711.09	12.0	-1.630	4.340	...	56.1	52.1	57.7	73.1	49.3
5665.55	14.0	-2.040	4.920	34.4	...	...	...	17.5	...
5684.49	14.0	-1.420	4.950	...	22.0	...	...	...	...
5690.43	14.0	-1.870	4.930	...	14.5	...	...	...	...
5701.10	14.0	-2.050	4.930	...	...	16.3	...	17.7	...
5708.40	14.0	-1.470	4.950	...	...	39.1	...	...	...
5772.15	14.0	-1.750	5.080	37.0	17.8	...	...	34.1	17.8
5793.07	14.0	-2.060	4.930	...	...	...	...	22.9	...
5948.54	14.0	-1.230	5.080	67.5	41.8	39.4	43.6	65.2	47.3
6142.49	14.0	-1.480	5.620	19.7	...	...	...	...	...
6145.02	14.0	-1.370	5.610	...	9.4	...	...	23.3	...
6155.13	14.0	-0.760	5.620	70.0	...	36.9	...	...	...
6243.82	14.0	-1.300	5.616	...	...	...	...	31.7	...
6244.48	14.0	-1.320	5.616	...	...	...	...	43.1	...
6721.84	14.0	-0.939	5.860	...	...	19.8	...	...	...
7003.57	14.0	-0.830	5.960	39.3	21.7	24.1	...	46.5	...
7005.89	14.0	-0.730	5.980	...	...	36.0	27.6	57.3	...
7034.90	14.0	-0.880	5.870	62.9	...	...	...	52.1	...
7405.77	14.0	-0.820	5.610	73.3	49.7	54.6	42.9	78.1	...
7415.95	14.0	-0.730	5.610	...	57.8	...	37.8	...	58.5
7423.50	14.0	-0.580	5.620	74.8	59.8	...	42.6	77.5	60.2
7680.27	14.0	-0.590	5.863	...	39.6	...	...	...	42.6
7800.00	14.0	-0.720	6.180	...	...	...	...	33.3	...
7918.38	14.0	-0.510	5.954	74.0	31.5	35.7	30.2	52.2	...
7932.35	14.0	-0.370	5.964	...	36.8	41.4	37.9	...	...
7944.00	14.0	-0.210	5.984	...	52.9	49.7	44.8	92.3	...
6347.09	14.1	0.260	8.120	52.6	36.5	41.1	40.8	...	...
6371.35	14.1	-0.050	8.120	...	28.0	23.6	23.2	24.2	30.5
4283.01	20.0	-0.224	1.890	...	93.3	...	98.2	...	...

Table C.5: Equivalent Width Measurements, Table 5 of 5, continued

λ (Å)	Ion	loggf	EP	2566-412	2062-482	2398-036	2397-014	2679-442	2682-560
4289.37	20.0	-0.300	1.880	...	87.4	...	87.1	...	69.4
4318.66	20.0	-0.210	1.900	...	95.9	95.4	97.2	...	...
4425.44	20.0	-0.360	1.880	...	86.4	95.3	97.2	...	...
4435.69	20.0	-0.520	1.890	...	93.3	92.1	89.6	...	...
4456.61	20.0	-1.660	1.900	66.8	25.3	30.2	40.3	55.0	...
4526.93	20.0	-0.420	2.710	...	47.8	47.8	40.4	...	...
4578.56	20.0	-0.558	2.520	58.9	46.1	49.2	50.1	66.7	42.5
4685.27	20.0	-0.940	2.930	...	19.5	...	...	46.9	...
5260.39	20.0	-1.780	2.520	...	...	6.5	...	...	6.2
5261.71	20.0	-0.730	2.520	77.0	52.4	57.1	46.7	89.2	50.3
5349.47	20.0	-0.310	2.710	...	49.5	...	52.7	...	...
5512.99	20.0	-0.266	2.930	57.3	41.1	42.8	...	...	...
5588.76	20.0	0.358	2.510	...	99.3	97.5	90.2	...	96.2
5590.13	20.0	-0.710	2.510	72.4	54.5	48.8	48.1	84.1	...
5601.28	20.0	-0.438	2.520	...	63.9	62.9	50.1	89.3	60.0
5857.46	20.0	0.240	2.930	...	72.1	75.1	76.5	...	...
6102.73	20.0	-0.790	1.880	...	77.9	85.3	81.4	...	...
6161.30	20.0	-1.270	2.520	49.5	17.8	...	...	43.1	...
6166.44	20.0	-1.140	2.520	54.0	30.8	28.7	25.7	49.2	...
6169.04	20.0	-0.800	2.520	...	50.9	42.5	51.0	66.0	...
6169.56	20.0	-0.480	2.520	...	67.2	61.4	66.9	82.3	...
6449.82	20.0	-0.550	2.520	99.0	57.6	57.5	56.9	73.1	...
6455.61	20.0	-1.300	2.520	46.3	22.1	21.9	...	28.5	...
6471.67	20.0	-0.690	2.520	81.6	51.6	50.7	51.0	71.8	...
6493.79	20.0	-0.110	2.520	...	84.4	83.7	81.8	...	85.1
6499.65	20.0	-0.820	2.520	71.1	46.6	48.6	48.2	73.9	48.8
6717.69	20.0	-0.524	2.710	91.5	59.4	55.8	60.9	84.5	61.4
7148.15	20.0	0.218	2.710	...	90.3	92.2	86.4	...	95.8
4400.39	21.1	-0.540	0.610	...	84.1	86.6	66.9	85.0	71.2
5239.82	21.1	-0.765	1.450	50.5	40.2	43.3	31.1	42.6	...
5526.82	21.1	0.020	1.770	81.5	67.8	65.7	58.8	66.9	58.7

Table C.5: Equivalent Width Measurements, Table 5 of 5, continued

λ (Å)	Ion	loggf	EP	2566-412	2062-482	2398-036	2397-014	2679-442	2682-560
5640.99	21.1	-1.130	1.500	...	35.3	...	...	32.7	...
5657.88	21.1	-0.600	1.510	47.8	62.1	60.2	37.8	66.7	...
5669.04	21.1	-1.120	1.500	...	23.0	32.3	...	...	...
3924.53	22.0	-0.940	0.020	...	29.6	...	35.3	...	...
3958.22	22.0	-0.176	0.050	...	66.6	69.3	66.1	76.7	73.8
3998.64	22.0	-0.060	0.050	...	72.5	...	78.6	...	58.5
4512.74	22.0	-0.480	0.840	65.7	32.8	29.4	24.1	48.0	...
4518.03	22.0	-0.325	0.830	51.1	34.8	31.8	21.3	65.5	...
4533.25	22.0	0.476	0.850	93.3	...	...	64.4	79.9	...
4534.78	22.0	0.280	0.840	87.7	65.1	59.4	57.0	...	57.7
4548.77	22.0	-0.354	0.830	57.9	39.8	43.1	25.8	...	...
4555.49	22.0	-0.490	0.850	...	28.5	36.0	17.5	41.1	...
4617.28	22.0	0.390	1.750	45.0	30.7	31.8	28.0	52.2	20.3
4623.10	22.0	0.170	1.740	...	19.0	16.1	...	...	...
4681.92	22.0	-1.070	0.050	...	...	...	34.0	...	...
4758.12	22.0	0.425	2.250	...	9.9	13.3	...	...	...
4759.28	22.0	0.514	2.250	...	16.0	...	...	34.2	...
4840.88	22.0	-0.450	0.900	53.7	28.9	28.0	...	39.9	...
5064.66	22.0	-0.990	0.050	...	50.1	...	38.7	...	...
5113.45	22.0	-0.780	1.440	...	...	...	...	21.3	...
5145.47	22.0	-0.574	1.460	...	...	...	...	19.6	...
5147.48	22.0	-2.012	0.000	...	...	...	...	26.3	...
5173.75	22.0	-1.118	0.000	...	...	...	...	...	39.2
5192.98	22.0	-1.006	0.020	76.2	40.6	39.4	41.7	68.6	...
5210.39	22.0	-0.884	0.050	69.6	50.9	48.3	46.7	69.5	31.5
5490.15	22.0	-0.933	1.460	...	...	...	...	11.4	...
6258.10	22.0	-0.355	1.440	...	...	...	...	39.9	...
6258.71	22.0	-0.240	1.460	...	...	...	...	47.1	...
6261.11	22.0	-0.480	1.430	27.5	...	14.2	...	...	...
6554.24	22.0	-1.220	1.440	13.5	...	...	...	...	...
3987.61	22.1	-2.730	0.610	...	37.5	61.6	...	...	32.0

Table C.5: Equivalent Width Measurements, Table 5 of 5, continued

λ (Å)	Ion	loggf	EP	2566-412	2062-482	2398-036	2397-014	2679-442	2682-560
4028.35	22.1	-1.000	1.890	...	70.8	78.7	72.3	62.9	64.8
4394.06	22.1	-1.770	1.220	...	58.2	62.8	59.1	66.7	67.8
4395.84	22.1	-1.970	1.240	...	62.0	60.0	51.4	55.4	...
4399.77	22.1	-1.270	1.240	...	...	...	87.3	...	...
4417.72	22.1	-1.430	1.160	...	96.0	89.0	79.6	90.7	82.4
4418.33	22.1	-1.990	1.240	...	52.3	67.8	49.2	...	...
4444.56	22.1	-2.210	1.120	...	52.8	56.7	33.7	66.4	42.3
4450.49	22.1	-1.450	1.080	...	...	...	91.9	...	...
4544.02	22.1	-2.410	1.240	...	...	33.4	...	...	...
4568.33	22.1	-2.650	1.220	...	...	21.1	...	...	...
4583.42	22.1	-2.720	1.160	23.7	15.3	...	13.0	24.7	...
4589.95	22.1	-1.790	1.240	...	73.0	75.2	67.4	...	...
4636.32	22.1	-3.020	1.165	...	14.1	...	...	...	...
4657.20	22.1	-2.150	1.240	...	39.8	...	...	...	...
4708.67	22.1	-2.210	1.240	46.5	35.6	46.3	...	53.7	...
4779.98	22.1	-1.370	2.048	...	61.0	54.9	49.5	61.9	53.4
4798.54	22.1	-2.430	1.080	...	...	38.0	30.8	33.2	...
4805.09	22.1	-1.120	2.061	...	74.7	78.2	73.6	...	68.1
4865.62	22.1	-2.590	1.120	...	...	...	...	43.8	...
4874.01	22.1	-0.790	3.090	...	21.4	31.9	...	...	...
4911.20	22.1	-0.330	3.120	...	40.8	...	...	56.3	...
5154.07	22.1	-1.920	1.570	71.2	64.7	58.5	51.2	66.4	...
5185.91	22.1	-1.350	1.890	...	56.9	62.6	52.7	66.9	...
5211.53	22.1	-1.160	2.590	33.9	34.9	26.8	...	30.7	...
5336.79	22.1	-1.630	1.580	63.7	59.7	72.9	55.4	63.8	62.2
5381.01	22.1	-1.970	1.570	...	40.6	45.8	41.8	66.6	...
5418.78	22.1	-2.110	1.580	42.8	37.1	36.1	38.7	59.5	...
4115.18	23.0	0.070	0.290	...	...	...	...	45.3	...
4116.47	23.0	-0.310	0.280	...	...	...	...	31.9	...
4389.98	23.0	0.200	0.280	...	...	32.7	...	...	...
4875.49	23.0	-0.810	0.040	...	...	...	...	18.6	...

Table C.5: Equivalent Width Measurements, Table 5 of 5, continued

λ (Å)	Ion	loggf	EP	2566-412	2062-482	2398-036	2397-014	2679-442	2682-560
3951.97	23.1	-0.744	1.480	50.7	49.9	50.7	39.2	...	...
4261.35	24.0	-0.690	2.913	...	...	...	...	36.6	...
4337.55	24.0	-1.090	0.968	63.7	...	...	...	68.7	...
4351.05	24.0	-1.430	0.968	...	33.7	...	35.4	57.4	...
4496.84	24.0	-1.140	0.941	...	...	...	...	...	65.7
4511.90	24.0	-0.343	3.090	32.3	...	...	...	...	...
4535.12	24.0	-1.020	2.544	...	...	10.3	...	15.6	...
4545.95	24.0	-1.370	0.941	...	41.9	35.1	52.9	...	...
4580.04	24.0	-1.660	0.941	54.7	41.2	41.3	36.4	62.2	34.7
4591.39	24.0	-1.740	0.968	...	24.8	...	...	...	...
4600.74	24.0	-1.250	1.004	...	55.4	...	...	...	...
4616.12	24.0	-1.190	0.983	83.6	48.6	...	42.9	60.8	...
4626.17	24.0	-1.330	0.968	70.6	49.0	43.3	36.3	56.7	43.6
4646.15	24.0	-0.740	1.030	...	66.6	59.8	76.1	93.6	...
4651.28	24.0	-1.460	0.983	61.8	35.0	31.9	26.3	...	...
4652.15	24.0	-1.040	1.004	79.3	56.4	61.2	...	79.0	52.8
4708.02	24.0	0.070	3.168	...	17.8	...	...	33.2	...
4718.43	24.0	0.240	3.195	...	...	23.9	...	...	...
4724.41	24.0	-0.733	3.090	30.8	...	...	...	...	...
4730.72	24.0	-0.192	3.080	...	...	...	...	32.1	...
4737.35	24.0	-0.100	3.090	...	...	21.9	...	...	...
4789.34	24.0	-0.330	2.544	...	21.7	...	...	30.2	...
4801.03	24.0	-0.130	3.120	...	...	16.7	...	22.9	...
4829.37	24.0	-0.510	2.545	...	19.8	20.6	...	24.3	...
4936.34	24.0	-0.250	3.113	21.5	...	...	...	...	...
5110.75	24.0	-1.320	2.709	...	...	...	...	11.0	...
5247.57	24.0	-1.590	0.961	53.9	30.4	33.7	28.3	55.5	...
5296.69	24.0	-1.360	0.983	...	43.1	...	38.3	68.6	41.6
5297.39	24.0	0.000	2.900	...	38.4	35.7	...	...	...
5300.74	24.0	-2.000	0.983	...	14.7	...	...	37.3	...
5345.80	24.0	-0.950	1.004	84.1	67.2	69.9	63.7	96.0	68.2

Table C.5: Equivalent Width Measurements, Table 5 of 5, continued

λ (Å)	Ion	loggf	EP	2566-412	2062-482	2398-036	2397-014	2679-442	2682-560
5348.31	24.0	-1.210	1.004	69.6	53.7	46.9	50.8	79.2	47.9
5409.77	24.0	-0.670	1.030	...	79.6	78.9	78.9	...	82.1
5783.09	24.0	-0.500	3.320	27.3	...	...	...	...	...
5785.02	24.0	-0.379	3.320	26.5	...	...	...	...	...
5787.93	24.0	-0.083	3.320	29.6	...	...	...	18.0	...
6978.49	24.0	0.143	3.460	...	...	...	...	29.4	...
4554.99	24.1	-1.373	4.070	...	29.1	30.0	...	...	27.9
4558.65	24.1	-0.656	4.070	85.2	67.7	69.1	63.6	73.6	66.1
4588.20	24.1	-0.826	4.070	61.4	56.8	63.1	54.9	60.7	55.9
4592.06	24.1	-1.419	4.070	45.3	...	...	27.3	26.7	...
4616.63	24.1	-1.210	4.073	...	33.1	39.5	20.2	36.2	32.7
4848.23	24.1	-0.999	3.870	53.5	49.6	49.3	35.9	62.5	...
5237.33	24.1	-1.155	4.070	...	36.8	35.7	39.3	33.5	...
5313.59	24.1	-1.640	4.070	...	18.3	14.6	...	...	...
4055.55	25.0	-0.080	2.140	...	75.2	72.7	...	...	...
4709.72	25.0	-0.339	2.890	39.2	21.7	19.6	11.4	34.1	...
4761.53	25.0	-0.138	2.950	64.0	25.1	26.6	...	...	...
4783.43	25.0	0.042	2.300	...	71.5	79.9	73.6	...	74.6
4823.51	25.0	0.144	2.320	...	71.5	78.6	72.5	96.6	71.8
5432.55	25.0	-3.795	0.000	26.6	...	...	...	...	...
6013.50	25.0	-0.252	3.070	54.7	...	25.1	...	...	...
6021.80	25.0	0.030	3.080	56.1	24.6	37.5	30.8	57.2	41.3
3891.93	26.0	-0.734	3.415	...	...	...	48.2	92.0	...
3916.74	26.0	-0.604	3.237	...	63.8	66.0	...	83.8	...
3917.18	26.0	-2.155	0.990	...	88.5	99.0	82.1	...	89.5
3949.96	26.0	-1.251	2.176	...	78.1	93.9	78.0	...	...
4114.45	26.0	-1.303	2.832	...	58.2	55.0	67.6	61.5	...
4132.91	26.0	-1.006	2.845	...	...	72.2	69.1	...	...
4134.69	26.0	-0.649	2.832	...	...	...	85.3	...	...
4139.94	26.0	-3.629	0.990	...	29.9	37.6	38.3	59.5	27.7
4147.68	26.0	-2.104	1.485	...	84.1	84.6	72.6	...	...

Table C.5: Equivalent Width Measurements, Table 5 of 5, continued

λ (Å)	Ion	loggf	EP	2566-412	2062-482	2398-036	2397-014	2679-442	2682-560
4157.79	26.0	-0.403	3.417	...	80.1	70.4	75.2	...	...
4174.92	26.0	-2.969	0.915	...	74.2	...	62.3	...	...
4175.64	26.0	-0.827	2.845	...	87.1	73.6	65.8	78.4	80.7
4184.91	26.0	-0.869	2.832	88.3	72.2	74.2	70.7	76.7	69.2
4187.05	26.0	-0.548	2.450	...	...	99.6	...	...	...
4216.19	26.0	-3.356	0.000	...	85.7	77.9	77.3	...	90.6
4217.56	26.0	-0.484	3.430	...	66.4	72.6	66.7	...	...
4222.22	26.0	-0.967	2.450	...	88.1	93.2	81.5	93.1	84.7
4229.77	26.0	-3.427	1.485	...	...	...	38.2	...	...
4233.61	26.0	-0.604	2.482	...	99.5	...	...	...	...
4238.81	26.0	-0.233	3.397	...	81.5	95.4	89.0	93.0	...
4282.41	26.0	-0.779	2.176	...	98.0	...	...	...	85.9
4375.94	26.0	-3.031	0.000	...	...	95.0	99.2	...	87.5
4388.41	26.0	-0.682	3.603	...	68.2	57.4	56.0	93.3	58.4
4389.25	26.0	-4.583	0.052	41.5	32.8	22.1	...	62.0	19.1
4430.62	26.0	-1.659	2.223	...	75.6	84.3	...	...	...
4439.89	26.0	-3.002	2.279	...	...	...	...	21.4	...
4442.35	26.0	-1.255	2.198	...	91.4	97.0	98.9	...	98.5
4442.84	26.0	-2.792	2.176	...	...	15.9	...	...	...
4447.73	26.0	-1.342	2.223	...	85.1	88.0	87.8	...	82.8
4461.66	26.0	-3.210	0.087	...	85.8	...	82.4	...	...
4489.75	26.0	-3.966	0.121	82.7	55.8	60.6	65.1	85.2	...
4494.57	26.0	-1.136	2.198	...	97.2	96.7	96.6	...	99.8
4517.52	26.0	-1.860	3.071	58.4	28.9	26.8	31.8	...	...
4547.85	26.0	-1.010	3.546	...	50.0	57.8	54.6	69.9	64.7
4566.52	26.0	-2.380	3.300	...	...	...	...	25.8	...
4602.01	26.0	-3.154	1.608	...	...	31.0	30.1	63.7	27.8
4602.95	26.0	-2.220	1.485	...	76.2	79.9	78.4	85.1	74.2
4630.12	26.0	-2.587	2.279	...	35.3	34.7	38.6	50.1	...
4632.92	26.0	-2.913	1.608	...	59.8	...	40.5	...	55.8
4635.85	26.0	-2.360	2.840	...	...	17.6	...	25.2	...

Table C.5: Equivalent Width Measurements, Table 5 of 5, continued

λ (Å)	Ion	loggf	EP	2566-412	2062-482	2398-036	2397-014	2679-442	2682-560
4647.43	26.0	-1.351	2.949	...	52.8	64.0	58.4	82.5	...
4683.56	26.0	-2.320	2.832	...	...	16.3	...	26.9	17.2
4690.14	26.0	-1.640	3.687	31.2	21.3	23.5	...	...	17.4
4733.59	26.0	-2.990	1.485	73.0	48.6	50.1	42.0	62.9	50.5
4741.53	26.0	-1.760	2.830	55.8	35.9	35.6	33.1	45.7	33.3
4745.80	26.0	-1.270	3.654	44.0	30.6	...	28.3	...	...
4788.76	26.0	-1.763	3.237	...	32.5	39.4	25.5	43.0	...
4789.65	26.0	-0.910	3.547	60.6	54.9	49.0	49.2	62.4	...
4798.27	26.0	-1.174	4.186	39.4	...	...	...	...	...
4802.88	26.0	-1.510	3.642	45.7	...	21.4	20.0	35.0	...
4835.87	26.0	-1.470	4.103	...	22.0	...	...	...	...
4839.52	26.0	-1.820	3.270	39.4	21.5	...	...	46.1	...
4844.01	26.0	-2.050	3.547	...	...	14.3	...	30.3	...
4871.33	26.0	-0.362	2.865	...	...	...	...	...	99.5
4872.14	26.0	-0.567	2.882	...	...	91.2	...	...	...
4882.14	26.0	-1.640	3.420	51.8	32.5	34.7	30.5	50.0	30.9
4892.87	26.0	-1.290	4.220	...	12.4	...	...	35.2	...
4903.32	26.0	-0.926	2.882	...	81.2	87.0	83.1	...	84.6
4905.14	26.0	-2.020	3.929	...	...	...	...	18.3	...
4917.24	26.0	-1.160	4.191	...	...	32.7	...	...	...
4924.77	26.0	-2.114	2.279	66.2	42.3	57.2	49.8	75.3	50.4
4938.82	26.0	-1.077	2.875	...	71.8	74.9	69.5	88.3	61.1
4939.69	26.0	-3.340	0.859	76.1	56.2	56.4	57.5	78.0	55.1
4962.58	26.0	-1.182	4.178	36.0	...	...	...	...	...
4966.09	26.0	-0.871	3.332	...	68.5	69.7	66.2	89.6	74.0
5067.16	26.0	-0.970	4.220	...	29.3	37.4	...	55.7	...
5068.77	26.0	-1.042	2.940	...	74.1	72.4	74.3	...	73.5
5074.75	26.0	-0.230	4.220	...	70.8	71.2	66.5	92.2	73.4
5079.74	26.0	-3.220	0.990	...	57.2	...	61.1	...	...
5083.35	26.0	-2.958	0.958	...	67.7	71.0	61.6	87.1	71.3
5088.16	26.0	-1.680	4.150	...	...	...	...	20.7	...

Table C.5: Equivalent Width Measurements, Table 5 of 5, continued

λ (Å)	Ion	loggf	EP	2566-412	2062-482	2398-036	2397-014	2679-442	2682-560
5090.78	26.0	-0.400	4.260	72.1	40.6	45.4	36.5	63.6	50.1
5109.66	26.0	-0.980	4.300	63.4	30.9	31.7	35.7	52.3	...
5123.73	26.0	-3.068	1.011	...	64.0	67.8	64.6	83.6	...
5125.12	26.0	-0.080	4.220	...	78.8	84.0	84.1	...	77.6
5127.37	26.0	-3.307	0.915	77.8	56.7	65.7	59.7	85.7	58.6
5131.48	26.0	-2.515	2.223	61.1	37.2	...	38.1	62.2	...
5133.69	26.0	0.200	4.180	...	88.8	81.9	86.8	...	99.9
5141.74	26.0	-2.238	2.424	...	39.1	41.8	36.1	63.8	38.4
5150.85	26.0	-3.037	0.990	...	63.6	59.2	63.9	83.3	72.3
5151.92	26.0	-3.322	1.011	...	49.9	...	52.1	...	61.9
5162.28	26.0	0.020	4.180	...	80.8	70.2	75.9	...	94.1
5166.28	26.0	-4.195	0.000	82.7	61.3	65.4	57.0	91.7	...
5171.61	26.0	-1.793	1.485	...	99.2	...	...	...	...
5187.92	26.0	-1.371	4.143	34.0	...	...	...	...	...
5191.47	26.0	-0.551	3.038	...	90.1	92.4	91.9	...	...
5192.35	26.0	-0.421	2.998	...	...	...	99.4	...	...
5194.95	26.0	-2.090	1.557	...	84.4	84.6	79.3	96.8	78.2
5198.72	26.0	-2.135	2.223	75.5	58.3	54.4	54.7	73.3	54.3
5202.34	26.0	-1.838	2.176	...	93.9	...	91.4	...	...
5216.28	26.0	-2.150	1.608	86.3	84.0	83.6	76.0	...	74.4
5217.40	26.0	-1.162	3.211	98.0	54.2	56.2	63.1	85.4	54.5
5225.53	26.0	-4.789	0.110	38.2	23.4	18.1	...	43.3	...
5242.46	26.0	-0.967	3.634	...	49.4	43.3	43.3	71.0	...
5243.78	26.0	-1.120	4.256	...	16.8	20.4	...	37.8	...
5247.06	26.0	-4.946	0.087	62.9	...	...	...	44.7	...
5250.22	26.0	-4.938	0.121	51.5	25.0	18.5	...	49.1	...
5254.95	26.0	-4.764	0.110	...	...	...	44.8	...	...
5266.56	26.0	-0.385	2.998	...	99.9	...	...	...	...
5281.80	26.0	-0.834	3.038	...	95.4	78.7	78.6	...	91.3
5283.63	26.0	-0.525	3.241	...	88.7	93.6	86.1	...	...
5288.53	26.0	-1.510	3.680	53.3	...	...	...	48.1	...

Table C.5: Equivalent Width Measurements, Table 5 of 5, continued

λ (Å)	Ion	loggf	EP	2566-412	2062-482	2398-036	2397-014	2679-442	2682-560
5295.32	26.0	-1.670	4.415	...	...	...	...	16.4	...
5302.31	26.0	-0.720	3.283	...	70.0	73.2	68.2	96.6	79.6
5307.37	26.0	-2.987	1.608	...	47.5	...	43.9	68.6	44.6
5322.01	26.0	-2.803	2.279	43.1	...	...	...	...	...
5332.92	26.0	-2.776	1.557	68.7	43.5	57.8	43.3	70.4	55.7
5339.94	26.0	-0.720	3.266	...	81.3	74.9	70.0	...	81.0
5364.87	26.0	0.228	4.446	99.1	75.1	72.3	72.8	97.2	...
5365.40	26.0	-1.020	3.573	54.0	40.2	43.8	39.9	56.8	...
5367.47	26.0	0.443	4.415	...	80.4	72.3	73.8	...	77.3
5369.97	26.0	0.536	4.371	...	81.3	79.5	91.1	...	85.6
5373.70	26.0	-0.760	4.470	53.0	21.1	...	23.4	35.9	...
5376.84	26.0	-2.280	4.294	...	...	...	...	11.9	...
5379.58	26.0	-1.514	3.695	...	20.2	...	...	44.8	...
5383.38	26.0	0.645	4.312	...	88.8	96.3	97.7	...	96.0
5389.49	26.0	-0.400	4.410	73.4	38.3	40.1	45.5	59.6	...
5393.18	26.0	-0.715	3.241	...	79.9	76.6	74.3	...	84.0
5398.29	26.0	-0.710	4.446	67.3	30.8	29.8	29.2	55.8	33.8
5405.36	26.0	-1.390	4.390	28.8	...	...	...	...	7.1
5406.78	26.0	-1.720	4.370	21.2	...	...	...	...	...
5409.14	26.0	-1.200	4.370	37.5	...	...	...	...	...
5410.91	26.0	0.398	4.473	...	69.1	74.4	72.2	90.9	...
5415.20	26.0	0.642	4.386	...	85.8	84.0	90.3	...	93.3
5417.04	26.0	-1.660	4.415	15.8	...	...	...	15.9	...
5424.08	26.0	0.520	4.320	...	...	92.3	...	...	...
5445.04	26.0	0.040	4.390	...	66.5	64.2	66.0	...	74.8
5461.56	26.0	-1.800	4.446	...	...	...	...	12.1	...
5466.39	26.0	-0.620	4.370	...	30.7	31.5	38.2	52.6	...
5466.99	26.0	-2.230	3.573	...	...	...	...	15.8	...
5473.90	26.0	-0.690	4.150	...	38.1	38.4	33.5	53.0	...
5483.10	26.0	-1.410	4.150	30.8	...	...	...	29.2	...
5487.77	26.0	-0.620	4.140	...	40.6	47.2	52.2	...	47.5

Table C.5: Equivalent Width Measurements, Table 5 of 5, continued

λ (Å)	Ion	loggf	EP	2566-412	2062-482	2398-036	2397-014	2679-442	2682-560
5497.52	26.0	-2.830	1.010	...	77.3	77.6	78.3	94.6	81.4
5501.48	26.0	-3.047	0.958	...	68.3	74.9	67.5	85.7	...
5506.79	26.0	-2.797	0.990	...	81.8	77.9	79.3	97.9	82.3
5522.45	26.0	-1.520	4.209	37.0	...	...	...	...	...
5525.55	26.0	-1.080	4.230	44.7	...	...	...	...	...
5553.58	26.0	-1.310	4.430	...	...	...	20.0	...	...
5554.88	26.0	-0.350	4.550	69.9	39.2	39.1	44.7	76.7	47.6
5560.22	26.0	-1.160	4.435	...	14.1	...	...	36.8	14.0
5567.39	26.0	-2.670	2.610	...	19.4	16.6	...	52.2	...
5569.63	26.0	-0.486	3.417	...	79.7	79.5	73.5	94.9	86.2
5576.10	26.0	-0.940	3.430	98.6	66.7	65.2	71.5	83.0	...
5624.04	26.0	-1.220	4.390	46.6	...	14.5	...	...	...
5624.54	26.0	-0.755	3.420	...	80.4	71.0	69.6	83.7	73.1
5641.44	26.0	-1.080	4.260	...	...	...	...	35.3	...
5653.89	26.0	-1.540	4.390	...	...	...	...	21.6	...
5662.52	26.0	-0.573	4.178	73.9	52.6	54.1	...	66.8	...
5667.52	26.0	-1.500	4.480	...	...	...	...	23.6	...
5679.02	26.0	-0.820	4.650	45.6	23.5	27.1	...	35.1	...
5686.53	26.0	-0.446	4.548	51.2	27.2	36.8	40.3	55.3	...
5701.56	26.0	-2.216	2.559	67.7	41.4	50.8	45.6	44.1	...
5705.98	26.0	-0.490	4.610	...	31.4	...	...	58.1	...
5717.84	26.0	-1.100	4.284	...	17.6	...	...	...	23.8
5731.77	26.0	-1.270	4.256	44.6	...	...	...	...	...
5752.04	26.0	-0.940	4.550	...	...	21.3	...	32.9	...
5753.12	26.0	-0.688	4.260	64.6	36.9	...	...	73.9	...
5762.99	26.0	-0.410	4.210	80.7	58.4	59.2	52.2	70.4	56.3
5775.09	26.0	-1.298	4.220	42.1	25.4	...	...	...	...
5806.73	26.0	-1.030	4.608	...	...	15.0	...	...	...
5816.38	26.0	-0.601	4.548	45.1	26.4	22.6	24.4	44.6	...
5852.23	26.0	-1.300	4.548	...	...	...	...	21.4	...
5859.60	26.0	-0.550	4.550	70.1	32.2	27.1	31.5	44.4	...

Table C.5: Equivalent Width Measurements, Table 5 of 5, continued

λ (Å)	Ion	loggf	EP	2566-412	2062-482	2398-036	2397-014	2679-442	2682-560
5862.35	26.0	-0.330	4.550	...	43.7	45.2	45.4	72.0	42.9
5883.81	26.0	-1.260	3.960	...	...	...	...	41.3	...
5905.68	26.0	-0.770	4.652	...	22.8	14.7	...	...	...
5927.80	26.0	-1.070	4.652	...	...	...	...	23.3	...
5929.68	26.0	-1.380	4.548	...	...	...	...	14.8	...
5930.19	26.0	-0.140	4.650	56.7	43.5	45.8	41.9	57.2	42.7
5934.67	26.0	-1.120	3.929	46.3	33.2	32.5	23.1	47.6	37.0
5952.72	26.0	-1.340	3.980	31.8	...	...	...	34.6	...
5956.71	26.0	-4.608	0.859	24.9	...	...	...	29.8	...
5976.79	26.0	-1.330	3.940	...	24.2	...	...	48.8	...
5983.69	26.0	-0.660	4.550	61.4	27.6	26.8	...	...	...
5984.83	26.0	-0.260	4.730	79.9	...	...	41.1	56.5	...
6003.02	26.0	-1.110	3.880	72.2	42.0	42.0	...	55.9	...
6024.05	26.0	0.030	4.550	88.7	62.2	55.3	61.1	77.6	69.7
6027.06	26.0	-1.089	4.076	56.0	29.3	...	...	46.9	...
6055.99	26.0	-0.370	4.730	48.2	28.7	28.7	...	50.3	...
6065.49	26.0	-1.530	2.608	89.5	71.2	77.9	63.8	86.6	74.9
6078.50	26.0	-0.330	4.790	63.3	25.0	...	34.0	40.0	...
6079.02	26.0	-1.100	4.652	...	...	...	...	29.0	20.8
6127.90	26.0	-1.400	4.140	32.0	...	...	...	...	...
6136.62	26.0	-1.400	2.453	...	79.4	77.1	...	96.2	...
6137.00	26.0	-2.950	2.198	52.5	29.1	...	...	46.3	...
6137.70	26.0	-1.403	2.588	...	83.0	73.8	71.1	88.0	84.2
6151.62	26.0	-3.299	2.176	29.1	...	...	...	24.7	...
6157.73	26.0	-1.220	4.076	47.1	23.8	21.6	...	43.2	...
6165.36	26.0	-1.474	4.143	27.2	...	...	...	21.1	11.2
6173.34	26.0	-2.880	2.223	51.8	29.5	26.2	...	48.1	...
6180.20	26.0	-2.650	2.730	43.7	...	...	...	39.6	...
6188.00	26.0	-1.670	3.943	...	...	...	...	31.2	...
6191.57	26.0	-1.416	2.433	...	78.1	79.1	84.4	95.2	...
6200.32	26.0	-2.437	2.608	66.7	29.9	...	37.5	54.4	...

Table C.5: Equivalent Width Measurements, Table 5 of 5, continued

λ (Å)	Ion	loggf	EP	2566-412	2062-482	2398-036	2397-014	2679-442	2682-560
6213.44	26.0	-2.482	2.223	65.7	41.7	43.2	30.2	64.1	...
6219.29	26.0	-2.433	2.198	71.3	50.2	39.6	39.8	65.3	...
6229.23	26.0	-2.805	2.845	...	...	...	...	19.0	...
6230.74	26.0	-1.281	2.559	...	94.7	95.4	87.2	...	93.0
6240.65	26.0	-3.173	2.223	37.9	...	...	...	...	...
6246.33	26.0	-0.877	3.603	...	63.8	66.3	66.3	83.2	61.3
6252.56	26.0	-1.687	2.404	99.4	70.2	75.3	68.5	86.6	...
6254.26	26.0	-2.430	2.280	85.3	58.5	56.9	...	88.5	...
6265.14	26.0	-2.550	2.176	69.1	43.4	41.0	44.1	59.9	...
6270.23	26.0	-2.609	2.858	30.8	...	...	...	34.5	...
6290.97	26.0	-0.730	4.730	...	...	36.4	19.9	...	...
6297.80	26.0	-2.740	2.223	71.7	39.9	...	...	52.0	...
6301.51	26.0	-0.718	3.654	...	64.3	...	68.5	...	...
6302.50	26.0	-1.110	3.690	62.1	55.3	32.6	...	...	...
6315.31	26.0	-1.230	4.140	...	...	20.7	...	...	...
6322.69	26.0	-2.426	2.588	...	35.4	...	31.1	46.0	...
6330.85	26.0	-1.720	4.733	...	...	...	...	...	9.7
6335.33	26.0	-2.177	2.198	63.6	58.9	60.1	54.3	82.3	55.3
6344.15	26.0	-2.923	2.433	...	...	...	...	39.3	...
6355.04	26.0	-2.291	2.845	64.8	21.8	29.3	...	...	18.3
6358.69	26.0	-4.468	0.859	...	24.3	20.0	...	...	...
6380.75	26.0	-1.376	4.186	40.8	17.3	16.1	...	25.2	...
6393.61	26.0	-1.576	2.433	...	83.3	79.9	75.2	...	82.8
6400.01	26.0	-0.290	3.603	...	89.1	85.2	...	...	...
6408.03	26.0	-1.020	3.690	80.2	47.9	49.9	41.4	66.3	...
6411.66	26.0	-0.718	3.654	...	66.6	71.0	68.2	85.3	...
6430.85	26.0	-2.006	2.176	...	66.9	77.0	68.1	89.6	...
6469.21	26.0	-0.730	4.830	43.8	...	...	...	30.4	...
6475.63	26.0	-2.940	2.560	...	12.3	11.7	...	...	...
6481.87	26.0	-2.984	2.279	51.2	...	...	...	34.7	...
6494.98	26.0	-1.273	2.404	...	98.5	98.3	92.5	...	...

Table C.5: Equivalent Width Measurements, Table 5 of 5, continued

λ (Å)	Ion	loggf	EP	2566-412	2062-482	2398-036	2397-014	2679-442	2682-560
6495.74	26.0	-0.840	4.830	24.5	...	...	...	...	...
6498.94	26.0	-4.687	0.958	19.7	...	...	...	26.1	...
6546.24	26.0	-1.540	2.760	91.2	62.3	...	59.0	...	...
6677.99	26.0	-1.418	2.692	...	79.5	87.2	66.2	98.5	...
6726.67	26.0	-1.070	4.610	...	...	...	...	27.8	...
6733.15	26.0	-1.480	4.640	20.0	...	...	...	...	...
6750.16	26.0	-2.621	2.424	56.6	37.4	30.2	26.1	55.8	28.8
6810.27	26.0	-0.986	4.607	30.3	...	...	...	39.1	...
6820.37	26.0	-1.290	4.638	...	...	...	...	16.7	...
6843.65	26.0	-0.890	4.548	46.0	...	...	...	37.8	...
6855.18	26.0	-0.740	4.560	...	30.4	28.0	29.8	43.9	...
6857.25	26.0	-2.160	4.070	20.5	...	...	...	7.8	...
6858.15	26.0	-0.930	4.608	...	...	...	...	31.0	...
6862.50	26.0	-1.470	4.560	16.9	...	...	...	...	...
6978.85	26.0	-2.450	2.480	66.5	...	31.4	...	63.3	29.6
6999.88	26.0	-1.460	4.100	34.7	...	...	...	31.4	16.4
7022.95	26.0	-1.150	4.190	...	...	19.6	...	...	...
7038.22	26.0	-1.200	4.220	57.5	...	22.5	...	37.2	...
7107.46	26.0	-2.040	4.190	21.6	...	...	...	...	...
7127.57	26.0	-1.360	4.990	14.9	...	...	...	...	...
7130.92	26.0	-0.750	4.220	65.3	37.2	36.7	38.1	59.2	...
7132.98	26.0	-1.630	4.070	24.8	...	...	...	...	...
7142.52	26.0	-1.030	4.950	23.9	...	...	...	15.7	...
7284.84	26.0	-1.700	4.140	29.4	...	...	...	21.4	...
7288.74	26.0	-1.280	4.220	36.1	25.4	...	...	25.8	...
7306.56	26.0	-1.690	4.180	27.5	...	...	...	21.4	...
7411.16	26.0	-0.280	4.280	84.6	55.9	55.6	54.0	79.6	...
7418.67	26.0	-1.380	4.140	38.9	...	...	...	...	...
7440.92	26.0	-0.720	4.910	...	...	...	...	32.0	11.1
7445.75	26.0	0.030	4.260	...	69.4	64.6	61.5	91.7	69.3
7568.91	26.0	-0.940	4.280	56.8	...	32.9	...	54.3	...

Table C.5: Equivalent Width Measurements, Table 5 of 5, continued

λ (Å)	Ion	loggf	EP	2566-412	2062-482	2398-036	2397-014	2679-442	2682-560
7583.79	26.0	-1.890	3.020	51.9	39.6	35.9	35.9	56.2	...
7586.04	26.0	-0.130	4.310	97.1	45.8	52.5	67.8	89.2	...
7588.31	26.0	-1.210	5.030	...	...	...	...	...	6.2
7748.27	26.0	-1.750	2.950	...	43.1	...	46.9	65.2	47.9
7751.12	26.0	-0.850	4.990	...	...	...	...	20.6	...
7780.57	26.0	-0.040	4.470	94.4	49.4	61.2	...	86.4	66.6
7807.92	26.0	-0.620	4.990	...	...	...	...	37.9	...
4178.86	26.1	-2.443	2.583	...	72.8	77.1	88.4	...	...
4233.17	26.1	-1.809	2.583	...	...	...	98.8	...	...
4416.82	26.1	-2.600	2.778	...	64.2	72.5	62.4	59.0	...
4491.40	26.1	-2.640	2.856	...	65.4	67.5	58.7	69.4	...
4508.30	26.1	-2.350	2.856	76.2	70.1	84.0	68.1	73.3	76.8
4520.23	26.1	-2.620	2.807	78.1	65.5	...	67.7	71.5	70.4
4541.52	26.1	-2.970	2.856	...	53.7	...	53.1	...	...
4555.89	26.1	-2.250	2.828	...	...	...	...	74.5	...
4576.34	26.1	-2.920	2.844	58.1	52.4	58.7	45.4	50.3	58.4
4582.83	26.1	-3.062	2.844	43.2	40.5	51.2	40.1	37.5	41.6
4583.84	26.1	-1.740	2.807	...	...	...	95.2	...	...
4620.52	26.1	-3.188	2.828	...	33.8	44.1	36.3	35.9	...
4629.34	26.1	-2.480	2.810	...	79.4	81.4	76.2	85.1	...
4635.31	26.1	-1.580	5.956	...	...	15.5	...	...	...
4656.98	26.1	-3.570	2.891	...	...	...	...	19.1	...
5100.66	26.1	-4.200	2.807	...	...	...	...	...	10.8
5132.67	26.1	-4.090	2.807	27.4	...	...	...	...	...
5197.58	26.1	-2.054	3.230	...	69.7	75.0	64.5	68.9	79.3
5234.63	26.1	-2.210	3.221	69.3	73.0	75.1	60.6	63.4	76.0
5264.81	26.1	-3.233	3.230	53.6	36.9	34.1	24.4	42.6	32.1
5284.11	26.1	-3.200	2.891	66.9	...	48.0	41.2	54.7	...
5325.56	26.1	-2.570	3.221	...	29.2	...	32.8	...	...
5414.08	26.1	-3.482	3.221	35.1	13.1	15.7	...	...	...
5425.26	26.1	-3.390	3.199	...	29.1	30.4	21.8	23.6	...

Table C.5: Equivalent Width Measurements, Table 5 of 5, continued

λ (Å)	Ion	loggf	EP	2566-412	2062-482	2398-036	2397-014	2679-442	2682-560
5534.85	26.1	-2.860	3.245	50.1	50.0	47.0	50.4	56.9	...
6149.25	26.1	-2.840	3.889	...	...	22.6	28.6	...	...
6239.95	26.1	-3.570	3.889	...	...	...	...	...	12.8
6247.56	26.1	-2.430	3.892	39.1	44.2	42.4	37.0	44.9	...
6416.93	26.1	-2.880	3.892	41.8	26.0	29.9	...	...	32.6
6432.68	26.1	-3.500	2.891	...	22.1	29.0	...	...	...
6456.39	26.1	-2.190	3.903	71.6	61.9	...	...	52.7	...
6516.08	26.1	-3.372	2.891	...	36.7	37.8	37.3	...	...
7222.40	26.1	-3.400	3.890	...	...	...	...	13.5	...
7449.34	26.1	-3.310	3.890	...	...	...	...	...	10.4
7711.73	26.1	-2.680	3.900	...	...	33.7	...	...	...
4121.33	27.0	-0.320	0.920	...	96.9	78.3	83.2	...	81.2
5369.56	27.0	-1.590	1.740	...	...	...	...	31.6	...
3858.30	28.0	-0.970	0.420	...	...	93.1	...	...	...
4686.22	28.0	-0.580	3.600	...	22.5	18.0	23.6	47.8	...
4831.18	28.0	-0.320	3.610	...	32.8	32.6	41.7	47.7	30.7
4857.40	28.0	-0.830	3.740	...	...	...	...	26.1	...
4866.27	28.0	-0.210	3.539	47.1	42.7	...	...	62.7	...
4904.42	28.0	-0.190	3.540	...	48.5	54.0	45.5	72.0	43.0
4913.98	28.0	-0.630	3.740	...	...	...	...	30.5	...
4935.83	28.0	-0.380	3.940	45.1	29.1	21.4	23.5	33.2	...
4953.21	28.0	-0.580	3.740	...	18.2	...	...	49.7	...
5082.35	28.0	-0.540	3.660	47.9	14.6	25.8	...	34.2	...
5084.11	28.0	-0.060	3.680	77.1	44.9	47.5	43.0	67.9	...
5088.54	28.0	-1.080	3.850	...	...	...	...	20.2	...
5094.42	28.0	-1.120	3.830	...	...	...	...	9.9	...
5102.97	28.0	-2.660	1.680	...	...	...	...	14.7	...
5115.40	28.0	-0.140	3.830	...	35.0	36.8	41.2	54.4	45.0
5578.72	28.0	-2.640	1.680	...	...	27.1	...	48.0	...
5587.86	28.0	-2.140	1.930	...	...	11.7	...	33.0	...
5589.36	28.0	-1.140	3.900	...	...	...	...	8.7	...

Table C.5: Equivalent Width Measurements, Table 5 of 5, continued

λ (Å)	Ion	loggf	EP	2566-412	2062-482	2398-036	2397-014	2679-442	2682-560
5593.74	28.0	-0.840	3.900	20.4	...	...	...	22.3	...
5682.20	28.0	-0.469	4.100	...	...	...	...	33.0	...
5754.67	28.0	-1.850	1.930	68.6	25.9	...	...	46.7	...
5805.22	28.0	-0.638	4.170	...	...	...	...	24.9	...
5892.87	28.0	-2.340	1.990	...	24.6	25.2	...	...	19.3
6108.12	28.0	-2.430	1.680	58.9	...	18.1	...	33.2	...
6175.37	28.0	-0.535	4.090	40.0	...	...	...	...	...
6176.81	28.0	-0.529	4.090	39.4	...	...	...	28.7	...
6223.98	28.0	-0.910	4.106	33.4	...	...	...	...	...
6314.66	28.0	-1.770	1.930	...	...	...	...	51.1	...
6767.77	28.0	-2.170	1.830	72.0	33.7	40.2	...	58.1	...
6772.31	28.0	-0.987	3.660	...	...	...	...	32.3	...
7122.20	28.0	0.048	3.540	79.3	50.4	51.7	45.5	71.8	43.9
7414.50	28.0	-2.570	1.990	29.9	...	...	23.6	...	...
7422.27	28.0	-0.129	3.630	69.7	46.0	52.2	38.3	60.9	...
7715.59	28.0	-1.010	3.700	28.5	...	...	...	...	...
7727.62	28.0	-0.162	3.680	83.4	49.9	47.8	...	61.9	...
7748.89	28.0	-0.130	3.700	60.8	36.6	27.2	31.5	53.2	35.1
7788.93	28.0	-2.420	1.950	62.5	33.3	32.0	24.3	...	...
7797.59	28.0	-0.180	3.900	...	27.0	...	...	41.6	22.1
5105.54	29.0	-3.720	1.380	66.8	24.2	...	22.9	68.4	...
4722.16	30.0	-0.390	4.030	...	43.3	44.7	39.4	...	42.8
4810.54	30.0	-0.170	4.080	64.7	42.9	49.7	40.1	65.4	...
4607.34	38.0	0.280	0.000	...	...	16.6	...	...	...
4161.79	38.1	-0.600	2.940	...	...	16.7	...	...	...
3950.36	39.1	-0.490	0.100	...	36.2	56.0	54.3	...	...
4883.69	39.1	0.070	1.080	49.6	39.1	39.6	35.4	47.7	42.5
5087.43	39.1	-0.170	1.080	...	24.8	...	21.0	29.4	39.4
5200.41	39.1	-0.570	0.990	...	...	...	...	21.2	...
5205.73	39.1	-0.340	1.030	38.2	...	...	...	...	...
5402.78	39.1	-0.510	1.840	...	...	...	...	13.4	...

Table C.5: Equivalent Width Measurements, Table 5 of 5, continued

λ (Å)	Ion	loggf	EP	2566-412	2062-482	2398-036	2397-014	2679-442	2682-560
4208.99	40.1	-0.510	0.710	...	33.8	31.2	20.9	41.5	...
4496.97	40.1	-0.890	0.710	...	...	...	...	...	67.2
5853.69	56.1	-0.910	0.600	65.3	49.1	47.5	45.9	51.4	50.2
6496.90	56.1	-0.380	0.604	...	84.6	82.7	84.8	91.7	89.0
3995.75	57.1	-0.060	0.170	...	...	...	19.4	...	...

Appendix D

Hyperfine Line Lists

We present below the hyperfine line lists for Sc, V, Mn, Co, Cu, Ba, and La used in the analysis of Chapter 4. For iron peak elements Sc, V, Mn, Co, and Cu, we use the Kurucz line list tables[1]. We assume a solar isotopic composition for Cu (69.17% ^{63}Cu, 30.83% ^{65}Cu; Anders & Grevesse 1989). For neutron capture elements Ba and La, we use line lists from Gallagher et al. (2010) and Lawler et al. (2001), respectively. We assume a Solar System isotopic composition for Ba (2.4% ^{134}Ba, 6.6% ^{135}Ba, 7.9% ^{136}Ba, 11.3% ^{137}Ba, and 71.8% ^{138}Ba). La has only one stable isotope, ^{139}La.

[1] http://kurucz.harvard.edu/linelists.html

Table D.1: Hyperfine Line List

λ (Å)	Ion	EP	log gf	Ref	λ (Å)	Ion	EP	log gf	Ref
4400.379	21.1045	0.605	-1.983	KUR	5641.014	21.1045	1.499	-2.056	KUR
4400.383	21.1045	0.605	-1.175	KUR	5641.016	21.1045	1.499	-2.040	KUR
4400.383	21.1045	0.605	-1.788	KUR	5657.886	21.1045	1.506	-1.126	KUR
4400.387	21.1045	0.605	-1.403	KUR	5657.888	21.1045	1.506	-1.696	KUR
4400.387	21.1045	0.605	-1.735	KUR	5657.893	21.1045	1.506	-1.696	KUR
4400.390	21.1045	0.605	-1.689	KUR	5657.894	21.1045	1.506	-1.524	KUR
4400.390	21.1045	0.605	-1.761	KUR	5657.895	21.1045	1.506	-1.538	KUR
4400.392	21.1045	0.605	-1.983	KUR	5657.899	21.1045	1.506	-1.538	KUR
4400.393	21.1045	0.605	-1.860	KUR	5657.901	21.1045	1.506	-2.220	KUR
4400.393	21.1045	0.605	-2.075	KUR	5657.902	21.1045	1.506	-1.549	KUR
4400.394	21.1045	0.605	-1.788	KUR	5657.904	21.1045	1.506	-1.549	KUR
4400.395	21.1045	0.605	-2.705	KUR	5657.906	21.1045	1.506	-1.722	KUR
4400.396	21.1045	0.605	-1.735	KUR	5657.906	21.1045	1.506	-3.646	KUR
4400.396	21.1045	0.605	-2.082	KUR	5657.908	21.1045	1.506	-1.722	KUR
4400.398	21.1045	0.605	-1.761	KUR	5657.909	21.1045	1.506	-1.898	KUR
4400.398	21.1045	0.605	-1.860	KUR	5667.136	21.1045	1.499	-1.834	KUR
4400.398	21.1045	0.605	-2.559	KUR	5667.141	21.1045	1.499	-2.030	KUR
4400.399	21.1045	0.605	-2.082	KUR	5667.148	21.1045	1.499	-2.030	KUR
5239.813	21.1045	1.454	-0.770	KUR	5667.154	21.1045	1.499	-3.215	KUR
5526.770	21.1045	1.767	-2.665	KUR	5667.157	21.1045	1.499	-2.034	KUR
5526.775	21.1045	1.767	-2.262	KUR	5667.163	21.1045	1.499	-2.034	KUR
5526.779	21.1045	1.767	-1.452	KUR	5667.167	21.1045	1.499	-2.289	KUR
5526.779	21.1045	1.767	-2.050	KUR	5669.038	21.1045	1.499	-1.500	KUR
5526.783	21.1045	1.767	-1.247	KUR	5669.044	21.1045	1.499	-1.597	KUR
5526.783	21.1045	1.767	-1.940	KUR	5669.047	21.1045	1.499	-1.722	KUR
5526.786	21.1045	1.767	-1.181	KUR	5684.190	21.1045	1.506	-1.573	KUR
5526.787	21.1045	1.767	-1.919	KUR	5684.191	21.1045	1.506	-2.062	KUR
5526.788	21.1045	1.767	-1.185	KUR	5684.193	21.1045	1.506	-2.761	KUR
5526.789	21.1045	1.767	-0.523	KUR	5684.204	21.1045	1.506	-1.866	KUR
5526.790	21.1045	1.767	-1.246	KUR	5684.205	21.1045	1.506	-1.946	KUR
5526.790	21.1045	1.767	-2.028	KUR	5684.206	21.1045	1.506	-2.321	KUR
5526.791	21.1045	1.767	-0.644	KUR	5684.215	21.1045	1.506	-2.321	KUR
5526.792	21.1045	1.767	-1.368	KUR	5684.216	21.1045	1.506	-2.066	KUR
5526.793	21.1045	1.767	-0.780	KUR	5684.217	21.1045	1.506	-2.050	KUR
5526.793	21.1045	1.767	-1.551	KUR	6245.621	21.1045	1.506	-1.582	KUR
5526.794	21.1045	1.767	-0.936	KUR	6245.629	21.1045	1.506	-2.322	KUR
5526.795	21.1045	1.767	-1.121	KUR	6245.631	21.1045	1.506	-1.753	KUR
5526.795	21.1045	1.767	-1.355	KUR	6245.636	21.1045	1.506	-3.322	KUR
5526.795	21.1045	1.767	-1.697	KUR	6245.638	21.1045	1.506	-2.139	KUR
5640.989	21.1045	1.499	-1.563	KUR	6245.640	21.1045	1.506	-1.960	KUR
5640.996	21.1045	1.499	-2.052	KUR	6245.644	21.1045	1.506	-2.904	KUR
5641.001	21.1045	1.499	-1.856	KUR	6245.646	21.1045	1.506	-2.106	KUR
5641.001	21.1045	1.499	-2.751	KUR	6245.647	21.1045	1.506	-2.231	KUR
5641.006	21.1045	1.499	-1.936	KUR	6245.650	21.1045	1.506	-2.670	KUR
5641.010	21.1045	1.499	-2.311	KUR	6245.651	21.1045	1.506	-2.165	KUR
5641.010	21.1045	1.499	-2.311	KUR	6245.652	21.1045	1.506	-2.649	KUR

Table D.1: Hyperfine Line List

λ (Å)	Ion	EP	log gf	Ref	λ (Å)	Ion	EP	log gf	Ref
6245.655	21.1045	1.506	-2.524	KUR	4116.444	23.0051	0.275	-1.706	KUR
6245.656	21.1045	1.506	-2.348	KUR	4116.444	23.0051	0.275	-1.961	KUR
6245.657	21.1045	1.506	-2.427	KUR	4116.448	23.0051	0.275	-1.507	KUR
4111.730	23.0051	0.300	-1.232	KUR	4116.448	23.0051	0.275	-1.706	KUR
4111.730	23.0051	0.300	-1.428	KUR	4116.448	23.0051	0.275	-3.614	KUR
4111.735	23.0051	0.300	-1.207	KUR	4116.454	23.0051	0.275	-1.443	KUR
4111.735	23.0051	0.300	-1.218	KUR	4116.454	23.0051	0.275	-1.507	KUR
4111.735	23.0051	0.300	-1.428	KUR	4116.454	23.0051	0.275	-2.371	KUR
4111.742	23.0051	0.300	-1.080	KUR	4116.463	23.0051	0.275	-1.443	KUR
4111.742	23.0051	0.300	-1.104	KUR	4116.463	23.0051	0.275	-1.474	KUR
4111.742	23.0051	0.300	-1.207	KUR	4116.463	23.0051	0.275	-1.654	KUR
4111.751	23.0051	0.300	-0.913	KUR	4116.474	23.0051	0.275	-1.248	KUR
4111.751	23.0051	0.300	-1.061	KUR	4116.474	23.0051	0.275	-1.474	KUR
4111.751	23.0051	0.300	-1.104	KUR	4116.474	23.0051	0.275	-1.655	KUR
4111.762	23.0051	0.300	-0.744	KUR	4116.486	23.0051	0.275	-0.956	KUR
4111.762	23.0051	0.300	-1.061	KUR	4116.486	23.0051	0.275	-1.655	KUR
4111.762	23.0051	0.300	-1.072	KUR	4379.180	23.0051	0.300	-0.846	KUR
4111.776	23.0051	0.300	-0.585	KUR	4379.185	23.0051	0.300	-0.728	KUR
4111.776	23.0051	0.300	-1.072	KUR	4379.185	23.0051	0.300	-1.298	KUR
4111.776	23.0051	0.300	-1.149	KUR	4379.193	23.0051	0.300	-0.610	KUR
4111.792	23.0051	0.300	-0.437	KUR	4379.193	23.0051	0.300	-1.087	KUR
4111.792	23.0051	0.300	-1.149	KUR	4379.193	23.0051	0.300	-2.298	KUR
4111.792	23.0051	0.300	-1.364	KUR	4379.203	23.0051	0.300	-0.498	KUR
4111.811	23.0051	0.300	-0.301	KUR	4379.203	23.0051	0.300	-0.991	KUR
4111.811	23.0051	0.300	-1.364	KUR	4379.203	23.0051	0.300	-2.091	KUR
4115.142	23.0051	0.286	-1.735	KUR	4379.216	23.0051	0.300	-0.394	KUR
4115.145	23.0051	0.286	-1.455	KUR	4379.216	23.0051	0.300	-0.955	KUR
4115.145	23.0051	0.286	-1.735	KUR	4379.216	23.0051	0.300	-2.063	KUR
4115.145	23.0051	0.286	-2.756	KUR	4379.232	23.0051	0.300	-0.298	KUR
4115.149	23.0051	0.286	-1.317	KUR	4379.232	23.0051	0.300	-0.971	KUR
4115.149	23.0051	0.286	-1.455	KUR	4379.232	23.0051	0.300	-2.143	KUR
4115.149	23.0051	0.286	-2.057	KUR	4379.250	23.0051	0.300	-0.208	KUR
4115.155	23.0051	0.286	-1.251	KUR	4379.250	23.0051	0.300	-1.053	KUR
4115.155	23.0051	0.286	-1.317	KUR	4379.250	23.0051	0.300	-2.335	KUR
4115.155	23.0051	0.286	-1.610	KUR	4379.271	23.0051	0.300	-0.124	KUR
4115.164	23.0051	0.286	-1.244	KUR	4379.271	23.0051	0.300	-1.271	KUR
4115.164	23.0051	0.286	-1.251	KUR	4379.271	23.0051	0.300	-2.724	KUR
4115.164	23.0051	0.286	-1.279	KUR	4406.582	23.0051	0.300	-1.830	KUR
4115.175	23.0051	0.286	-1.016	KUR	4406.582	23.0051	0.300	-2.026	KUR
4115.175	23.0051	0.286	-1.244	KUR	4406.588	23.0051	0.300	-1.805	KUR
4115.175	23.0051	0.286	-1.309	KUR	4406.588	23.0051	0.300	-1.816	KUR
4115.188	23.0051	0.286	-0.797	KUR	4406.588	23.0051	0.300	-2.026	KUR
4115.188	23.0051	0.286	-1.309	KUR	4406.596	23.0051	0.300	-1.678	KUR
4115.188	23.0051	0.286	-1.513	KUR	4406.596	23.0051	0.300	-1.702	KUR
4115.203	23.0051	0.286	-0.610	KUR	4406.596	23.0051	0.300	-1.805	KUR
4115.203	23.0051	0.286	-1.513	KUR	4406.606	23.0051	0.300	-1.511	KUR

Table D.1: Hyperfine Line List

λ (Å)	Ion	EP	log gf	Ref	λ (Å)	Ion	EP	log gf	Ref
4406.606	23.0051	0.300	-1.659	KUR	5627.624	23.0051	1.080	-1.743	KUR
4406.606	23.0051	0.300	-1.702	KUR	5627.624	23.0051	1.080	-1.947	KUR
4406.619	23.0051	0.300	-1.342	KUR	5627.634	23.0051	1.080	-1.450	KUR
4406.619	23.0051	0.300	-1.659	KUR	5627.634	23.0051	1.080	-1.678	KUR
4406.619	23.0051	0.300	-1.670	KUR	5627.634	23.0051	1.080	-1.743	KUR
4406.635	23.0051	0.300	-1.183	KUR	5627.642	23.0051	1.080	-1.678	KUR
4406.635	23.0051	0.300	-1.670	KUR	5627.642	23.0051	1.080	-1.685	KUR
4406.635	23.0051	0.300	-1.747	KUR	5627.642	23.0051	1.080	-1.713	KUR
4406.654	23.0051	0.300	-1.035	KUR	5627.649	23.0051	1.080	-1.685	KUR
4406.654	23.0051	0.300	-1.747	KUR	5627.649	23.0051	1.080	-1.751	KUR
4406.654	23.0051	0.300	-1.962	KUR	5627.649	23.0051	1.080	-2.044	KUR
4406.675	23.0051	0.300	-0.899	KUR	5627.654	23.0051	1.080	-1.751	KUR
4406.675	23.0051	0.300	-1.962	KUR	5627.654	23.0051	1.080	-1.889	KUR
4864.703	23.0051	0.017	-2.164	KUR	5627.654	23.0051	1.080	-2.491	KUR
4864.708	23.0051	0.017	-2.164	KUR	5627.658	23.0051	1.080	-1.889	KUR
4864.708	23.0051	0.017	-2.340	KUR	5627.658	23.0051	1.080	-2.169	KUR
4864.715	23.0051	0.017	-2.000	KUR	5627.658	23.0051	1.080	-3.190	KUR
4864.715	23.0051	0.017	-2.465	KUR	5627.659	23.0051	1.080	-2.169	KUR
4864.715	23.0051	0.017	-2.590	KUR	5703.574	23.0051	1.050	-1.415	KUR
4864.725	23.0051	0.017	-1.992	KUR	5703.574	23.0051	1.050	-1.415	KUR
4864.725	23.0051	0.017	-2.026	KUR	5703.574	23.0051	1.050	-1.716	KUR
4864.725	23.0051	0.017	-3.018	KUR	5703.575	23.0051	1.050	-0.778	KUR
4864.738	23.0051	0.017	-1.743	KUR	5703.575	23.0051	1.050	-0.994	KUR
4864.738	23.0051	0.017	-2.153	KUR	5703.575	23.0051	1.050	-1.243	KUR
4864.753	23.0051	0.017	-1.527	KUR	5703.575	23.0051	1.050	-1.251	KUR
4875.462	23.0051	0.040	-2.616	KUR	5703.575	23.0051	1.050	-1.277	KUR
4875.464	23.0051	0.040	-2.331	KUR	5703.575	23.0051	1.050	-1.404	KUR
4875.464	23.0051	0.040	-2.586	KUR	5703.575	23.0051	1.050	-1.591	KUR
4875.468	23.0051	0.040	-2.143	KUR	5703.575	23.0051	1.050	-1.841	KUR
4875.468	23.0051	0.040	-2.586	KUR	5703.575	23.0051	1.050	-2.269	KUR
4875.468	23.0051	0.040	-2.637	KUR	5670.832	23.0051	1.080	-1.093	KUR
4875.474	23.0051	0.040	-2.052	KUR	5670.832	23.0051	1.080	-2.101	KUR
4875.474	23.0051	0.040	-2.198	KUR	5670.832	23.0051	1.080	-3.402	KUR
4875.474	23.0051	0.040	-2.762	KUR	5670.844	23.0051	1.080	-1.198	KUR
4875.481	23.0051	0.040	-1.943	KUR	5670.844	23.0051	1.080	-1.890	KUR
4875.481	23.0051	0.040	-2.030	KUR	5670.844	23.0051	1.080	-3.004	KUR
4875.481	23.0051	0.040	-2.984	KUR	5670.854	23.0051	1.080	-1.314	KUR
4875.491	23.0051	0.040	-1.745	KUR	5670.854	23.0051	1.080	-1.817	KUR
4875.491	23.0051	0.040	-2.084	KUR	5670.854	23.0051	1.080	-2.800	KUR
4875.491	23.0051	0.040	-3.394	KUR	5670.863	23.0051	1.080	-1.443	KUR
4875.503	23.0051	0.040	-1.581	KUR	5670.863	23.0051	1.080	-1.811	KUR
4875.503	23.0051	0.040	-2.280	KUR	5670.863	23.0051	1.080	-2.703	KUR
4875.517	23.0051	0.040	-1.440	KUR	5670.870	23.0051	1.080	-1.589	KUR
5627.612	23.0051	1.080	-1.044	KUR	5670.870	23.0051	1.080	-1.858	KUR
5627.612	23.0051	1.080	-1.947	KUR	5670.870	23.0051	1.080	-2.703	KUR
5627.624	23.0051	1.080	-1.231	KUR	5670.875	23.0051	1.080	-1.759	KUR

Table D.1: Hyperfine Line List

λ (Å)	Ion	EP	log gf	Ref	λ (Å)	Ion	EP	log gf	Ref
5670.875	23.0051	1.080	-1.963	KUR	6090.218	23.0051	1.080	-1.195	KUR
5670.875	23.0051	1.080	-2.858	KUR	6090.218	23.0051	1.080	-1.336	KUR
5670.878	23.0051	1.080	-1.963	KUR	6090.223	23.0051	1.080	-1.282	KUR
5670.878	23.0051	1.080	-2.159	KUR	6090.223	23.0051	1.080	-1.450	KUR
5670.880	23.0051	1.080	-2.226	KUR	6090.225	23.0051	1.080	-2.646	KUR
5727.027	23.0051	1.080	-0.685	KUR	6090.226	23.0051	1.080	-1.304	KUR
5727.027	23.0051	1.080	-1.693	KUR	6090.227	23.0051	1.080	-1.838	KUR
5727.027	23.0051	1.080	-2.994	KUR	6090.228	23.0051	1.080	-2.236	KUR
5727.039	23.0051	1.080	-0.790	KUR	6090.229	23.0051	1.080	-1.395	KUR
5727.039	23.0051	1.080	-1.482	KUR	6090.231	23.0051	1.080	-1.583	KUR
5727.039	23.0051	1.080	-2.596	KUR	6090.231	23.0051	1.080	-2.014	KUR
5727.049	23.0051	1.080	-0.906	KUR	6090.232	23.0051	1.080	-1.889	KUR
5727.049	23.0051	1.080	-1.409	KUR	6090.233	23.0051	1.080	-1.838	KUR
5727.049	23.0051	1.080	-2.392	KUR	6090.233	23.0051	1.080	-1.868	KUR
5727.058	23.0051	1.080	-1.035	KUR	3577.838	25.0055	2.113	-1.044	KUR
5727.058	23.0051	1.080	-1.403	KUR	3577.838	25.0055	2.113	-1.555	KUR
5727.058	23.0051	1.080	-2.295	KUR	3577.838	25.0055	2.113	-2.652	KUR
5727.065	23.0051	1.080	-1.181	KUR	3577.845	25.0055	2.113	-0.911	KUR
5727.065	23.0051	1.080	-1.450	KUR	3577.845	25.0055	2.113	-1.367	KUR
5727.065	23.0051	1.080	-2.295	KUR	3577.845	25.0055	2.113	-2.521	KUR
5727.070	23.0051	1.080	-1.351	KUR	3577.853	25.0055	2.113	-0.781	KUR
5727.070	23.0051	1.080	-1.555	KUR	3577.853	25.0055	2.113	-1.312	KUR
5727.070	23.0051	1.080	-2.450	KUR	3577.853	25.0055	2.113	-2.618	KUR
5727.074	23.0051	1.080	-1.555	KUR	3577.864	25.0055	2.113	-0.659	KUR
5727.074	23.0051	1.080	-1.751	KUR	3577.864	25.0055	2.113	-1.350	KUR
5727.076	23.0051	1.080	-1.818	KUR	3577.864	25.0055	2.113	-2.953	KUR
6039.710	23.0051	1.063	-1.995	KUR	3577.877	25.0055	2.113	-0.546	KUR
6039.715	23.0051	1.063	-1.814	KUR	3577.877	25.0055	2.113	-1.538	KUR
6039.716	23.0051	1.063	-1.296	KUR	3577.893	25.0055	2.113	-0.442	KUR
6039.719	23.0051	1.063	-1.783	KUR	4055.519	25.0055	2.141	-1.721	KUR
6039.720	23.0051	1.063	-1.588	KUR	4055.520	25.0055	2.141	-1.466	KUR
6039.723	23.0051	1.063	-1.847	KUR	4055.523	25.0055	2.141	-1.523	KUR
6039.723	23.0051	1.063	-1.994	KUR	4055.524	25.0055	2.141	-1.402	KUR
6039.726	23.0051	1.063	-2.046	KUR	4055.525	25.0055	2.141	-1.721	KUR
6039.726	23.0051	1.063	-2.711	KUR	4055.529	25.0055	2.141	-1.458	KUR
6039.727	23.0051	1.063	-1.995	KUR	4055.531	25.0055	2.141	-1.227	KUR
6039.728	23.0051	1.063	-3.954	KUR	4055.532	25.0055	2.141	-1.523	KUR
6039.729	23.0051	1.063	-1.814	KUR	4055.538	25.0055	2.141	-1.489	KUR
6039.729	23.0051	1.063	-2.301	KUR	4055.539	25.0055	2.141	-1.035	KUR
6039.730	23.0051	1.063	-1.783	KUR	4055.541	25.0055	2.141	-1.458	KUR
6039.731	23.0051	1.063	-1.847	KUR	4055.548	25.0055	2.141	-1.671	KUR
6039.731	23.0051	1.063	-2.046	KUR	4055.550	25.0055	2.141	-0.850	KUR
6090.199	23.0051	1.080	-0.692	KUR	4055.552	25.0055	2.141	-1.489	KUR
6090.207	23.0051	1.080	-0.833	KUR	4055.564	25.0055	2.141	-0.679	KUR
6090.213	23.0051	1.080	-0.997	KUR	4055.565	25.0055	2.141	-1.671	KUR
6090.213	23.0051	1.080	-1.532	KUR	4709.693	25.0055	2.886	-0.949	KUR

Table D.1: Hyperfine Line List

λ (Å)	Ion	EP	log gf	Ref	λ (Å)	Ion	EP	log gf	Ref
4709.698	25.0055	2.886	-1.941	KUR	6013.478	25.0055	3.070	-0.766	KUR
4709.701	25.0055	2.886	-1.941	KUR	6013.499	25.0055	3.070	-0.978	KUR
4709.706	25.0055	2.886	-1.120	KUR	6013.518	25.0055	3.070	-1.251	KUR
4709.711	25.0055	2.886	-1.759	KUR	6013.527	25.0055	3.070	-1.455	KUR
4709.713	25.0055	2.886	-1.759	KUR	6013.533	25.0055	3.070	-1.661	KUR
4709.717	25.0055	2.886	-1.305	KUR	6013.538	25.0055	3.070	-1.309	KUR
4709.721	25.0055	2.886	-1.728	KUR	6013.547	25.0055	3.070	-1.330	KUR
4709.723	25.0055	2.886	-1.728	KUR	6013.552	25.0055	3.070	-1.485	KUR
4709.726	25.0055	2.886	-1.497	KUR	6013.562	25.0055	3.070	-1.807	KUR
4709.729	25.0055	2.886	-1.793	KUR	6013.566	25.0055	3.070	-1.853	KUR
4709.730	25.0055	2.886	-1.793	KUR	6013.566	25.0055	3.070	-2.409	KUR
4709.733	25.0055	2.886	-1.672	KUR	6013.567	25.0055	3.070	-2.029	KUR
4709.735	25.0055	2.886	-1.991	KUR	6021.746	25.0055	3.073	-2.668	KUR
4709.736	25.0055	2.886	-1.991	KUR	6021.772	25.0055	3.073	-1.451	KUR
4709.737	25.0055	2.886	-1.736	KUR	6021.774	25.0055	3.073	-2.316	KUR
4739.072	25.0055	2.939	-1.041	KUR	6021.795	25.0055	3.073	-1.275	KUR
4739.072	25.0055	2.939	-1.518	KUR	6021.798	25.0055	3.073	-2.191	KUR
4739.088	25.0055	2.939	-1.416	KUR	6021.804	25.0055	3.073	-0.533	KUR
4739.088	25.0055	2.939	-1.518	KUR	6021.813	25.0055	3.073	-1.249	KUR
4739.088	25.0055	2.939	-1.590	KUR	6021.817	25.0055	3.073	-2.270	KUR
4739.100	25.0055	2.939	-1.416	KUR	6021.821	25.0055	3.073	-0.673	KUR
4739.101	25.0055	2.939	-1.548	KUR	6021.827	25.0055	3.073	-1.316	KUR
4739.101	25.0055	2.939	-3.125	KUR	6021.834	25.0055	3.073	-0.831	KUR
4739.109	25.0055	2.939	-1.548	KUR	6021.837	25.0055	3.073	-1.492	KUR
4739.109	25.0055	2.939	-1.916	KUR	6021.843	25.0055	3.073	-1.015	KUR
4761.499	25.0055	2.951	-1.025	KUR	6021.846	25.0055	3.073	-1.522	KUR
4761.507	25.0055	2.951	-0.564	KUR	6021.847	25.0055	3.073	-1.237	KUR
4761.511	25.0055	2.951	-0.928	KUR	4121.294	27.0059	0.922	-0.993	KUR
4761.519	25.0055	2.951	-1.041	KUR	4121.301	27.0059	0.922	-1.098	KUR
4761.524	25.0055	2.951	-0.928	KUR	4121.308	27.0059	0.922	-1.214	KUR
4761.536	25.0055	2.951	-1.472	KUR	4121.313	27.0059	0.922	-1.343	KUR
5432.506	25.0055	0.000	-4.377	KUR	4121.316	27.0059	0.922	-2.001	KUR
5432.510	25.0055	0.000	-5.155	KUR	4121.318	27.0059	0.922	-1.489	KUR
5432.535	25.0055	0.000	-5.155	KUR	4121.321	27.0059	0.922	-1.790	KUR
5432.538	25.0055	0.000	-4.640	KUR	4121.322	27.0059	0.922	-1.659	KUR
5432.541	25.0055	0.000	-4.992	KUR	4121.324	27.0059	0.922	-1.717	KUR
5432.561	25.0055	0.000	-4.992	KUR	4121.326	27.0059	0.922	-1.863	KUR
5432.564	25.0055	0.000	-4.971	KUR	4121.327	27.0059	0.922	-1.711	KUR
5432.566	25.0055	0.000	-4.987	KUR	4121.329	27.0059	0.922	-1.758	KUR
5432.580	25.0055	0.000	-4.987	KUR	4121.329	27.0059	0.922	-2.126	KUR
5432.583	25.0055	0.000	-5.418	KUR	4121.331	27.0059	0.922	-1.863	KUR
5432.584	25.0055	0.000	-5.089	KUR	4121.332	27.0059	0.922	-2.059	KUR
5432.594	25.0055	0.000	-5.089	KUR	4121.336	27.0059	0.922	-2.758	KUR
5432.595	25.0055	0.000	-6.117	KUR	4121.336	27.0059	0.922	-3.302	KUR
5432.596	25.0055	0.000	-5.351	KUR	4121.337	27.0059	0.922	-2.603	KUR
5432.601	25.0055	0.000	-5.351	KUR	4121.338	27.0059	0.922	-2.603	KUR

Table D.1: Hyperfine Line List

λ (Å)	Ion	EP	log gf	Ref	λ (Å)	Ion	EP	log gf	Ref
4121.338	27.0059	0.922	-2.700	KUR	5218.202	29.0063	3.814	-0.758	KUR
4121.338	27.0059	0.922	-2.904	KUR	5218.202	29.0063	3.814	-1.904	KUR
5352.045	27.0059	3.574	0.060	KUR	5218.202	29.0065	3.814	0.050	KUR
5369.569	27.0059	1.739	-2.854	KUR	5218.202	29.0065	3.814	-0.758	KUR
5369.569	27.0059	1.739	-2.854	KUR	5218.202	29.0065	3.814	-1.904	KUR
5369.569	27.0059	1.739	-3.155	KUR	5782.053	29.0065	1.641	-2.924	KUR
5369.577	27.0059	1.739	-2.690	KUR	5782.059	29.0063	1.641	-2.924	KUR
5369.577	27.0059	1.739	-2.716	KUR	5782.062	29.0065	1.641	-3.225	KUR
5369.577	27.0059	1.739	-3.030	KUR	5782.066	29.0063	1.641	-3.225	KUR
5369.590	27.0059	1.739	-2.433	KUR	5782.074	29.0065	1.641	-2.526	KUR
5369.590	27.0059	1.739	-2.682	KUR	5782.078	29.0063	1.641	-2.526	KUR
5369.590	27.0059	1.739	-3.280	KUR	5782.105	29.0065	1.641	-2.526	KUR
5369.607	27.0059	1.739	-2.217	KUR	5782.106	29.0063	1.641	-2.526	KUR
5369.607	27.0059	1.739	-2.843	KUR	5782.117	29.0063	1.641	-2.526	KUR
5369.607	27.0059	1.739	-3.708	KUR	5782.117	29.0065	1.641	-2.526	KUR
5105.503	29.0065	1.388	-3.720	KUR	5782.170	29.0063	1.641	-2.079	KUR
5105.505	29.0063	1.388	-3.720	KUR	5782.173	29.0065	1.641	-2.079	KUR
5105.506	29.0065	1.388	-2.766	KUR	4554.001	56.1137	0.000	-0.636	GAL
5105.509	29.0063	1.388	-2.766	KUR	4554.002	56.1137	0.000	-1.033	GAL
5105.509	29.0065	1.388	-2.720	KUR	4554.002	56.1137	0.000	-0.636	GAL
5105.510	29.0065	1.388	-3.896	KUR	4554.003	56.1135	0.000	-0.636	GAL
5105.511	29.0063	1.388	-2.720	KUR	4554.004	56.1135	0.000	-1.033	GAL
5105.512	29.0063	1.388	-3.896	KUR	4554.004	56.1135	0.000	-0.636	GAL
5105.515	29.0065	1.388	-2.653	KUR	4554.034	56.1134	0.000	0.170	GAL
5105.517	29.0063	1.388	-2.653	KUR	4554.034	56.1136	0.000	0.170	GAL
5105.519	29.0065	1.388	-2.398	KUR	4554.036	56.1138	0.000	0.170	GAL
5105.520	29.0063	1.388	-2.398	KUR	4554.050	56.1135	0.000	-0.189	GAL
5105.530	29.0065	1.388	-2.750	KUR	4554.053	56.1135	0.000	-0.636	GAL
5105.531	29.0063	1.388	-2.750	KUR	4554.053	56.1137	0.000	-0.189	GAL
5105.536	29.0063	1.388	-2.148	KUR	4554.054	56.1135	0.000	-1.337	GAL
5105.536	29.0065	1.388	-2.148	KUR	4554.056	56.1137	0.000	-0.636	GAL
5105.558	29.0063	1.388	-1.942	KUR	4554.057	56.1137	0.000	-1.337	GAL
5105.560	29.0065	1.388	-1.942	KUR	5853.686	56.1137	0.604	-2.066	GAL
5218.190	29.0065	3.814	-0.728	KUR	5853.687	56.1135	0.604	-2.066	GAL
5218.191	29.0063	3.814	-0.728	KUR	5853.687	56.1137	0.604	-2.009	GAL
5218.192	29.0065	3.814	-0.406	KUR	5853.688	56.1135	0.604	-2.009	GAL
5218.192	29.0065	3.814	-0.774	KUR	5853.689	56.1135	0.604	-2.215	GAL
5218.193	29.0063	3.814	-0.406	KUR	5853.689	56.1137	0.604	-2.215	GAL
5218.193	29.0063	3.814	-0.774	KUR	5853.690	56.1134	0.604	-1.010	GAL
5218.196	29.0063	3.814	-0.156	KUR	5853.690	56.1135	0.604	-2.620	GAL
5218.196	29.0063	3.814	-0.661	KUR	5853.690	56.1135	0.604	-1.914	GAL
5218.196	29.0063	3.814	-1.728	KUR	5853.690	56.1135	0.604	-1.466	GAL
5218.196	29.0065	3.814	-0.156	KUR	5853.690	56.1136	0.604	-1.010	GAL
5218.196	29.0065	3.814	-0.661	KUR	5853.690	56.1137	0.604	-2.620	GAL
5218.196	29.0065	3.814	-1.728	KUR	5853.690	56.1137	0.604	-1.914	GAL
5218.202	29.0063	3.814	0.050	KUR	5853.690	56.1137	0.604	-1.466	GAL

Table D.1: Hyperfine Line List

λ (Å)	Ion	EP	log gf	Ref	λ (Å)	Ion	EP	log gf	Ref
5853.690	56.1138	0.604	-1.010	GAL	3988.573	57.1139	0.403	-1.263	LAW
5853.691	56.1135	0.604	-2.215	GAL	3995.708	57.1139	0.173	-1.282	LAW
5853.692	56.1137	0.604	-2.215	GAL	3995.711	57.1139	0.173	-1.458	LAW
5853.693	56.1135	0.604	-2.009	GAL	3995.716	57.1139	0.173	-1.109	LAW
5853.693	56.1137	0.604	-2.009	GAL	3995.721	57.1139	0.173	-3.209	LAW
5853.694	56.1135	0.604	-2.066	GAL	3995.724	57.1139	0.173	-1.282	LAW
5853.694	56.1137	0.604	-2.066	GAL	3995.728	57.1139	0.173	-1.098	LAW
6496.898	56.1137	0.604	-1.886	GAL	3995.734	57.1139	0.173	-1.780	LAW
6496.899	56.1135	0.604	-1.886	GAL	3995.738	57.1139	0.173	-1.109	LAW
6496.901	56.1137	0.604	-1.186	GAL	3995.743	57.1139	0.173	-1.256	LAW
6496.902	56.1135	0.604	-1.186	GAL	3995.750	57.1139	0.173	-1.084	LAW
6496.906	56.1135	0.604	-0.739	GAL	3995.757	57.1139	0.173	-1.098	LAW
6496.906	56.1137	0.604	-0.739	GAL	3995.771	57.1139	0.173	-0.686	LAW
6496.910	56.1134	0.604	-0.380	GAL	3995.779	57.1139	0.173	-1.256	LAW
6496.910	56.1136	0.604	-0.380	GAL	4086.695	57.1139	0.000	-1.266	LAW
6496.910	56.1138	0.604	-0.380	GAL	4086.698	57.1139	0.000	-1.108	LAW
6496.916	56.1135	0.604	-1.583	GAL	4086.702	57.1139	0.000	-1.119	LAW
6496.916	56.1137	0.604	-1.583	GAL	4086.705	57.1139	0.000	-1.292	LAW
6496.917	56.1135	0.604	-1.186	GAL	4086.707	57.1139	0.000	-0.696	LAW
6496.918	56.1137	0.604	-1.186	GAL	4086.708	57.1139	0.000	-1.094	LAW
6496.920	56.1135	0.604	-1.186	GAL	4086.710	57.1139	0.000	-1.790	LAW
6496.922	56.1137	0.604	-1.186	GAL	4086.711	57.1139	0.000	-3.219	LAW
3988.445	57.1139	0.403	-1.362	LAW	4086.712	57.1139	0.000	-1.468	LAW
3988.446	57.1139	0.403	-1.839	LAW	4086.717	57.1139	0.000	-1.292	LAW
3988.452	57.1139	0.403	-1.140	LAW	4086.719	57.1139	0.000	-1.119	LAW
3988.454	57.1139	0.403	-19.790	LAW	4086.720	57.1139	0.000	-1.108	LAW
3988.454	57.1139	0.403	-1.362	LAW	4086.721	57.1139	0.000	-1.266	LAW
3988.464	57.1139	0.403	-1.041	LAW	4333.718	57.1139	0.173	-1.282	LAW
3988.466	57.1139	0.403	-1.985	LAW	4333.723	57.1139	0.173	-1.109	LAW
3988.468	57.1139	0.403	-1.140	LAW	4333.725	57.1139	0.173	-1.458	LAW
3988.482	57.1139	0.403	-1.015	LAW	4333.731	57.1139	0.173	-1.098	LAW
3988.484	57.1139	0.403	-1.355	LAW	4333.733	57.1139	0.173	-3.209	LAW
3988.486	57.1139	0.403	-1.041	LAW	4333.740	57.1139	0.173	-1.282	LAW
3988.504	57.1139	0.403	-1.068	LAW	4333.742	57.1139	0.173	-1.256	LAW
3988.507	57.1139	0.403	-0.969	LAW	4333.744	57.1139	0.173	-1.780	LAW
3988.510	57.1139	0.403	-1.015	LAW	4333.753	57.1139	0.173	-1.109	LAW
3988.532	57.1139	0.403	-1.263	LAW	4333.758	57.1139	0.173	-1.084	LAW
3988.535	57.1139	0.403	-0.683	LAW	4333.771	57.1139	0.173	-1.098	LAW
3988.538	57.1139	0.403	-1.068	LAW	4333.775	57.1139	0.173	-0.686	LAW
3988.569	57.1139	0.403	-0.455	LAW	4333.791	57.1139	0.173	-1.256	LAW